NO_x Removal by LNT-SCR Dual-layer Catalysts

A Dissertation

Presented to

the Faculty of the Department of Chemical and Biomolecular Engineering

University of Houston

In Partial Fulfillment

of the Requirements for the Degree

Doctor of Philosophy

in Chemical Engineering

by

Yi Liu

December 2012

NO_x Removal by LNT-SCR Dual-Layer Catalysts

_____

Yi Liu

Approved:

_____

Co-Chair of the Committee
Dan Luss, Professor,
Chemical and Biomolecular Engineering

_____

Co-Chair of the Committee
Michael P. Harold, Professor,
Chemical and Biomolecular Engineering

Committee Members:

_____

Vemuri Balakotaiah, Professor,
Chemical and Biomolecular Engineering

_____

Shankar Chellam, Professor,
Civil and Environmental Engineering

_____

Allan Jacobson, Professor,
Department of Chemistry

_____

Suresh K. Khator, Associate Dean,
Cullen College of Engineering

_____

Ramanan Krishnamoorti, Professor and Chair,
Chemical and Biomolecular Engineering

Acknowledgements

I would like to thank my PhD advisors, Profs. Dan Luss and Michael P. Harold, for their support during the past four years. Dr. Luss brought me to this lab and gave me the freedom to study and think without restriction. I also learnt a lot from his personality and research attitudes. Dr. Harold supported me from every aspect during my research. Discussions with him were always productive and inspiring. I deeply appreciate the help from Dr. Luss and Dr. Harold during my career planning.

I am grateful to my family, my wife, father, mother and grandparents. They shared my happiness and sadness for the past four years. This was not an easy journey. It is my great treasure to have their support. I sincerely thank my wife, Emillia Meiting Huang. She accompanies me, takes care of my life and is going to give birth to our first child, Katheryn Liu. I devote this dissertation to my wife and the coming baby.

I want to thank my colleagues both in the University of Houston and in Cummins. It was always enjoyable to have technical discussions with them. I also had a very good time hanging out with them. They made my life exciting and colorful in Houston and in Columbus.

NO_x Removal by LNT-SCR Dual-layer Catalysts

An Abstract

of a

Dissertation

Presented to

the Faculty of the Department of Chemical and Biomolecular Engineering

University of Houston

In Partial Fulfillment

of the Requirements for the Degree

Doctor of Philosophy

in Chemical Engineering

by

Yi Liu

December 2012

Abstract

The increasingly strict emission standards have driven the progress of NO_x storage and reduction (NSR) technology. NO_x is stored in a lean NO_x trap (LNT) catalyst during fuel-lean mode and reduced to N_2 during fuel-rich mode.

First, we investigated the impact of ceria on NSR in an Pt/Ce LNT catalyst. The physisorbed oxygen over the ceria-containing LNT catalyst led to a spatio-temporal temperature rise in the monolith upstream after the cyclic introduction of H_2/CO to a pre-oxidized catalyst. The stored oxygen over ceria enhanced NO storage by in-situ NO_2 formation, while it competed with NO_2 for storage sites. During the NO_x reduction over the Pt/Ceria, the Pt surface purgation was the first step and the oxygen reduction preceded the NO_x reduction.

Second, we studied the NSR by dual-layer catalysts consisting of a selective catalytic reduction (SCR) catalyst layer on top of a LNT catalyst. During periodic switching between lean and rich feeds, the LNT layer reduced NO_x to N_2 and NH_3. The SCR layer trapped the latter leading to additional NO_x reduction.

The dual-layer catalysts exhibited high N_2 selectivity and low NH_3 selectivity over the temperature range of 150-400 ºC. The NO_x conversion was incomplete due to undesired NH_3 oxidation. The dual-layer catalyst has a higher NO_x conversion and N_2 selectivity than the LNT catalyst when H_2O and CO_2 were present in the feed.

Ceria was used to adjust the dual-layer catalyst performance. The ceria addition increased NO_x storage capacity, promoted hydrothermal durability and mitigated CO poisoning. However, ceria decreased the high-temperature NO_x conversion by promoting NH_3 oxidation. Ceria zoning led to the highest NO_x reduction for both low- and high- temperatures due to the beneficial interaction of ceria and H_2.

The impact of catalyst design and operation strategy was evaluated. The low-temperature NO_x conversion of an aged dual-layer catalyst was increased by a high SCR catalyst loading. The ratio of lean to rich feed duration and the total cycle time were optimized to improve the NO_x conversion. The results suggest the dual-layer catalyst could be used to reduce precious metal loading and improve the fuel economy.

Table of Contents

List of Figures

List of Tables

Nomenclatures

DOC	Diesel Oxidation Catalyst
DRIFTS	Diffuse Reflection Infrared Spectrometer
EGR	Exhaust Gas Recirculation
EPA	Environmental Protection Agency
FTIR	Fourier Transform Infrared Spectrometer
HC	Hydrocarbon
LNT	Lean NO_x trap
NSR	NO_x Storage and Reduction
MS	Mass Spectroscopy
SCR	Selective Catalytic Reduction
SEM	Scanning Electron Microscope
TWC	Three-Way Catalyst
TEM	Transmission Electron Microscope
TPD	Temperature Programmed Desorption
TPR	Temperature Programmed Reduction
XRD	X-Ray Diffraction

Chapter 1 Introduction and Background

1.1 Introduction

Mixtures of NO and NO_2, referred to NO_x, are air pollutants. Breathing of NO_x irritates the lungs and causes coughing. The atmospheric NO_x leads to the acid rain. The reactions among NO_x and other pollutants, such as hydrocarbons, generate smog. Hence, it is important to reduce the NO_x emission for environmental protection. Most of NO_x emission is from vehicles. Figure 1-1 shows the 2011 distribution of NO_x emissions based on the data from U.S. Environmental Protection Agency [1]. Fuel consumption, industrial processes and other processes contribute to 49% of the total NO_x emission, while 51% of the total NO_x emission is from the tailpipes of passenger cars, trucks and construction machines. Most of these are powered by lean burn diesel engines.

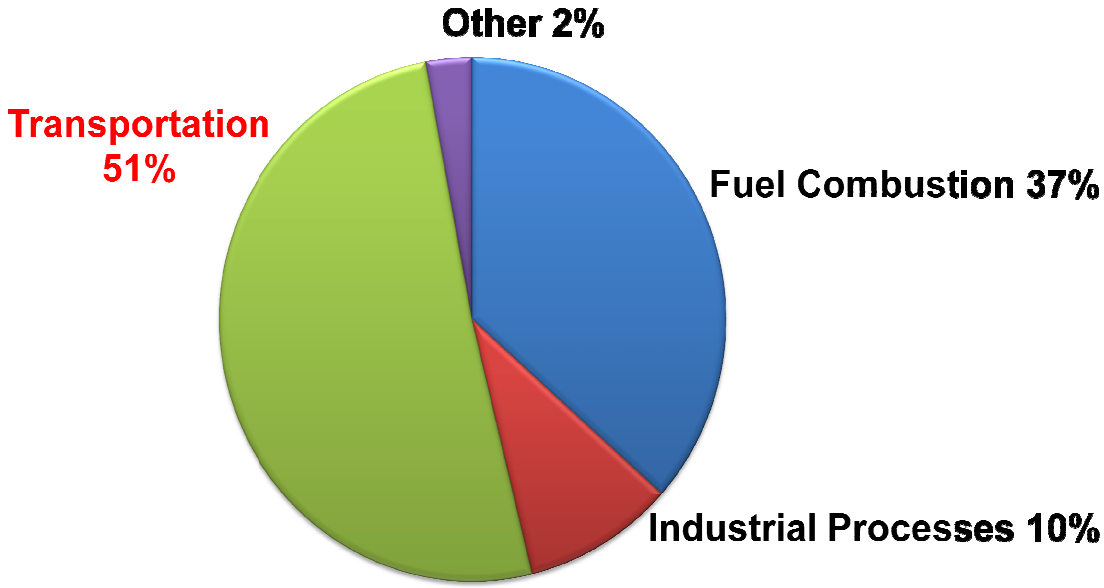

Figure 1-1 The distribution of 2011 NO_x emissions according to the U.S. Environmental Protection Agency.

Compared to conventional spark-ignition gasoline engines, lean burn diesel engines provide higher power output, longer mechanical durability and better fuel economy [2-5]. The main advantages of lean burn diesel engine originate from the lean fuel combustion. The oxidized environment during the diesel combustion yields elevated flame temperature and thus high fuel efficiency. The oxygen-rich high-temperature fuel combustion produces excessive NO_x emission via the reactions between nitrogen and oxygen.

To reduce NO_x pollutant, U.S. government posts has issued strict regulations on NO_x emission from lean burn diesel-powered vehicles. A representative example is the NO_x regulation on heavy duty vehicles. Table 1-1 compares the regulations on heavy duty vehicle emission issued at different years [2]. In 1998, the vehicle could have met the NO_x emission limit without using an after-treatment system. In 2003, the allowed NO_x emission was reduced by 50% and the vehicle could still meet the NO_x emission regulation by a suitable engine management, such as exhaust gas recirculation. In 2007, the NO_x emission limit was reduced to 50% of the previous level. This required use of a catalytic NO_x abatement to meet the regulated emission level. In 2010, the NO_x emission standard was lowered by another 80% to 0.2 g/bhp-hr. In the 2013 U.S. EPA regulation is expected to lower the allowed NO_x emission to a lower level than that in 2010. Hence, meeting the NO_x emission regulated limit has slowed the wide application of lean burn diesel vehicles. Considerable research and development effort for NO_x reduction has been carried out in the past 20 years. This dissertation will focus on the NO_x abatement by the dual-layer catalyst consisting of selective catalytic reduction and lean NO_x trap catalysts.

Table 1-1 U.S. Regulations of limiting emissions by heavy duty vehicles.

	1998	2003	2007	2010
NO_x (g/bhp-hr)	4	2	1	0.2
PM (g/bhp-hr)	0.1	0.1	0.01	0.01
HC (g/bhp-hr)	1.3	0.5	0.5	0.14

1.2 State-of-the-art Technologies of NO_x Emission Abatement

Several technologies are available for NO_x emission abatement including exhaust gas recirculation (EGR), hydrocarbon-selective catalytic reduction (HC-SCR), urea-selective catalytic reduction (urea-SCR) and NO_x storage and reduction (NSR).

1.2.1 Exhaust Gas Recirculation (EGR)

Exhaust gas recirculation is a common-used technique for NO_x emission abatement. A portion of the exhaust gas is recirculated into the engine cylinder, replacing some fresh cool air. This lowers the fuel combustion temperature and thus reduces the NO_x formation by nitrogen oxidation. However, EGR reduces the amount of available oxygen for fuel combustion and diminishes the advantages of lean burn diesel engine. The low oxygen level leads to incomplete fuel combustion and lowers fuel economy. The emitted hydrocarbon and soot level are increased as well [3-4]. The high HC and particulate matter emission cause a heavy burden on other after-treatment units, such as diesel oxidation catalyst (DOC) and diesel particulate filter (DPF). Significant effort has been spent on the research and development of DOC and DPF to control the HC and particulate matter in the exhaust. Other penalties associated with EGR include higher

engine temperature, heavier cooling system burden and increased engine oil acidity [3-4]. These EGR limitations reduce the engine longevity.

1.2.2 Hydrocarbon-Selective Catalytic Reduction (HC-SCR)

HC-SCR is a NO_x reduction technology for lean burn diesel engine analogous to the well-established three-way catalytic converter (TWC) for spark-ignition gasoline engine. Hydrocarbons, such as propane and butane, are generated by the partial combustion of on-board fuel and serve as the reducing agents. Under steady-state conditions, hydrocarbon selectively reacts with NO_x to generate N_2,

$$NO_x + \text{Hydrocarbon} \longrightarrow N_2 + CO_2 + H_2O. \quad (1)$$

The adsorption of the hydrocarbon and NO_x on the catalyst is required to suppress the undesired hydrocarbon oxidation [5-6]. A typical HC-SCR catalyst consists of Ag, Co and Cu for NO_x adsorption and alumina or zeolites for HC adsorption. Among these, Cu/ZSM-5 and Ag/Al_2O_3 receive most attention [7-8].

Although HC-SCR has attracted great interest due to the simple engine management and low catalyst cost, the narrow operating temperature window and low catalytic selectivity has prevented its commercialization [5-8].

1.2.3 Urea-Selective Catalytic Reduction (urea-SCR)

Urea-SCR is a widely-applied NO_x abatement technology for heavy-duty diesel vehicles, which involves the reaction between NH_3 and NO_x in the presence of excess O_2. In stationary applications and heavy-duty vehicles, this involves NH_3 injection or of its

precursor urea into the engine exhaust, where it mixes with NO_x and O_2. Another option is use of reductants to react with stored NO_x in the LNT to produce NH_3. The gas mixture fed to the SCR reactor undergoes one of the following global reactions:

Standard SCR $4NO + 4NH_3 + O_2 \Leftrightarrow 4N_2 + 6H_2O$, (2)

Fast SCR $NO + NO_2 + 2NH_3 \Leftrightarrow 2N_2 + 3H_2O$, (3)

NO_2 SCR $6NO_2 + 8NH_3 \Leftrightarrow 7N_2 + 12H_2O$. (4)

Following considerable research Fe- and Cu-exchanged zeolites are commonly used as urea-SCR catalysts. Colombo et al. [9] reported that a Cu-based zeolite had a higher NH_3 storage capacity than a comparable Fe-based zeolite. It also had a higher catalytic activity for the standard SCR and ammonia oxidation reactions, as well as a lower sensitivity to NO_2/NO_x feed ratio. Fedeyko et al. [10] measured the catalytic behavior of the Fe/Cu zeolites via FT-IR spectroscopy and found that NH_3 had a stronger site blocking effect on the Fe-zeolite than on the Cu zeolite. Metkar et al. [11] found that the standard SCR rate on Fe/ZSM-5 was of slightly negative order with respect to NH_3. Kamasamudram et al. [12] applied a four-step experimental protocol to assess the catalytic functions of different SCR catalysts. The differences between the Cu- and Fe-zeolites during low temperature transient operation were due to differences in their NH_3 coverage-dependent adsorption. Cu-zeolite was less sensitive to the NO_2/NO_x ratio and more active at low temperatures at which the ammonia coverage was high [13]. Metkar et al. [14] compared the NO_x reduction by three Fe-zeolite and Cu-zeolite combined configurations as “sequential brick,” “mixed washcoat” and “dual-layer.” The NO_x reduction efficiency of a dual-layer catalyst with Fe-zeolite on top of Cu-zeolite was

comparable to that obtained from sequential bricks. Washcoat diffusion limitations for the former favored the dual-layer Fe/Cu configuration.

While urea-SCR has a lower catalyst cost than the PGM-containing LNT, an expensive on-board urea infrastructure is necessary. Other associated problems include safety concerns, urea fouling and NH_3 slip [15, 16].

1.2.4 NO_x Storage and Reduction (NSR)

NSR is carried out periodically in two steps, a lean storage step and a rich regeneration step on a multi-functional catalyst, named as lean NO_x trap catalyst (LNT). A schematic of the NO_x storage and reduction is shown in Figure 1-2. NO_x generated from the fuel combustion is captured and stored on LNT catalysts in the presence of excess O_2 when the engine is operated in conventional fuel-lean mode. At typical space velocities (30,000 to 100,000 hr^{-1}), the lean mode lasts for 1-2 minutes, following which the feed is switched to a much shorter, 3-20 s fuel-rich exhaust feed. This can be accomplished by injecting supplemental diesel fuel into the engine in order to consume the excess O_2, which produces a rich mixture of hydrocarbons, CO, and H_2 for the LNT regeneration. The primary reaction products are the desired N_2, CO_2, and H_2O as well as undesired NH_3 and N_2O. The periodic operation with high frequency demands the LNT catalyst to perform rapid NO_x storage and reduction. Hence, a high loading of precious group metals (PGM), i.e., Pt, Pd and Rh, is used to conduct rapid redox reactions over the LNT catalyst [17]. The LNT catalyst contains also barium and/or potassium as NO_x storage sites and γ-Al_2O_3 as a support. A detailed review of NSR process will be

presented in the next section. Although the LNT catalyst does not require a complex urea-infrastructure, the high loading of expensive metals, such as platinum group metal (PGM) and ceria, limits the LNT application to light duty diesel vehicles.

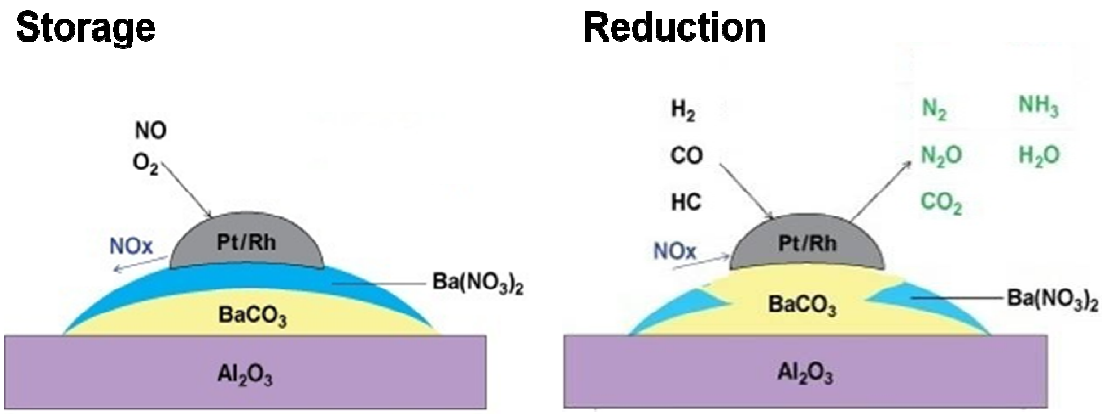

Figure 1-2 Schematic of NO_x storage and reduction over $Pt/Ba/Al_2O_3$ LNT catalyst.

1.3 Review of Previous NSR Studies

NO_x storage and reduction technology has been investigated extensively. Olsson et al. [18] examined the detailed kinetics of NO_x storage and release over a $Pt/Ba/Al_2O_3$ lean NO_x trap. A kinetic model was developed to simulate the NO oxidation to NO_2, NO_2 storage on BaO and NO_x release during the lean-rich cycle. Kabin et al. [19] used bench-top and a TAP reactor to study NO_x storage over powder and monolithic lean NO_x trap catalyst. The nitration and disproportionation pathways were found to be the main NO_x storage routines. Pt participated in the following three processes: NO oxidation to NO_2, NO_2 decomposition to NO and NO_2 spillover to BaO. They investigated the impact of barium loading, space velocity, lean-rich cycle and reductant concentration on the NO_x storage and reduction [20]. Clayton et al. [21] studied the performance and spatio-temporal

product distribution of a lean NO_x trap using hydrogen as reductant. The produced nitrogen may be generated by two competing routines, one from the H_2 reduction of stored NO_x and the second from a sequential reduction by NH_3. Kumar et al. [22] studied NO_x storage and reduction by isotopic experiments using temporal analysis of products. The evolution of N-containing species confirmed the importance of Pt-Ba interface for NO_x storage and reduction. The experiments suggested the existence of fast sites close to Pt, and slow sites far away from Pt. The crystalline diffusion of NO_x from the fast to the slow sites was investigated using a TAP reactor [23].

The NSR modeling has achieved great progress. Sharma et al. [24] simulated the generic features of NO_x storage and reduction by a one-dimensional two-phase model under periodic operations. Divesh et al. [25] developed a global kinetic model for NO_x storage and reduction under anaerobic regeneration. The modeling predictions matched the experimental observations of Clayton et al. Xu et al. [26] developed a microkinetic model that determined the NO_x surface coverage and explained the experimental product selectivities over a $Pt/Ba/Al_2O_3$ catalyst. Shakya et al. [27] used a crystalline-scale model to unify the NO_x storage and reduction on the fast and slow sites. The model indicated that Pt dispersion had a strong impact on NO_x conversion and product selectivities, especially NH_3.

1.3.1 The Impact of Ceria Addition

Ceria (CeO_2) is often added as an effective promoter to after-treatment catalysts. Most previous studies focus on the oxygen storage capacity (OSC) and storage/release

kinetics of ceria catalysts. Gorte [28] provided a comprehensive review of ceria application in catalysis. Damyanova et al. [29] reported that the efficient OSC of ceria facilitated the redox process during catalytic oxidation, which widened the air-to-fuel window. Yao et al. [30] conducted temperature programmed experiments over a series of ceria-containing catalysts and concluded that the interaction between the platinum and cerium provided superior oxygen storage capacity at low temperatures [30]. This was important during the "cold-start" of a vehicle during which most of the noxious emissions occurred. The transfer of oxygen occurred via the precious metal, which implied a "spillover" at the metal/ceria interface. For this reason a high metal dispersion was paramount to providing the requisite interfacial perimeter to facilitate the oxygen exchange.

Ceria is also important for NSR process in terms of catalyst performance and durability. Ji et al. [31] reported that the addition of ceria to Ba-based LNT catalyst resulted in additional NO_x storage capacity and that NO_x stored on ceria could be reduced more easily due to the lower thermal stability of ceria-based nitrates. This had important implications at low temperatures (< 250 ^oC) encountered during start-up or low-load operation. Researchers at Honda suggested that in-situ hydrogenation using H_2 generated by the ceria-promoted water-gas-shift (WGS) reaction provided complete and effective LNT regeneration [32, 33].

In addition to providing NO_x storage sites and to enhancing WGS activity, ceria improves the catalyst durability and sulfur resistance. Hatanaka et al. [34] reported that the interaction between oxidized Pt and ceria led to the formation of nanocomposite oxides. The resulting Pt-O-Ce bond inhibited Pt sintering and helped keep the Pt in a well-

dispersed state in an oxidizing environment. Kwak et al. [35] used ceria as a supporting material for Pt/Ba. No measureable Pt sintering or BaS formation was observed during desulfation up to 600 °C.

1.3.2 The Impact of H_2O and CO_2

The presence of H_2O and CO_2 in the feed, obviously present as combustion products, affects the LNT performance. The addition of H_2O decreases the NO oxidation rate but has only a minor influence on the cycle-average NO_x conversion. The presence of CO_2 leads to the formation of $BaCO_3$, which has a higher thermal stability than BaO. Thus, the NO_x conversion decreases. Ren et al. [36] studied the impact of both H_2O and CO_2 on deNO_x efficiency of LNT catalysts. Cyclic NO_x conversion decreased sharply upon CO_2 addition, while H_2O addition had a minor impact. Mulla et al. [37] reported that water vapor in the feed decreased the Pt active sites and thus inhibited NO oxidation to NO_2. Lietti et al. [38] proposed that water could promote NH_3 formation during the reduction of stored NO_x, while CO_2 strongly inhibited the reduction of nitrates by H_2 or NH_3. Frola et al. [39] used in-situ surface FTIR to analyze NO_x storage. They determined that CO_2 inhibited nitrite formation and subsequent nitrate formation. Lindholm et al. [40] investigated the influence of H_2O and CO_2 over different LNT catalysts. H_2O adsorption decreased NO_x storage on alumina, while CO_2 inhibited NO_x storage on barium. NH_3 formation was promoted by CO_2 at low temperatures.

1.3.3 The Impact of Reductant Composition

The choice of reductant has a great impact on the LNT catalyst performance. LNT regeneration with H_2 has been studied extensively [17-46]. However, CO concentration in the feed could be higher than that of H_2 during actual catalyst regeneration. The NO_x reduction with CO could go through reaction pathways with isocyanate/cyanate formation and reactions. Forzatti et al. [47] used transient response methods and FTIR to study stored NOx reduction by CO over a $Pt/Ba/Al_2O_3$ under dry conditions. They proposed a Pt-catalytized reaction pathway including the reduction of nitrates by CO to nitrite and a sequential reduction of nitrites to isocyanate/cyanate species. The formed isocyanate/cyanate reacted with the stored nitrites and produced nitrogen during the rich feed. The residual isocyanate/cyanate species were oxidized by the O_2 and NO_x during the lean feed to N_2 and surface nitrites. Castoldi et al. [48] employed the same methods to study NO_x reduction by CO over a $Pt/K/Al_2O_3$ LNT catalyst. The NCO-related reaction pathways were still the main routes for NO_x reduction, while the reaction between NCO and nitrates to generate N_2 was faster over $Pt/K/Al_2O_3$ than over $Pt/Ba/Al_2O_3$. DiGiulio et al. [49] investigated the regeneration of Pt- and Rh-Ba/Al_2O_3 LNT catalyst with the CO and propylene. The surface isocyanate species were identified as key intermediates by in-situ FTIR spectroscopy. The reactions of NCO with NO_x and O_2 to N_2 were catalytized by the precious metal catalyst, while NH_3 formation from the NCO hydrolysis was not.

According to comparative studies on different reducing agents, H_2 has been identified as a more effective reductant for surface nitrate regeneration than CO or hydrocarbon, especially at low temperatures. Szailer et al. [50] used in-situ FTIR and time-

resolved XRD to compare the reduction by H_2 and CO over a $Pt/Ba/Al_2O_3$. The surface nitrates were effectively reduced by H_2 at low temperatures. When CO was used as a reductant, the formed NCO species adsorbed on the surface of metal oxides and only reacted with NO_x from thermal decomposition at high temperatures. In the presence of H_2O, the hydrolysis of NCO species led to NH_3 and CO_2 formation. James et al. [51] compared CO with H_2 as the reductant of stored NO_x over a conventional LNT catalyst. CO facilitated the decomposition of barium nitrates, but could not reduce the released NO_x to N_2 due to the strong bonding between CO and Pt. H_2 could assist both the nitrate decomposition and NO_x reduction. Poulston et al. [52] found that H_2 was a better reductant than CO for regeneration of aged LNT catalyst. Li et al. [53] tested a $Pt/Rh/Ba/Al_2O_3$ LNT catalyst with different reductants, including HC, CO and H_2. CO was found out to be the most active reductant in terms of catalyst regeneration and N_2 production and H_2 the most efficient below 200 ºC. Scholz et al. [54] compared NO_x regeneration capacities of several reducing agents, including H_2, CO and C_2H_4, over a $Pt/Ba/Al_2O_3$ catalyst at 300 ºC. The addition of H_2O could prevent CO and C_2H_4 poisoning of Pt. Three reductants had comparable reduction efficiencies. Jozsa et al. [55] investigated the regeneration of LNT catalysts by CO, C_3H_6 and H_2 by temperature programmed desorption and reduction studies. H_2 was the most effective reducing agent, especially at low temperatures.

1.3.4 The Formation and Role of NH_3

The formation and role of byproduct ammonia during NSR has been extensively studied. Nova et al. [41] proposed that NH_3 was a key intermediate for N_2 formation and

could be produced in high selectivity when H_2 was used as the reductant. Mulla et al. [42] found that NH_3 was formed during the regeneration of stored NO_x, acting as an H-atom carrier. Wang et al. [43] investigated the effect of regeneration conditions on NH_3 formation under simulated diesel exhaust. The NH_3 selectivity increased with the steam reforming activity due to the generation of H_2. Lietti et al. [44] further determined that the reaction of ammonia with nitrates was a major route for nitrogen formation. Clayton et al. [45] identified favorable cyclic conditions for NH_3 formation; i.e., high H_2/NO_x, moderate temperature, and low Pt dispersion. The temperature leading to a maximum NH_3 production decreased with an increase in Pt dispersion. They attributed this to the limiting transport rate of stored NO_x to the Pt/Ba interface; i.e., transport limitations led to a localized higher H_2/NO_x ratio that is favorable for NH_3 production [21].

1.4 Alternative NO_x Reduction Technologies

Active research efforts aim to design a catalyst that avoids the need for a urea feed and achieves the required NO_x reduction while minimizing the amount of expensive PGM in the LNT. A possible solution is the combination of NSR and LNT, referred to as LNT/SCR technology. Several LNT/SCR configurations or architectures were proposed in patents by Ford (Gandhi et al. [56-58]). One configuration is a sequential dual-brick LNT/SCR in which the upstream LNT catalyst brick stores NO_x and reduces NO_x to a mixture of N_2 and NH_3, followed by a SCR catalyst brick that utilizes the generated NH_3 to reduce the unreacted NO_x that escapes from the LNT. This configuration operating strategy was similar to the conventional LNT but circumvented the need for an urea feed.

Daimler AG commercialized a DOC-LNT-DPF-SCR aftertreatment system to meet US tier 2 bin 8 NO_x emission standard for a 3.0 L diesel engine [59]. Their study showed that low NO_x emission could be achieved for US tier 2 bin 5 by reducing the oxygen storage components in the LNT catalysts [60]. Eaton Inc. applied a similar configuration to reduce NO_x emission from heavy-duty diesel vehicles [61]. These results indicated that a dual brick LNT/SCR configuration enabled NO_x abatement of both light- and heavy-duty diesel vehicles. A variant of the LNT-SCR dual-brick configuration is the LNT-SCR multi-brick system proposed by Gandhi et al. [56] and investigated by Ford researchers. Xu et al. [62] showed that this architecture could reduce the LNT PGM loading by up to 50% and achieve the same conversion.

These findings have motivated academic research to gain a better understanding of the LNT-SCR series configuration. Lindholm et al. [63] conducted experiments using a dual bed catalyst system comprising a $Pt/Ba/Al_2O_3$ LNT catalyst followed by a Fe-beta SCR catalyst. The combined system performance was superior to that of the single LNT catalyst at all temperatures. Pereda-Ayo et al. [64] studied a similar configuration as Lindholm et al. with Fe-zeolite Beta downstream of $Pt/Ba/Al_2O_3$. Using 3% H_2 during the LNT regeneration at 300 ºC, they achieved NO_x removal efficiency and N_2 selectivity as high as 98% and 97%, respectively. Seo et al. [65] determined that 1:1 was the optimal LNT to SCR volume ratio with regard to catalyst cost and NH_3 slip. They also compared the deNOx performance of a LNT-SCR series configuration to that of a single LNT catalyst following hydrothermal aging and sulfur poisoning. NO_x conversion from the combined system was 10-30% higher than that of the LNT catalyst [66]. Bonzi et al. [67]

studied both the double-bed and mixture architecture of $Pt/Ba/Al_2O_3$ LNT catalyst and Fe/ZSM-5 SCR catalysts. The LNT/SCR catalysts performed better than LNT catalysts alone under all conditions. Forzatti et al. [68] proposed a two-step in-series pathway to explain the temporal evolution of N_2 production. The first step was the formation of ammonia via a reaction of NO_x with H_2 and the second was the reaction between the formed ammonia and stored NO_x. With the second step identified as the rate-determining step, the downstream or mixed SCR catalyst could reduce NH_3 slip for NO_x elimination. Castoldi et al. [69] found that the presence of H_2O and CO_2 in the dual-bed and mixed LNT-SCR catalysts lowered the NO_x storage due to $BaCO_3$ formation, but improved N_2 selectivity during NH_3 oxidation on the LNT. Some researchers studied the regeneration of LNT-SCR dual-bed and mixture catalysts with CO. Corbos et al. [70] used CO to reduce the stored NO_x using different mixtures of LNT and SCR catalysts. The physical mixture of $Pt\text{-}Rh/Ba/Al_2O_3$ and Cu/ZSM-5 had the highest activity regardless of either the reductants, reduction time or the presence of H_2O. Cu/ZSM-5 facilitated the reactions between CO and NO_x to form surface NCO species. The hydrolysis of NCO species led to NH_3 generation and the following NO_x reduction by the SCR catalyst. They found that the highest NO_x conversion from the LNT-SCR mixture catalyst occurred when both H_2 and CO were used as reductants. Researchers from the University of Kentucky and Ford motor Co. [71] investigated the LNT-SCR multi-brick catalyst with H_2, CO and C_3H_6 as reductants. Some NO_x was reduced by the adsorbed hydrocarbons over Cu-zeolite, besides the conventional NH_3-SCR pathway.

Dual-layer architecture is a competing alternative to the sequence of LNT-SCR bricks. Nakatsuji and co-workers from Honda [72] proposed a dual-layer catalyst comprising a solid acid (Bronsted acid-based zeolite) on top of Pt/OSC. NO_x was stored on the OSC function during the lean phase, while NH_3 formed by the stored NO_x. NH_3 was stored on the solid acid function during the rich feed. During the lean feed, NO_x was partially reduced by adsorbed NH_3. Honda reported the use of a SCR-on top of Pt/OSC composite to meet NO_x emission standards of US tier 2 bin 5 [32, 33]. While Honda's work provoked interest in this configuration, they did neither provide complete information about the catalyst nor propose the mechanism of the reactions on the LNT-SCR dual-layer catalyst.

1.5 Research Objectives and Thesis Outline

Considerable research efforts have been directed towards development of various NO_x abatement technologies in the past as described in the previous sections. These studies enhanced our understandings and knowledge of the reaction mechanisms and controlling parameters, enabling the development of improved NO_x abatement technologies. As a result, novel LNT and SCR catalyst configurations are currently under development. Most previous research efforts have been spent on the LNT/SCR sequential architecture, while the dual-layer architecture has received much less attention. The optimal catalyst composition, reaction mechanisms, reactor configurations and operating strategies of the dual-layer catalysts have not yet been determined. This prevents appropriate comparisons between LNT/SCR sequential and dual-layer architectures.

The goal of this dissertation is to provide the understanding and ability to predict the factors affecting the dual-layer catalyst performance. It consists of an experimental study of NO_x reduction by LNT/SCR dual-layer monolithic catalysts. This study began with the investigation of the impact of ceria on LNT catalyst. Although ceria has been well recognized as an essential promoter to the LNT catalyst, the impact of ceria oxygen storage capacity on NO_x storage and reduction process is still unclear. Hence, two parallel studies were carried out. First, the spatio-temporal features of periodic oxidation/reduction operation over a flat ceria-catalyzed monolithic plate were studied. This illustrated the impact of ceria oxygen storage capacity on the transient redox reactions and transport process. Second, the evolution of surface species over a $Pt/CeO_2/Al_2O_3$ catalyst was studied during NO_x storage and reduction. This elucidated the link between ceria oxygen and NO_x storage ability.

In addition to gaining an understanding of LNT catalyst, the metal-exchanged SCR catalysts were synthesized using the wet ion exchange method. This enabled the preparation of a series of LNT/SCR dual-layer catalysts with different SCR and LNT combinations. The properties of dual-layer catalysts were investigated in two stages. In the first stage, the dynamic NO_x reduction performance of dual-layer catalysts was studied under a variety of operating conditions. This provided the basic information about the NO_x reduction mechanisms, the impact of catalyst composition and the catalyst durability. In the second stage, several controlling parameters were optimized to improve the fuel economy and reduce the loading of expensive metals, such as Pt and ceria. This

required optimization of the ceria zoning in LNT layer, the SCR catalyst loading and the operating policy.

This dissertation consists of the following parts. Chapter 2 describes the experimental setups and procedures used for catalyst synthesis and testing. Chapter 3 reports the spatio-temporal temperature profiles and effluent concentrations of periodic oxidation of H_2 and CO over a $Pt/CeO_2/Al_2O_3$ catalyst. Chapter 4 reports the surface species formed over the $Pt/CeO_2/Al_2O_3$ catalyst during NO_x storage and reduction. Chapter 5 reports the reaction mechanisms and performance of a series of LNT-SCR dual-layer catalysts for NO_x reduction. Chapter 6 reports lean NO_x reduction with H_2 and CO over a series of LNT-SCR dual-layer catalyst. Chapter 7 summarizes the main conclusions of this study and recommends future research.

Chapter 2 Experimental

2.1 Catalysts

Both lean NO_x trap (LNT) and selective catalytic reduction (SCR) catalysts were used in this study. The details about the catalyst composition and preparation were reported below.

2.1.1 Lean NO_x Trap Catalysts

NO_x storage and reduction (NSR) technology is carried out over the lean NO_x trap (LNT) catalyst with rapid cycling between storage and regeneration operation. When engine is running for the 30-60 s fuel-lean feed, NO_x and O_2 are stored on the LNT catalyst. Before significant NO_x breaks through, the feed is shifted to a 5-20 s fuel-rich feed, which contains hydrocarbons, CO and H_2 formed by incomplete combustion of injected fuel. The rich feed regenerates the stored NO_x forming N_2 and some NH_3.

The LNT catalyst used in this study contains platinum, rhodium, barium, ceria, ɣ-Al_2O_3 and cordierite support. Pt is an active component to catalyze the NO oxidation to NO_2 and facilitate NO_2 spillover during the lean phase, while Rh effectively catalyzes the reduction of stored NO_x to N_2 and NH_3 during the rich phase. Barium, the alkali earth metal component, is used to store NO_x during the lean phase and release NO_x during the rich phase. Ceria serves as an effective promoter for oxidation reactions, NO_x storage and catalyst regeneration. The high surface area ɣ-Al_2O_3 is deposited onto the cordierite support as the catalyst carrier.

The powder and monolithic catalysts used in the experiments were provided by BASF Catalyst LLC (Iselin, New Jersey). Information about the LNT catalysts is reported in Table 2-1.

Table 2-1 The composition of the LNT catalysts used in this study.

Catalyst	PtCe	LNT1	LNT2	LNT3
Pt (g/in^3)	0.056	0.046	0.046	0.046
Pt (wt%)	2.43	1.00	1.00	1.00
Rh (g/in^3)	0.000	0.006	0.006	0.006
Rh (wt%)	0.00	0.13	0.13	0.13
Ba (g/in^3)	0.00	0.69	0.69	0.69
Ba (wt%)	0.00	15.00	15.00	15.00
Ce (g/in^3)	0.30	0.00	0.78	1.56
Ce (wt%)	13.04	0.00	17.00	34.00
Al_2O_3 (g/in^3)	1.944	3.858	3.078	2.298
Al_2O_3 (wt%)	84.53	83.87	66.91	49.96
Loading (g/in^3)	2.3	4.6	4.6	4.6

2.1.2 Selective Catalytic Reduction Catalysts

Fe/ZSM-5 catalyst powder was provided by Sud-Chemie (Munich, Germany). We synthesized Cu/ZSM-5 catalyst powder by the following wet ion exchange method. NH_4/ZSM5 powder having a Si/Al ratio of 23 was acquired from Zeolyst International, Inc (PA, USA). A protonated powder (H/ZSM-5) was obtained by calcining NH_4/ZSM-5 at 550 °C for 5 hr. The H/ZSM-5 was converted to Na/ZSM-5 by dispersing the catalyst

powder in 0.1 M $NaNO_3$ (Sigma-Aldrich) solution. The ion exchange was conducted for 24 hr with continuous stirring at ambient temperature and neutral pH of ca. 7. The powder was obtained following filtration and washing in a centrifuge (Avanti® J-E BioSafe, Beckman Coulter) and drying overnight at 120 °C. The Na^+ exchange and drying were repeated twice to maximize the exchange ratio. The Na/ZSM-5 powder was obtained after calcination at 550 °C for 5 hr. The Cu/ZSM-5 was prepared by contacting Na/ZSM-5 with a 0.02 M copper acetate (Sigma-Aldrich) aqueous solution in a constant stirring environment for 24 hr at ambient temperature. The solution pH was adjusted to ca. 6 by 0.1 M acetic acid solution. The Cu^{2+}/Al^{3+} ratio was in range of 0.5 to 1. The ion exchange procedure was repeated three times. Finally, the Cu/ZSM-5 was obtained by calcining the powder at 550 °C for 5 hr. The Cu loading in the Cu/ZSM-5 was determined as 2.0-2.5 wt % by Inductively Coupled Plasma-Atomic Emission Spectroscopy (ICP-AES, UH ICP analytical research lab).

The SCR catalyst was washcoated on the clean cordierite monolith (400 channels per square inch) using the following procedure. An aqueous slurry comprising of 32 wt% catalyst powder, 8 wt% boehmite and balance water was ball-milled for 24 hr to obtain catalyst particles with a size in the range of 1 to 5 µm. The slurry pH was adjusted to ca. 6 by adding 0.1 M acetic acid before washcoating. The SCR monolith was prepared by dip-coating an empty monolith in the slurry containing 40% solid in balanced water for 30 s from each end. The excess slurry was cleared by feeding compressed air sequentially into both ends for 10 s. The washcoated monolith was then dried at 120 °C overnight. The washcoating procedure was repeated until the desired loading was obtained. The final step involved the calcination of the monolithic catalyst at a temperature ramp of

23 °C/hr and then holding it at 550 °C for 5 hr. The typical loading of the monolith washcoat after one time of dip-coating and following calcination was in the range of 0.8 to 1.0 g/in^3.

2.1.3 LNT-SCR Dual-layer and Mixture Catalysts

LNT monolithic catalysts and SCR powder catalysts were used to prepare the SCR-top LNT-bottom dual-layer catalysts. The LNT monolith was calcined at 550 °C for 5 hr before washcoating to avoid barium leaching. The washcoat slurry containing SCR catalyst was prepared as described above. The dual-layer monoliths were synthesized by depositing a SCR layer on top of the LNT bottom layer.

A schematic of a SCR-LNT dual-layer catalyst is shown in Figure 2-1 (a). The SEM images of LNT catalysts before and after SCR washcoating are shown in Figure 2-1 (b). The LNT layer had a non-uniform thickness due to the thicker loading in the corners. The washcoat thickness of the monolith channel was measured with a scanning electron microscope (SEM; JEOL JSM-6330F). The thinnest peripheral average of the LNT layer was about 60-80 µm and the maximum thickness was about 260-290 µm at the corners. After washcoating, a uniform layer of SCR catalyst (thickness of 40 to 50 µm) was deposited on top of the LNT layer. This catalyst is referred to as a dual-layer LNT-SCR. The Pt, Rh, Ba, Ce, Cu, Fe, Si, Al and O concentrations in the dual-layer catalysts were measured using energy dispersive spectroscopy (EDX/EDS). To study the interlayer mixing, both fresh and aged dual-layer catalysts were analyzed by SEM-EDS.

Hydrothermal aging was accomplished by calcining the fresh dual-layer catalyst at 600 °C in air for 100 hr.

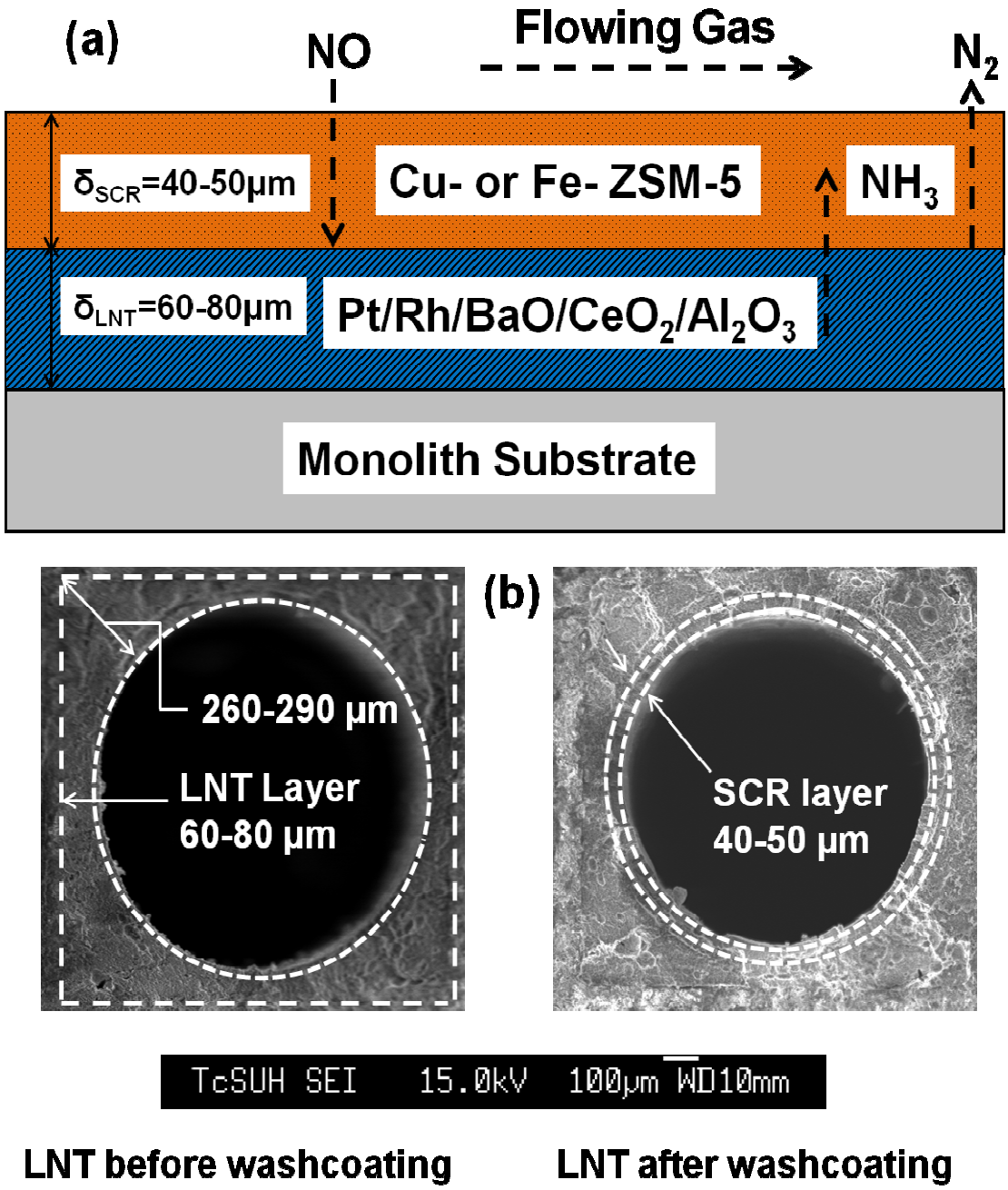

Figure 2-1 (a) Schematic of a dual-layer catalyst; (b) cross-section SEM micrographs of LNT1 catalyst before and after SCR washcoating.

The same dip-coating procedure was used to prepare the mixed washcoat LNT-SCR monolithic catalysts having a washcoat loading of about 3.0 g/in^3 (LNT1 2.1 g/in^3; Cu/ZSM-5 0.9 g/in^3). The LNT1 catalyst powder was obtained by scratching it from the washcoated monolith.

2.2 Experimental Setup enabling IR Thermography and Mass Spectroscopy

Figure 2-2 is a schematic of the experimental setup used to monitor the spatio-temporal temperature on the monolithic plate and the real-time effluent concentrations. The main components of this setup included a gas supply system, a reactor, an Infra-red camera, a mass spectrometer and data-acquisition system.

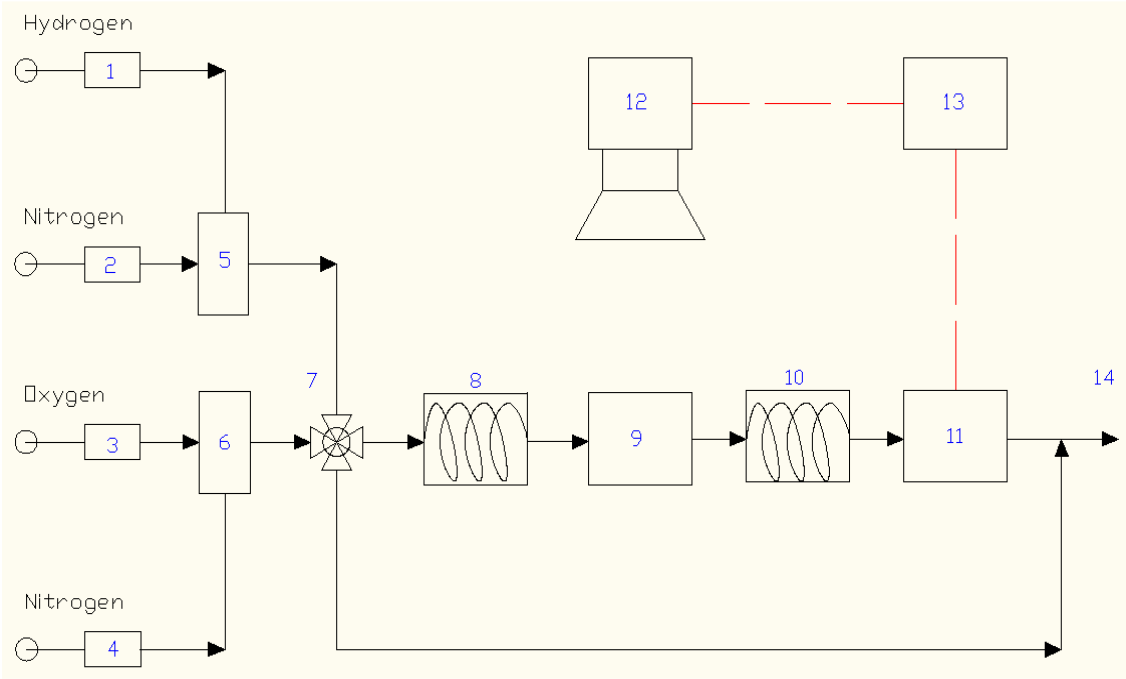

Figure 2-2 A schematic experimental setup. 1~4. Mass flow controller; 5~6. In-line static gas mixer; 7. Four-way switching valve; 8. Heating band; 9. Reactor; 10. Cooling pool; 11. Mass Spectrometer ; 12. Infrared camera; 13. Computer; 14. Exhaust hood.

2.2.1 Gas Supply System

The gas supply system was a series of gas cylinders and mass flow controllers to produce the required lean and rich mixtures.

The reactive gases, including N_2, H_2, O_2, CO and Ar, were acquired by Matheson Tri-Gas. The gas pressures were maintained at 60 psig by the pressure regulators on the cylinders. Check valves were installed after the regulators to avoid gas backflow.

Mass flow controllers (1179A, MKS with accuracy of ±1%) with four channel power supply/readout boxes (247D, MKS Inc.) were used to control the gas flow rates. The four channel power supply/readout box was the electrical power supply and the set point source to the mass flow controllers. The desirable flow rate was obtained by tuning the output analog signal from the four channel power supply/readout box to the mass flow controller. The actual flow rate was calculated based on the feedback analog signals from the mass flow controller to the four channel power supply/readout box. Each mass flow controller was calibrated over the whole flow range using either a digital flow meter (< 200 standard cm^3/min) or a bubble meter (>200 standard cm^3/min). To ensure accurate measurement, the mass flow controllers were re-calibrated every month. The feed gases with desired flow rates were mixed in inline static mixers before entering the reactor system.

Swagelok stainless steel pipes (316 L) with a nominal diameter of ¼ inches were used in the gas feed system. The sealing of the gas supply system was checked by feeding an Ar flow under a pressure of 80 psig. The bubble soup was dropped on every pipe joint.

The leaking joint might be covered by continuous bubbles, while no bubble formed over the well-sealed joint.

2.2.2 Reactor System

The reactor system consisted of a reactor, an infrared camera enabling reactor imaging, a four-way automatic switching valve (Valco Instruments Co. Inc.) placed upstream of the reactor, two electrical heating tapes wrapping along the gas inlet tube, and two ceramic heaters heating around the reactor.

The four-way switching valve with an electric actuator was used to switch between feed streams. A two-position control module and a VCOM software were used to control the switching timing manually and automatically, respectively.

Both heating tapes and ceramic heaters were controlled by a microprocessor based temperature controllers (CN 2110, OMEGA Engineering, Inc.). The thermocouples, monitoring gas and reactor temperatures, provided input signals to the temperature controllers. The temperature controllers provided the electrical power to the heating tapes and ceramic heaters based on the thermocouple signals. The temperature variation was limited to ± 3% of the set-point temperature.

A side view of reactor is shown in Figure 2-3. Cylindrical monolithic cores (diameter=3.8 cm, length=7.6 cm) were cut and polished to a two-channel thick layer flat plate sample (32 channels; width=2.1 cm, length=7.6 cm). The samples contained Pt (2.43 wt%, 50% dispersion,) and CeO_2 (13.0 wt %) on a γ-Al_2O_3 washcoat (loading of 2.3 g/in^3) on the cordierite structure. The washcoat mass was 350 mg. The two-layered

monolith sample was horizontally glued to the reactor holder and sealed inside the reactor. The bottom and two sides of rectangular reactor were made of 304L stainless steel due to high thermal expansion resistance. The IR transparent quartz window was used as the reactor top, enabling IR camera imaging of the whole monolithic plate surface. The gaps between the stainless steel base and the quartz window were sealed by graphite gaskets (American Packing & Gasket). A leakage test was carried out under an 80 psig Ar flow to ensure the appropriate sealing. To generate a nearly isothermal condition in the reactor, small mineral wool insulation bricks were placed between the monolith and reactor walls. The reactor temperature was monitored and controlled by four K-type thermocouples: one at the bottom of reactor, linked to the temperature controller of ceramic heaters, to manipulate the reactor temperature; The other three thermocouples were delicately located at different positions along the monolith to make sure the isotherm condition. The thermocouple signals were recorded and processed by an OMB-DAQ-54 USB data acquisition system (OMEGA Engineering, Inc.), connecting to computer.

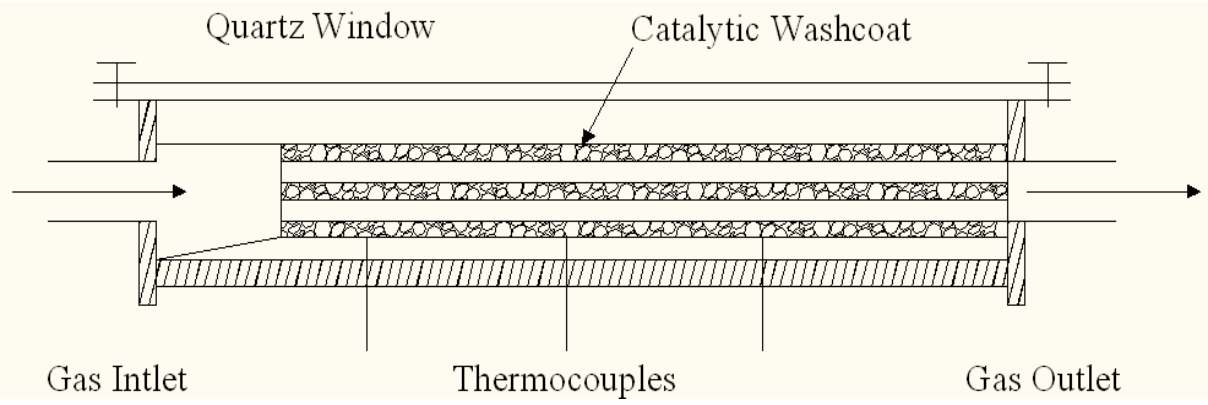

Figure 2-3 A schematic side view of reactor.

2.2.3 Analysis and Data-acquisition System

The analysis and data-acquisition system was composed of an infrared camera (FLIR, SC4000 Systems) and a mass spectroscopy (Pfeiffer Vacuum, GSD 300).

The IR thermograph enables based on the surface infrared radiation non-invasive and visible temperature measurement. The infrared energy from a material is related to its surface temperature. The material can be categorized into two types as black body and grey body. Black body can adsorb all the incident radiation and emit all the released energy, while grey body adsorbs and emits only a fraction of that of a black body. Real material behavior is close to that of a grey body. The theoretical infrared radiation per unit surface area of a grey body is described by the Stefan-Boltzmann formula

$$E = \varepsilon . \ \sigma . \ T^4 \ (W/m^2) \qquad (1)$$

where ε is the emissivity of the grey body, σ is the Stenfan-Boltzmann constant and T is the absolute surface temperature. A higher body temperature leads to higher infrared radiation.

The spatio-temporal radiation of the monolithic plate was measured by the high speed (up to 432 frame/s) mid-wavelength infrared imaging camera (FLIR, SC4000 Systems). The SC4000 camera enables a fast frame rate of 420 Hz using a 320X256 matrix of Focal Plane Arrays (FPA). The Indium Antimonide (InSb) detector is sensitive to a spectral range of 3.0 to 5.0 μm wavelength. The incorporated integrated circuit controls the frame rate or integration time, performs the non-uniformity correction, replaces the bad pixel, converts the analog signals to digital signals and generates thermal imaging video. The specifications of the IR camera are reported in Table 2-2.

Table 2-2 Specifications of the SC4000 Infrared Camera System.

Detector	Indium Antimonide (InSb)
Resolution	320 X 256
Spectra Range	3.0-5.0 µm
Pixel Pitch	30 X 30 µm
Dynamic Range	14 bits
Date Rate	50 MHz
Full Frame Rate	432 Hz
Len Focal Length	25 mm
Maximum Temperature	350 °C
Control	USB Global Ethernet
Power	24 VDC

The digital signals from the IR camera are recorded, processed and visualized by the ExaminIR™ software (ThermoVision®, FTIR). The IR camera integration time is also controlled by the ExaminIR™ software. Each integration time corresponds to a certain temperature range. The optimal integration time for different temperature ranges, spanning from -10 to 350 °C, is reported in Table 2-3. The accurate temperature measurement (± 0.5 °C) can be obtained by applying the optimal integration time. To enable temperature measurements above 350 °C, an InSb Neutral Density High Temperature filter (ND2 Filter, FLIR) is mounted on the back of IR camera lens. This enables to extend the temperature measurement up to 2000 °C.

Table 2-3 The optimal temperature ranges to the integration time ranges.

Range	Integration Time (millisecond)	Celsius	Fahrenheit
1	1.003	-10 to 55	-10 to 12
2	0.547	10 to 90	50 to 194
3	0.12	50 to 150	122 to 302
4	0.06	80 to 200	176 to 392
5	0.012	150 to 350	302 to 662

The IR thermography requires appropriate instrumental calibration. A two-point non-uniformity correction (NUC) was conducted after installing the ND2 filter to IR camera. This correction compensated for any bad pixel and guaranteed a smooth imaging. The correction was carried out in the ExaminIR^{TM} software using special calibration plates. Two black body calibration plates were heated to two temperatures: one at 25 °C and one at 500°C. The measured temperature in this study was within the range from 25 °C to 500 °C. The IR camera collected the IR spectra from the two heated black bodies and the NUC calibration was performed by the incorporated integrated circuit.

The calibration of the IR camera signals from a luminance count to temperature was carried out using the ExaminIR^{TM} software before each experiment. The monolith plate in the reactor was heated to the desired temperature and three in-reactor K-type thermocouples measured the monolith temperature. In a thermal steady state, the three thermocouples had the same temperature reading with a less than 1% variation. The luminance counts in IR camera at this selected temperature were equivalent to the set point temperature. This process was repeated for several temperatures to cover the whole temperature range encountered during the experiments. The in-reactor temperature calibration accounted for the transmission losses through the quartz window, the ambient reflection radiation and the atmospheric radiation. Hence, an accurate measurement of the surface temperature on the monolith plate could be achieved. After proper calibration, the difference in the measured temperature from the IR camera and thermocouples were within 0.5 °C.

A GSD 300 Pfeiffer Vacuum mass spectrometer measured the reactor effluent concentrations. Mass spectroscopy is a well established analytical technique to identify chemical compounds by measuring their molecular mass. The instrument consists of a capillary inlet, a quadrupole mass spectrometer, a diaphragm vacuum pump and a high efficient turbo pump. The gas is pumped and flows in a temperature-regulated stainless steel capillary. The gas inlet can be heated up to 350 °C to avoid liquid condensation or fouling. The gas flow in capillary is about 2 sccm and it takes about 500 milliseconds to reach the mass spectrometer. The mass spectrometer measures a molecular mass ranging from 1 to 200 amu using a Faraday type detector. The feed gas is vaporized and ionized over the tungsten filament. The ion fragments are sorted by the radio frequency quadrupole electric and magnetic fields. The relative abundance of each ion type is collected and recorded by the analyzer. The identity and concentration of each compound are determined based on the ion fragment mass number and the corresponding ion current. This process is carried out under a pressure below 1 X 10^{-5} mbar. The vacuum in the system is generated by the diaphragm vacuum pump and the turbo pump.

A Quadstar^{TM} 422 software (Balzers Instrument) is used for the tune-up, calibration and measurement by the mass spectrometer . The electrical voltage over ion source can be tuned by a “Tune Up” program. The mass peak width and height are optimized to improve the system sensitivity. A “Parameter Setup” program is used to adjust the ion fragment mass scale and define the internal calibration standard. An internal calibration standard is assigned to a mass number of a chosen gaseous compound. The calibration factor for the internal calibration standard is fixed, while the

calibration factors for other mass numbers are varied based on their relative ion current to the chosen mass number. Once the concentration of the chosen gas compound is fixed, the concentrations of other gas species can be determined by their calibration factors

$$C_{g,m} = \mathrm{C_{I,n}} * \frac{\mathrm{S_{g,m}}}{\mathrm{S_{I,n}}}, \quad (2)$$

where the mass number n is used as an internal calibration standard, $C_{g,m}$ is the undetermined gas concentration on mass number m, $C_{I,n}$ is the known gas concentration on mass number n, $S_{g,m}$ is the calibration factor on the mass number m and $S_{I,n}$ is the calibration factor on the mass number n. The "Measurement" program enables temporal monitoring of ion currents and gaseous concentrations of several predefined mass numbers. The dwell time can be adjusted according to the experimental requirement. The smaller the dwell time, the higher the response frequency and the lower the measurement accuracy.

The mass spectrometer was calibrated before the experiments using specialty gases from Matheson Tri-Gas. The sampling capillary of the mass spectrometer was placed in the center of effluent gases flow tube for accuracy and fast response. 500 ppm Ar was fed as the inert trace gas. This provided an internal calibration standard of m/e=40 for concentration measurements. Each gaseous species was calibrated at three concentrations at its signature mass number, i.e., O_2 at m/e=32 and H_2O at m/e=18. When the ion source of mass spectrometer was stable, the calibration factor for a given mass number was insensitive to concentration variation. When the mass spectroscopy was in the idle status, a pure N_2 flow of 50 sccm was continually fed to stabilize the ion source.

2.3 Experimental Setup enabling Fourier Transform Infrared Spectroscopy and Mass Spectroscopy

This system utilizes on-line Fourier Transform Infrared Spectrometer (FTIR) and Mass Spectrometer (MS) to measure and record effluents from a cylindrical monolithic or reactor containing a powder catalyst. The bench-scale reactor setup contains a gas supply system, an automatic control system, an isothermal reactor and an analysis system.

2.3.1 Gas Supply System

The feed and calibration gases were acquired from Matheson Trig-Gas. Pressure regulators were installed on the gas cylinders to maintain the feed pressure around 40 psig. The gas flow rates were controlled by a series of mass flow controllers (MKS Inc.) before entering the inline static mixers. The mass flow controllers were calibrated every three months using a digital flow meter or a bubble meter. Water vapor was fed by a syringe pump (ISCO Model 500D). A dual actuated switching valve upstream of the reactor controlled the feed streams.

2.3.2 Automatic Control System

The automatic control system included an ADAM 5000 TCP module (Advantech) and Labtech® software. The ADAM 5000 TCP module collected the analog signals from the mass flow controllers, the switching valves, the pressure gauge and the thermocouples. The analog signals were digitized by the ADAM system. The data was shown on the graphical interface and recorded by the Labtech® software. The gas flow rates and

switching valve timing were controlled by the graphical user interface of Labtech® software. The digital signals from the Labtech® software was converted to a corresponding voltage signals by ADAM module and delivered to the mass flow controller and switching valves, respectively.

2.3.3 Reactor System

Two quartz tube reactors were used. One was a quartz tube reactor containing a monolithic catalyst. Cylindrical cores (diameter = 1.9 cm, length = 7.6 cm; 400 channels per square inch) were cut into small monolithic cores (28 channels; D = 0.8 cm, L = 2.0 cm). The monolith was wrapped by Fiberfrax® ceramic paper and positioned in the empty quartz tube flow reactor (1.2 cm diameter, 40.6 cm length; Technical Glass Products). The second was quartz tube reactor containing powder catalyst. A small quartz frit plate was installed in the middle of the quartz tube flow reactor. The powder catalyst was loaded on the top of the frit plate. A 1cm quartz wood layer was inserted on the top to fix the catalyst layer thickness below 1 cm.

The quartz tube reactor was placed inside a 500W vertical tube furnace (Mellen M300, Model SC11). The furnace had a 6” heated hone and the maximum operating temperature was 1100 ºC. The furnace temperature was controlled by a PS305 Mellen Temperature Control System, which enabled a temperature programming control.

Two 0.5 mm type-K stainless steel sheathed thermocouples (OMEGA Engineering Inc.) measured the temperature inside the reactor. One placed 0.5 cm upstream of the catalyst measured the feed temperature and the second placed in the

middle of the center channel of the monolith or inside the catalyst layer measured the catalyst temperature. These temperatures were monitored and recorded.

2.3.4 Analysis system

The effluents from the reactor were monitored by a Fourier Transform Infrared Spectroscopy (FT-IR; Thermo Nicolet Nexus 470) and a quadrupole mass spectrometer (QMS; Cirrus LM99, MKS inc.).

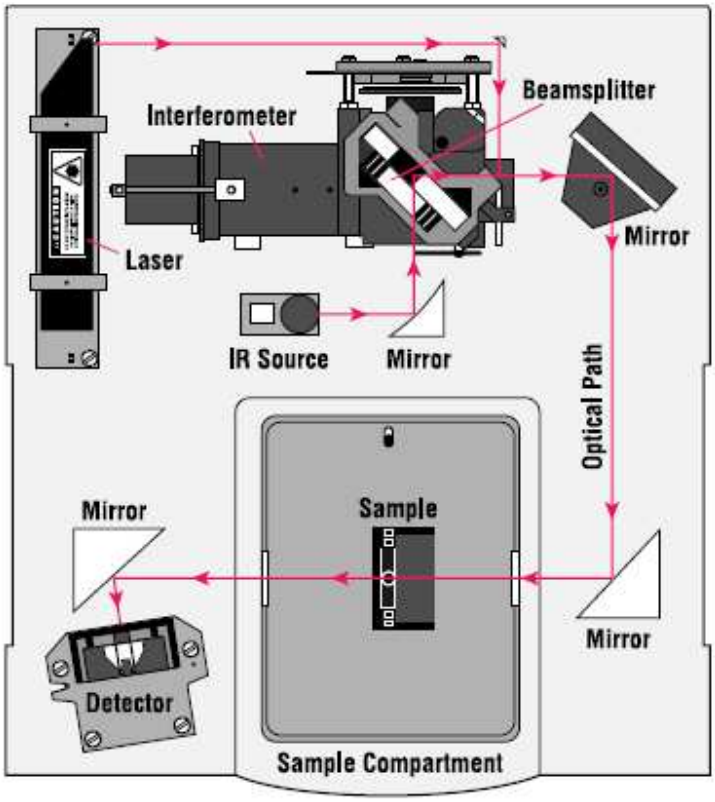

Figure 2-4 A schematic layout of ThermoNicolet IR spectroscopy.

FTIR is a non-invasive, precise and sensitive technique to identify a chemical compound and quantify its amount. Figure 2-4 provides a schematic layout of the

ThermoNicolet Fourier Transform Infrared Spectroscopy. The system consists of an infrared source, an interferometer, a sample, a detector and a computer. The IR source emits an infrared beam with special radiation energy from a black body source. The interferometer uses a beamsplitter to divide the IR beam into two beams. One beam travels a fixed length, while the second beam goes through a delicately changing path. A special interferogram signal is generated when these two beams meet again. Every infrared frequency is encoded into this interferogram signal. This speeds up the whole IR spectrum measurement so that it is of the order of one second. The exiting beam passes through the sample, which can be gaseous or solid. The characteristic frequencies of energy are absorbed by the sample. The unique molecular structure and bond vibrations in the sample lead to the fingerprint IR spectrum. The detector collects the transmitting interferogram signal. The Fourier transformation of the interferogram signals is decoded in the computer. As a result, the sample compound can be identified by the peaks in the IR spectrum and its concentration can be quantified by the size of the peaks.

In our experiment, the FT-IR was equipped with a specialty ultra-low volume gas cell (25 cm^3, Axiom, Mini Linear Flow Cell). This provided a short gas residence time of about 1.5 s at a flow rate of 1000 sccm. The OMNIC® software was used for the gas calibration and the online concentration measurement. The scanning frequency was one spectrum per s. The NO, NO_2, N_2O, NH_3, CO, CO_2 and H_2O calibrations in FTIR were conducted by feeding special gases of known concentrations and correlating their concentrations to the intensity of fingerprint bands in the IR spectrum. The gas concentration calibration was performed every half a year to ensure data accuracy. The

background IR spectrum was collected every day before the experiments. This spectrum removed all the instrumental characteristics and thus all the spectral features came from the gaseous samples.

A MKS Cirrus^{TM} quadrupole mass spectrometer monitored the H_2, O_2 and N_2 concentrations. The QMS were calibrated daily using special calibration gases from Matheson Tri-Gas before the start of the experiments. The vacuum chamber pressure was stabilized under a continuous Ar flow of 1000 sccm. The Faraday and Multiplier calibrations were conducted three times to ensure the ion source stability. Each gas was calibrated at three different concentrations, covering the concentration range in the experiments. When the feed did not contain CO_2, the nitrogen balance could be closed within 5%. When the feed contained CO_2, the amount of N_2 formed was obtained by closing the nitrogen balance because of the of the m/e=28 overlap with CO_2 in the QMS. The effluent flow time lags between the reactor system and FTIR and the reactor system and QMS were determined by replacing the reactor with an unloaded quartz tube. The time lags were subtracted in the data post-processing.

2.4 Experiments using Diffuse Reflection Infrared Spectroscopy

This reactor system was housed in the diffuse reflection infrared spectrometer (DRIFTS) to measure the surface species on the catalyst surface.

The experiments were carried out over a Thermo Nicolet 6700 FT-IR spectrometer equipped with a MCT detector. 60 mg catalyst powder sample was pressed into a small tablet and then loaded to the Praying Mantis^{TM} DRIFTS cell (Harrick

Scientific Products, Inc.) which had two KBr windows. The flowing gases were supplied from compressed gas cylinders (Matheson Tri-Gas) and controlled by MKS mass flow controllers. The total flow rate was kept at 50 sccm. The adsorption spectra of the in situ diffuse reflectance infrared upon catalyst exposure were collected scanning 64 times from 400 cm^{-1} to 4000 cm^{-1} at resolution of 4 cm^{-1} in OMINC® software. The background spectrum was collected before every experiment to eliminate the instrumental noises.

Chapter 3 Spatio-temporal Features of Periodic Oxidation of H_2 and CO over the PtCe Catalyst

3.1 Introduction

Ceria is well known as an oxygen storage component (OSC) in automobiles three-way catalytic converters (TWC) for gasoline spark-ignition engines. Ceria efficiently captures and releases oxygen due to the relative ease of shuttling between two oxidation states (Ce^{3+} and Ce^{4+}),

$Ce_2O_3 + 0.5\ O_2 \leftrightarrow 2\ CeO_2$ -368 kJ/mole Ce_2O_3. (R1)

This widens the air-to-fuel window for the exhaust abatement.

Working in tandem with the active precious metals such as Pt, ceria serves as a buffer by storing oxygen during lean periods and supplying oxygen during rich ones. Thus, highly exothermic reactions, such as hydrogen and CO oxidation, occur as a result of the switch from fuel-lean to fuel-rich modes

$H_2 + 2\ CeO_2 \rightarrow H_2O + Ce_2O_3$ 242 kJ/mole H_2, (R2a)

$CO + 2\ CeO_2 \rightarrow CO_2 + Ce_2O_3$ 283 kJ/mole CO. (R2b)

This exotherm leads to a complex spatio-temporal temperatural behavior of the ceria containing catalyst and causes undesired side effects, such as excessive fuel consumption and PGM sintering. The spatio-temporal behavior of the PtCe catalyst is considered in this study during a periodic feed shift from either H_2 and/or CO (rich phase) to O_2 (lean phase). The use of a very fast H_2 and CO oxidation as a probe reaction enables monitoring the storage/release process. The complex features of the co-oxidation of H_2 and CO mixtures closely mimic those of the exhaust of a catalytic converter. The spatial

and temporal resolution of the reaction system is obtained by a combination of infrared thermal imaging and gas phase composition measurements. The exothermicity of the H_2 and CO oxidation and the resolution of infrared imaging of a flat sheet of monolith catalyst are used to elucidate the coupling of the chemistry and transport processes on the model $Pt/CeO_2/Al_2O_3$ catalyst.

3.2 Experimental

3.2.1 X-ray Diffraction and High Resolution Transmission Electron Microscopy

X-ray diffraction spectra of fresh and aged $Pt/CeO_2/\gamma\text{-}Al_2O_3$ and fresh $Pt/\gamma\text{-}Al_2O_3$ were collected by a Siemens D5000 diffractometer equipped with a Braun Position Sensitive Detector with an angular range of 8° and a Cu Kα source radiation. The diffraction angles were taken from 21° to 80°, with a step scan of 0.02 °/step and a holding time of 10 s per step.

The surface morphology of fresh $Pt/CeO_2/\gamma\text{-}Al_2O_3$ was imaged by a JEOL 2010FX high resolution transmission electron microscope (HRTEM) at the University of Houston superconductivity center.

3.2.2 Temperature Programmed Methods

Temperature programmed reduction (TPR) and desorption (TPD) experiments were conducted in which 200 mg (1.93 ml) catalyst powder was loaded into a quartz tube (1.2 cm diameter, 40.6 cm length) and placed in a furnace (Mellen M300). In the H_2-TPR experiments the catalyst was pretreated with a 20 % O_2 in Ar flowing gas mixture during

a 20 °C/min temperature ramp from 25 °C to 500 °C. The catalyst was then held at 500 °C for 2 hours before cooling down to 50 °C. After sweeping the reactor with Ar for 10 minutes to remove any residual oxygen, it was heated from 50 °C to 900 °C at a rate of 20 °C/min in a reducing gas mixture of 1% H_2 in Ar. The effluent hydrogen concentration was recorded by a quadrupole mass spectrometer (QMS; Cirrus LM99, MKS inc.), while the water production was monitored by a FTIR (Thermo Nicolet Nexus 470).

The TPD experiments involved oxygen and water desorption from the catalyst during another temperature ramp. Two types of H_2O-TPD experiments were conducted to identify and quantify the different forms of adsorbed water. In the Type I H_2O-TPD, overall loosely- and strongly-bound water was probed. The catalyst was initially saturated with water by exposing the catalyst at 50 °C to a reactive gas mixture containing 10 % H_2 and 5 % O_2 at a flow rate of 200 ml/min. After the adsorption was complete, typically about 70 minutes, as indicated by a steady effluent H_2O concentration, the reactor was purged with pure Ar for 30 min to remove loosely-bound H_2O until its effluent concentration was negligible (<10 ppm). The sample was then ramped to 900 °C at a heating rate of 20 °C/min in Ar at a flow rate of 200 ml/min, while the exit concentration of water was measured by the FTIR.

In the Type II H_2O-TPD, strongly-bound water in the proximity of catalyst active sites was probed. The catalyst was first heated up to 900 °C under 2% H_2 in Ar and kept at 900 °C until no water was detected in the effluent. Then, a pure Ar stream was fed as the catalyst was cooled to 50 °C; during this process any residual H_2 was removed. When

the desired temperature was reached, 500 ppm O_2 in Ar was injected for 200 s to adsorb ca. 15 µmole oxygen onto the catalyst. Loosely-bound O_2 was removed in a pure Ar for stream for 10 min at 50 ^oC. Then the feed was switched to a mixture containing 500 ppm H_2 in Ar for 400 s; any loosely-bound H_2 and H_2O were removed by Ar until no water was detected. The catalyst was then heated from 50 to 900 °C at a heating rate of 20 °C /min under a pure Ar flow of 200 ml/min, while the effluent water concentration was recorded by the FTIR.

3.2.3 Oxygen Uptake Experiments

This set of experiments followed the reduction at 450 ^oC of the $Pt/CeO_2/Al_2O_3$ catalytic monolith in a flowing 5% H_2/Ar or CO/Ar gas mixture for 30 minutes until no water or CO_2 was emitted. The catalyst was then cooled down to the desired temperature and the residual hydrogen or CO was removed by Ar flow. Afterwards the feed was switched to a flowing gas mixture containing a prescribed concentration of O_2 (100 ppm to 5%) in Ar. Sufficient time was allowed for the O_2 to return to its feed value (about 10 minutes). The O_2 was then switched off and the sample was exposed to Ar for 30 minutes. Finally, the catalyst was exposed to a 1% H_2 or CO in Ar mixture. The oxygen uptake was determined by integrating the difference between the feed and effluent molar flow rates. The physisorbed O_2 was the amount of O_2 released immediately after the switch from the O_2/Ar to Ar feed. The chemisorbed form was the amount of O_2 remaining on the catalyst. This value was determined by the amount of CO_2 produced or H_2 consumed. (The H_2O signal was unreliable due to its slow desorption). An OSC

isotherm at a fixed temperature describes the chemisorbed O_2 as a function of the O_2 concentration.

3.2.4 Lean and Rich Cycle Experiments

The flat plate monolith sample was heated to the desired temperature under a flow of pure nitrogen at a specific space velocity. In most experiments the space velocity (298.15K, 1 atm basis) was 100,000 hr^{-1}, which corresponded to a total inlet flow rate of 4053 standard cm^3/min about a linear velocity of 2.11 m/s. After the monolith temperature stabilized, a stream of oxygen was fed creating a lean phase gas mixture of 5% O_2 in N_2. The monolith sample was exposed to the lean gas mixture for 100 s. The feed was then switched to a rich gas mixture containing 2% H_2 in N_2 to reduce the stored oxygen on the monolith for 10 or 20 s under the same space velocity. For comparison purposes a second set of experiments used 2% CO as the rich stream. In a third set of experiments, a gas mixture containing 1.5% CO and 0.5% H_2 in N_2 was fed in the rich gas mixture to better simulate a realistic exhaust stream. During the experiments, the spatio-temporal monolith temperature was monitored by the IR camera and the exit concentration was measured by the QMS. A periodic state was obtained after ca. 25 lean/rich (LR) cycles; the final three cycles were used to obtain the cycle-averaged results. Several different operating parameters were varied to determine their effects; including the monolith temperature, space velocity, and feed composition (% H_2, % O_2). Most experiments were repeated five times. The results reported are averages of these multiple

runs. The conversion measurements were accurate to within 1.5% while the monolith temperature was accurate to within 0.5 ^{o}C.

In some of the lean and rich cycling experiments a pulse of pure nitrogen was introduced between the lean-to-rich or rich-to-lean switches for a duration varying from 5 to 600 s. The pre-adsorbed O_2 or H_2 was swept from the catalyst before the introduction of the H_2 or O_2, respectively. Sweeping pre-adsorbed O_2 provided another way to quantify weakly and strongly bound (physisorbed and chemisorbed) oxygen.

So-called "inert" feed gas experiments were the same as the LR cycling experiments but with no oxygen in the lean phase. The purpose of the inert experiments was to quantify the hydrogen conversion during the LR cycling and N_2 pulse experiments.

3.3 Results and Discussion

3.3.1 Oxygen Storage on a PtCe Catalyst

The storage capacity of the PtCe catalyst is due to its crystal structure and surface morphology. X-ray diffraction, high resolution transmission electron microscopy and temperature programmed methods investigated the storage sites over the PtCe catalyst.

Figure 3-1 shows the X-ray diffraction of fresh and aged $Pt/CeO_2/\gamma\text{-}Al_2O_3$ catalyst and fresh $Pt/\gamma\text{-}Al_2O_3$ catalyst. Pattern 1 in that Figure is of the fresh $Pt/\gamma\text{-}Al_2O_3$ catalyst, Pattern 2 of the fresh $Pt/CeO_2/\gamma\text{-}Al_2O_3$ catalyst and Pattern 3 of the aged $Pt/CeO_2/\gamma\text{-}Al_2O_3$ catalyst. The indexing of diffraction peaks was based on the Bragg's law,

$$d_{hkl} = \frac{\lambda}{2\sin\theta}, \quad (1)$$

where λ is the wavelength of the X-ray which is 1.54 angstroms for the copper source; θ is the diffraction angle in degrees; d is the interatomic spacing in angstroms. The plane spacing of crystals is calculated by the following equations,

Cubic crystal $$\frac{1}{d_{hkl}^2} = \frac{h^2+k^2+l^2}{a^2}, \quad (2)$$

Hexagonal crystal $$\frac{1}{d_{hkl}^2} = \frac{4}{3}\left(\frac{h^2+hk+k^2}{a^2}\right) + \frac{l^2}{c^2}. \quad (3)$$

Here, a and c are the unit cell sizes in angstroms; h, k and l are the indexing planes. The diffraction peaks in Figure 3-1 can be indexed using the above equations. Take the CeO_2 peak indexing as an example. The CeO_2 has a fluorite structure and its unit cell size is about 5.42 Å. At the <1 1 1> plane, the d-spacing was calculated to be 3.13 Å by the equation (2) and the corresponding theta was calculated to be 14.23° by the equation (1). Hence, the <1 1 1> plane of CeO_2 crystal led to the diffraction peak with a 2theta value of 28.46° in the Pattern 2. The rest diffraction peaks of CeO_2 crystal was indexed using the same procedure.

The Pt unit cell structure is face centered cubic and its lattice parameter is estimated to be 3.92 Å. Only one <1 1 1> diffraction peak was observed at 39.44° and marked by the solid star symbol. The γ-Al_2O_3 has a hexagonal structure and its lattice parameters are estimated to be a=4.78Å and c=12.99Å. This led to the diffraction peaks at 31.51°, 37.02°, 45.87°, 60.77°, and 66.97° and they were marked by the solid triangular symbols. The fluorite structure CeO_2 generated diffraction peaks in 28.46°, 32.98°, 45.87°, 47.40°, 56.29°, 59.01°, 69.31°, 75.64°, and 78.96° which were marked by the solid circle symbols. Some γ-Al_2O_3 diffraction peaks, i.e., 31.51° and 60.77°, were not present in Pattern 2 and 3 due to the overlap with the ceria peaks.

The ceria particle size can be estimated by Scherrer's Formula

$$t = \frac{K*\lambda}{B*\cos\theta}, \quad (4)$$

where t is the particle size in angstroms; K is the crystallite shape constant as 0.9; λ the X-ray wavelength of 1.54 angstroms for the copper source; B the full width at half max or integral breadth, and θ the diffraction angle in degrees. Based on the Scherrer's Formula, the ceria particle sizes in Pattern 2 and Pattern 3 were 7.5 nm and 11.7 nm, respectively. On the other hand, the Pt peak was intercrossed with the γ-Al_2O_3 peak at 32.98° so that the Pt particle size could not be appropriately estimated.

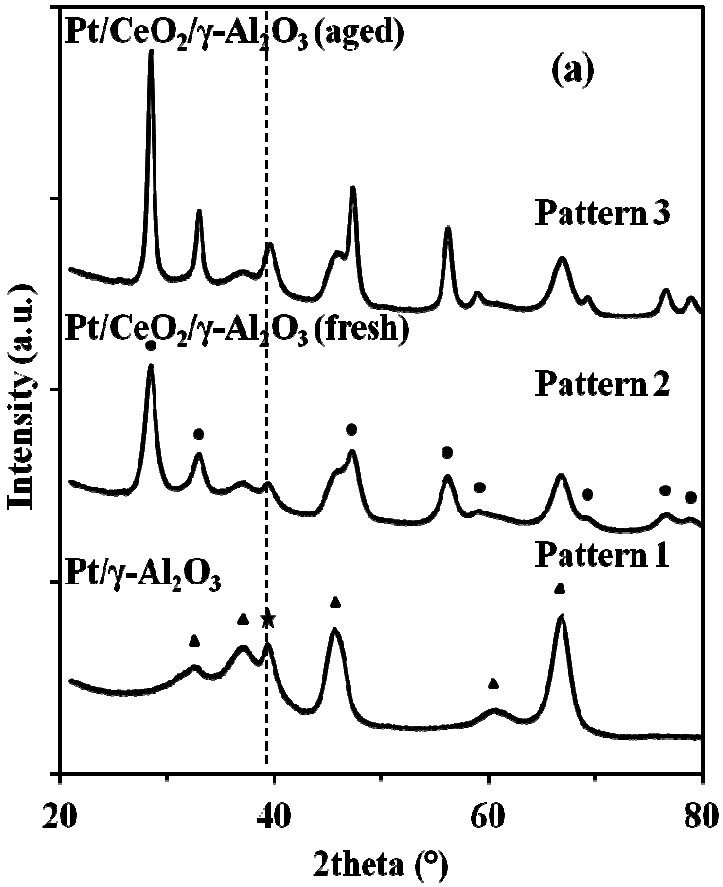

Figure 3-1 XRD spectrums of fresh Pt/ Al_2O_3 catalyst (Pattern 1), fresh Pt/CeO_2/ Al_2O_3 catalyst (Pattern 2) and aged Pt/CeO_2/ Al_2O_3 catalyst (Pattern 3). ★: Pt; ▲: Al_2O_3 ; ●: CeO_2.

The ceria addition has a strong impact on the Pt/γ-Al_2O_3 catalyst as shown in Pattern 1 and Pattern 2 in Figure 3-1. The intensity of the Pt diffraction peak in Pt/CeO_2/γ-Al_2O_3 is lower than that of Pt/ γ-Al_2O_3. This suggests a well-dispersed status of the Pt on the ceria surface [29]. The influence of calcining the catalyst in the air at 800 °C for 200 hr (aging) can be found by comparing Pattern 2 and Pattern 3. After aging, the intensity of the ceria peaks become sharper and the ceria particle size increases from 7.5 nm to 11.7 nm. The intensity of the Pt peak increases due to the sintering of the Pt and ceria particles as well as the weaker interaction between them. To obtain an accurate reflection of the catalyst performance, fresh Pt/CeO_2/γ-Al_2O_3 catalyst is used to study the surface morphology.

Figure 3-2 (a) shows the TEM images of the fresh PtCe catalyst before any sample preparation. The big white agglomerate crystals are the γ-Al_2O_3 grains. The black cubic objectives are the ceria nanoparticles. The Pt particle is not clearly visible on this picture due to the small particle size (2-5 nm). The catalyst powder aggregated together and was too dense to locate Pt particle. Hence, the catalyst powder was diluted and ball-milled with alcohol to get a better resolution in a smaller scale of 1-20 nm. Figure 3-2 (b) shows the HRTEM imaging of the fresh PtCe catalyst after dilution by alcohol. Different contacts between γ-Al_2O_3 and CeO_2 were observed and diverse interfaces between Pt and other metal particles were generated. As indicated by arrows, some Pt particles were deposited on the surface of both γ-Al_2O_3 and CeO_2 particles. Some Pt sites were on the juncture of γ-Al_2O_3 and CeO_2. The resulting interfaces between different metal particles have a strong impact on the storage and reduction processes, i.e., the oxidant spillover.

Hence, various storage sites are generated as a result of different contacting statuses between the metal particles.

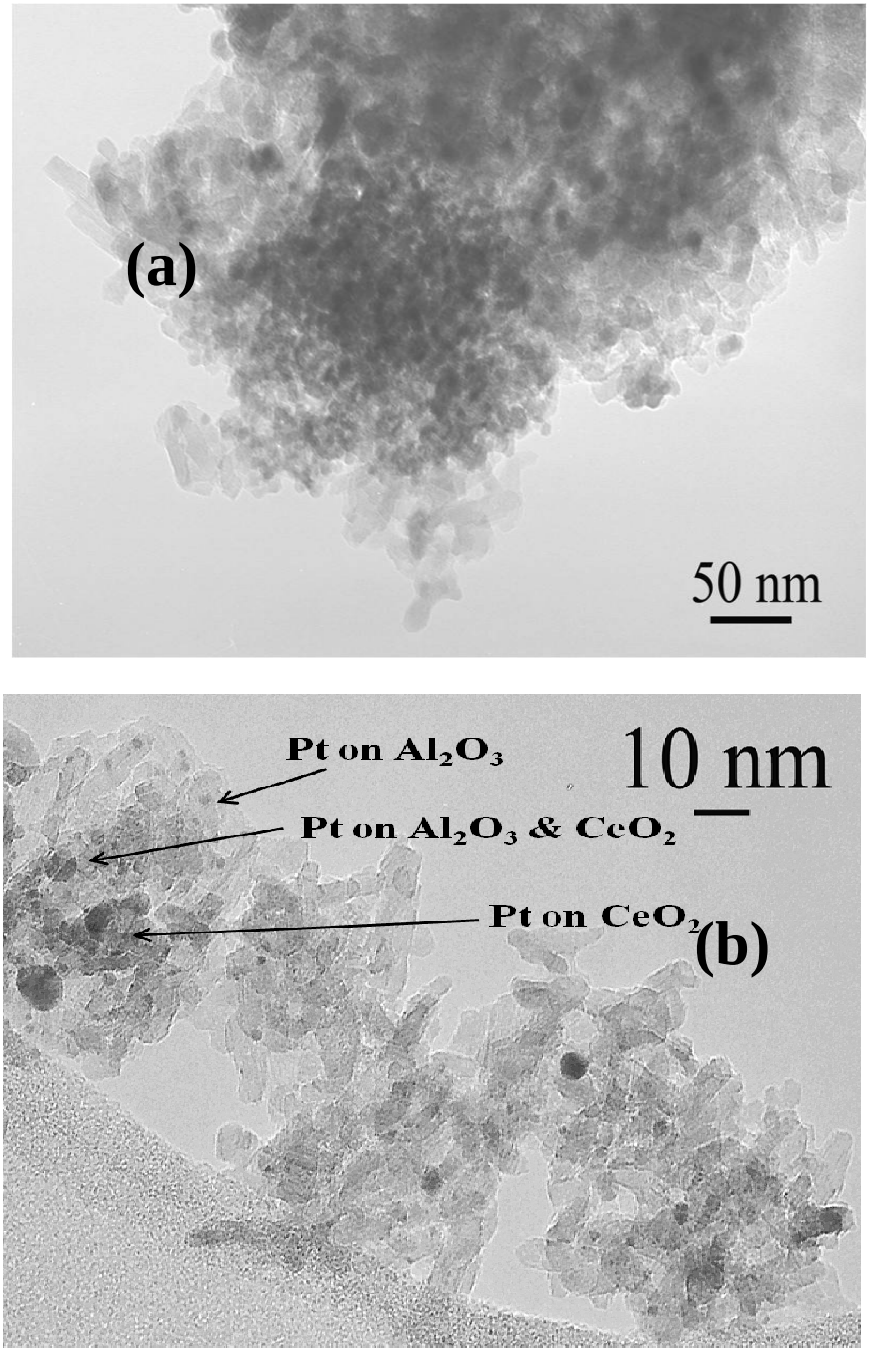

Figure 3-2 TEM images of the fresh PtCe catalyst (a) before alcohol dilution; (b) before alcohol dilution.

Temperature-programmed reduction and desorption of the pre-oxidized $Pt/CeO_2/Al_2O_3$ was used to determine the storage sites over the PtCe catalyst. Figure 3-3 shows the results of a temporal reduction of the oxidized PtCe catalyst during exposure to a 1% H_2/Ar mixture and subject to a 20 ^oC/min temperature ramp. The experiment shows that most of the H_2 was consumed in a temperature window between 50 and 200 ^oC. A sharp increase in the H_2 consumption occurred right after the H_2 admission. The H_2 consumption dropped sharply to a low level between 250 and 900 ^oC, with a small peak at 870 ^oC. Three additional consumption peaks are noted in Figure 3-3; at 300 s, 400 s, and 2400 s. The corresponding temperatures were 60 ^oC, 150 ^oC, and 190 ^oC, respectively. The small but nonzero H_2 concentration between 500 and 2400 s is the background signal.

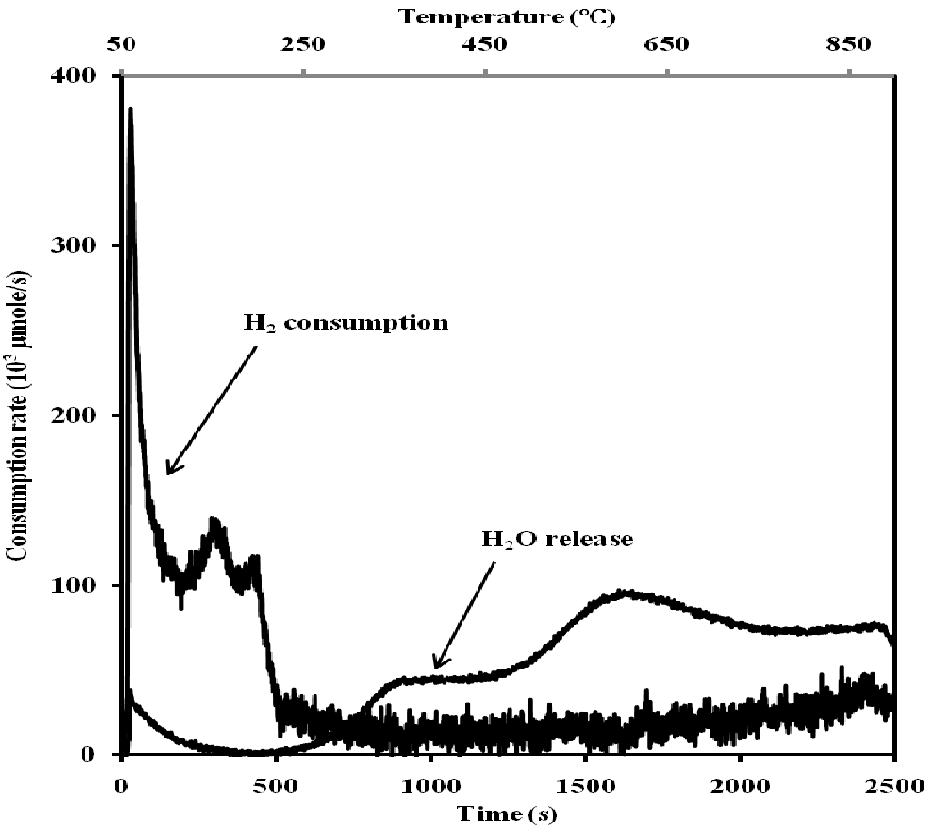

Figure 3-3 the H_2-TPR profile for the oxygen pretreated PtCe catalyst.

In the H_2-TPR, oxygen serves as the probing molecule to detect the storage sites. The H_2 reduction of stored oxygen confirms the existence of different surface storage sites as indicated by the multiple peaks in the H_2-TPR pattern in Figure 3-3. The type of oxygen consumed at various temperatures can be determined based on literature results and quantitative analysis. The lowest temperature peak undoubtedly corresponds to the scavenging of oxygen adatoms on the exposed Pt surface. Integration of the area under the temporal H_2 consumption rate quantifies the number of H_2 moles consumed over a prescribed time period. 28.6 μmoles of O (or H_2) were consumed up to 110 ^oC. This compares to 12.5 μmoles of exposed Pt in the catalyst sample. These results suggest that the reaction between hydrogen and oxygen adatoms adsorbed on Pt atoms occurs in a 2:1 stoichiometry, possibly due to the formation of PtO_2. Damyanova et al. [29] reported that the lowest temperature at which a H_2 consumption peak appeared is in the range of 260-320 ^oC on a 1 wt% Pt/12 wt% CeO_2/Al_2O_3 catalyst. The lower observed temperature range is probably due to the higher activity by the higher Pt loading of 2.43 wt% and the high dispersion of 50 %. Clayton et al. [73] found that the light-off temperature during the oxidation of H_2 by NO decreases by about 150 ^oC when the Pt loading was increased from 0.3 wt% to 2.2 wt%. Figure 3-3 also shows that an additional 34.6 μmoles of O (or H_2) are consumed between 110 and 200 ^oC. This value exceeds the total amount from a monolayer of O adatoms on the Pt by a factor of about 3. Clearly, the most likely source of the additional oxygen is from ceria in close proximity to the Pt crystallites [74]. The peak at ca. 150 ^oC (300 s) and the shoulder peak at ca. 190 ^oC (420 s) are attributed to consumption of oxygen supplied by the interaction between PtO_2 and CeO_2 with different

aggregation states given the high Ce loading of 13 wt% [75]. Yao [30] has shown that the presence of Pt shifts the intermediate H_2 consumption peaks from high temperatures of ca. 500 ^oC to much lower temperatures (ca. 100 ^oC). This is likely due to a spillover of O atoms from the CeO_2 phase to the Pt crystallites on which the reduction can occur. Finally, the fourth peak at 870 ^oC corresponds to the reduction of bulk cerium oxide CeO_2 to Ce_2O_3 as reported previously [29-30, 76]. Hence, the accessibility of storage sites is ranked as the Pt surface, the Pt-Ce interfaces and the ceria surface.

The water desorption from the PtCe catalyst was also studied to investigate the affinity of reaction product to the storage sites. There could be two types of adsorbed water: one close to the reaction sites and the other far away from the reaction sites. Hence, two types of H_2O-TPD were carried out. The type I H_2O-TPD shown in Figure 3-4 (a) reveals that different forms of water exists over the whole catalyst surface. The first peak between 150 and 200 ^oC probably corresponds to the desorption of weakly-bound water molecules from the catalyst. The second peak at ca. 325 ^oC is attributed to the elimination of surface hydroxyl groups from the Al_2O_3. The two high temperature peaks, at 600 ^oC and 850 ^oC indicates formation of water from Ce- and Al-related species. The type II H_2O-TPD experiments shown in Figure 3-4 (b) describes different forms of H_2O absorbed close to Pt sites. No peak for water desorption existed at low temperature (< 250 ^oC), while three peaks for water desorption were located at about 350 ^oC, 600 ^oC and 850 ^oC. The estimated amount of released water from these data was 28.1 µmoles, comparable to 12.5 µmole of exposed Pt sites.

A comparison of the H_2-TPR data (Figure 3-3) and H_2O-TPD data (Figure 3-4 (a)) is noteworthy. While the water desorption peaks above 350 ^oC have corresponding peaks in the H_2 consumption data, the large release of water below 200 ^oC in the Type I H_2O-TPD, probing the overall water adsorption, is not present in the H_2O trace of the H_2-TPR. This difference leads to a large disparity in the amount of water released during the H_2O-TPD (258 µmoles) and the amount of H_2 consumed during the TPR (115 µmole). These values are expected to be much closer. The difference may be explained by the type and amount of the different forms of H_2O as seen in the results from the Type II H_2O-TPD experiments shown in Figure 3-4 (b). No water desorption peak appears below 250 ^oC and the water release begins above 350 ^oC. The Type II TPD experiments probe only strongly-bound water in the proximity of the catalyst active sites. Hence, the significant water released below 200 ^oC is the desorption of weakly-bound water, while the strongly-bonded water was only removed at higher temperatures.

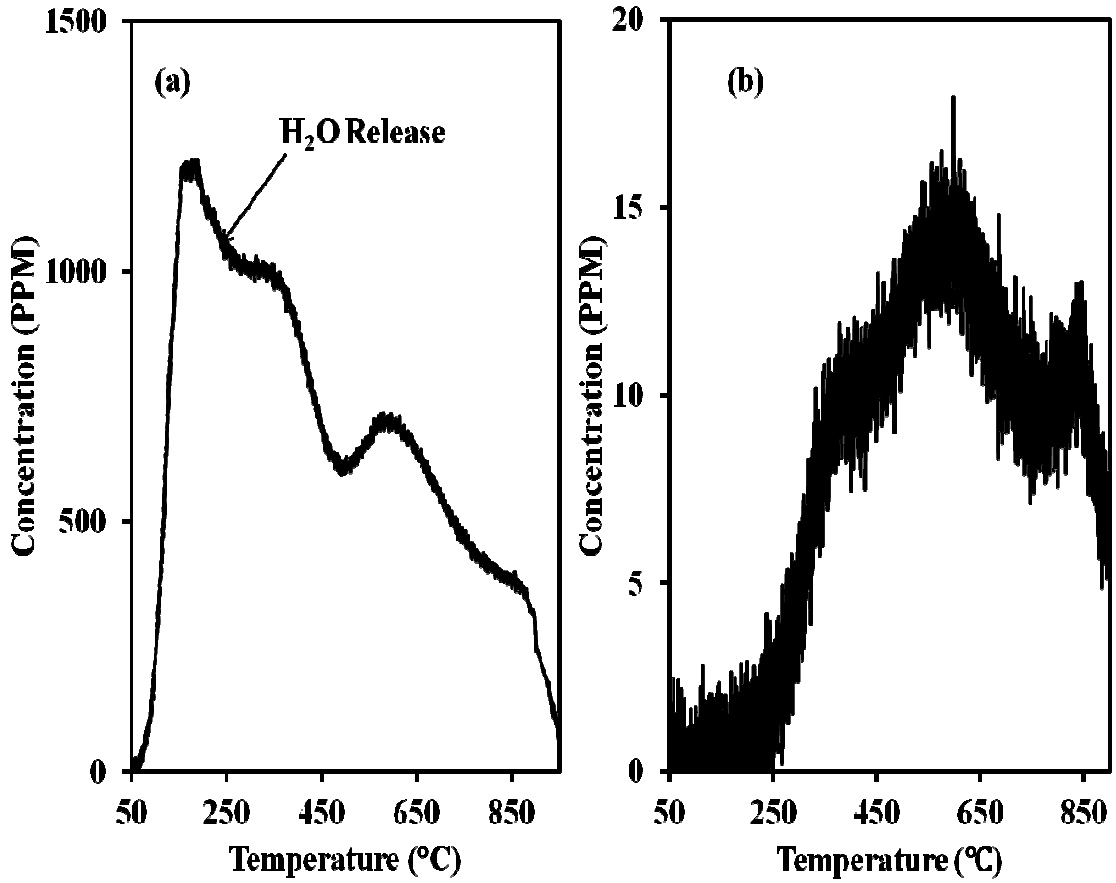

Figure 3-4 the H_2O-TPD profiles (a) type I and (b) type II.

The dependence of the stored oxygen on the feed O_2 concentration, shown as the ratio of oxygen partial pressure (P_{O2}) to the total pressure (P), is presented in Figure 3-5. The data are consistent with a Langmuir type isotherm. The available storage sites can be calculated by the Langmuir equation

$$\frac{N_{O_2}}{N_{total}} = \frac{\alpha * P_{O_2}}{1+\alpha * P_{O_2}} \ , \qquad (5)$$

where N_{O2} is the storage sites covered by oxygen, N_{total} is the total oxygen storage sites, α is a constant and P_{O2} is the partial pressure of oxygen. The OSC of the PtCe catalyst is determined to be 198.41 μmole O/ g washcoat at 350 ^{o}C.

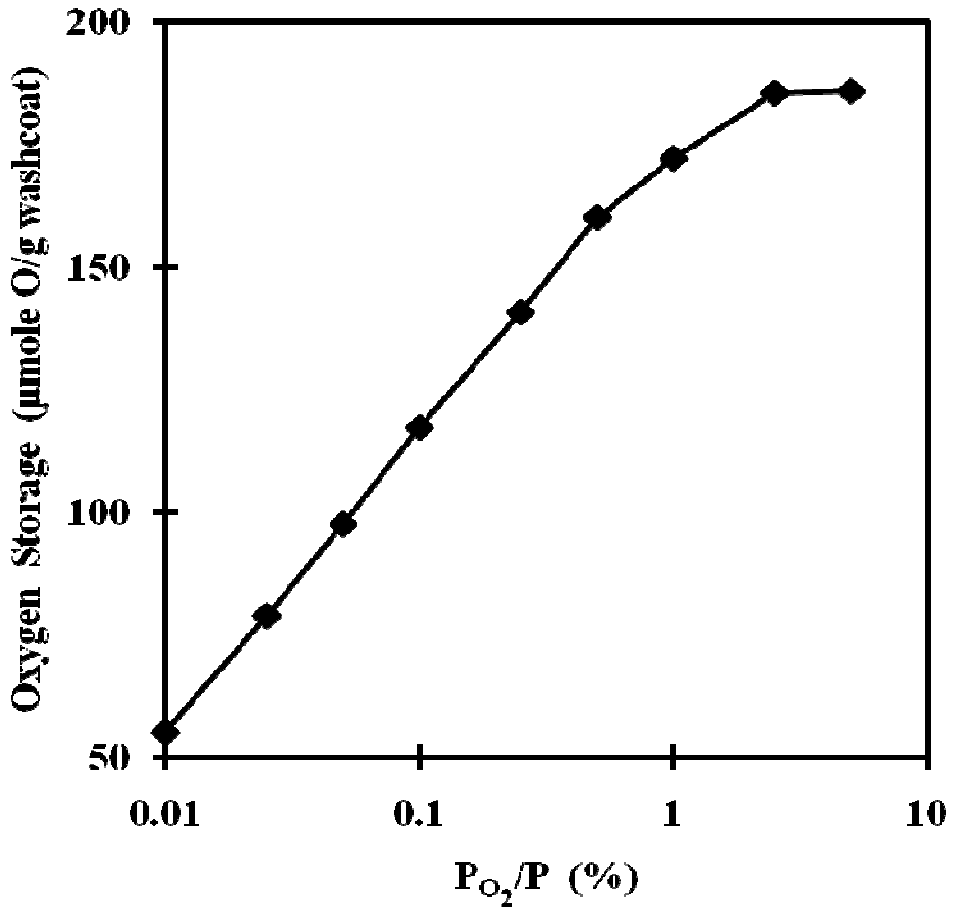

Figure 3-5 Dependence of oxygen storage capacity on the O_2 feed concentration. Space velocity of 100,000 hr^{-1} and feed temperature of 350 ^oC.

Table 3-1 reports the temperature dependence of the OSC (in μmole O/g washcoat) classified according to the physisorbed and chemisorbed forms. These data were obtained by pre-oxidizing the catalyst with a mixture of 100 ppm O_2/Ar at each temperature. The total OSC decreased sharply upon a temperature increase, while the physisorbed OSC was nearly constant. The chemisorbed OSC decreased with increasing temperature from a value of 201 μmole O/ g washcoat to 2 μmole O/g washcoat as the temperature was increased from 150 ^oC to 400 ^oC.

Table 3-1 Effect of temperature on stored oxygen obtained with 100 ppm O_2/Ar feed.

Temperature (℃)	**Total storage (μmole O /g washcoat)**	**Physical (μmole O /g washcoat)**	**Chemical (μmole O /g washcoat)**
150	226	25	201
250	180	25	155
350	79	25	54
400	26	24	2

As reported in Figure 3-5 and Table 3-1, the oxygen storage capacity (OSC) of the PtCe catalyst increases with increasing oxygen partial pressure and decreases upon raising the catalyst temperature. This suggests that the oxygen storage depends on both the catalyst properties and the operating conditions. The impact of operation parameters will be discussed later.

3.3.2 Lean and Rich Cycling Experiments

Figure 3-6 shows several H_2 breakthrough curves which provide important information on the oxygen storage. The solid LR graph describes the H_2 breakthrough during an LR experiment. During the LR experiment, the catalyst was exposed to periodic shifts between lean and rich feeds. The lean feed contained 5% O_2 in Ar for 100 s and the rich feed contained 2% H_2 in Ar for 20 s. The dashed LR graph is the H_2 breakthrough of an inert experiment at a monolith temperature of 350 ^oC. The same cycling protocol as the LR experiment was used during the inert experiment, while a feed of pure N_2 was fed instead of the O_2 for 100 s. The difference between these

breakthrough data under reaction and non-reaction (inert feed) conditions is the amount of hydrogen consumed which is equal to the total storage of oxygen. This figure also includes the breakthrough curves for a pulse experiment in which nitrogen was fed for 20 s between the L-to-R shifts. The rich stream contained a 2% H_2/N_2 mixture. It also shows a corresponding inert experiment in which nitrogen was fed for 120 s before a 20 s shift to the H_2/N_2 mixture. The difference between these two breakthrough graphs is the strongly bound oxygen. The figure also shows the breakthrough curves for an inert monolith and an empty reactor.

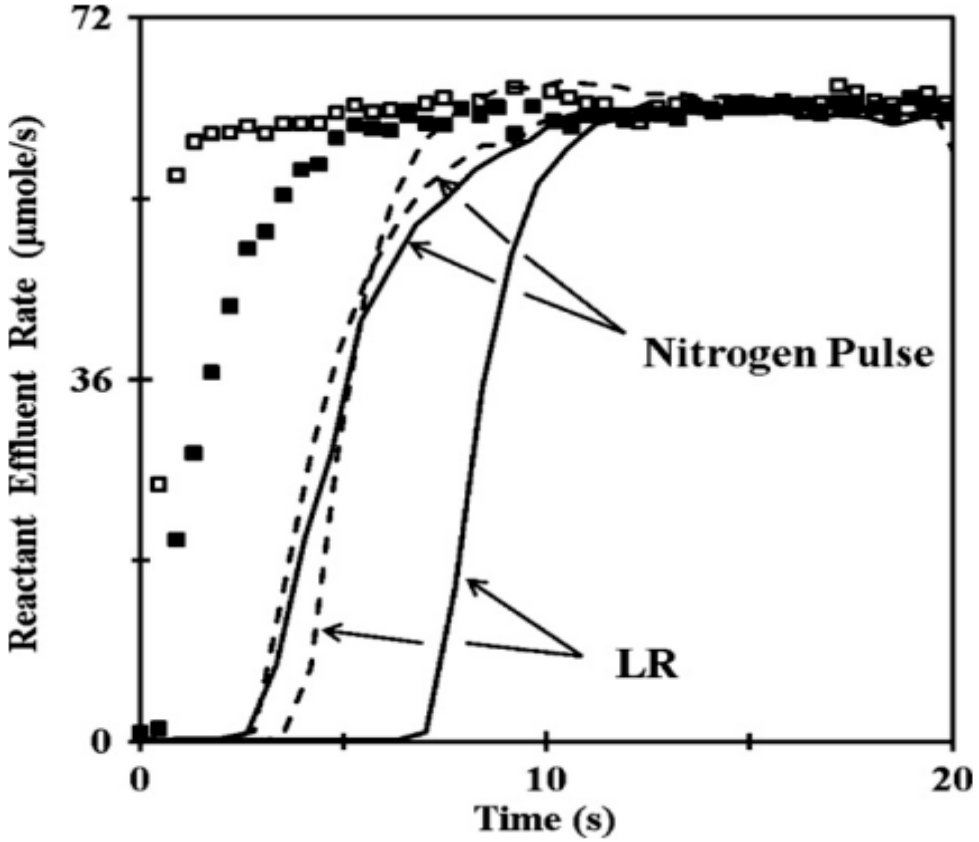

Figure 3-6 The H_2 breakthrough curves at a space velocity of 100,000 hr^{-1} and feed temperature of 350 ^oC. Solid line: LR or Nitrogen pulse experiments; Dash line: Inert LR or nitrogen pulse experiments in which nitrogen is injected for 20s between the L to R shift■ line: Inert experiments with inert monolith; □ line: Inert experiments with an empty reactor.

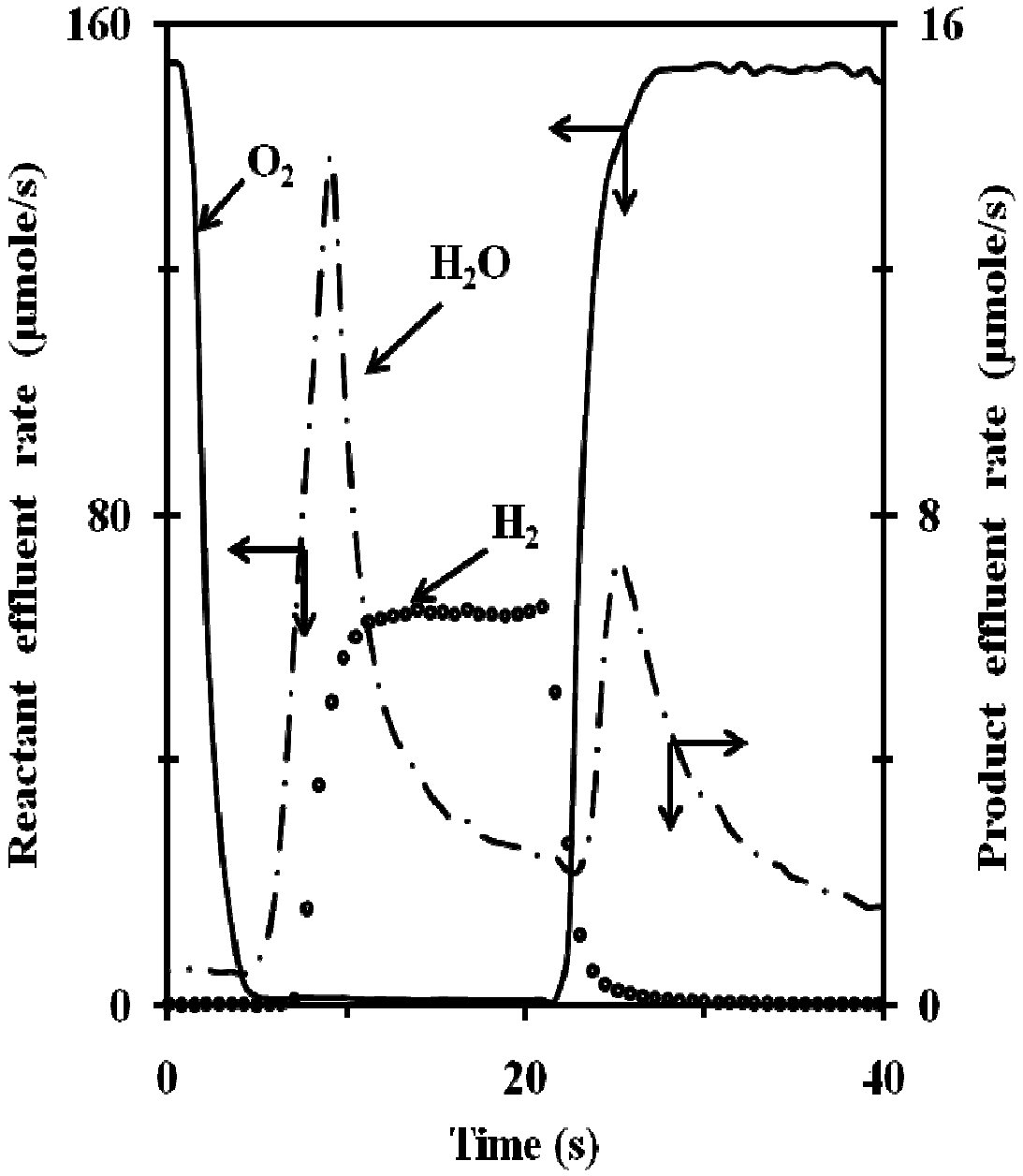

Figure 3-7 Temporal effluent concentration in a LR cycling experiment at a space velocity of 100,000 hr^{-1} and feed temperature of 350 °C. Lean gas contains 5% O_2 in N_2 and rich gas 2% H_2.

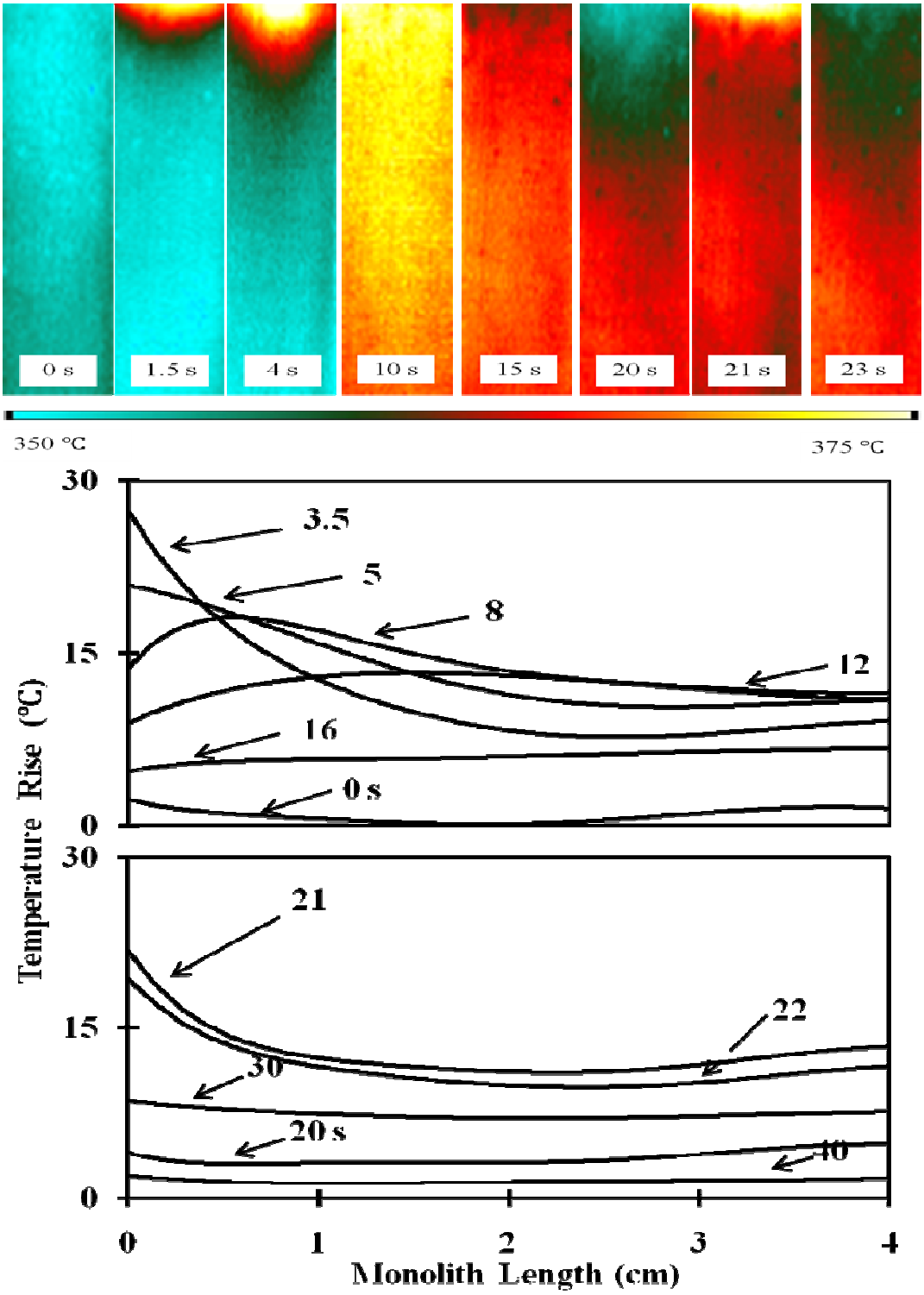

Figure 3-8 IR images and corresponding temporal temperature profiles along a monolith in a LR cycling experiment. Space velocity of 100,000 hr^{-1} and feed temperature of 350 °C.

The spatiotemporal temperature behavior of the PtCe catalyst was investigated by lean and rich cycling experiments. Figure 3-7 shows the temporal dependence of the outlet H_2, O_2 and H_2O concentrations when the pre-oxidized (in 5% O_2/N_2) monolith was exposed to a 2% H_2/N_2 feed for 20 s at an initial monolith temperature of 350 ^oC. After 20 s the feed was switched back to a 5% O_2/N_2 mixture. The effluent O_2 concentration rapidly decreased to zero within 5 s. At this point the oxidation product H_2O broke through from its background level, followed shortly by unreacted H_2 (ca. 7 s). The water concentration exhibited a maximum value of about 0.45% (or 14 µmole/s), decreasing to a value of about 0.07% (or 2 µmole/s) by the time the feed was switched at the 20 s mark. Upon the readmission of the O_2/N_2 mixture the effluent H_2 rapidly decreased to zero while a second peak of H_2O was observed, albeit somewhat less pronounced than the first one; i.e., a peak of 7 µmole/s.

The temporal concentration profiles do not convey the complexity of the reaction. Figure 3-8 shows the temporal evolution of the monolith temperature profiles during the lean and rich cycling experiments. Figure 3-8 (a) shows the 2-D IR images at five discrete times (0, 1.5, 4, 20, 21 s) while Figure 3-8 (b) and (c) show the corresponding monolith width-averaged temperature as a function of the monolith length. The nearly uniform initial temperature of 350 ^oC became highly non-uniform 3.5 s after the lean to rich switch. An upstream temperature peak of about 376 ^oC and a downstream temperature peak of about 358 ^oC were measured. This temperature rise is due to the exothermicity of the reaction between the H_2 and stored oxygen. The data shows that the oxidation occurred in a spatially non-uniform manner. With time, the steepness of the

temperature front became more moderate; the upstream temperature decreased while the downstream increased. This was caused by heat convection by the flowing gas and heat conduction along the monolith. The temperature nearly returned to its initial value at all points on the monolith twenty seconds after the H_2 injection, well after unreacted H_2 had emerged in the effluent. The breakthrough of H_2 indicates that all the accessible oxygen, both the weakly and strongly-held forms, has reacted at the given temperature. As the oxygen was readmitted, a similar hot spot was observed about 1 s after introduction of the lean feed. The effluent transient concentration in Figure 3-7 does not exhibit any features indicative of the complex transient temperature profiles.

To gain an understanding of the reduction, an inert sweep gas (N_2) was fed to the reactor at the shift from lean to rich feed. The duration of the N_2 purge was varied from 5 to 600 s at a fixed monolith temperature. The spatio-temporal temperature patterns during the rich phase in a N_2 pulse experiment are shown in Figure 3-9 at a monolith temperature of 350 ^oC and a nitrogen purge of 20 s. All other conditions were the same as in the previously-described LR experiments (Figure 3-7 and Figure 3-8). The spatio-temporal temperature patterns in Figure 3-9 (a) and (b) differ significantly from those in Figure 3-8 (a), (b) and (c), respectively. The temperature rise was only 3.5 ^oC and 7.5 ^oC after 0.5 and 1.5 s after the H_2-containing stream fed to the reactor, respectively. The maximum temperature rise of 8.4 ^oC was reached 2.5 s after the H_2-containing stream was fed to the reactor. A temperature wave travelled along the monolith in 3 s and the cooling commenced after that time as shown by the temperature profile at 3 s.

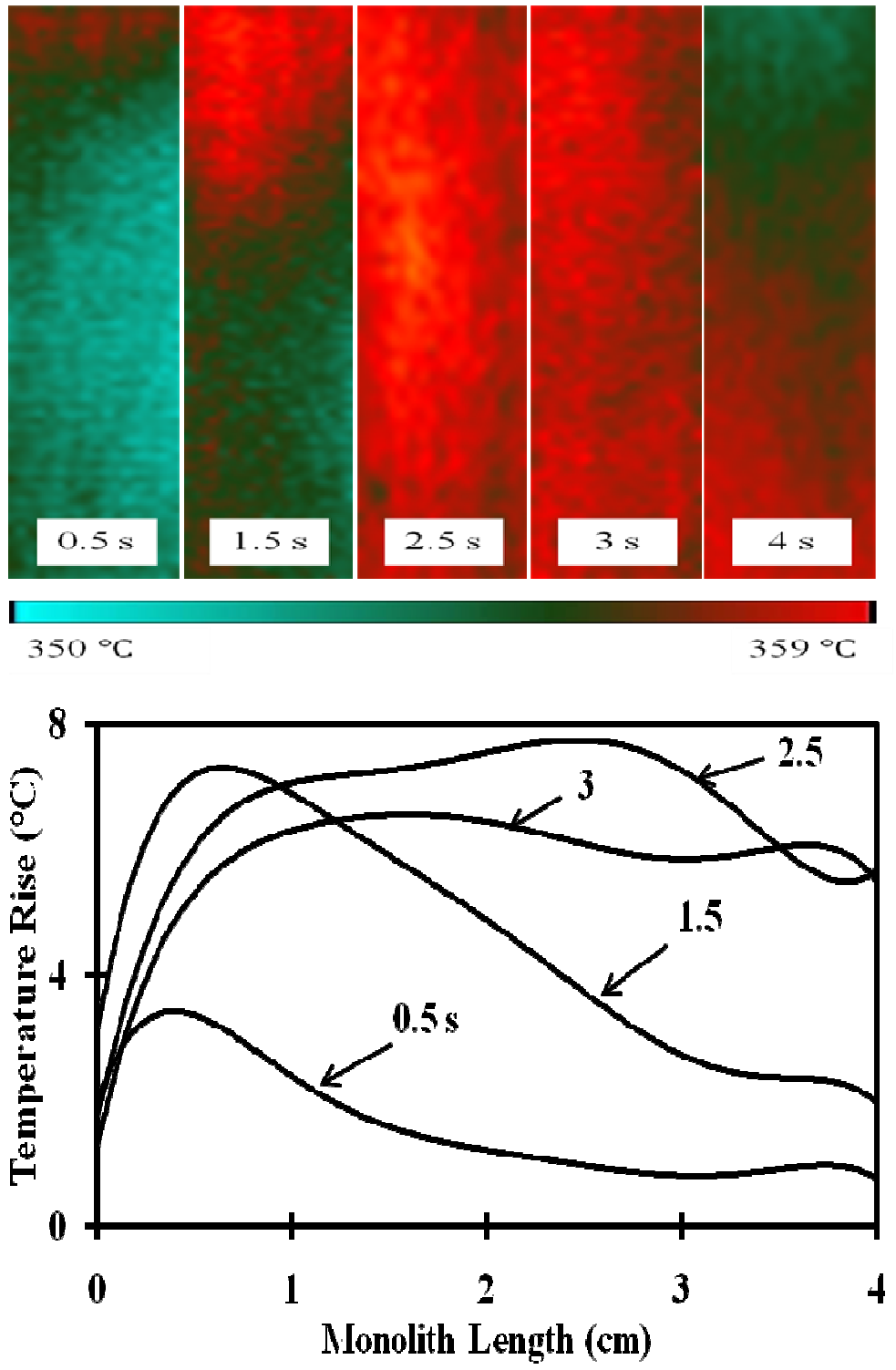

Figure 3-9 IR images and monolith temperature rise along a monolith in a nitrogen pulse experiment under the space velocity of 100,000 hr^{-1} and monolith temperature of 350 °C.

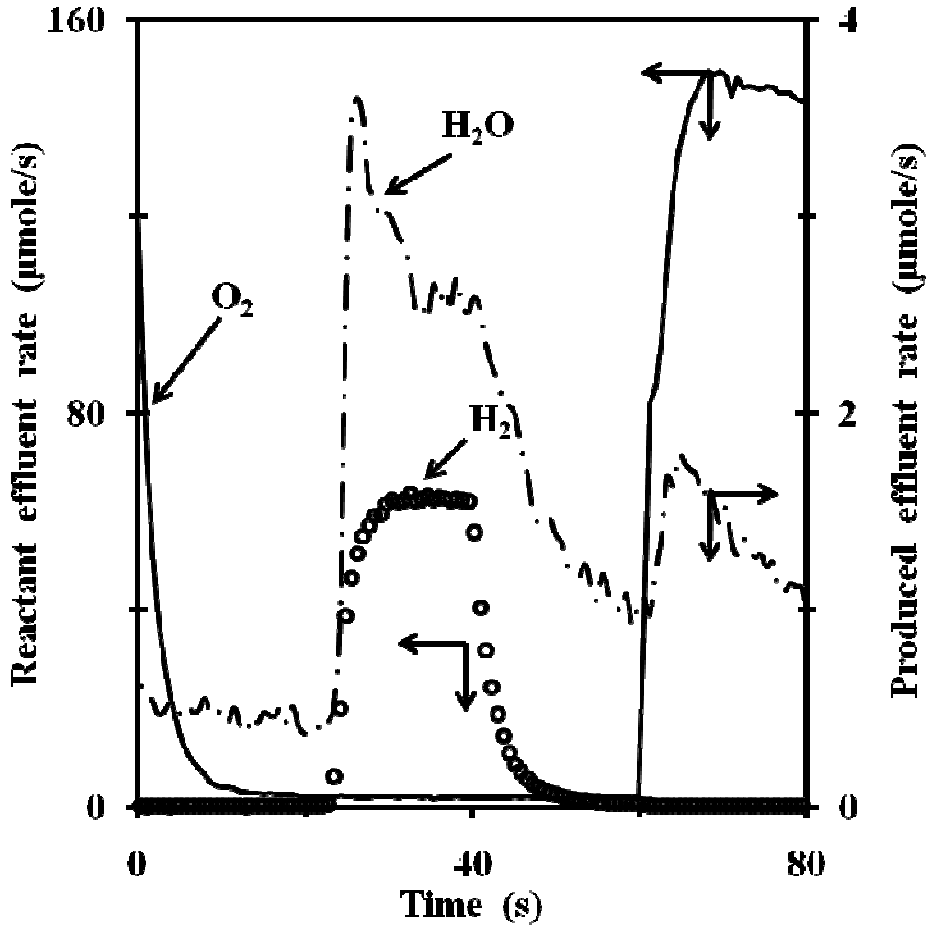

Figure 3-10 Temporal effluent concentration in a 20 s nitrogen pulse experiment. Space velocity was 100,000 hr^{-1} and feed temperature 350 °C.

The corresponding temporal dependence of the effluent gas composition during the N_2 sweep experiments is shown in Figure 3-10. The trends were qualitatively the same as in the experiment without the sweep gas (Figure 3-7), but a much smaller amount of H_2O was produced. The amount of H_2 that reacts can be determined by the difference between the H_2 breakthrough curve in the non-reactive experiment (absence of pre-stored oxygen) and reactive experiment (presence of pre-stored catalyst). Table 3-2 reports the H_2 consumed (in μmole H_2/g washcoat) and fraction converted (%) for several different

N_2 purge times at a monolith temperature of 350 ^oC. The H_2 consumption and conversion decreased with increasing purge duration. Without a purge, the maximum temperature rise was about 25 ^oC, while for a protracted, 300 s N_2 purge the maximum temperature rise was only 7.8 ^oC. The corresponding conversion of H_2 fed during the 20 s long reduction was 29.5% for the former case but only 5.6% for the latter.

Table 3-2 Effect of N_2 pulse time on H_2 consumption.

Pulse time (s)	**H_2 consumption (µmol H_2/g washcoat)**	**H_2 conversion (%)**	**ΔT_{max}(℃)**
0	960	29.5	25.1
5	630	19.4	15.6
10	448	13.8	12.3
15	243	7.5	10.1
20	211	6.5	8.4
300	181	5.6	7.8
600	187	5.7	7.7

The large differences in the temperature rise and H_2 converted in the N_2 sweep experiments are attributed to the amount and type of oxygen present at the start of the reduction. The inert gas stream removes the O_2 that is either weakly adsorbed on the catalyst or held up in the pores of the washcoat. The fraction of the oxygen removed depends on the duration of the sweep gas; the longer the sweep flows the more oxygen is removed. The data in Table 3-2 imply that most of the oxygen removed at 350 ^oC is

weakly held since 960 μmole H_2/g washcoat reacted with no sweep whereas only 181 μmole H_2/g washcoat reacted with a 300 s sweep. The latter amount clearly corresponds to a strongly-bound (chemisorbed) oxygen, comprising only ca. 19% of the total oxygen trapped during the pre-oxidation with the 5% O_2/N_2 mixture at 350 ^oC. The amount of oxygen that reacts in the switching experiments is consistent with the maximum storage capacity of 198.41 μmole O/g washcoat in the oxygen uptake experiments.

The experiments reveal that when no sweep is conducted, most of the oxygen that reacts at high temperatures, up to 81%, is physisorbed oxygen .This can be confirmed by comparing the results from the LR cycling and nitrogen pulse experiments. The much lower temperature rise of the hot spot after a protracted N_2 sweep at 350 ^oC (Figure 3-9) underscores the fact that only a small amount of the stored oxygen is chemisorbed. As Figure 3-8 (b) and (c) indicate, upstream ignition occurs right after introduction of the H_2. The rather stationary feature of the hot spot suggests that all the accessible upstream oxygen is consumed within 8 s. After that unreacted H_2 moves downstream. The local temperature rise increases the rate of H_2 oxidation, which has an intrinsic activation energy of 20-40 kJ/mole [77, 78]. While H_2 is completely consumed in the upstream, H_2-free N_2 gas flows downstream, removing the loosely-bound oxygen. Heat-up of the downstream section of the monolith by convection and conduction increases the chemisorbed oxygen release rate. By the time hydrogen reaches the downstream, the adsorbed oxygen has been largely depleted. This prevents formation of a downstream moving temperature front, which would have occurred if the adsorbed oxygen would not have been reduced by the N_2 flow.

Balances of the amount of hydrogen and oxygen fed and consumed in the monolith enable a check of our interpretation of this chain of events. Feeding the 2% H_2/N_2 mixture for 5 s supplies 302 μmole of H_2. During the first 3.5 s about 211 μmole of H_2 and O react. We previously determined that a 960 μmole O/g washcoat (or 336 μmole O for the 350 mg washcoat) is present at the start of the reduction. Of this, about 778 μmole O/g washcoat (or 273 μmole O for the 350 mg washcoat) is loosely-bound. Thus, sufficient oxygen is present to react with the H_2 in the upstream of the reactor. The amount of O_2 that can be removed by a 3.5 s N_2 sweep can be estimated from the data in Table 3-1. Interpolation between the no-sweep and the 5 s sweep predicts that about 729 μmole O/ g washcoat (255 μmole O) is consumed in the first 3.5 s. Thus, after the first 3.5 s in which the hydrogen is consumed in the upstream, the nitrogen sweep removes the majority of the oxygen adsorbed in the downstream of the monolith.

3.3.3 Impact of Operation Parameters

Figure 3-11 shows the dependence of the maximum temperature rise on the monolith temperature and space velocity during the LR cycling experiment. Interestingly, the highest temperature rise occurred at the lowest monolith temperature. The maximum temperature generally decreased with increasing monolith temperature. A moderate but reproducible increase was observed at 350 ^oC. These trends are an indicative of the dynamic nature of the oxygen exchange between Pt crystallites and the surrounding ceria phase. Temperature-programmed experiments (Figure 3-3) suggest that oxygen spillover occurs at the interface of the Pt and CeO_2, leading to reaction. Above 150 ^oC there is

evidence for enhanced oxygen exchange between Pt and ceria via spillover. Hence, the decrease in the peak temperature rise as the monolith temperature increased from 100 ^{o}C to 300 ^{o}C is likely due to the oxygen spillover from the Pt crystallites to the CeO_2. That is, the coverage of chemisorbed oxygen is highest at low temperature (Table 3-2). This enables more oxygen to react under these conditions. As the temperature is increased there is a sharp drop in amount of chemisorbed oxygen available to react. The modest but reproducible increase in the peak temperature rise at 350 ^{o}C may be attributed to an increase in the reaction rate. Water TPD experiments reveal that the strongly-bound water in the proximity of catalyst active sites begins to be released at a temperature of about 350 ^{o}C. Alexeev et al. [79] reported that surface hydroxyls on the support combine to form water. They argued that this frees up additional sites for reaction with a subsequent increase in the temperature. Thus, in the current study with the $Pt/CeO_2/Al_2O_3$ catalyst the release of the strongly-bound water in the proximity of the Pt crystallites may increase sites available for additional reaction and temperature increase. Finally, the decrease in the maximum temperature rise between 350 and 400 ^{o}C is likely due to O_2 desorption from the Pt as seen in Table 3-2.

The maximum temperature rise at the LR and RL switch exhibits a qualitatively different dependence on the monolith temperature. The RL switch leads to a reaction between pre-adsorbed/stored hydrogen and oxygen from the gas phase. The much lower temperature rise upon the RL switch indicates that the $Pt/CeO_2/Al_2O_3$ stores less H_2 than O_2. At 350 ^{o}C the estimated amount of H_2 that reacts is 37 μmoles, which is comparable to the amount of exposed Pt atoms of 21.9 μmoles (43.7*50%=21.9 μmoles). The lack of

a secondary source of stored hydrogen as in the case for oxygen limits the temperature rise. Below 250 ^{o}C the maximum temperature rise increases with temperature. Above 250 ^{o}C, the dependence of the maximum temperature rise on the monolith temperature is similar to that following the LR switch; i.e., it exhibits a local minimum and maximum. The interaction of transport and chemical rate processes contributes to the trends. For example, as the monolith temperature increases the equilibrium coverage of hydrogen on the Pt decreases. On the other hand, the amount of residual hydrogen in the monolith may increase with temperature because of the increasing diffusivity of hydrogen with temperature. In the temperature range of 250 ^{o}C to 400 ^{o}C, an increasing rate of oxygen spillover from the ceria to the Pt may increase the maximum temperature, and water desorption may lead to the maximum temperature at 350 ^{o}C.

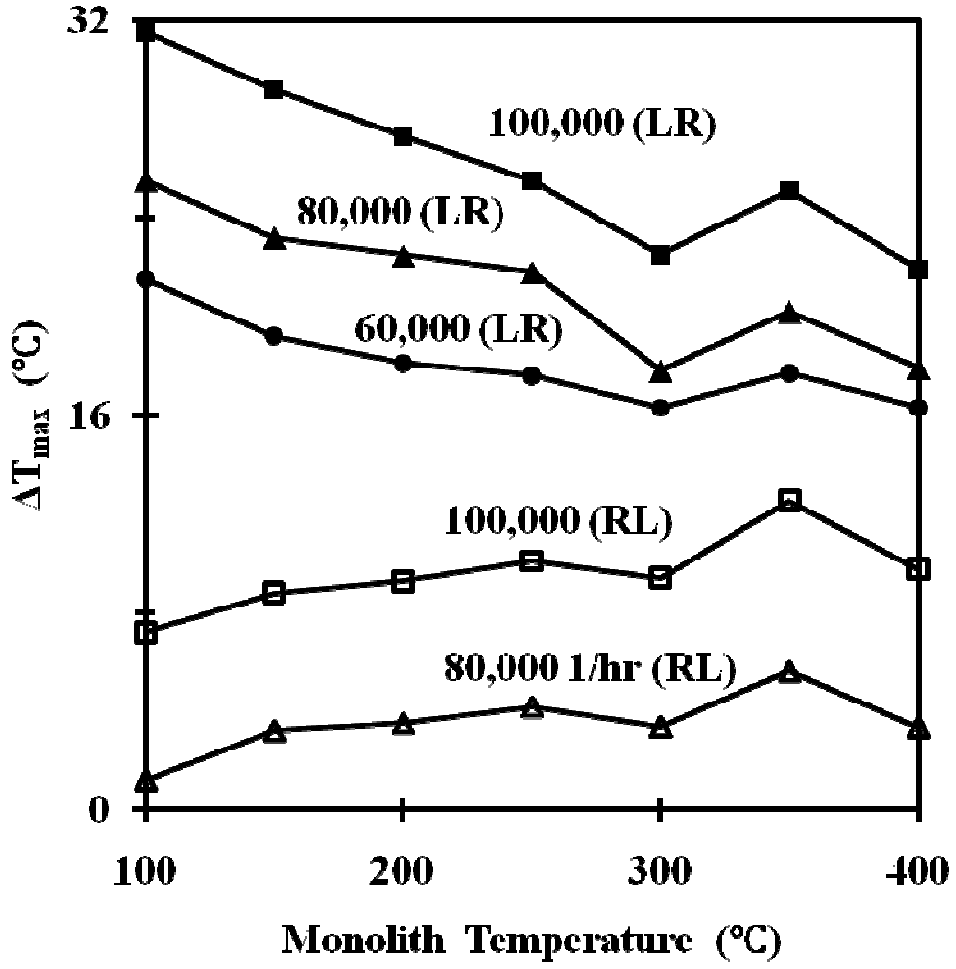

Figure 3-11 Impact of monolith space velocity on the maximum temperature rise during LR experiments.

The breakthrough graphs of the hydrogen in the cycling and inert LR experiments are shown in Figure 3-12 for monolith temperatures of 100 and 350 ^{o}C at a space velocity of 100,000 hr^{-1}. The data in Figure 3-12 suggests that the H_2 uptake at 100 ^{o}C is smaller than at 350 ^{o}C, a counterintuitive result. The breakthrough curves are the average of 25 LR cycles, so that accumulation of adsorbed hydrogen onto the washcoat during the initial rich feeds cannot be ruled out. This would lead to blockage of adsorption sites and

an apparent lower uptake at 100 ^{o}C. Due to a reduced likelihood of this happening at 350 ^{o}C, a somewhat reduced mass transfer resistance results in a longer breakthrough time at the higher temperature. A comparison of the H_2 breakthrough experiments for an empty reactor tube and bare monolith at 350 ^{o}C with that for the inert LR reveals that the washcoat delays the H_2 breakthrough by about 3 s. The delay is due to uptake of H_2 on the Pt in the washcoat. This indicates that H_2 adsorption/diffusion on the washcoat is the rate limiting process under non-reactive conditions.

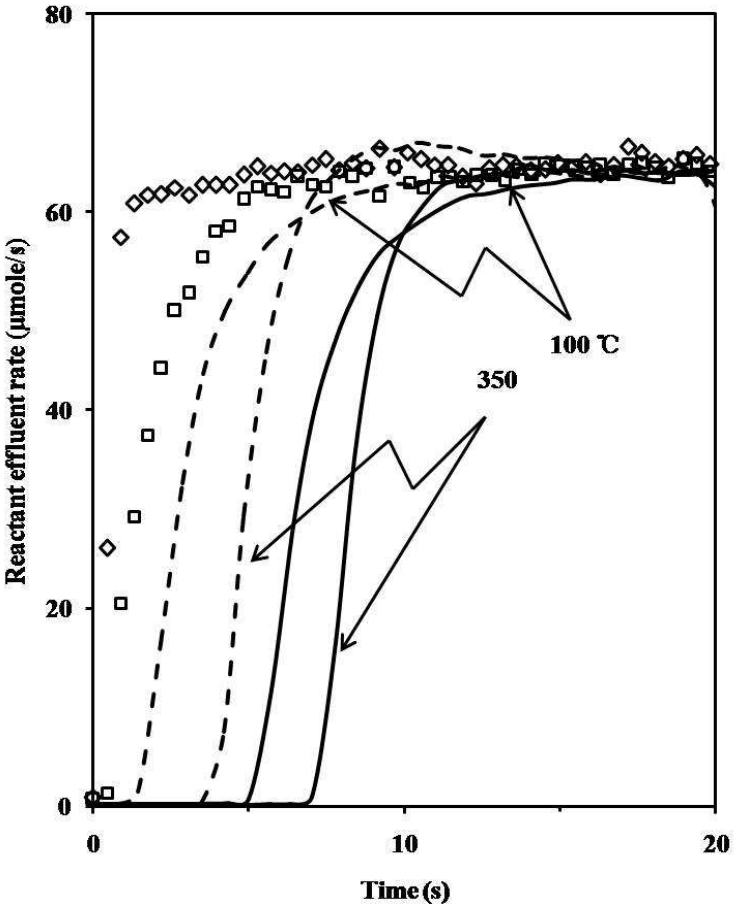

Figure 3-12 Impact of monolith temperature on breakthrough at the transition from lean to rich phase with a space velocity of 100,000 hr^{-1}. Dashed line: Inert experiment; Solid line: LR experiments; ◇Line: Inert experiment with an empty reactor at 350 °C; □Line: Inert experiment with an empty reactor at 350 °C.

Figure 3-13 describes the dependence of the H_2 breakthrough times and conversion on the monolith temperature. It shows that the time difference between the H_2 breakthrough in the LR and inert experiments is essentially independent of the temperature. Table 3-3 reports the H_2 breakthrough times and estimates of the H_2 reacted and converted at several temperatures. The tabulated data shows that at a constant space velocity the amount of reacted H_2 is essentially independent of the monolith temperature. This is due to the nearly fixed amount of physisorbed oxygen for a fixed oxygen concentration in the bulk gas.

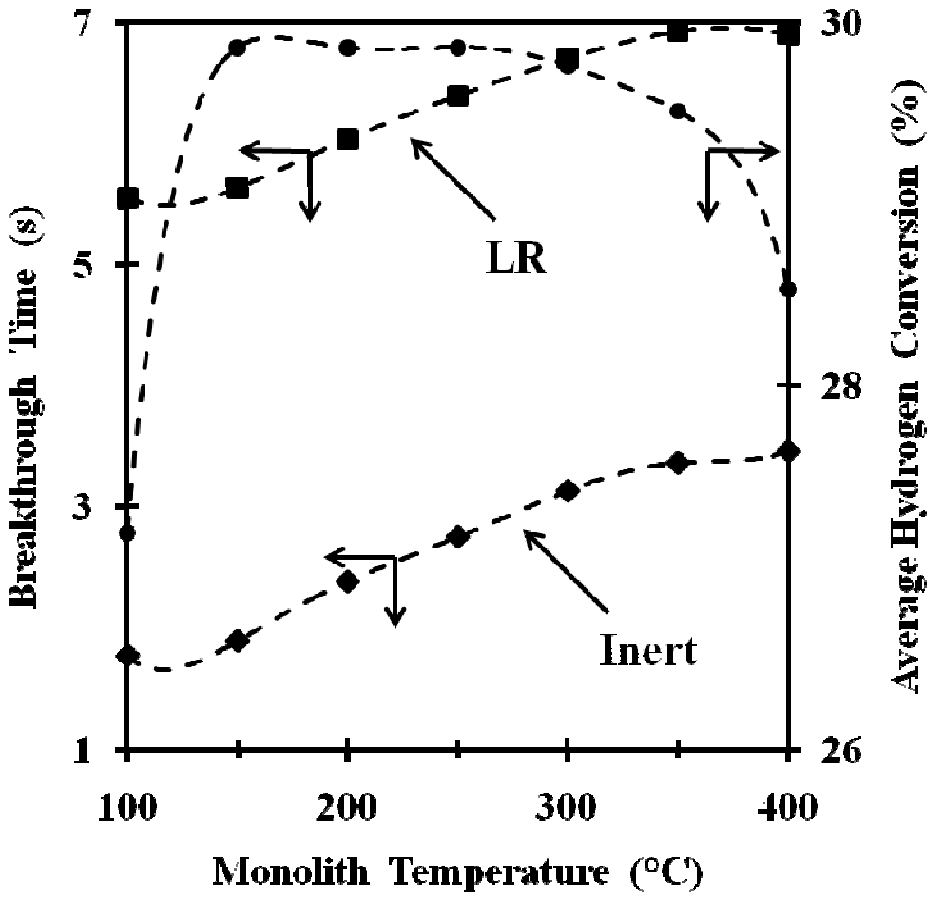

Figure 3-13 Dependence of H_2 breakthrough time in the LR cycling and inert experiments at the transition from lean to rich phase and of the average hydrogen conversion on monolith temperature.

Table 3-3 Impact of monolith temperature. T: monolith temperature; t_1: Breakthrough time for lean and rich cycling experiments; t_2: Breakthrough time for inert experiments.

T (℃)	t_1(s)	t_2(s)	t_1-t_2 (s)	T_{max} (s)	T_{Rmax}(℃)	H_2 consumption (µmole /g washcoat)	X_e (%)
100	5.6	1.8	3.8	3.8	31.5	885	27.2
150	5.6	1.9	3.7	3.8	29.2	972	29.9
200	6.0	2.4	3.7	3.7	27.3	976	30.0
250	6.4	2.8	3.6	3.7	25.5	972	29.9
300	6.7	3.1	3.6	3.6	22.5	969	29.8
350	6.9	3.4	3.6	3.6	25.1	960	29.5
400	6.8	3.4	3.4	3.4	21.9	929	28.5

The maximum temperature rise increases monotonically with space velocity for a constant monolith temperature (Figure 3-11). A higher space velocity increases the amount of H_2 fed during the rich feed so that more physisorbed oxygen is consumed at the beginning of the rich feed (Table 3-4). The increase of the space velocity also decreases the hydrogen breakthrough time in both the cycling and inert feed experiments. The breakthrough curves for H_2 in the LR experiments are shown in Figure 3-14 for three space velocities. At a high space velocity the heat generated by the upstream reaction is rapidly convected downstream due to the higher flow rate and heat transfer coefficient.

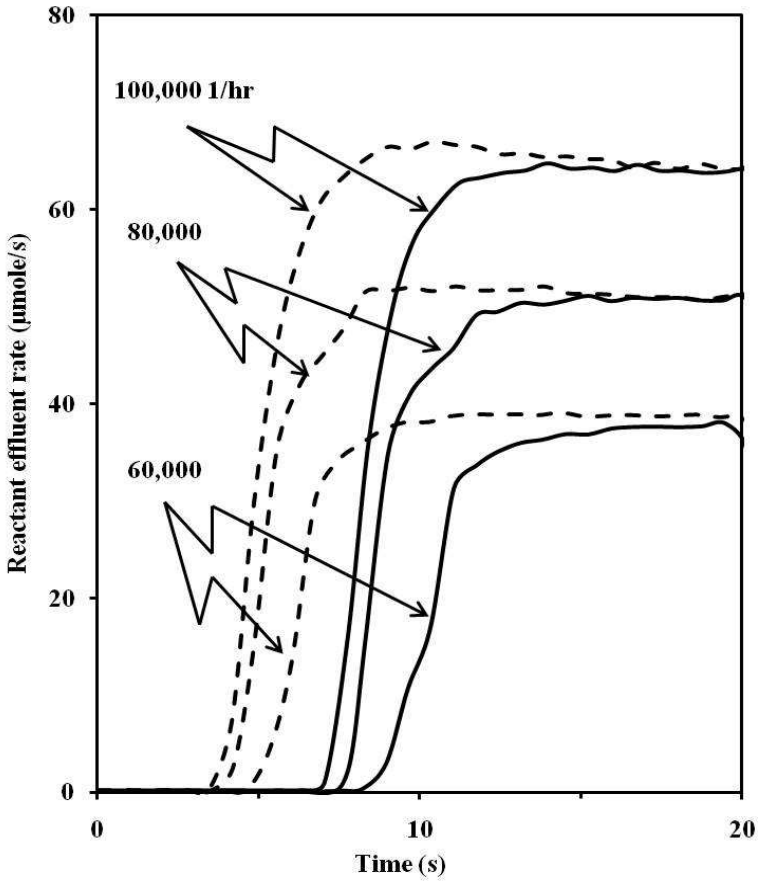

Figure 3-14 Impact of Space velocity on breakthrough with monolith temperature of 350 °C. Dash line: Inert experiment; Solid line: LR experiment.

Table 3-4 Impact of space velocities.T1: Breakthrough time for lean and rich cycling experiments; T2: Breakthrough time for Inert experiments.

Space velocity (1/hr)	**T_1(s)**	**T_2(s)**	**T_1-T_2(s)**	**T_{max} (s)**	**T_{Rmax}(℃)**	**H_2 consumption (µmole /g washcoat)**	**X_e(%)**
60000	8.3	4.3	4.0	4.1	17.7	481	37.6
80000	7.4	3.7	3.7	3.8	20.2	668	33.6
100000	6.9	3.4	3.5	3.6	25.1	960	29.5

An increase in the H_2 feed concentration results in a faster and more extensive reduction. Figure 3-15 (a) compares the temporal reactive and non-reactive effluent H_2 concentration for H_2 feed concentrations from 1 to 5 % at a fixed monolith temperature of 350 ^{o}C. Table 3-5 reports the data at the three concentrations. The catalyst in these experiments was subjected to the same pre-oxidation by a mixture of 5 % O_2/N_2. As expected, the breakthrough time is shorter for feeds with higher feed concentrations. A positive-order dependence of the hydrogen consumption on its concentration is apparent: The amount of H_2 consumed increases with feed concentration for a fixed initial concentration of oxygen. However, the H_2 conversion decreases (Figure 3-15 (b)).

The effect of the O_2 feed concentration on the H_2 consumption is shown in Figure 3-15 (b) and compiled in Table 3-5. The H_2 feed concentration in these experiments was 5 % and the temperature 350 ^{o}C. Increasing the O_2 concentration increases somewhat the total amount of H_2 that reacts during the reduction. Clearly a higher O_2 feed concentration increases the amount of stored oxygen. Hence, the H_2 conversion increases upon increasing O_2 feed concentration.

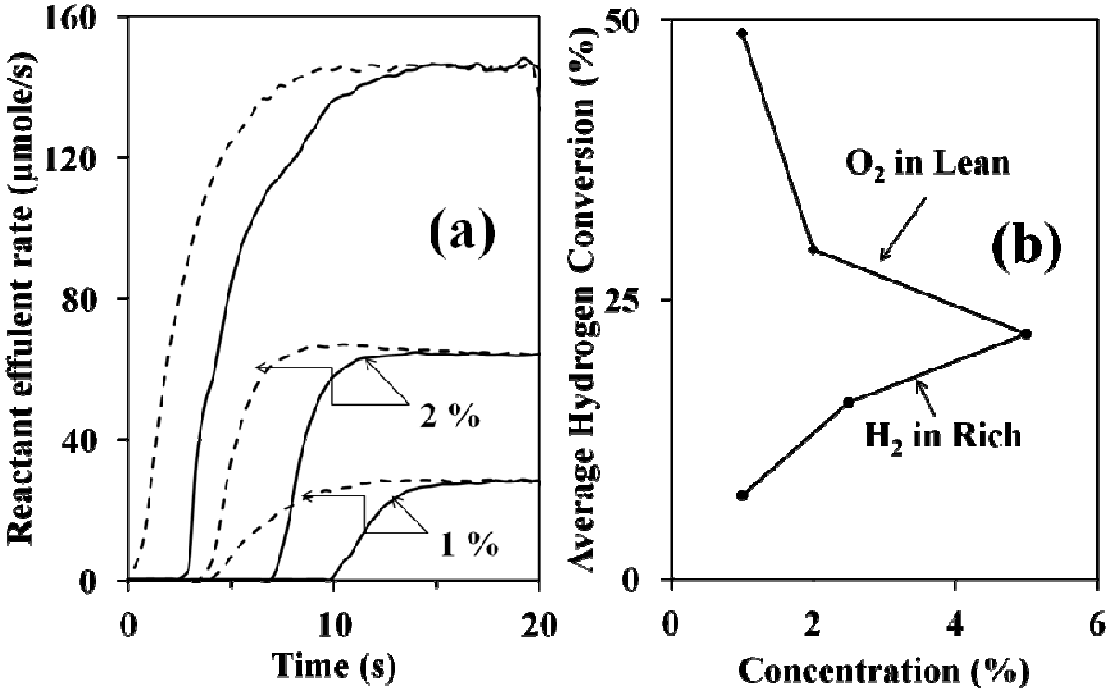

Figure 3-15 Impact of the reactant concentration on the average hydrogen conversion during a LR experiment. Feed temperature was 350 °C and space velocity 100,000 hr^{-1}.

Table 3-5 Impact of hydrogen and oxygen concentrations. T: monolith temperature; t_1: Breakthrough time for lean and rich cycling experiments; t_2: Breakthrough time for inert experiments.

H_2 (%)	O_2 (%)	t_1(s)	t_2(s)	t_1-t_2(s)	T_{max} (s)	T_{Rmax} (℃)	H_2 consumption (µmole /g washcoat)	X_e (%)
1	5	9.8	2.2	7.6	7.7	16.0	647	48.8
2	5	6.9	3.4	3.5	3.6	25.1	960	29.5
5	5	2.5	0	2.5	2.5	56.9	1851	21.9
5	2.5	2.2	0	2.2	2.2	44.1	1334	15.8
5	1	1.6	0	1.6	1.6	26.2	632	7.5

3.3.4 Use of CO and CO/H_2 Mixtures as Reductant

Experiments with CO and a CO/H_2 mixture with a 3:1 feed ratio were carried out following the same procedure as those for H_2 to closely mimic the actual vehicle exhaust. The experimental results in a temperature range from 100 ^oC to 400 ^oC are summarized in Table 3-6.

Table 3-6 Impact of different reductants. The Delay error is ± 0.2 s; the Tmax error is ± 0.4 ^oC; the error of consumed is ± 3.5 µmole O/ g washcoat.

Temp (^oC)		**100**	**150**	**200**	**250**	**300**	**350**	**400**
2 % CO	Delay (s)	2.2	2.8	4.5	4.7	5	5.2	4.3
	T_{max} (^oC)	4.5	11	25.7	27.8	30.9	33.1	29.3
	$N_{O2->CO2}$ (µmole O/ g washcoat)	238	635	707	759	776	809	788
2 % H_2	Delay (s)	5.6	5.8	6.1	6.4	6.7	6.9	6.8
	T_{max} (^oC)	32.2	29.2	27.5	25.6	22.5	24.8	22
	$N_{O2->H2O}$ (µmole O/ g washcoat)	886	973	978	972	969	960	929
1.5 % CO + 0.5 % H_2	Delay (s)	3	3.5	4.9	5.1	5.2	5.5	5.1
	T_{max} (^oC)	8.9	17.5	30.5	32.9	33.8	36.4	29.5
	$N_{O2->H2O+CO2}$ (µmole O/ g washcoat)	477	777	824	852	863	876	845

Table 3-6 (continued) Impact of different reductants. The Delay error is ± 0.2 s; the Tmax error is ± 0.4 °C; the error of consumed is ± 3.5 µmole O/ g washcoat.

	From H_2	144	212	268	281	279	276	247
	From CO	333	565	556	571	584	600	598
1.5 % CO	Delay (s)	2.6	3.2	4.7	5	5.2	5.4	4.6
	T_{max} (°C)	3.7	8.9	21.1	24.2	26.5	29.7	25.8
	$N_{O2->CO2}$ (µmole O/ g washcoat)	192	596	659	717	741	763	752

Typical effluent concentrations as a function of time for the different feeds are shown in Figures 3-16 and 3-17 at 350 °C and 100 °C, respectively. There are several noteworthy features. As shown in Figure 3-16 (a), upon the introduction of 2% CO, CO_2 was produced nearly immediately, indicating the reduction of adsorbed and stored oxygen by CO. The effluent O_2 decreased monotonically with time as the effluent CO increased monotonically with time. During the simultaneous breakthrough of CO and CO_2 a transient catalytic reaction occurred between CO and the surface oxygen. A peak CO_2 production occurred at the same time as the depletion of effluent O_2 (peak concentration of 1.2% at 3.6 s). The breakthrough of CO occurred shortly after the maximum in CO_2 production peak (5.2 s). That CO_2 continued to be produced even after the depletion of effluent O_2 indicated reaction between CO and stored oxygen supplied by the ceria to the Pt. When switching back to the lean feed from the rich feed at the 20 second mark, a sharper CO_2 production peak (~ 1.6 % maximum at ca. 21 s) appeared.

This peak indicated that the CO that was retained by the catalyst reacted with the gas phase O_2 that was admitted to the reactor.

The dynamic response of the H_2 feed was quite different from the CO feed, as shown in Figure 3-16 (b). One notable difference was the lack of a clear connection between the H_2O and H_2 breakthrough during the switches between rich and lean feeds. The formed water bound to the alumina-supported catalyst with varying degree of affinity as Figure 3-4 shows. The water breakthrough was therefore delayed and more protracted than that of CO_2. Therefore it certainly was not a reliable indicator of the transient H_2 oxidation. The results obtained with the 3:1 co-feed of CO and H_2 are shown in Figure 3-16 (c). Nothing unusual was noted at this relatively high temperature with the exception of some shifting in the breakthrough times and peak concentrations for CO_2 and H_2O.

More intricate results were obtained at lower monolith feed temperatures. Figure 3-17 shows the behavior at a much lower feed temperature of 100 ^oC at which the strong binding of CO to Pt becomes a dominant feature. Figure 3-17 (a) shows a significant decrease in the CO_2 production compared to that at the higher temperature (Figure 3-16 (a)). At 100 ^oC the maximum concentration of CO_2 produced was only 0.4 % after the shift from lean to rich phase compared to about 1.2% for that at 350 ^oC. The self-inhibition of the CO oxidation rate by CO is well known. At steady-state and for a sufficiently high CO/O_2, the Pt sites are mostly occupied by CO. Under these conditions the reaction is limited by CO desorption, and the rate is of -1 order in CO and the apparent activation energy is close to the CO binding energy (ca. 100 – 140 kJ/mole). At

low temperature LR experiments the Pt probably becomes rapidly covered with CO which limits the spillover of O adatoms from the proximal ceria phase.

The CO inhibition was more apparent when the catalyst was re-exposed to O_2 after the 20-s rich period. In comparison to the 350 ^{o}C data (Figure 3-16 (a)) the lower temperature breakthrough of O_2 was more protracted and had a somewhat staggered appearance (Figure 3-17 (a)). There was also a notable delay in the production of CO_2 which had a small but measureable peak of ~0.2 %. These trends suggest a slow uptake of oxygen by the catalyst due to the inhibition by the adsorbed CO. The pathway for re-oxidation of the ceria via the Pt crystallites is deterred. Only as CO desorbs or reacts, freeing up Pt sites, can O_2 dissociatively adsorb and spillover to the ceria. The noted delay in the evolution of CO_2 at 100 ^{o}C and its immediate appearance at 350 ^{o}C (Figure 3-16 (b)) underscores this impact of the CO inhibition on the transient features.

Whereas the effect of H_2 on the CO reduction was hardly noticeable at higher temperature, the situation was much different at 100 ^{o}C. The breakthrough of O_2 was much smoother for the 1.5% CO/0.5% H_2 rich feed (Figure 3-17 (c)). More apparent was the shorter delay in the production of CO_2 after the start of the lean phase. The maximum of CO_2 production appeared earlier at about 25 s with a high concentration of ~0.3%. The desorption-reaction process for the CO feed (Figure 3-16 (a)) was clearly much less pronounced, suggesting influence of the H_2 on the CO oxidation.

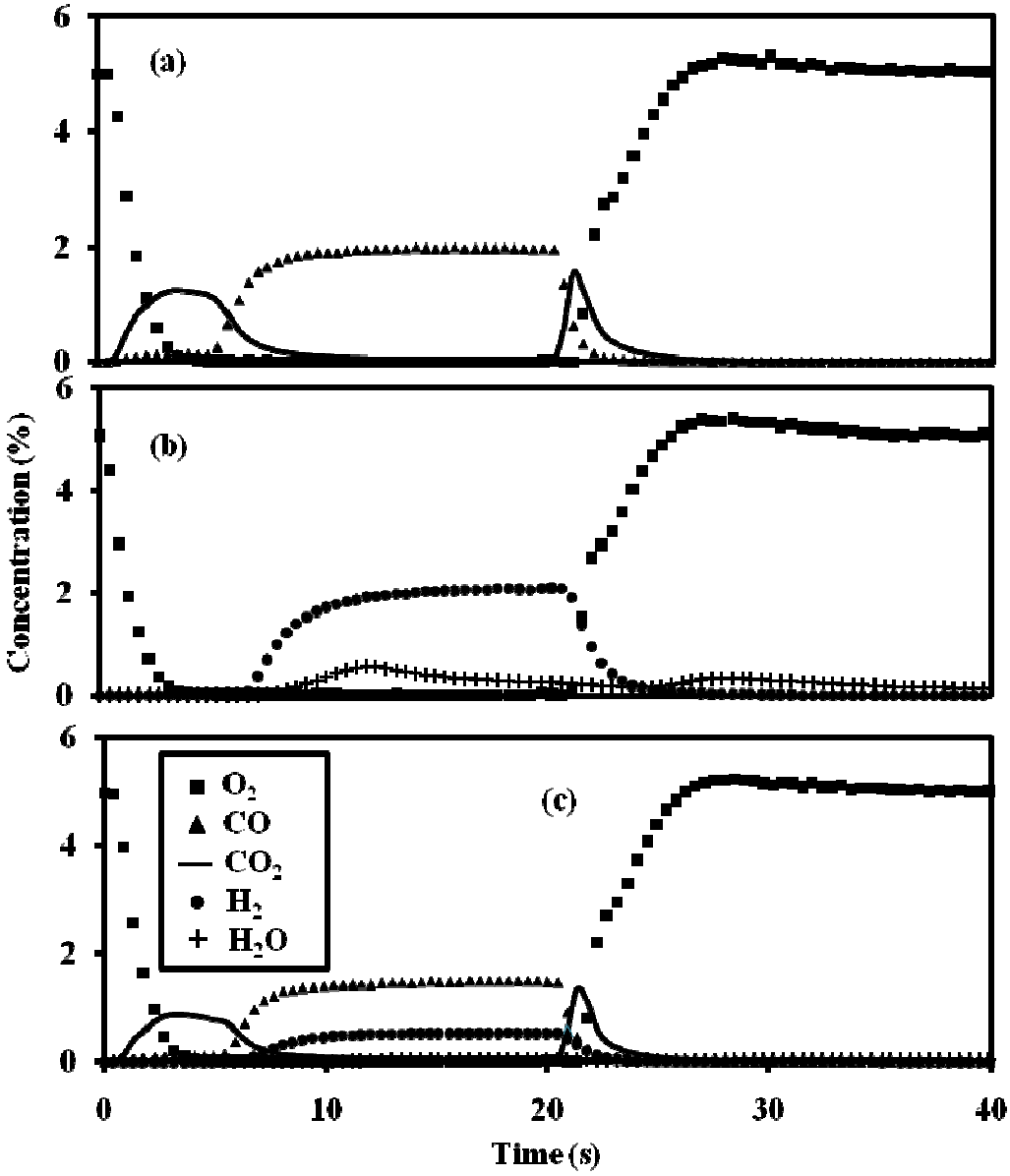

Figure 3-16 Temporal effluent concentration with different reductants in LR cycling experiments at a space velocity of 100,000 hr^{-1} and monolith temperature of 350 °C. (a) 2% CO as reductant; (b) 2% H_2 as reductant; (c) 1.5% CO and 0.5 % H_2 as reductant. The same legend applies to all three figures.

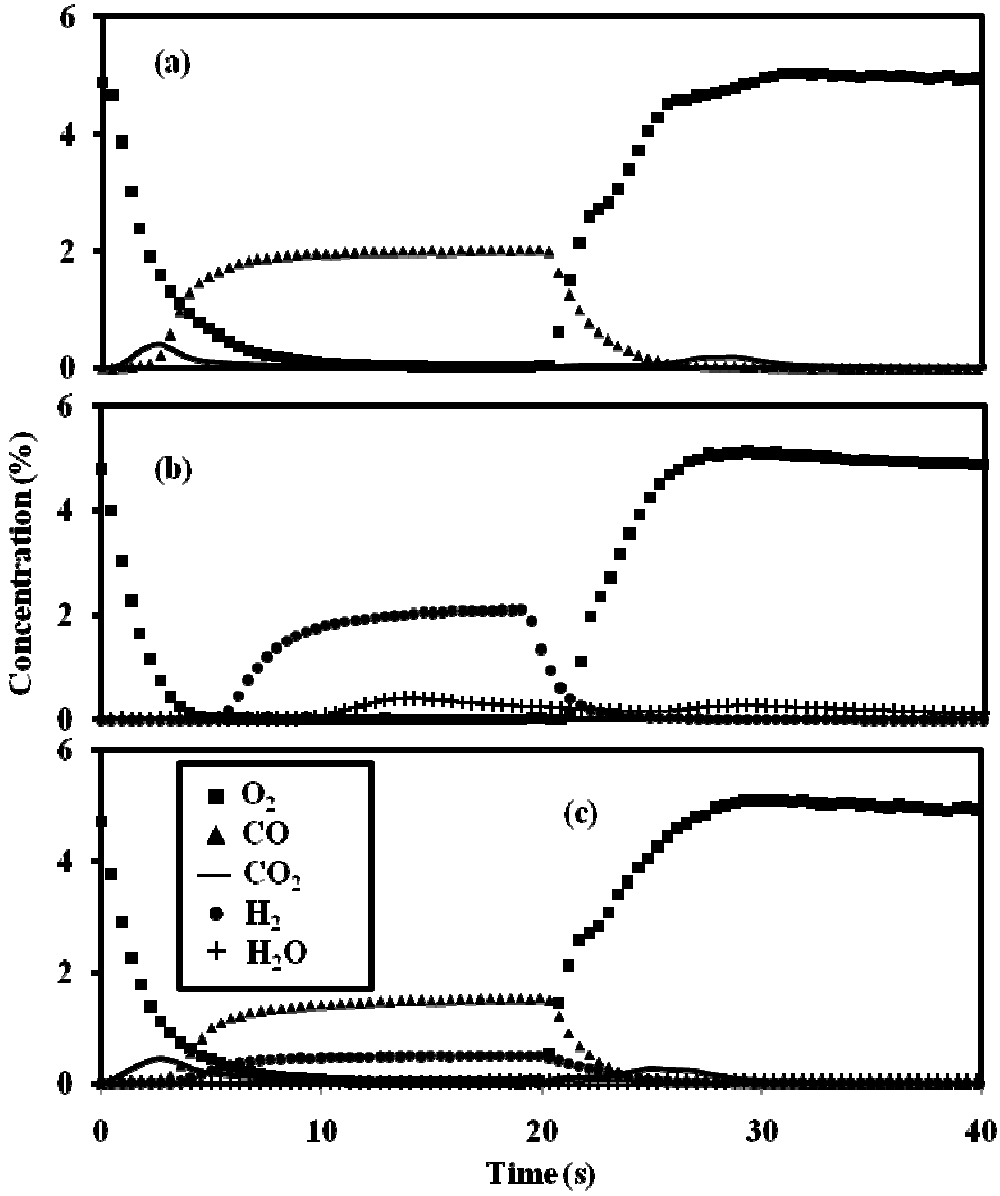

Figure 3-17 Temporal effluent concentration with different reductants in LR cycling experiments under the space velocity of 100,000 hr^{-1} and monolith temperature of 100 °C. (a) 2 % CO as reductant; (b) 2 % H_2 as reductant; (c) 1.5 % CO and 0.5 % H_2 as reductant. The legend applies to all the three figures.

Figure 3-18 (a) compares the amount of O_2 reduction/CO_2 production for reductants with different concentrations of H_2 and CO. For pure CO feed, the oxygen consumption, denoted by $N_{O2->CO2}$, is a sensitive function of the reductant concentration

and the monolith temperature. With 2% CO, the oxygen consumption of 238 µmole/g washcoat at 100 ^{o}C increases to 809 µmole/g washcoat at 350 ^{o}C. The consumption achieves exhibits a shallow maximum at 350 ^{o}C, decreasing to 788 µmole /g washcoat at 400 ^{o}C. With 1.5% CO the oxygen consumption increases from 192 µmole /g washcoat at 100 ^{o}C to 763 µmole /g washcoat at 350 ^{o}C and then decrease to 752 µmole /g washcoat at 400 ^{o}C. The increase of the oxygen consumption at higher CO concentration suggests that the periodic oxidation is limited by the residual amount of reagents during the switches. Of more interest is the comparison of the temperature dependence of the oxygen consumption by the pure CO and the CO/H_2 mixture feeds. While the dependence is qualitatively similar, more oxygen is reduced by the CO/H_2 mixture at 100 ^{o}C than that by either the 1.5 or 2.0 % pure CO feeds. This clearly indicates an enhancement of the CO oxidation by the H_2 at low temperatures. We discuss this finding below. As the temperature is increased above 150 ^{o}C, the consumption rate of the pure CO feed eventually exceeds that that for the CO/H_2 mixture. The CO experiments indicate that the external mass transport probably contributes to the oxidation rate especially at the high temperatures. As the H_2 diffusivity is 3–4 times higher than that of CO [80], the supply rate of the H_2 to the Pt sites exceeds that of the CO. Thus, after the consumption of the oxygen by the hydrogen less oxygen is available to react with the CO. This explains why $N_{O2->CO2}$ decreases when 0.5% H_2 is added to the feed containing 1.5% CO.

The enhancement of CO oxidation by H_2 has been previously reported in a number of studies. Salomons et al. [81-82] showed experimentally that H_2 addition reduces the light-off temperature for CO oxidation. Bhatia et al. [80] highlighted earlier

experimental studies that report interactions between adsorbed CO and H on Pt. Bhatia et al. have shown using either a microkinetic or global kinetic model that the reduction of the CO binding energy by the formation of a surface species such as HCO can predict the H_2 enhanced CO oxidation. The formation of another surface species like COOH encountered during water gas shift chemistry might also enhance the CO oxidation rate. The current study indicates that the enhancement can occur also under transient operation. This affects the performance of catalytic converters.

The experiments show rather different reactivity and temperature sensitivities of CO and H_2 reductions of oxidized ceria. As mentioned above, CO oxidation is quite sensitive to temperature, while H_2 oxidation is much less sensitive. Table 3-6 shows that the oxygen consumption rate achieves a maximum value of 978 µmole/g with H_2 as the reductant compared to 809 µmole /g for the same concentration of CO. H_2 is clearly the more effective reductant. Moreover, the temperature dependence of the oxygen consumption is much less pronounced for H_2 over the 100 to 400 ^oC range. These findings are consistent with the known rather low activation energy of H_2 oxidation [77-78, 83].

The spatio-temporal features of the four reducant feeds did not reveal new behavioral features of the hot spot and traveling front. Figure 3-18 (b) compares the maximum temperature rise values. For 2% CO the maximum ΔT_{max} is ca. 33 ^oC at a monolith feed temperature of 350 ^oC, whereas for 2% H_2 the maximum ΔT_{max} is ca. 32 ^oC at a monolith feed temperature of 100 ^oC. The decrease of the maximum temperature rise from 350 ^oC to 400 ^oC for CO could be due to the increased oxygen spillover from

the Pt to the CeO_2, as discussed earlier. These results underscore the fact that H_2 is a more effective reductant than CO at low temperature and a more reliable indicator of the surface oxygen, in line with the results from previous studies [80-82, 84-87]. Over the entire range of monolith temperatures the maximum temperature rise for the CO/H_2 feed mixture is higher than that for the CO feed. This is a clear manifestation of the H_2 enhancement of the CO oxidation.

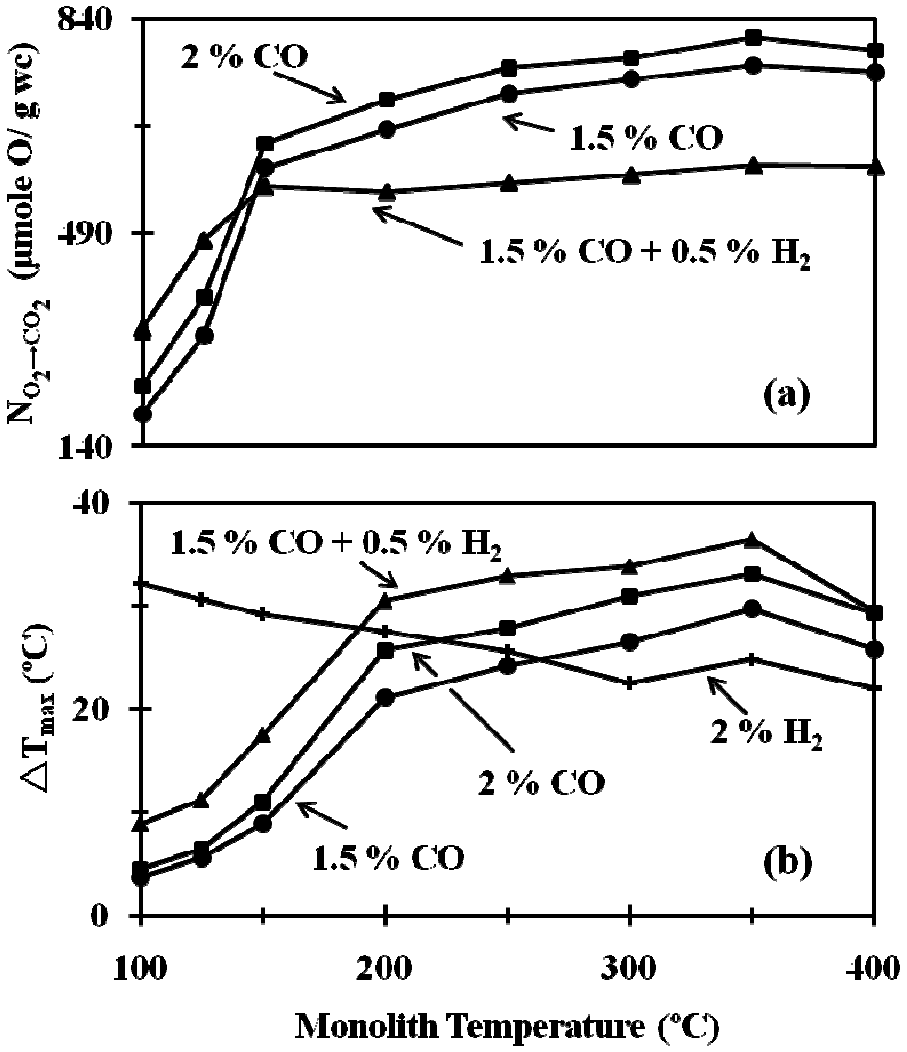

Figure 3-18 Impact of monolith temperature at a space velocity of 100,000 hr^{-1} on (a) oxygen consumption by CO oxidation (b) maximum temperature rise. Feed composition of ■ 2 % CO; ● 1.5 % CO and 0.5 % H_2; ▲ 2 % H_2.

3.4 Conclusions

The combined use of infrared thermal imaging and gas phase composition measurements enabled a spatial and temporal resolution of the periodic oxidation–reduction of a model $Pt/CeO_2/Al_2O_3$ monolith catalyst under cyclic feed of oxygen and either hydrogen, CO or a CO/H_2 mixture.

The spatio-temporal temperature behavior is rather intricate as a hot spot forms immediately upon the feed switch. While the hydrogen is consumed in the monolith upstream right after the lean-to-rich (LR) transition the almost pure nitrogen flow sweeps most of loosely-bound oxygen in the downstream. This prevents a downstream movement of the upstream temperature front. The maximum temperature rise after a LR switch is much higher that following the RL switch, because the oxygen adsorbed on the Pt is replenished by spillover from the CeO_2 during the LR switch. However, the hydrogen adsorbed on the Pt is not replenished after its consumption following the RL switch. The breakthrough pattern of the hydrogen effluent is indicative of the adsorption conditions in the washcoat. An increase in the monolith temperature decreases the difference between the maximum temperature rise obtained following the LR and the RL switches. The highest maximum temperature rise under both RL and LR switches is obtained at about 350 ^oC due to water desorption at that temperature, as revealed by the TPD experiments. This frees up occupied Pt sites that increases the reaction rate and heat generation.

The nonuniform spatial temperature is due to a strong coupling between the chemistry and transport. It indicates that prediction of the apparent kinetics of the

Pt/CeO_2 regeneration based on the feed and effluent species concentrations can be misleading. Any kinetic model must be able to either account for the complex spatial temperature patterns or be based on experiments in which these gradients are eliminated. This conclusion is applicable to any exothermic transient reaction.

Feeds of a 3:1 mixture of CO and H_2 generated intricate transient effects. The qualitative features of the hot spot formation and traveling thermal front are not influenced by the reductant type. Quite interesting interactions between the transient oxidations of CO and H_2 are evident especially at low temperature. Previous studies have shown that H_2 can enhance the steady-state light-off of CO oxidation. This study shows that this enhancement exists also under periodic conditions when the supply of oxygen to the catalyst is from the ceria. Undoubtedly the transport of oxygen via spillover to the Pt crystallites participates in the process.

Chapter 4 NO_x Storage and Reduction over the PtCe Catalyst

4.1 Introduction

This study is a continuation of previous studies on the impact of lean NO_x trap catalyst composition on its performance. The conventional Pt/Ba/γ-Al_2O_3 LNT catalyst has been extensively investigated both in university and industrial laboratories. Ceria is added to the LNT catalysts to overcome some inherent deficiencies, such as SO_x poison [35, 89], PGM aging [88] and unstable surface area [34]. On the other hand, ceria addition causes undesirable side effects, such as excessive fuel consumption and expensive catalyst cost. A fundamental understanding of the role of ceria in LNT catalyst is essential to understand its advantages and disadvantages during NO_x storage and reduction.

NO_x can be stored over ceria due to its oxidizing nature [90, 91]. This increases the NO_x storage capacity, especially at low temperatures. However, the accompanying oxygen storage requires a high reductant consumption to regenerate the catalyst. The interaction between Pt and ceria complicates the storage and reduction of NO_x. The interactions between Pt and ceria facilitates the mutual spillover of O_2 and NO_x during the fuel-lean operation and H_2 and CO during the fuel-rich operation. This changes the storage and reduction chemistries and generates different storage mechanisms. For example, the storage sites close to PGM, “fast sites”, can be filled and regenerated faster than the sites far away from the PGM, “slow sites”. The stored species over the fast and slow sites are different. Hence, it is important to determine the surface species formed over ceria during the NSR process.

The storage and reduction of NO_x was investigated by contacting a model Pt/Ce/γ-Al_2O_3 catalyst with different gaseous mixtures. Diffuse reflection infrared Fourier transform spectroscopy (DRIFTS) and temperature programmed methods were carried out to determine the NO_x and O_2 storage and reduction over the PtCe catalyst.

4.2 Experimental

4.2.1 In situ Diffuse Reflection Infrared Fourier Transform Spectroscopy

The evolution of surface species on the PtCe catalyst was investigated by the diffuse reflection infrared Fourier transform spectroscopy, detecting the vibration modes of adsorbed molecules. The DRIFTS experiments were carried out using a Thermo Nicolet 6700 FT-IR spectrometer equipped with a MCT detector. 60 mg catalyst was loaded into the DRIFTS cell (Harrick Scientific Products, Inc.) equipped with two KBr windows. To ensure a similar surface status before storage, the PtCe catalyst was pretreated at 500 °C in a 5% H_2 in He gas mixtures for 1 hour before every run. The catalyst was then cooled down to 50 °C in a pure He flow of a flow rate of 50 sccm. The IR background spectrum was collected as a reference with a resolution of 4 cm^{-1} from 400 cm^{-1} to 4000 cm^{-1} for 64 scans before every experiment. This eliminated the instrumental and environmental noise. During the experiments, the PtCe catalyst was exposed to gaseous reactants, comprising of 1000 ppm NO_x with or without 5% O_2 in a He flow for 30 minutes. After 30 min of NO_x storage, the catalyst was purged by pure He for 30 minutes to remove the physisorbed surface species. The temporal IR spectrum with accumulation of 64 scans was collected at 1, 4, 10, 20, 30 and 60 min.

4.2.2 Temperature Programmed Methods

The temperature programmed experiments were carried out to study the surface reactions and the species adsorption on the PtCe catalyst. A PtCe powder catalyst was loaded in the quartz tube flow reactor equipped with a quartz frit plate. The catalyst layer thickness was kept below 1 cm by inserting an inert quartz wool on the top. Before conducting any the temperature programmed experiment, the catalyst was pretreated in 5% H_2 at 500 °C until no water was detected in the effluent and then cooled down to 50 °C under a pure Ar flow at a flow rate of 200 sccm. The real-time effluent concentrations were monitored by a quadrupole mass spectrometer (QMS; Cirrus LM99, MKS inc.) and a FTIR (Thermo Nicolet Nexus 470) during the temperature programmed experiments.

In the NO_x-TPD experiments, a gas flow, containing 5000 ppm NO or NO_2 in Ar, was fed to saturate the PtCe catalyst at 50 °C for 30 min until the effluent concentration was the same as that of the feed. The physisorbed species were then removed by purging the catalyst with a pure Ar flow until the NO_x effluent concentrations were below 10 ppm (typically about 30 minutes). The catalyst temperature was then increased from 50 to 500 °C with a temperature ramp of 20 °C/min in a pure Ar flow. In some experiments, 5% O_2 was fed to the PtCe catalyst along with NO_x during the oxidant storage.

During the H_2-TPR experiments, the PtCe catalyst was pretreated with different oxidants consisting of NO_x and O_2 mixtures. During the pretreatment, the catalyst was contacted with 5000 ppm NO or NO_2 at 50 ^oC until the effluent concentration was the same as the feed concentration. The catalyst surface was then purged by a pure Ar flow for 30 min. Following this, 2000 ppm H_2 in an Ar flow was fed to catalyst and the

catalyst temperature was increased to 500 ^{o}C with a temperature ramp of 20 ^{o}C/min. In some experiments, 5% O_2 was fed to the PtCe catalyst along with 5000 ppm NO or NO_2 during the oxidant storage to generate different surface species.

4.2.3 NO_x Storage and Reduction

The deNO_x performance of the PtCe catalyst was tested by running the NO_x storage and reduction experiments. Before the experiments, the PtCe catalyst was pretreated in 5% H_2 at 500 °C until no water effluent and then cooled down to the desired temperature under a pure Ar flow at a flow rate of 1000 sccm. A schematic of experimental procedure of NO_x storage and reduction is shown in Figure 4-1.The first step was the oxidant (O_2, NO and NO_2) storage. 500 ppm of NO or NO_2 with or without 5% O_2 was fed to catalyst for 10 min. The difference between the feed and exit concentrations enabled the measurement of oxidant storage capacity at different temperatures. The second step was an Ar purge. The physisorbed species were removed by a pure Ar flow for 10 min. The chemisorbed species was determined from the difference between the physisorbed species and the total adsorption. The comparison between the chemisorbed and physisorbed species at different temperatures enabled an evaluation of the thermal stability of the surface species. The third step was the surface reduction. 5% H_2 was fed to catalyst, while the catalyst temperature was increased to 500 °C with a temperature ramp of 25 °C/min. This reduction enabled the closure of N balance and provided information about the nitrogen and oxygen storage.

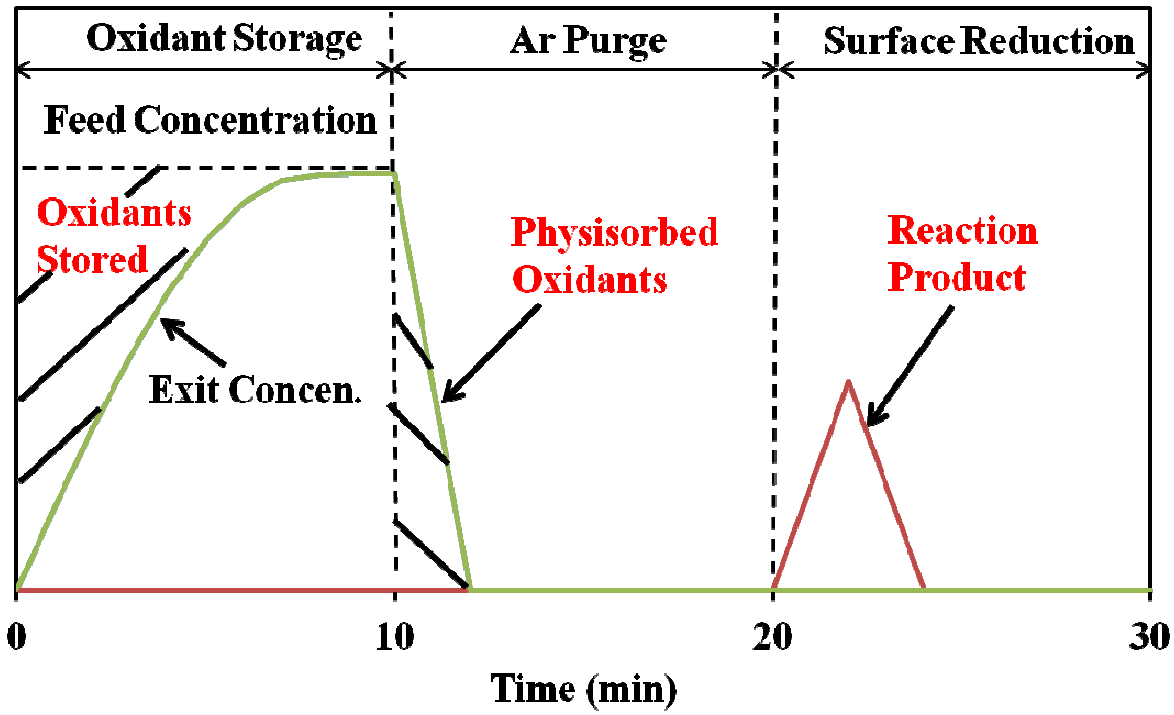

Figure 4-1 A schematic description of NOx storage and reduction experiment.

4.3 Results and Discussion

4.3.1 NO_x Storage Mechanisms over the PtCe Catalyst

In situ NO_x storage was carried out over the PtCe catalyst in the DRIFTS cell. The PtCe catalyst was pre-reduced before the experiment as described earlier. Figure 4-2 (a) shows the temporal evolution of DRIFTS spectra upon the exposure of PtCe to 1000 ppm NO in He at 50 °C. The assignment of bands was done based on Table 4-1. Initially, the NO was adsorbed only on the Pt sites. Only one strong band was observed at 1760 cm^{-1} with a shoulder at around 1700 cm^{-1}, both of which were due to the Pt-NO stretching [92, 93]. The intensity of the Pt-NO peak barely changed in the first 30 minutes. This indicated the saturation of Pt sites. After 10 minutes, NO was stored as nitrates with bands at 1270,

1450, 1560 and 1620 cm^{-1} [92-96]. After NO storage for 30 minutes, the catalyst was purged by He for 30 minutes. The intensity of the Pt-NO peak decreased, while the nitrate peaks intensified. This suggested that the Pt nitrosyl species were unstable and transformed to the surface nitrates. Figure 4-2 (b) describes the adsorption spectra over Pt/ceria as a function of time of exposure to 1000 ppm NO and 5% O_2 in He at 50 °C. The strong Pt mononitrosyl peak at 1760 cm^{-1} appeared immediately, while the bands of nitrates at 1240-1270 cm^{-1} and 1450-1620 cm^{-1} showed up after 4-30 min of adsorption. The monodentate, chelating bidentate and bridging bidentate nitrates were observed at 1450, 1560 and 1620 cm^{-1}, respectively [97, 98]. After 30 min of He purge, the unstable Pt-NO peak decreased, but the nitrate bands remained essentially unchanged.

Figure 4-2 (c) shows the IR spectra after 30 min of O_2 pretreatment. The band around 1650 cm^{-1} was due to the oxidation of Ce_2O_3 to CeO_2. Figure 4-2 (d) shows the time-resolved NO adsorption spectra over Pt/ceria after exposure to 5% O_2 for 1 hour at 50 °C. The strong Pt-NO peak at 1760 cm^{-1} and the nitrate peak at 1270 cm^{-1} emerged at the same time. The large shoulder at around 1650 cm^{-1} appeared after the oxygen treatment of Pt/ceria as shown in Figure 4-2 (c) and thus did not reflect the NO_x adsorption. Other nitrate peaks emerged as those in Figure 4-2 (b). The DRIFTS spectrum barely changed from 4 to 30 min. He purge had little impact on the surface nitrate species, except on the Pt nitrosyl. In sum, the Pt nitrosyl was the dominant species upon the catalyst exposure to NO, while the surface nitrate formation was enhanced in the presence of O_2.

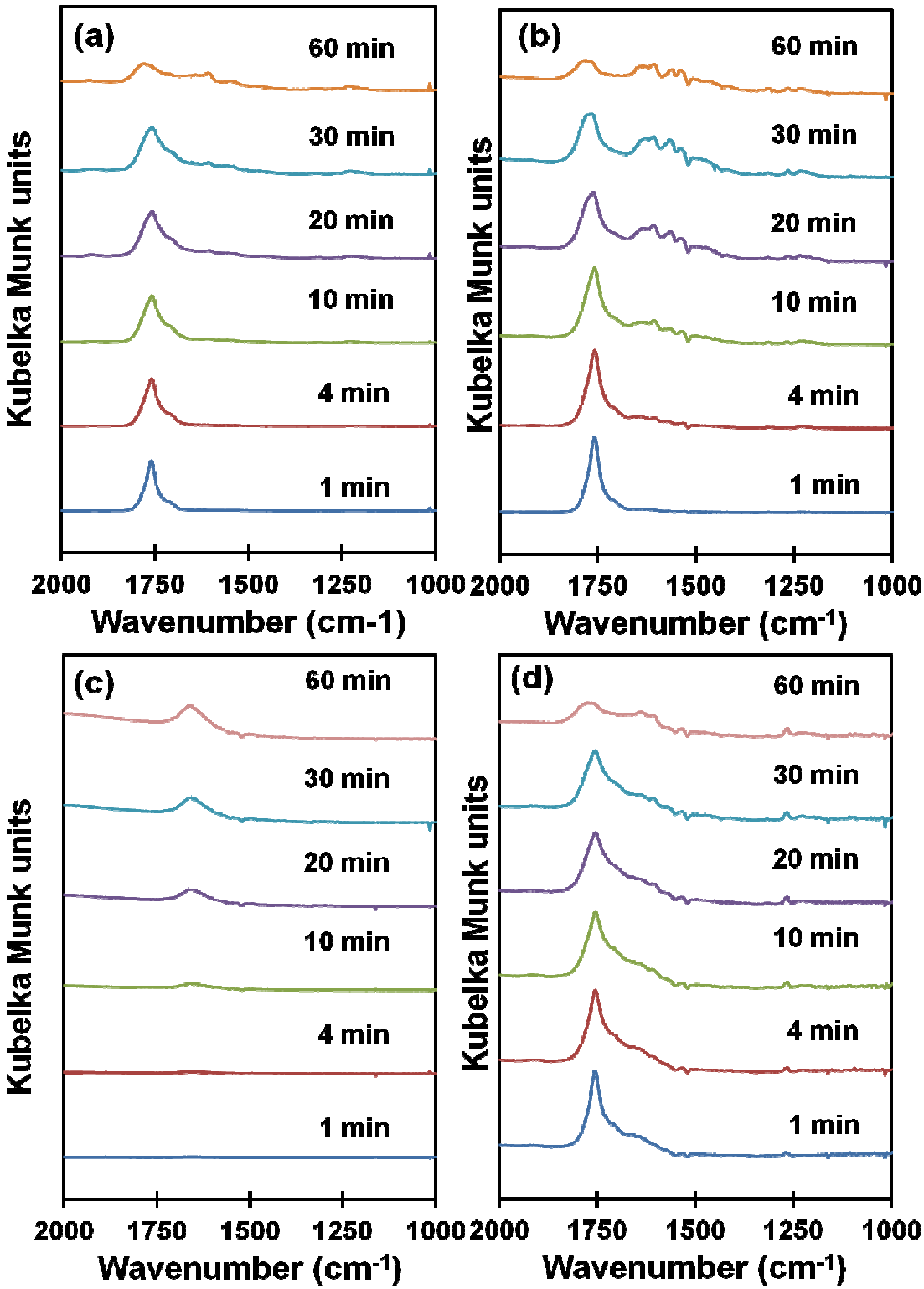

Figure 4-2 Temporal IR spectrum following exposure of Pt/ceria at 50 °C to (a) 1000 ppm NO; (b) 1000 ppm NO and 5% O_2; (c) 5% O_2; (d) 1000 ppm NO after 5% O_2.

Table 4-0-1 The assignment of IR bands

Peak assignment	Species	Ref
1240-1270	the bridging nitrate on Ce	96,97,101, 102
1420-1460	monodentate nitrito and nitrate on Ce	92,94,97,101, 102
1450	monodentate nitrate on Ce	97,100,101, 102
1560	chelating bidentate nitrate on Ce	95,96,97,101, 102, 103
1620	bridging bidentate nitrate on Ce or Al	94,95,96,97,101, 102, 103
1650-1700	NO_2	104
1740-1760	N_2O_4	97,101, 102,104
1700-1760	Mononitrosyl on Pt	92,93,97,98,101, 102

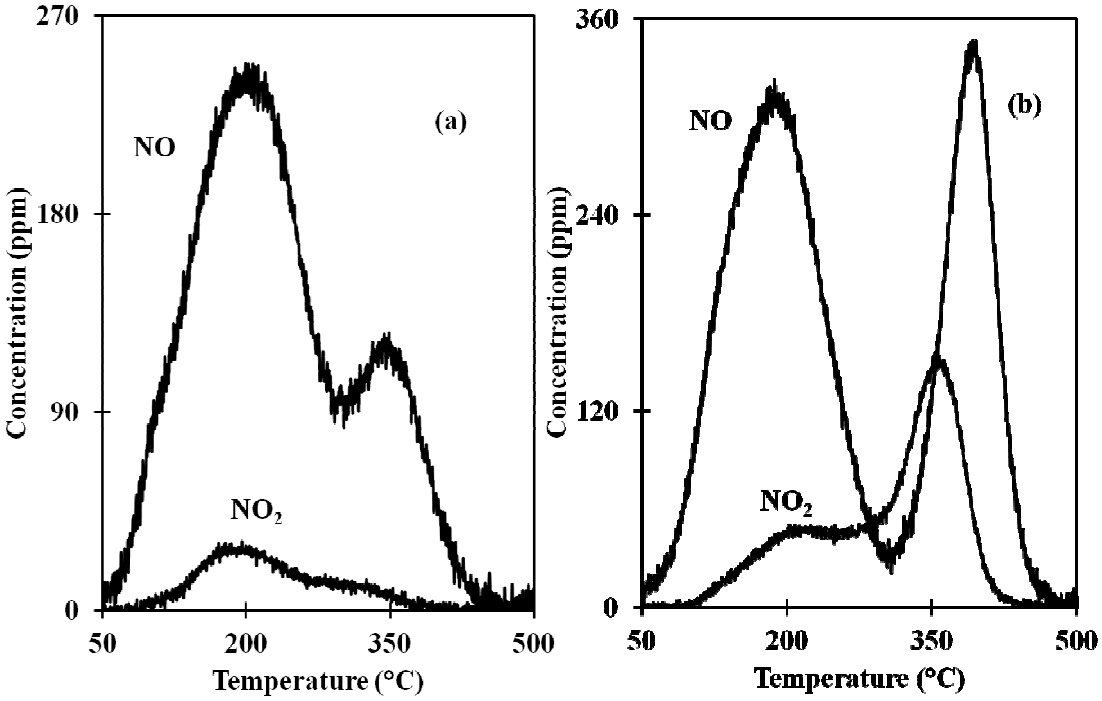

Figure 4-3 Exit concentration as a function of temperature during (a) NO-TPD and (b) NO+O_2-TPD.

In addition to the DRIFTS experiments, TPD experiments were carried out to study the adsorbed surface species. Figure 4-3 shows the NO-TPD and NO+O_2-TPD profiles. During the NO-TPD, NO was the main gas product during the temperature ramp

and two desorption peaks appeared at 200 and 350 °C. An NO_2 release peak was observed at 200 °C. The desorption peak at 200 °C was assigned to the decomposition of Pt-NO species. Approximately 15.2 µmol NO was desorbed before 300 °C. The amount of NO adsorbed was almost double to the amount of exposed Pt (7.9 µmol), suggesting a 2:1 stoichiometry. The NO_2 desorption peak at 200 °C and the NO desorption peak at 350 °C were attributed to the decomposition of surface nitrates. Above 350 °C, the released NO_2 dissociated to NO. During the NO+O_2-TPD, two similar NO release peaks were observed and the magnitude of the second NO release peak was much higher than the corresponding one in the NO-TPD. Another NO_2 desorption peak appeared at 350 °C in additional to the desorption peak at 200 °C. More NO_x release was observed when NO was fed with O_2. No NO_x release was observed when the catalyst temperature was higher than 500 °C, indicating the depletion of adsorbed species. This is in line with the production of NO_2 by oxidation of NO on the Pt.

According to the results from DRIFTS and TPDs, NO storage over Pt/ceria proceeds through a Pt-catalyzed route. As indicated in Figure 4-2 (a) and Figure 4-3 (a), storage only occurs on the Pt surface initially as the immediate appearance of Pt-NO bands. After the saturation of Pt sites, the NO storage stops. A small amount of surface nitrates exists and most of storage sites on the ceria are not utilized. That is, NO coverage on the Pt inhibits the NO storage on ceria. This can be verified by the NO-TPD experiment. The moles of NO released is comparable to the twice of the moles of Pt loaded and most of storage sites over ceria are not used. Oxygen is necessary to alleviate this NO poisoning.

When NO is fed with O_2, the formation and storage of surface nitrates over ceria increases as indicated in Figure 4-2 (b) and Figure 4-3 (b). This oxygen promotion of NO storage can be done by two possible pathways. The first pathway is that more CeO_2 formation under excess oxygen increases the nitrite oxidation to nitrate. Philipp et al. [105] used DRIFT spectroscopy to investigate NO adsorption and NO/O_2 co-adsorption on ceria. They observed that NO adsorption was dominated by the nitrite formation and ceria promoted nitrate formation by oxidizing nitrite species under excess oxygen environment. However, no nitrite formation or subsequent nitrite oxidation was observed in our DRIFTS experiments. The second pathway is that Pt enhances the in-situ NO_2 formation and the sequential nitration. To verify this conjecture, the oxygen pre-saturation is applied to the catalyst before the NO storage. In this condition, the NO_2 formation is limited by the stored oxygen. As shown in Figure 4-2 (d), , the nitration stops after 10 minutes and the intensity of nitrate peaks stays unchanged due to the exhaust of stored oxygen. Hence, the overall NO storage over Pt/ceria is limited by NO_2 formation, which is a Pt-catalyzed route.

The adsorption spectra upon the exposure of Pt/ceria to 1000 ppm NO_2 in He at 50 °C for different times is shown in Figure 4-4 (a). The rising peaks at 1400-1620 cm^{-1} after 4 min NO_2 adsorption were attributed to the surface nitrates and the minor peaks at 1320 and 1800 cm^{-1} reflected the strong NO_2 adsorption [97-104]. The nitrate band at 1240-1270 and1400-1600 cm^{-1} increased rapidly up to 30 minute. Some weakly-adsorbed surface NO_2 was removed by the 30 min He purge as indicated by the decrease of the bands at 1320 and 1800 cm^{-1}. The temporal spectra following the exposure of Pt/ceria to

1000 ppm NO_2 and 5% O_2 at 50 °C is shown in Figure 4-4 (b). The nitrate bands at 1270 and 1560 cm^{-1} emerged initially. From 4 to 30 minute, the bands at 1320, 1420, 1560, 1620 and 1800 cm^{-1} kept growing. The surface nitrate species barely changed after the 30 min He purge. Compared to Figure 4-4 (a), the intensity of the nitrate peaks decreased in the presence of O_2. In sum, the NO_2 storage proceeded by the surface nitration. The good utilization of storage sites over Pt/Ce leads to a larger amount of NO_x stored than forming the Pt nitrosyl.

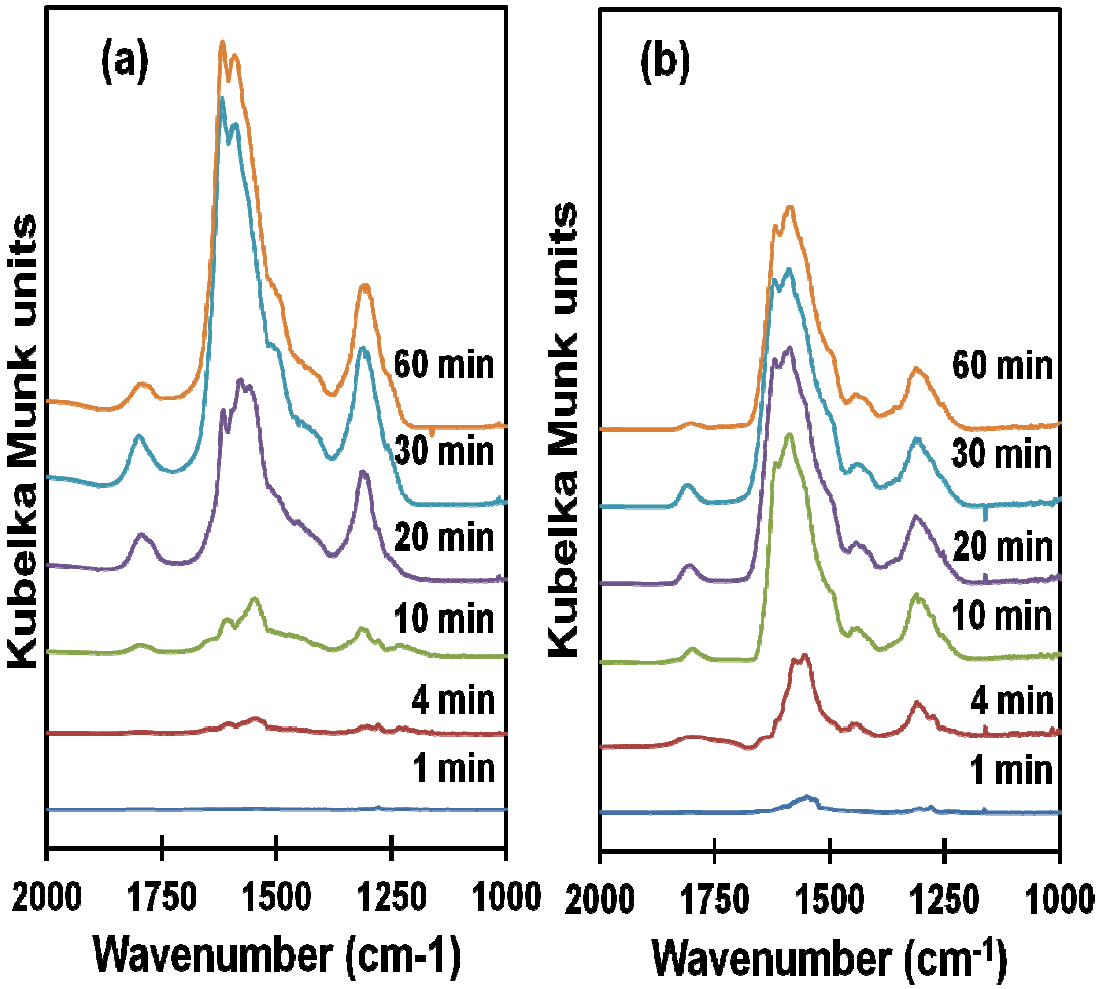

Figure 4-4 Temporal IR spectrum upon the exposure of the Pt/ceria at 50 °C to (a) 1000 ppm NO_2 and (b) 1000 ppm NO_2 and 5% O_2.

Figure 4-5 shows the NO_2-TPD and NO_2+O_2-TPD profiles. The peak assignments were based on reports from other research groups [103, 106-108]. The first peak of NO_2 desorption at 150 °C corresponded to the decomposition of monodentate nitrate. The second peak of NO_2 desorption at 350 °C corresponded to the decomposition of monodentate nitrate to the bidentate nitrates. The third peak of NO_x corresponded to the decomposition of surface nitrates and NO_2 dissociation to NO and O_2. No NO release was found below 350 °C. In the NO_2+O_2-TPD spectrum, there were three similar NO_2 desorption peaks as those in the NO_2-TPD, while the magnitude of all these three peaks decreased. At the same time, a new NO release peak was found at 150 °C. Comparing NO_2- and NO_2+O_2-TPDs, oxygen decreased the amount of NO_x stored.

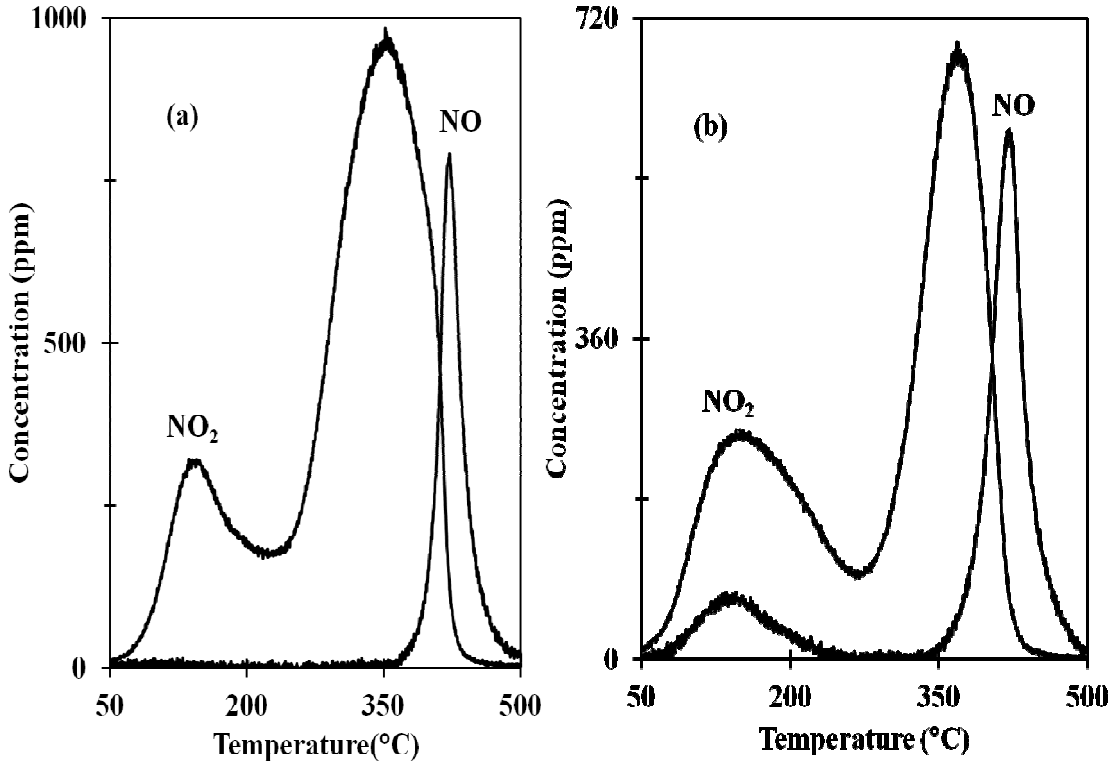

Figure 4-5 Exit concentration as a function of temperature during (a) NO_2-TPD and (b) NO_2+O_2-TPD profiles.

Although the NO storage is a Pt-catalyzed route, the NO_2 storage over the PtCe catalyst is not. Significant amount of surface nitrate was formed when the pre-reduced catalyst was exposed to NO_2, while the formation of Pt-NO species was limited. This means that Pt is not needed for NO_2 storage over ceria. No nitrite formation was observed. However, the oxygen addition to the NO_2 feed diminished the NO_2 storage. This is evident when comparing the intensity of various nitrate peaks in the DRIFTS spectrums in Figure 4-4 and the amount of NO_x released during the TPDs in Figure 4-5. More nitrate formation and a higher NO_x release are obtained using NO_2 as the sole oxidant. The degrading effect could be due to the competitive storage between NO_2 and O_2. Some storage sites over ceria are occupied by oxygen and a complete nitration cannot proceed. The amount of NO_x released decreases from 75 µmole (saturated with NO_2) to 53 µmole (saturated with NO_2+O_2). A clear evidence is the initial NO release during TPD, as shown in Figure 4-5 (b). This NO peak could come from the reaction between the released NO_2 and the un-nitrated sites. The disproportionation of NO_2 would lead to the nitration of oxygen-occupied storage sites and the formation of NO.

Hence, the NO and NO_2 storage over ceria may go through Pt-catalyzed and non Pt-catalyzed pathways, respectively. Oxygen addition is important for the Pt-catalyzed NO_2 formation, while harmful to the non Pt-catalyzed NO_2 storage. All the adsorbed NO_x is stored as surface nitrates, which decompose when the temperature is higher than 400 °C.

The observed NO_x storage mechanisms over the Pt/Ce are similar to those over the Pt/Ba LNT catalyst. The Pt-catalyzed NO oxidation to NO_2 is the key step for the NO

storage. Kabin et al. [20] reported that the NO_x trapping efficiency of a Pt/Ba LNT catalyst depends on its reactivity for NO oxidation to NO_2. Oxygen has an important role to enhance the NO storage. Bhatia et al. [109] determined that the oxygen adsorption is the rate-determining step for NO oxidation over a series of Pt/Ba LNT catalysts. The NO_2 storage over Pt/Ba or Pt/Ce can proceed via a disproportionation or nitration pathway, generating NO. Kabin et al. [19] observed the NO_2 storage over the Pt/Ba LNT catalysts through the nitration routine using the TAP reactor. Hence, the NO_x storage over Pt/Ce and Pt/Ba has the similar phenomenological modes.

4.3.2 NO_x Reduction Mechanisms over the PtCe Catalyst

Figure 4-6 (a) shows that only two H_2 consumption peaks exist in the H_2-TPR spectra for the NO pretreated catalyst. The first peak corresponds to the reduction of the surface species from Pt, likely Pt nitrosyl as indicated by the DRIFTS experiments. The second peak corresponds to the reduction of surface species at the interface between ceria and Pt. Two H_2O release peaks were observed along with the H_2 consumption peaks and the H_2O release peak at 350 °C corresponded to the reduction of surface hydroxyl groups from γ-Al_2O_3 [79, 110]. An NH_3 release peak, following the H_2O release peak, emerged at the second H_2 consumption peak. Compared to the case with oxygen pretreatment (Figure 3-3), one hydrogen consumption peak at 150 °C was missing, indicating that fewer storage sites were available. Meanwhile, the ratio of reduced oxygen to nitrogen was in the range from 2.75 to 2.82, higher than the stoichiometric ratio of 2.625 ($Ce(NO_3)_4$->Ce_2O_3). Excessive oxygen was stored during the NO storage and/or the oxygen storage

could be crucial for NO storage. Figure 4-6 (b) shows the H_2-TPR profile for the NO and O_2 pretreated catalyst. Similar to H_2-TPR profile from the oxygen pre-adsorbed catalyst, three H_2 consumption peaks were found and the H_2 consumption intensified in the temperature range between 75 and 200 °C. The reappearance of H_2 consumption peak at 150 °C indicated that more N and O storage sites were accessible when NO were fed with O_2. Higher H_2O and NH_3 release was obtained from the NO+O_2 pretreated catalyst than that from the NO pretreated catalyst. The ratio of reduced oxygen to nitrogen was in the range of 2.49~2.59, implying a $2NO_3^-$ to O^{2-} reduction. As a result, the oxygen addition increased the catalyst storage capacity with a reasonable N: O ratio. Figure 4-6 (c) shows the H_2-TPR spectrum following NO_2 pretreatment. The first peak of H_2 consumption peak corresponded to the reduction of Pt surface. The NH_3 peak occurred after the H_2O release peak. The second and third peaks of H_2 consumption corresponded to the reduction of a variety of surface species on the interfaces between Pt and ceria. An interesting peak spilt was found in the second H_2 consumption peak. A similar peak spilt was also observed in the H_2O release peak, while the NH_3 release peak did not exhibit a peak spilt. The amount of stored nitrogen and oxygen found after the NO_2 pretreatment were larger than those from the NO and NO+ O_2 pretreatment, in line with the fact that NO_2 was the strongest oxidizer. The ratio of reduced oxygen to nitrogen was in the range of 2.95 to 3.10, higher than that after NO+O_2 pretreatment. Figure 4-6 (d) shows the H_2-TPR spectrum for the NO_2+O_2 pretreated catalyst. The profile was similar to Figure 4-6 (c), while another peak spilt appeared at the former first H_2 consumption peak (<100 °C). The competitive storage between NO_2 and O_2 on the same storage sites may lead to the

peak spilt. H_2O release appeared before the release of NH_3, in agreement with observation in Figure 4-6 (c). Less nitrogen and oxygen was stored on catalyst after NO_2+O_2 pretreatment than that from NO_2 pretreatment. The decrease of storage sites could be due to the competitive storage between NO_2 and O_2.

As shown in the H_2-TPRs, different storage sites exist on the PtCe catalyst providing place for NO_x storage. The reactivity of the storage sites depends not only on the amount and accessibility of the storage sites, but also on the oxidizing ability of storage agents. The higher the oxidizing ability, the more storage sites are available. The storage capacity of the PtCe catalyst increases with an oxidant ranking of NO, O_2 and NO_2. When NO is used the sole oxidant, the storage only happens over the Pt and some Pt-Ce surfaces as indicated by H_2-TPR in Figure 4-5 (a). When oxygen is fed to catalyst, higher storage capacity can be obtained due to a better utilization of Pt-Ce interfaces than the case with NO. Two H_2 consumption peaks exist in the temperature range between 100 and 200 °C for the case with oxygen, while only one H_2 consumption peak exists for the case with NO. More storage sites are available when the PtCe catalyst is pretreated with NO_2. The intensity of two H_2 consumption peaks in the temperature range between 100 and 200 °C becomes intensified. Hence, Pt surface is always available for NO_x storage, while the NO_x storage over other sites, such as Pt-Ce interfaces, may depend on the oxidizing ability of storage agents.

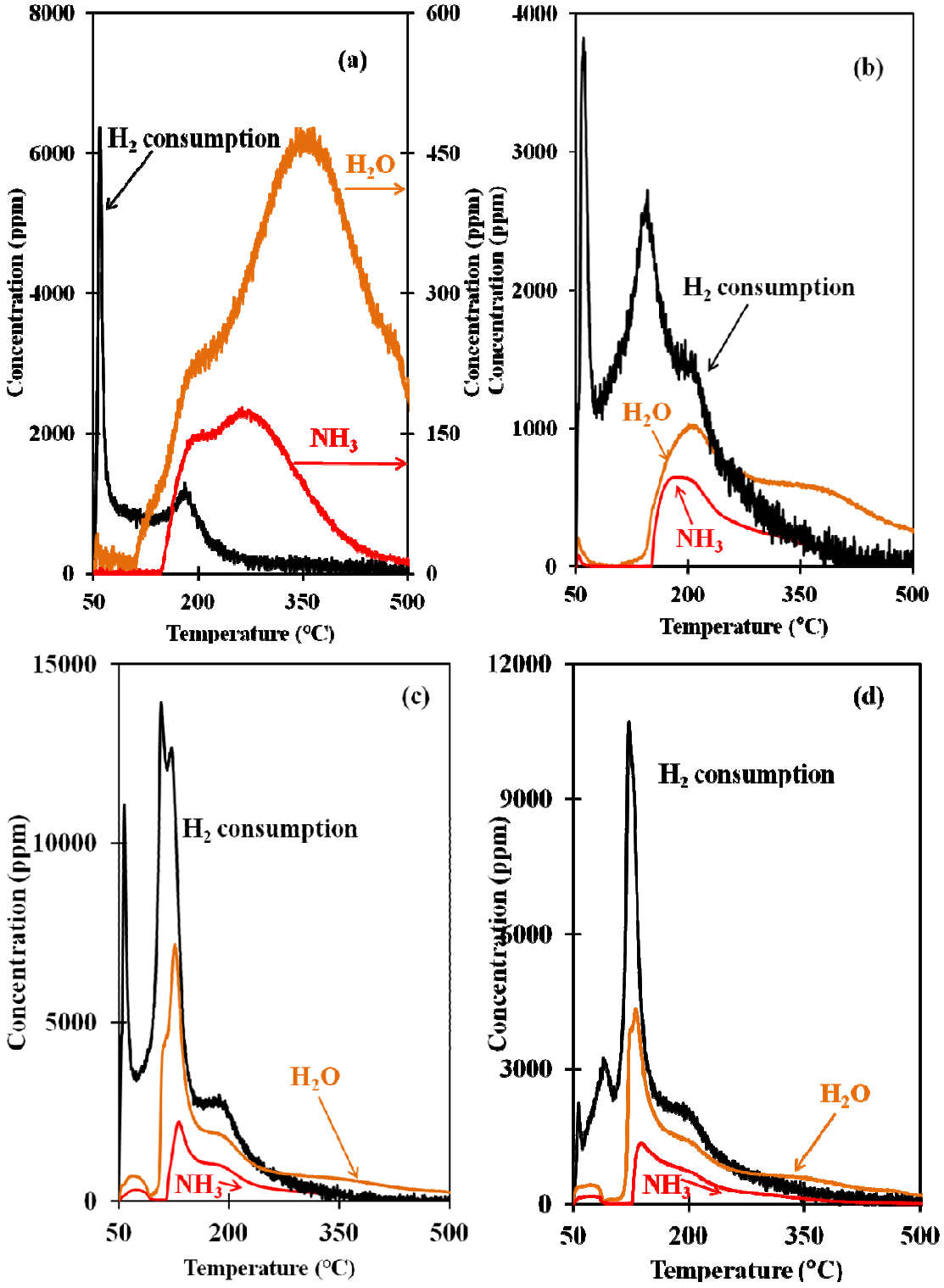

Figure 4-6 The H_2-TPR spectrum for the PtCe catalyst pretreated by (a) NO; (b) NO+O_2; (c) NO_2 and (d) NO_2+O_2.

The reduction of stored NO_x over Pt/ceria is a Pt-catalyzed pathway. Since Pt is the most active component in the catalyst, the first step of NO_x reduction is always the purging of Pt surface. After the removal of adsorbed species from the Pt, the oxygen reduction over ceria is the next step for NO_x reduction. This is evident from Figure 4-5. The H_2O release peak always appears before the NH_3 release peak. In the second H_2 consumption peak (150-200 °C), a similar split in the H_2 peak can be observed in the H_2O profile without a reflection on the NH_3 profile. Hence, the stored oxygen needs to be removed before NO_x reduction over ceria. This excessive oxygen storage over Pt/ceria requires a large amount of reductant and a sufficiently long reduction duration to achieve the NO_x reduction. The reduction of the rest stored NO_x over Pt/Ce is complete below 200 ºC, since there is no H_2 peak observed above 200 ºC. The NO_x reduction over the Pt/Ce and the Pt/Ba is similar. Nova et al. [111] reported that the Pt in vicinity of Ba catalyzes the reduction of stored nitrates and thus the reduction can proceed at temperatures below the thermal decomposition of stored NO_x.

4.3.3 Optimal NO_x Storage and Reduction over Pt/Ceria

The above results indicate that the oxygen storage capacity of Pt/ceria is partially beneficial to NO storage and detrimental to NO_x reduction. The excessive oxygen storage may also lead to high fuel penalty during the NO_x reduction. A series of experiments with different NO_x mixtures were conducted to determine the optimal condition for NO_x storage and reduction. The amount of NO_x storage under different temperatures is shown in Figure 4-7 (a) and summarized in Table 4-2. The highest amount of NO_x storage was

achieved at 150 °C, when NO_2 was the only feed. As the temperature increases, the amount of NO_x stored was essentially the same when using $NO+O_2$, NO_2 and NO_2+O_2 as oxidants. At 400 °C, the PtCe catalyst loses its storage capacity regardless of the oxidants.

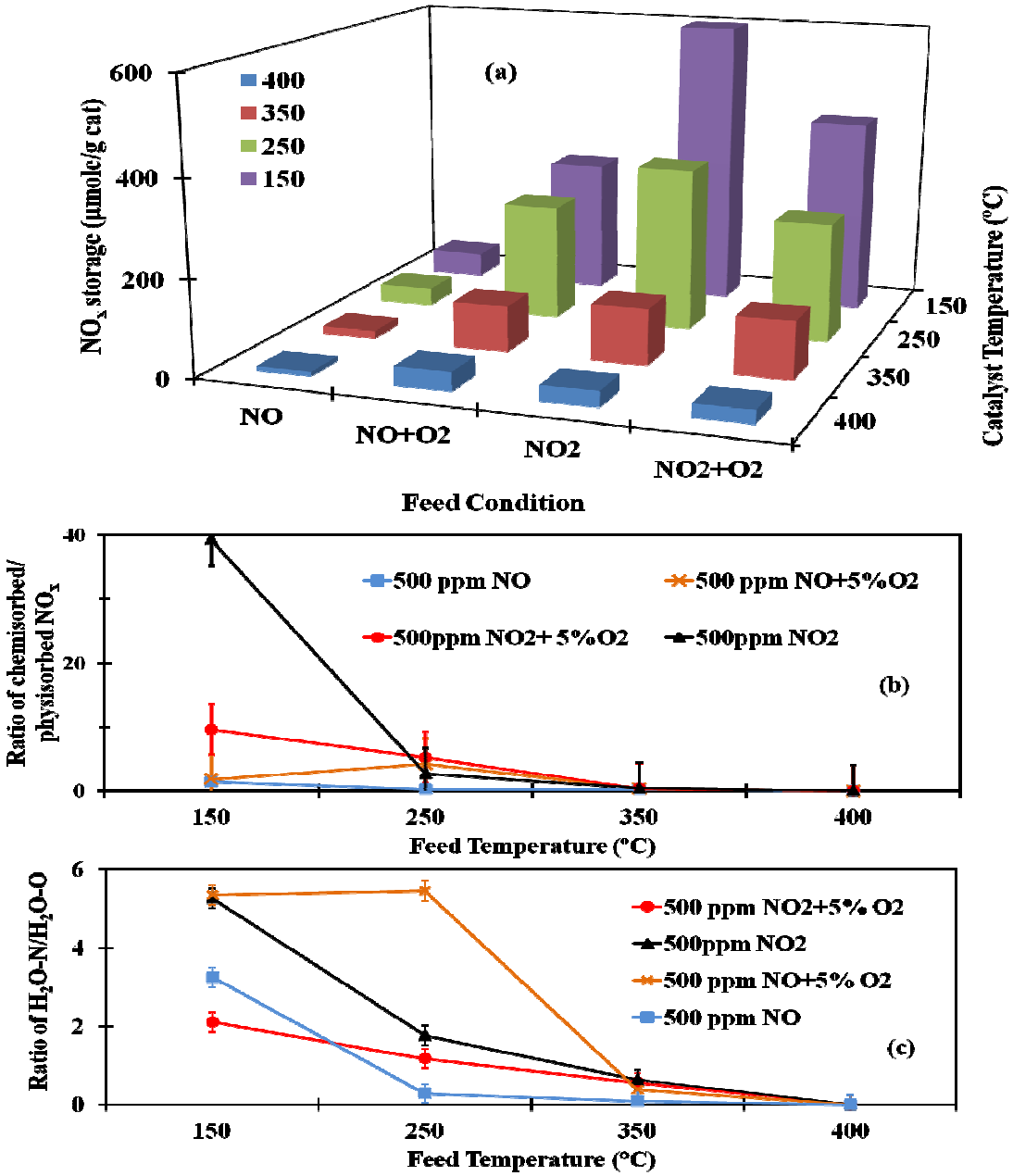

Figure 4-7 A comparison of NO_x storage with different oxidants at different temperatures; (a) NO_x storage; (b) ratio of of chemisorbed to physisorbed species; (c) the ratio of H_2O-N/H_2O-O.

Table 4-2 NO_x storage as a function of feed temperature.

Temperature (ºC)		**150**	**250**	**350**	**400**
NO	Total NO_x Uptake (μmole/g wc)	50	36.8	15.4	9.3
	Physisorbed (μmole/g wc)	20.8	29.2	12.3	9.3
	Chemisorbed (μmole/g wc)	29.2	7.6	3.1	0
$NO+O_2$	Total NO_x Uptake (μmole/g wc)	277.6	240.6	95.4	39.3
	Physisorbed (μmole/g wc)	99.2	46.1	70.7	39.3
	Chemisorbed (μmole/g wc)	178.4	194.5	24.7	0
NO_2	Total NO_x Uptake (μmole/g wc)	603.1	340.7	116.9	32.3
	Physisorbed (μmole/g wc)	15	86.2	84.6	32.3
	Chemisorbed (μmole/g wc)	588.1	228.4	32.3	0
NO_2+O_2	Total NO_x Uptake (μmole/g wc)	406.1	248.5	119.9	27.6
	Physisorbed (μmole/g wc)	38.4	40	90.8	27.7
	Chemisorbed (μmole/g wc)	367.6	208.5	29.3	0

Figure 4-7 (b) shows the ratio of chemisorbed NO_x over physisorbed NO_x. The chemisorbed NO_x is defined as the strongly adsorbed NO_x and the physisorbed NO_x as the weakly adsorbed NO_x, which can be removed by an Ar purge. The high ratio of chemisorbed NO_x over physisorbed NO_x means a high thermal stability of stored NO_x. The NO_2 storage generates highly stable nitrates at 150 °C, while the $NO+O_2$ storage leads to highly stable nitrates at 250 °C. No chemisorbed species is available when the temperature is above 400 °C, agreeing with the TPD results. Moreover, one can define the fuel penalty over Pt/ceria by comparing the stored NO_x to the stored oxygen. A ratio of H_2O-N/H_2O-O is defined as "H_2O from stored NO_x/ H_2O from oxygen", based on the reactions (1) to (4):

(1) $2Ce(NO_3)_4+24H_2 \Leftrightarrow Ce_2O_3+6NH_3+15H_2O$,

H_2O-N=15/6*NH_3 formed in Reduction,

(2) $2Ce(NO_3)_4+15H_2 \Leftrightarrow Ce_2O_3+3N_2+15H_2O$,

H_2O-N=15/3*N_2 formed in Reduction,

(3) $Pt(NO)_2+5H_2 \Leftrightarrow Pt+2NH_3+2H_2O$,

H_2O-N=NH_3 formed in Reduction,

(4) $Pt(NO)_2+2H_2 \Leftrightarrow Pt+N_2+2H_2O$,

H_2O-N=2*N_2 formed in Reduction,

and H_2O-O= Total H_2O formed in Reduction - H_2O-N.

The higher the ratio of "H_2O-N/H_2O-O", the smaller is the fuel penalty. The reaction (3) and (4) are only used in calculating the H_2O-N/H_2O-O ratio of "500 ppm NO" at 150 °C. Since according to Figure 4-2 (a) the Pt-NO disappears above 200 °C, the Pt-NO is assumed to be the dominant surface species at 150 °C with only NO. Figure 4-7 (c) shows the fuel penalty associated with all the cases. The lowest fuel penalty is obtained at 250 °C, when NO and O_2 are fed together. The oxygen addition to NO leads to the in-situ NO_2 formation and the sequential nitrate formation maximizes the NO_x storage. When the temperature is above 250 °C, the fuel penalty is very high due to the small NO_x storage. Hence, the optimal NO_x storage and reduction over Pt/ceria, in terms of thermal stability and fuel penalty, is obtained at 250 °C using NO and O_2 as the oxidants.

4.5 Conclusions

The NO_x storage and reduction on the PtCe catalyst was studied by DRIFTS, TPD and H_2-TPR. The main findings are:

1. NO storage is a Pt-catalyzed process. Oxygen can enhance the NO storage via the in-situ NO_2 formation and sequential nitration. NO_2 storage is not a Pt-catalyzed process. Oxygen competes with NO_2 for the storage sites.

2. The PtCe storage capacity depends on the amount of the storage sites and the oxidizing ability of storage agents.

3. The reduction of Pt is the first step of the catalyst regeneration and the oxygen reduction occurs prior to NO_x reduction over ceria.

4. Pt/ceria can serve as a N_{Ox} storage catalyst in a temperature window between 150°C and 350°C. The optimal N_{Ox} storage and reduction is at 250 °C using NO and O_2.

The above findings provide a fundamental understanding of the role of ceria in the LNT catalyst. The NO_x storage and reduction mechanisms over the Pt/Ce are analogous to those over the Pt/Ba. This knowledge can be used to conduct the optimization of the LNT catalyst composition, such as the metal zoning.

Chapter 5 NO_X Reduction Using Dual-Layer Monolithic Catalysts

5.1 Introduction

The LNT-SCR dual-layer catalyst is a potential alternative to the sequential LNT-SCR multi-brick catalyst for NO_x reduction. The dual-layer catalyst operation requires periodic shifts between fuel-lean and fuel-rich feeds. NO_x and O_2 are stored on the LNT layer during the fuel-lean phase, while NH_3 forms by the stored NO_x during the fuel-rich phase. NH_3 is stored on the Brønsted acid sites over the SCR layer during the fuel-rich feed. During the fuel-lean feed, NO_x is partially reduced by the adsorbed NH_3 on the SCR layer. Therefore, the expensive urea feed system for SCR catalyst is replaced by NH_3 produced on the LNT catalyst. The burden of NO_x reduction over the LNT catalyst is weakened due to its consumption on the SCR layer. This reduces the required amount of costly LNT catalyst. Hence, the LNT-SCR dual-layer technology has the potential to reduce the PGM loading for NO_x reduction in the aftertreatment system.

In this study, the dual-layer monolithic catalysts comprising a SCR layer deposited on-top of a LNT layer was prepared and its performance tested. We investigated the impacts of the type of SCR catalyst (Fe-, Cu-), H_2O and CO_2 addition, LNT ceria loading, and temperature on the cycle-averaged NO_x conversion and product distribution. Finally, the effects of aging on the catalyst performance are examined. The findings are interpreted in terms of the individual performance features of the LNT and SCR catalysts. This study provides insight and understanding of the dynamic performance of a dual-layer LNT-SCR. This information is essential for any attempt to

minimize the amount of required expensive PGM. Moreover, the results enable a comparison of the performance of dual-layer architecture with the sequential architecture.

5.2 Experimental

Lean-rich cycling experiments, consisting of periodic shifts between the lean and rich feeds, were carried out to evaluate the deNO_x performance of LNT and dual-layer catalysts. Unless otherwise stated, a lean feed, containing 500 ppm NO and 5% O_2 in Ar, was fed for 60 s. It was followed by a rich feed containing 2.5% H_2 in Ar for 5 s. The cycle average H_2: NO feed ratio was 1.04 times higher than the stoichiometric ratio needed for NH_3 formation by the overall reaction

$$16H_2+4NO+3O_2 \rightarrow 4NH_3 +10\ H_2O\ . \qquad \text{(R1)}$$

The total gas flow rate was 1000 sccm (GHSV= 60,000 hr^{-1}, calculated based on total monolith volume and standard temperature and pressure). It took approximately 10 minutes to reach a periodic state and at least 50 cycles were run at each temperature. The final ten cycles were averaged to determine the cycle-averaged NO conversion and product selectivity for a particular operating condition. The feed temperature was increased from 100 to 400 ºC in steps of 50 ºC. At each temperature, the cycle-averaged quantities were determined. The NO conversion was calculated by

$$X_{NO} = 1 - \frac{\int_0^{\tau_s} F_{NO}(t)dt}{\int_0^{\tau_l} F_{NO}^{i}(t)dt}\ . \qquad (1)$$

When large amount of NO_2 was present, the NO_x conversion was calculated by

$$X_{NO_x} = 1 - \frac{\int_0^{\tau_s} [F_{NO}(t)+F_{NO_2}(t)]dt}{\int_0^{\tau_l} F_{NO}^{i}(t)dt} = X_{NO} - \frac{\int_0^{\tau_s} F_{NO_2}(t)dt}{\int_0^{\tau_l} F_{NO}^{i}(t)dt}\,. \qquad (2)$$

The NH_3 and NO_2 selectivity were calculated by

$$S_{NH_3/NO_2} = \frac{\int_0^{\tau_s} F_{NH_3/NO_2(t)}dt}{\int_0^{\tau_l} F_{NO}^i dt - \int_0^{\tau_s} F_{NO}(t)dt} \ , \quad (3)$$

and the N_2 and N_2O selectivity were calculated by

$$S_{N_2/N_2O} = \frac{\int_0^{\tau_s} 2 * F_{N_2/N_2O(t)}dt}{\int_0^{\tau_l} F_{NO}^i dt - \int_0^{\tau_s} F_{NO}(t)dt} \ . \quad (4)$$

Here τ_l and τ_s are the duration of the lean phase feed and a lean-rich total cycle (s). F_{NO}^i is the NO feed rate and $F_{NO}(t), F_{NH_3}(t), F_{NO_2}(t), F_{N_2O}(t), F_{N_2}(t)$ the corresponding effluent molar flow rates (mole/s). In some cycling experiments, 2.5 % H_2O and 2.0 % CO_2 were added to the carrier gas (Ar) flow.

A series of steady state experiments was conducted to evaluate the catalyst properties. The total flow rate was 1000 sccm in all the experiments. The standard SCR reaction was used to assess the activity of the Fe/ZSM-5 and Cu/ZSM-5 SCR catalysts, both of which had the same loading of 0.9 g/in^3. The feed contained 500 ppm NO, 500 ppm NH_3, and 5% O_2 in Ar. During the NH_3 and NO_2 storage experiments, 500 ppm of NH_3 or NO_2 was fed to the catalyst for 20 minutes. The total NH_3 or NO_x uptake was calculated by subtracting the amount of effluent from that fed. The physisorbed species were swept by a 10-min Ar purge. After that, the monolith temperature was increased by a temperature ramp of 20 °C/min to 450 °C in Ar. The amount of NH_3 or NO_x released was referred to as chemisorbed species. The nitrogen balance was closed by comparing the sum of physisorbed and chemisorbed species with the total feed amount. The balance closed within 5 %. NH_3 oxidation was carried out with a feed gas containing 500 ppm NH_3 and 5 % O_2 in Ar. to quantify the rate of this important side reaction. The reaction

order of NH_3 oxidation was determined from experiments in which the NH_3 concentration varied from 200 to 1000 ppm. The total flow rate was decreased to 500 sccm and the O_2 concentration was fixed at 5 %. The NH_3 conversion was less than 15 % at 150 ºC. The apparent reaction rate was calculated by

$$r_{NH_3} = \frac{F_{in} X_{NH_3}}{m_{w.c.}}, \quad (5)$$

where F_{in} is the feed rate of NH_3 (mole/s), X_{NH_3} the NH_3 conversion (%) and $m_{w.c.}$ the washcoat mass (g).

5.3 Results and Discussion

5.3.1 Comparison of Effluents from LNT and Dual-layer Catalysts

Figure 5-1 (a) shows typical temporal effluent concentration from the Pt/Rh/Ba/γ-Al_2O_3 LNT catalyst (LNT1) during a 60 s lean and 5 s rich cycle at a feed temperature of 250 °C. The insert Figure 5-1 (b) describes the effluent during the 5 s rich regeneration and subsequent five seconds of lean feed. The temporal effluent is characteristic of a LNT regeneration using H_2 as the reductant. A NO release peak ("NO spike" or "NO puff") appeared at the beginning of the rich feed. Nearly coincident with the NO spike was N_2O evolution. N_2 and NH_3 appeared consecutively with some overlap. For this operating condition, the maximum N_2 and NH_3 effluent concentrations were 3550 ppm and 2610 ppm, respectively. By integrating the areas under the effluent graphs, the computed NH_3 yield (6.1 μmole) was comparable to that of N_2 (7.8 μmole). The rather large amount of generated NH_3 pointed out the potential for a dual-layer catalyst application. That is, by adding a top-layer of SCR catalyst, the slipping NH_3 could be

captured and converted selectively to N_2 by the standard SCR reaction between NH_3, NO and O_2. The decrease of the NH_3 slip increased the NO conversion. A second pair of N_2 and N_2O peaks formed during the lean feed. These were followed by a nearly 30 s period in which no species containing N were measured, indicating that NO oxidation and NO_x storage were the main processes that occurred during the remainder of the lean feed. About 35 s after the shift to a lean feed, some NO emerged. Its concentration gradually increased during the remainder of the lean feed, due to the expected saturation of the NO_x storage sites.

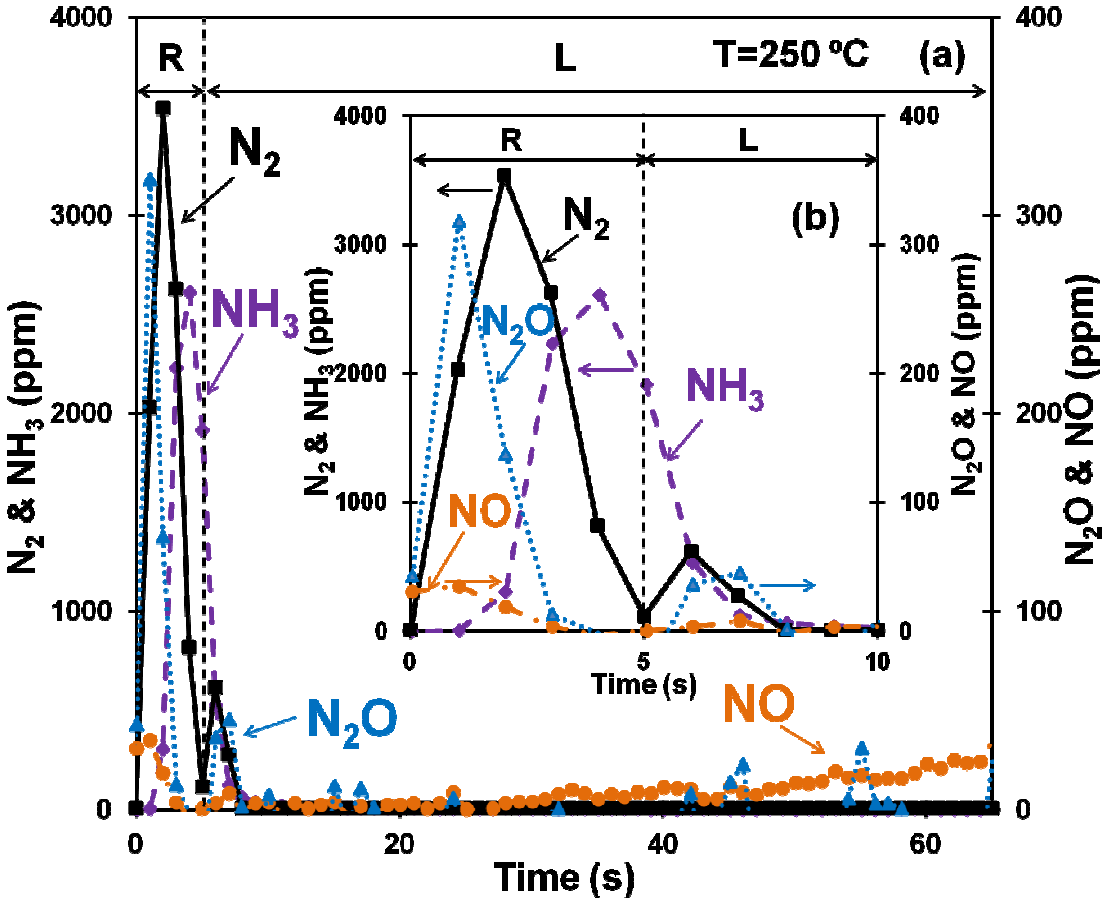

Figure 5-1 (a) Effluent from the Pt/Rh/Ba LNT1 catalyst over a period of 0-65 s; (b) Insert shows effluent over 0-10 s.

The species evolution from the LNT1 catalyst agrees with reports by other investigators. The occurrence of the NO_x spike at the beginning of the rich feed is an important feature of LNT regeneration [21, 31, 37-38]. Ji et al. [31] attributed its formation to the rate of NO_x reduction being slower than that of nitrate decomposition. The sequential appearance of N_2O, N_2, and NH_3 is also a common feature. At the beginning of the regeneration the conditions are more favorable for N_2O production; i.e., a high local NO/H ratio. As the regeneration proceeds, deeper reduction (decreasing NO/H ratio) favors NH_3 formation. The NH_3 produced upstream travels downstream and reacts with stored NO_x, producing N_2, as reported among others by Mulla et al. [37], Lietti et al. [38, 41, 47], and Clayton et al. [21]. The small N_2 and N_2O peaks at the beginning of the lean feed are attributed to the oxidation of NH_3. Clayton et al. [21, 73] speculated that the oxidation of accumulated NH_x species from the previous rich feed could be responsible for N_2 formation during the subsequent lean feed.

Figure 5-2 compares the performance of the Pt/Rh/Ba/Al_2O_3 LNT1 catalyst (Figure 5-2 (a)) to the dual layer CuZ/LNT1 (Figure 5-2 (b)) and FeZ/LNT1 catalysts (Figure 5-2 (c)). Each plot compares the cycle-averaged NO conversion and product selectivities as a function of feed temperature between 100 to 400 °C. The black line and points describe the NO conversion and the shaded/colored bars the product selectivities. For each catalyst the NO conversion and N_2 selectivity increased monotonically with feed temperature, while the N_2O selectivity decreased (except for the FeZ/LNT1 that produced a slight maximum). Using the LNT1 catalyst, the maximum NH_3 selectivity was about

40 % at 150 °C. A large amount of NH_3 was produced in the temperature range of 150 to 300 °C. These trends are consistent with previously reported results [45].

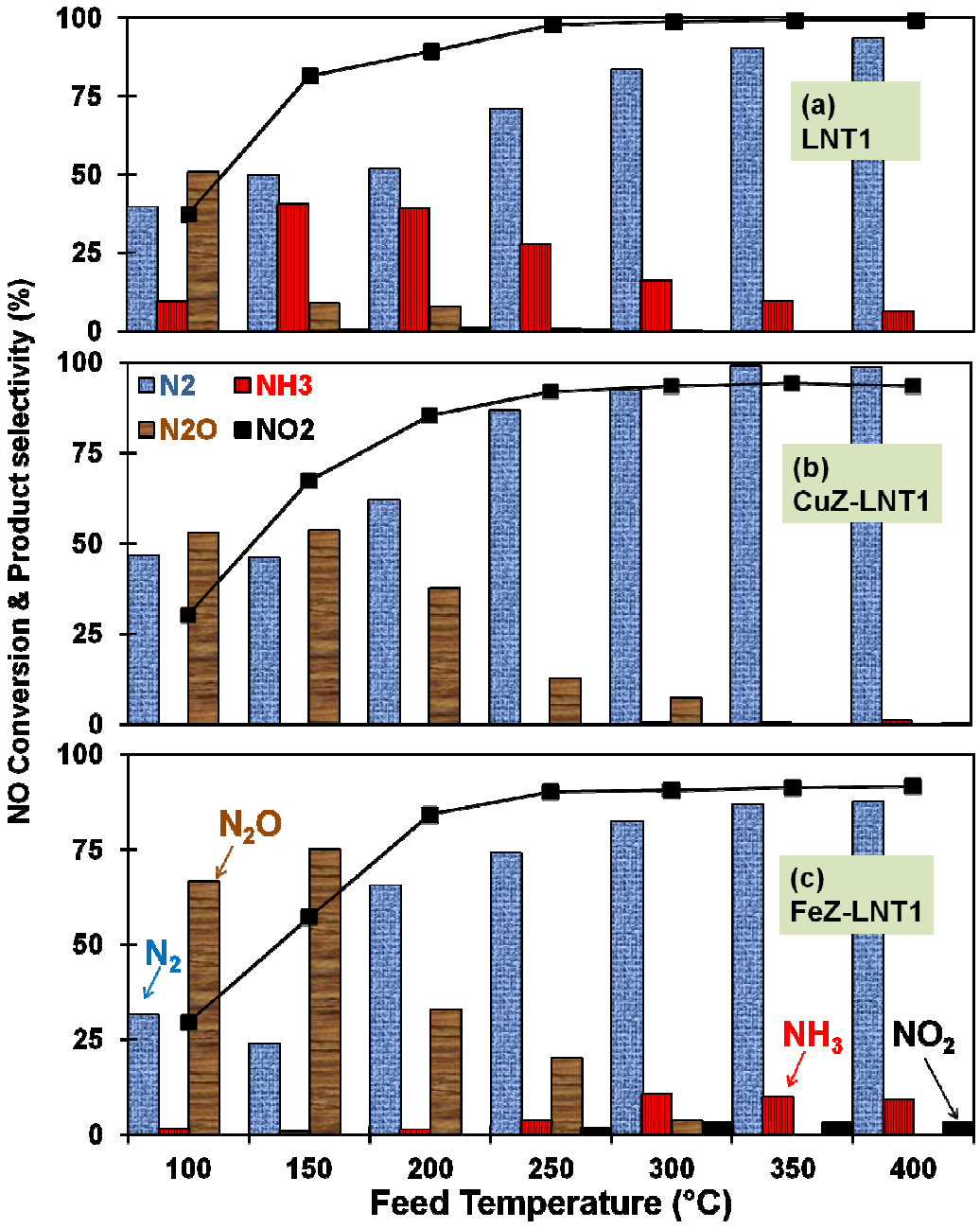

Figure 5-2 Time averaged performance of (a) LNT1 catalyst; (b) CuZ-LNT1 multilayer catalyst; (c) FeZ-LNT1 multilayer catalyst. The black curves with square points are the NO conversion and the color bars are the product selectivities. The same is used format for NO conversion and product selectivities in other similar figures.

It is important to select a suitable SCR catalyst for the dual-layer application. The SCR layer is exposed to a range of NH_3 and NO/NO_2 concentrations along the monolith channels due to reactions in the underlying LNT layer. The dependence of the NO_x conversion and NH_3 selectivity on the temperature is evidence for this fact (Figure 5-2 (a)). The ability of the zeolitic SCR catalyst to adsorb NH_3 is essential for additional NO_x reduction. The SCR layer activity should be high and minimally inhibited by the adsorbed NH_3. For this reason, we tested the performance of two dual-layer catalysts, one containing Fe-exchanged ZSM-5 and the other CuZ, coated on top of the same LNT base layer. Both zeolitic layers had the same loading and were exposed to the same cyclic feed; i.e., 60 s lean, 5 s rich. Figure 5-2 (b) shows the feed temperature dependence of the NO conversion and product selectivity of the CuZ/LNT1 dual-layer catalyst. Similar to the LNT1 layer alone (Figure 5-1 (a)), the NO conversion and N_2 selectivity increase monotonically with feed temperature. On the other hand, the NH_3 produced by the LNT was completely converted. An additional effect of the Cu-zeolite layer is a moderate increase in N_2O for feed temperatures lower than 250 °C. Figure 5-2 (c) shows the NO conversion and product selectivity of the FeZ/LNT1 dual-layer catalyst. The NO conversion and N_2 selectivity for both the LNT1 and CuZ/LNT1 increased with the feed temperature, while the N_2O selectivity generally decreased. However, the FeZ/LNT1 catalyst had some NH_3 slip, higher N_2O selectivity, and a somewhat lower NO conversion and N_2 selectivity over the LNT1 and CuZ/LNT1 the entire temperature range.

In order to examine differences between the two SCR zeolite catalysts, we compared their respective NH_3 storage and SCR activities. Figure 5-3 compares the

temperature dependencies; i.e., 20-minute NH_3 storage capacity and NO conversion for a standard SCR feed (containing NO, O_2, and NH_3) for both Cu/ZSM-5 and Fe/ZSM-5. The NH_3 storage capacity and NO conversion of the FeZ catalyst were lower than that of the CuZ catalyst over the entire temperature range. The CuZ catalyst adsorbed more NH_3 and its SCR activity was higher. Hence, the Cu/ZSM5 was used as the SCR catalyst in our study.

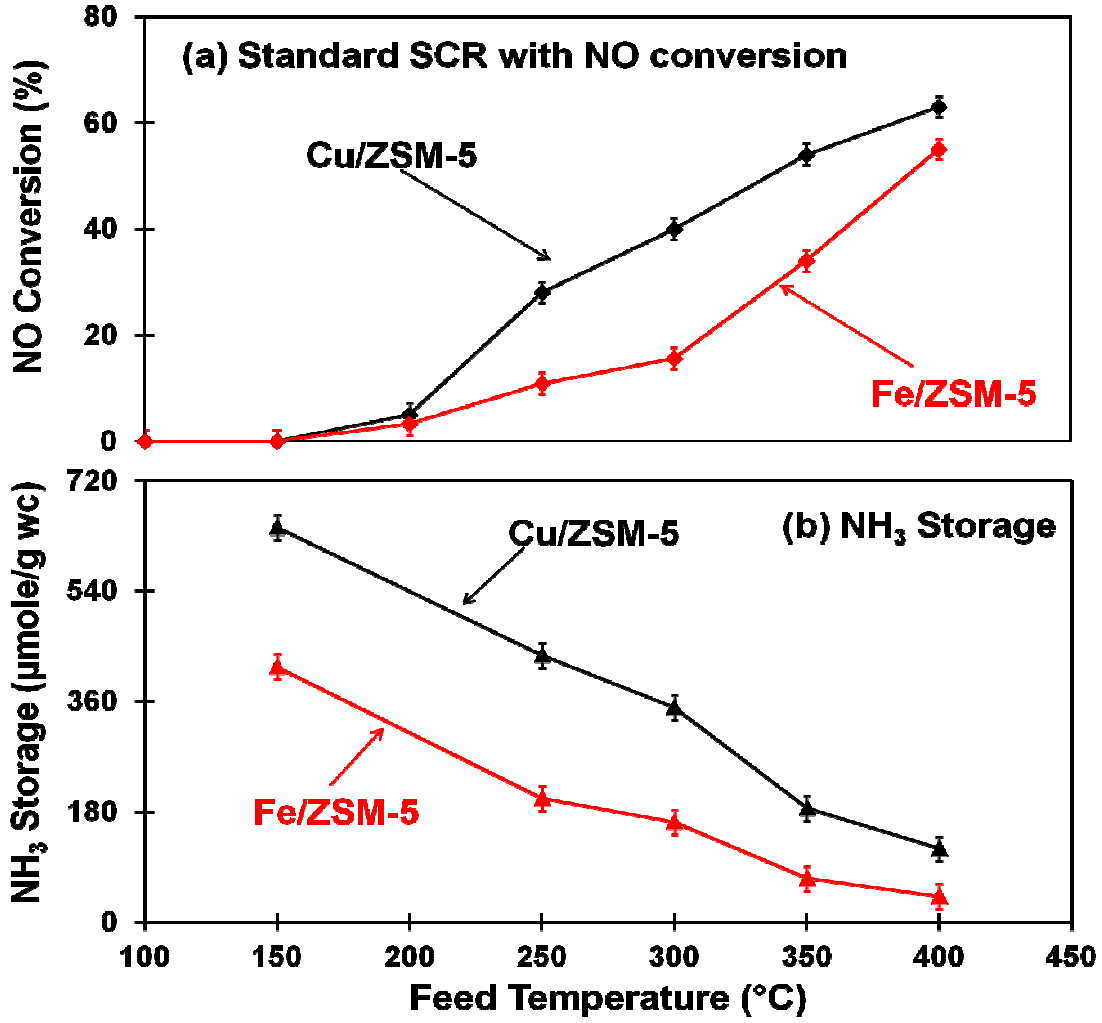

Figure 5-3 (a) NO conversion and (b) NH_3 storage capacity on Fe- (black) and Cu-ZSM-5 (red) samples. Both monoliths have the same washcoat loading as 0.9 g/in^3.

The rather high N_2O selectivity from the two dual-layer catalysts for temperatures below 250 ºC suggests that the N_2O dissociation and reaction with stored NH_3 over the SCR catalyst is negligible. This is due to the limited catalyst activity at low temperatures. Groothaert et al. [112] reported the N_2O dissociation to N_2 over a Fe/ZSM-5 commences above 400 ºC and the presence of oxygen inhibits N_2O dissociation. N_2O dissociation over Cu/ZSM-5 only starts above 400 ºC. Zhang et al. [113] investigated the reduction of N_2O by NH_3 and O_2 over a Fe-MOR zeolite catalyst. The reaction occurs at temperatures exceeding 350 ºC. Hence, the N_2O produced from dual-layer catalyst is not likely to dissociate or react with the stored NH_3 over SCR catalysts. The source of the N_2O is discussed later.

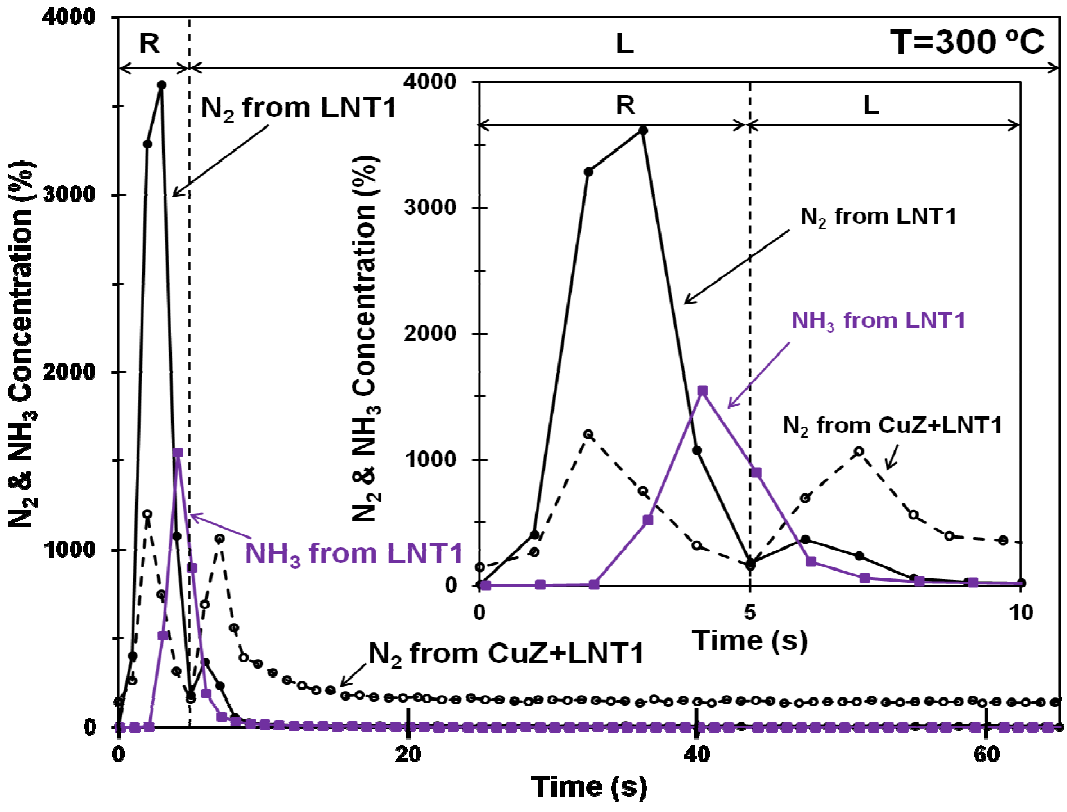

Figure 5-4 Comparison of N_2 and NH_3 Effluent from LNT1 & CuZ-LNT1.

Figure 5-4 compares the transient N_2 and NH_3 concentrations formed by the LNT1 and dual-layer CuZ/LNT1 catalysts under the same operating conditions. It illustrates the advantages of the dual-layer catalyst concept. The behavior of the LNT1 catalyst at 300 ^oC was similar to that at lower temperature (e.g., 250 ^oC, Figure 5-1). At 300 ^oC a NH_3 peak of 1550 ppm was immediately followed a large N_2 peak of 3600 ppm. A second smaller N_2 peak of 370 ppm appeared at the beginning of the lean phase. The most notable impact of coating the LNT1 catalyst with a layer of Cu/ZSM5 was the elimination of the NH_3 slip. In addition, the N_2 emission was more uniformly distributed over the rich and lean phases of the cycle. For example, during the rich phase, the N_2 peak was 1200 ppm using the CuZ/LNT1 catalyst, compared to 3600 ppm using the LNT1 catalyst. At the beginning of the lean phase, the CuZ/LNT1 catalyst has a N_2 peak of 1100 ppm, appearing of comparable magnitude to that during the rich stage. It was followed by a much lower, continuous N_2 formation during the remainder of the lean phase. In comparison, the LNT1 catalyst generated a much smaller N_2 peak (350 ppm) during the lean feed. The SCR top-layer clearly modified the temporal effluent concentrations. The top SCR layer captured NH_3 generated during the rich phase by the LNT layer. Since the rich gas did not not contain NO or O_2, no N_2 could be produced from the SCR catalyst. The stored NH_3 reacted with NO and O_2 fed during the subsequent lean phase. The N_2 peak at the beginning of the lean feed was an indication of NH_3 oxidation. NH_3 generated by the LNT1 catalyst during the rich step was trapped on the CuZ catalyst and then reacted with NO and O_2 during the lean phase. The maximum concentration of N_2 that could be produced at steady-state by the standard SCR reaction

(1) was 500 ppm, as the stoichiometry constraint being $NO/NH_3 = 1$. Thus, the NH_3 oxidation accounted for the additional N_2 in the lean N_2 peak, which was larger than 1000 ppm. During the remainder of the lean phase, the continuous N_2 production was an evidence of the SCR reactions (1-3). The sustained evolution of N_2 from the dual-layer catalyst at a rather low concentration (150-160 ppm) was likely a result of slow ammonia desorption and diffusion from the zeolite layer.

The NH_3 formation and consumption in the dual-layer catalysts clearly differ from those in the LNT catalyst. NH_3 is an important intermediate during the regeneration of stored NO_x in LNT catalysts, as reported by Mulla et al. [37], Lietti et al. [38, 39] and Clayton et al. [45]. Its conversion to N_2 occurs by reaction with the downstream stored NO_x. The reaction rate depends on several factors, including the temperature, and the presence of H_2, among other factors. In contract, NH_3 generated in the LNT layer of the dual-layer catalyst diffuses into the adjacent zeolite layer where it can be adsorbed on the Cu and Brønsted acid sites. SCR reactions between the NH_3 and $NO/NO_2/O_2$ produce N_2 as the main product and N_2O as a byproduct. During the rich phase, the NH_3 adsorption leads to its disappearance as well as to a decrease of the N_2 peak. During the lean phase, the stored NH_3 is consumed by the SCR and NH_3 oxidation reactions. Undesired NH_3 oxidation increases the N_2 peak during the lean feed. This observation agrees with results reported by Nakatsuji et al. [72].

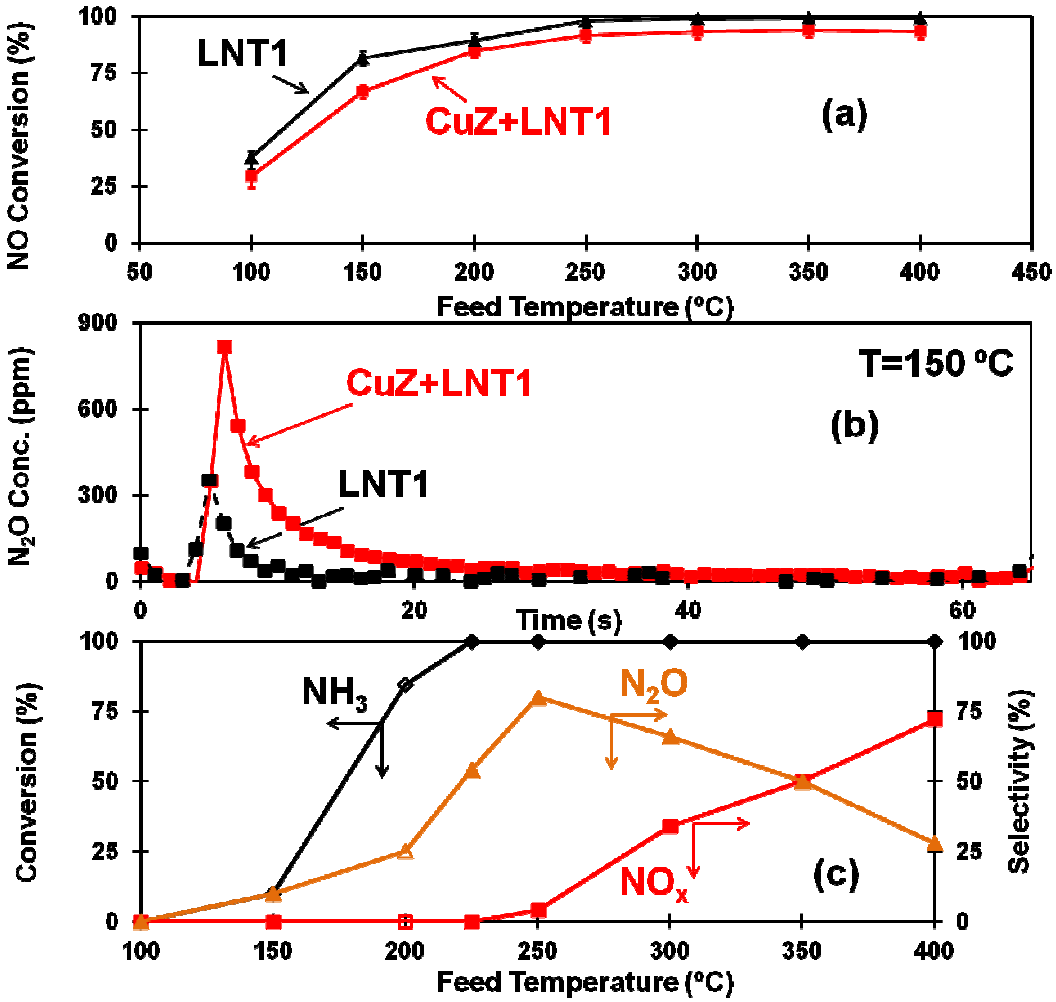

Figure 5-5 (a) Comparison of NO conversion between LNT1 and dual-layer catalyst; (b) Comparison of N_2O effluent from LNT and dual-layer catalyst; (c) NH_3 oxidation to NO_x on LNT1 (the empty symbol denotes the result from unsteady state experiment).

The NO_x conversion achieved by the dual-layer catalyst can be lower than that achieved by the LNT catalyst alone, as shown in Figure 5-5 (a). This is an unexpected finding and does not agree with previously published results using other LNT/SCR configurations [62-69]. This counterintuitive trend results from an interaction between the two layers, and the reasons for the lower conversion are different for the low and high temperatures.

Figure 5-3 (a) shows that at temperatures below 250 °C the Cu/ZSM5 steady-state activity for standard SCR reaction is rather low. However, the zeolite still can store NH_3 produced in the LNT layer. In addition to the desired conventional SCR reactions occurring on the SCR catalyst, which generate N_2, the stored NH_3 may be consumed by the following competing reactions (R2-R6):

$2NH_3 + 2NO_2 \rightarrow N_2 + NH_4NO_3 + H_2O$, (R2)

$NH_4NO_3 \rightarrow N_2O + 2\ H_2O$, (R3)

$NH_3 + Pt \rightarrow NH_3\text{-}Pt$, (R4)

$O_2 + 2Pt \rightarrow 2\ O\text{-}Pt$, and (R5)

$NH_3\text{-}Pt + 2\ O\text{-}Pt \rightarrow 0.5\ N_2O + 1.5\ H_2O + 3\ Pt$. (R6)

Figure 5-5 (b) compares the N_2O effluent concentration for both the LNT1 and dual-layer CuZ/LNT1 catalysts at 150 °C. The dual-layer catalyst generates more N_2O than the LNT catalyst during the lean phase. The N_2O may be formed by either one or both of two possible pathways. Reactions R2 and R3 comprise the formation and decomposition of NH_4NO_3. However, this pathway is not likely to occur to an appreciable extent because (i) it requires formation of NO_2, and NO oxidation is rather slow at 150 ºC on these catalysts [109], and (ii) NH_4NO_3 decomposition is slow below 250 ºC [112]. The second more viable route represented by steps R4 – R6 involves the adsorption and oxidation of NH_3 on the Pt crystallites of the LNT catalyst. The formation of N_2O during Pt-catalyzed NH_3 oxidation is well established [114, 115]. Figure 5-5 (c) reports the NH_3 conversion and NO_x ($NO + NO_2$) and N_2O selectivities during NH_3 oxidation over the same LNT1 catalyst. The NH_3 conversion is over 80% at 200 °C and

the N_2O selectivity is about 25%. The NH_3 conversion and the N_2O selectivity increase to 100% and 75%, respectively, by 250 °C. Figure 5-6 reports the measured reaction rates for NH_3 oxidation over the three LNT catalysts at 150 ºC. The positive dependence of the reaction rate on NH_3 concentration suggests that NH_3 trapped in the SCR layer diffuses to the underlying LNT layer where it is readily oxidized. This promotes NH_3 oxidation to N_2O at low temperatures.

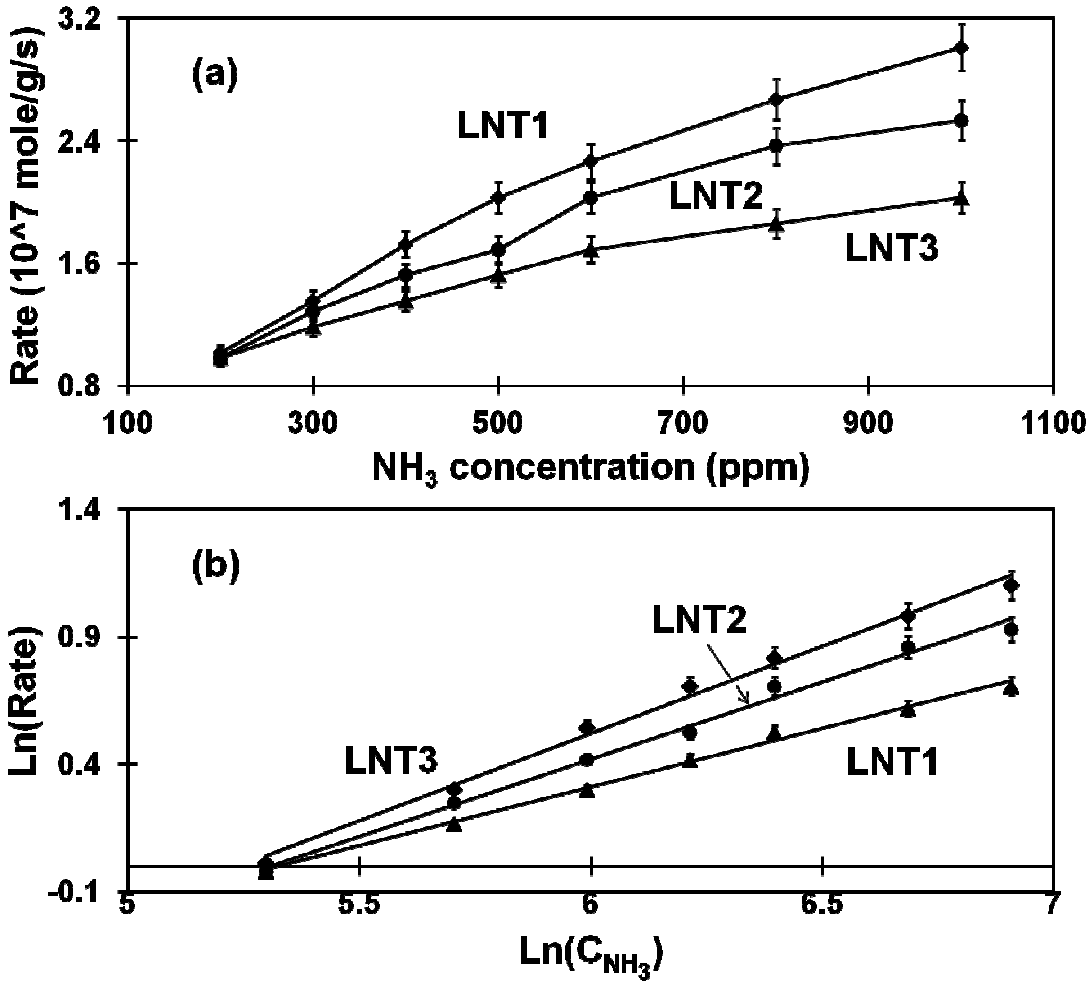

Figure 5-6 (a) The apparent reaction order of NH_3 oxidation over three LNT catalysts. The feed contains 500 ppm NH_3 and 5% O_2 at 150 °C. Part (b) is the logarithm plot of part (a). For LNT1, y = 0.460x - 2.449, R^2=0.9957; For LNT2, y=0.607x-3.2178, R^2 = 0.9922; For LNT3, y = 0.684x - 3.5823, R^2 = 0.9935.

At temperatures exceeding 250 °C, NO conversion by the dual-layer catalyst is still slightly lower than that by the LNT catalyst. At these temperatures, complete NH_3 conversion is obtained with increasing NO_x selectivity (Figure 5-5 (c)). The increase in the NO_x selectivity with temperature is a result of the consumption of NH_3. The NH_3 that is trapped likely intensifies the NH_3 oxidation to NO_x on the Pt, resulting in a lower NO conversion.

In order to assess the importance of segregating the NSR and SCR functions (as separate layers), experiments were conducted in which a mixture of LNT and SCR catalysts was deposited on the monolith and its performance tested. The LNT catalyst powder was obtained by scraping the washcoat off an LNT1 monolith. Figure 5-7 (a) describes the NO conversion and product selectivity at various temperatures. Surprisingly, the NO conversion for the mixed washcoat catalyst was lower than that of both the LNT and dual-layer catalyst. The selectivities of N_2 and N_2O decreased with increasing temperature, while the NO_2 and NH_3 selectivities increased significantly. Figure 5-7 (b) shows the effluent N_2, NO_2 and NH_3 during a rich-lean cycle at 300 ºC. A large amount of N_2 and NO_2 was produced during the lean phase and NH_3 release while some N_2 formed during the rich phase. The poor performance of the mixed washcoat catalyst is attributed to NH_3 oxidation by O_2. The results cannot be explained by the formation of ammonia nitrate (or nitrite) at low temperatures. If these reactions occurred, much more N_2O than NO_2 would have been observed; see reaction R2 above. That NO_2 is the main product for T > 250 °C is a strong evidence for both NH_3 and NO oxidation. The working concept of the segregated dual layer catalyst is that NH_3 stored in the SCR layer reacts

with NO_x that diffuses from the underlying LNT layer or from the bulk gas during the subsequent storage step. Thus, unreacted NO_x is able to react with NH_3 in the presence of excess O_2; i.e., standard SCR reaction. In contrast, on the mixed washcoat catalyst NH_3 that is produced during the rich feed reacts less selectively with O_2 on the highly active PGM sites during the storage step. Apparently, the mixed washcoat catalyst does not effectively utilize NH_3 for stored NO_x regeneration and N_2 formation. While NO_x reduction to N_2, N_2O, and NH_3 occurs during the rich phase, the NH_3 is consumed by O_2 before it can be trapped and react with NO and O_2. The poor utilization of NH_3 decreases the overall NO_x conversion. This oxidation rate increases at high temperatures for both reactions, although the reverse reaction of NO oxidation becomes important above 350 ^oC. This explanation agrees with the observation that NO_2 selectivity increases at high feed temperatures. Other researchers [70] reported that LNT-SCR mixture powder catalyst had a better deNO_x performance than LNT catalyst alone. The cause for the disagreement with the previous studies remains unknown. In conclusion, the mixed catalyst was not studied any further due to its inferior performance to that of the dual-layer catalyst.

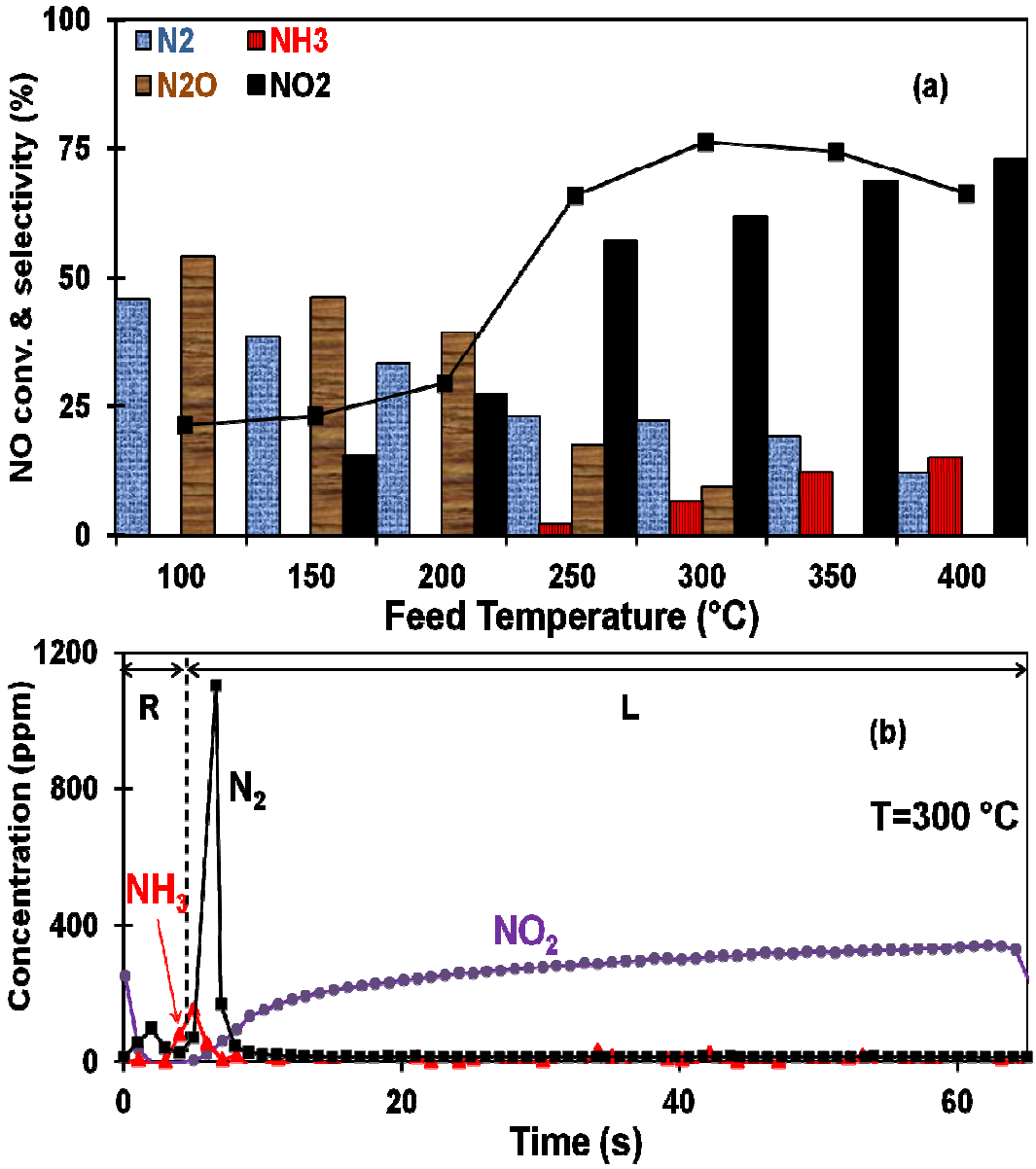

Figure 5-7 (a) Performance of LNT1-CuZ mixed washcoat catalyst; (b) average N_2, NH_3 and NO_2 effluents during a lean-rich cycle at 300 °C.

5.3.2 Impact of H_2O and CO_2

A gas mixture containing 2.5 % H_2O and/or 2.0 % CO_2 was used to evaluate the catalyst performance in the presence of these combustion products. Figures 5-8 (a-c)

show the NO conversion and product selectivity for temperatures from 200 to 400 ºC of LNT1 using a feed to which contains either H_2O or both CO_2 and H_2O, and Cu-zeolite coated LNT1 using a feed containing both H_2O and CO_2. Experiments with feed temperatures below 200 ºC were not conducted to avoid complications by water adsorption and condensation.

Figure 5-8 (a) describes the dependence of NO_x conversion and product selectivity on the temperature for a feed containing 2.5% H_2O. The NO_x conversion increased with temperature up to 350 ºC and then very slightly decreased at 400 ºC. The N_2 selectivity increased with temperature, while NH_3, N_2O and NO_2 selectivity decreased. Compared to Figure 5-2 (a), the NO conversion decreased by only 2-3% upon the H_2O addition. The NH_3 and N_2O selectivity increased by 2-8% at the expense of a 2-10% decrease in the N_2 selectivity. Hence, H_2O addition had a small but adverse influence on NO_x conversion, and changed the product selectivity to some extent.

The dependence of NO_x conversion and product selectivity on the feed temperature for a feed containing of 2.5 % H_2O and 2.0 % CO_2 is shown in Figure 5-8 (b). Adding CO_2 led to a much larger decrease in the NO conversion than H_2O alone, especially at low temperatures; e.g., 45 % decrease at 200 ºC compared to the case without CO_2. The N_2 selectivity increased with the increasing temperature while the NH_3 and NO_2 decreased. N_2O appeared only at 200 ºC.

The formation of $BaCO_3$ in the presence of CO_2 degrades the performance of the LNT catalyst. Some NO_x storage sites are occupied by CO_2 and thus higher NO and NO_2 slippage occurs during the lean feed. The NO_2/NO ratio during a lean-rich cycle at 250 º

C is shown in Figure 5-9 (a). The formed $BaCO_3$ has a higher thermal stability than that of barium nitrates [36, 39, 44] and this higher stability adversely affects the product selectivity. As reported by Lindholm et al. [40], $BaCO_3$ inhibits the N_2 formation through reactions between nitrates and NH_3. This results in a lower N_2 selectivity and a higher NH_3 selectivity. Another reason for the higher NH_3 selectivity is the accumulation of $BaCO_3$ around the PGM crystallites. Under this condition, the in-situ H_2: NO_x ratio is higher which favors NH_3 formation. The deeper regeneration also avoids the N_2O formation.

The dual-layer catalyst performance for a feed containing CO_2 and H_2O is better than that for the LNT alone, as shown in Figure 5-8 (c). The NO conversion and N_2 selectivity increased with temperature up to 350 ºC and then decreased slightly at 400 ºC. The N_2O selectivity decreased with temperature. A minute NH_3 release was observed above 350 ºC. Figure 5-9 (b) and (c) compare the NO_x conversion and N_2 selectivity of the CuZ-LNT1 dual-layer catalyst and the LNT1 catalyst. Considering the large amount of NO_2 generated (Figure 5-9 (a)), the NO_x (rather than NO) conversion is reported here. The dual-layer catalyst had a higher NO_x conversion below 300 ºC, and it was essentially equivalent to that of the LNT1 catalyst above 300 ºC. The dual-layer catalyst had a higher N_2 selectivity than LNT1 catalyst over the entire temperature range.

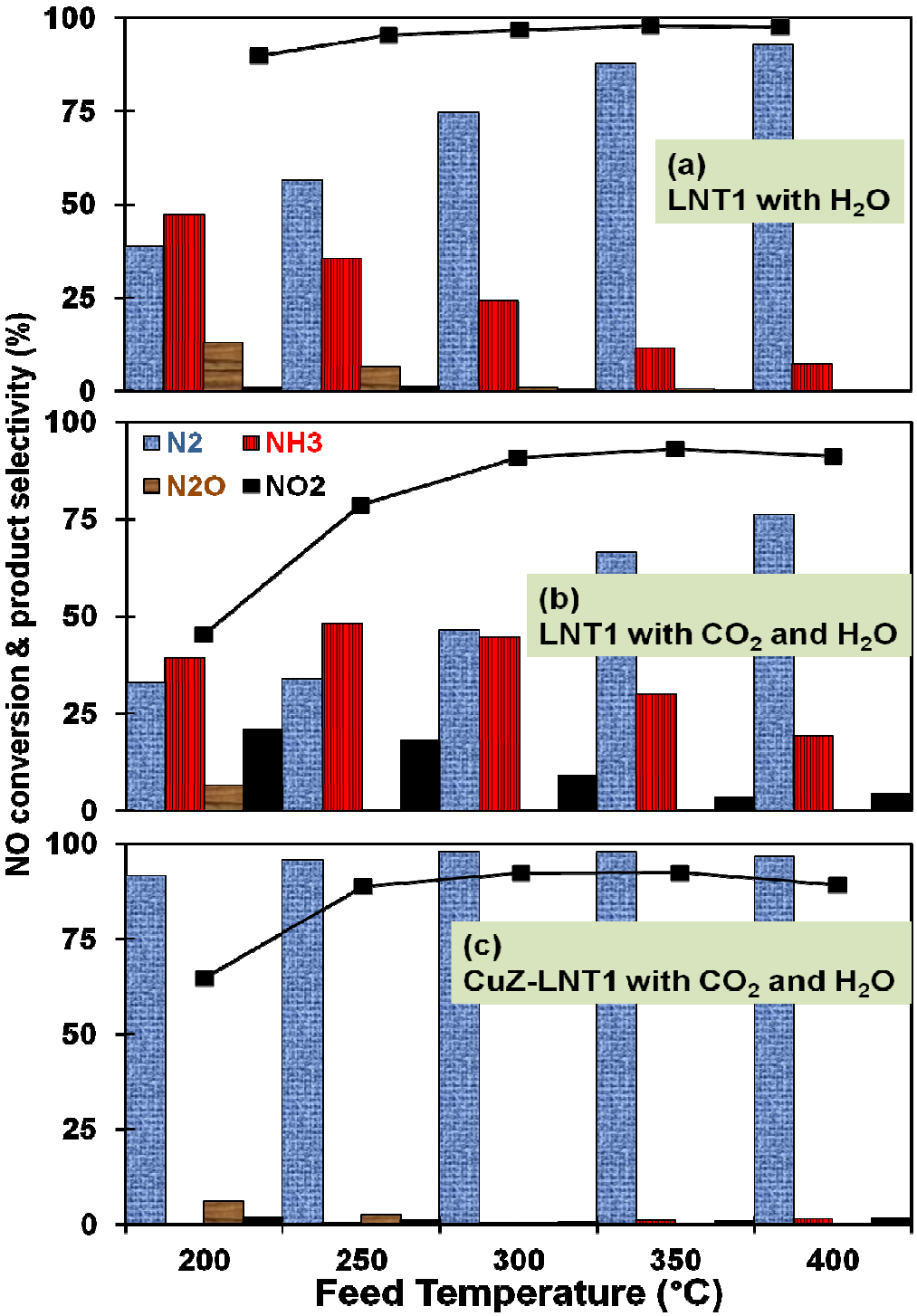

Figure 5-8 (a) Performance of LNT1 catalyst with 2.5% H_2O in the feed; (b) Performance of LNT1 catalyst with 2.5% H_2O and 2.0% CO_2 in the feed; (c) Performance of CuZ-LNT1 catalyst with 2.5% H_2O and 2.0% CO_2 in the feed. Feed temperature was higher than 200 ºC to avoid the water condensation.

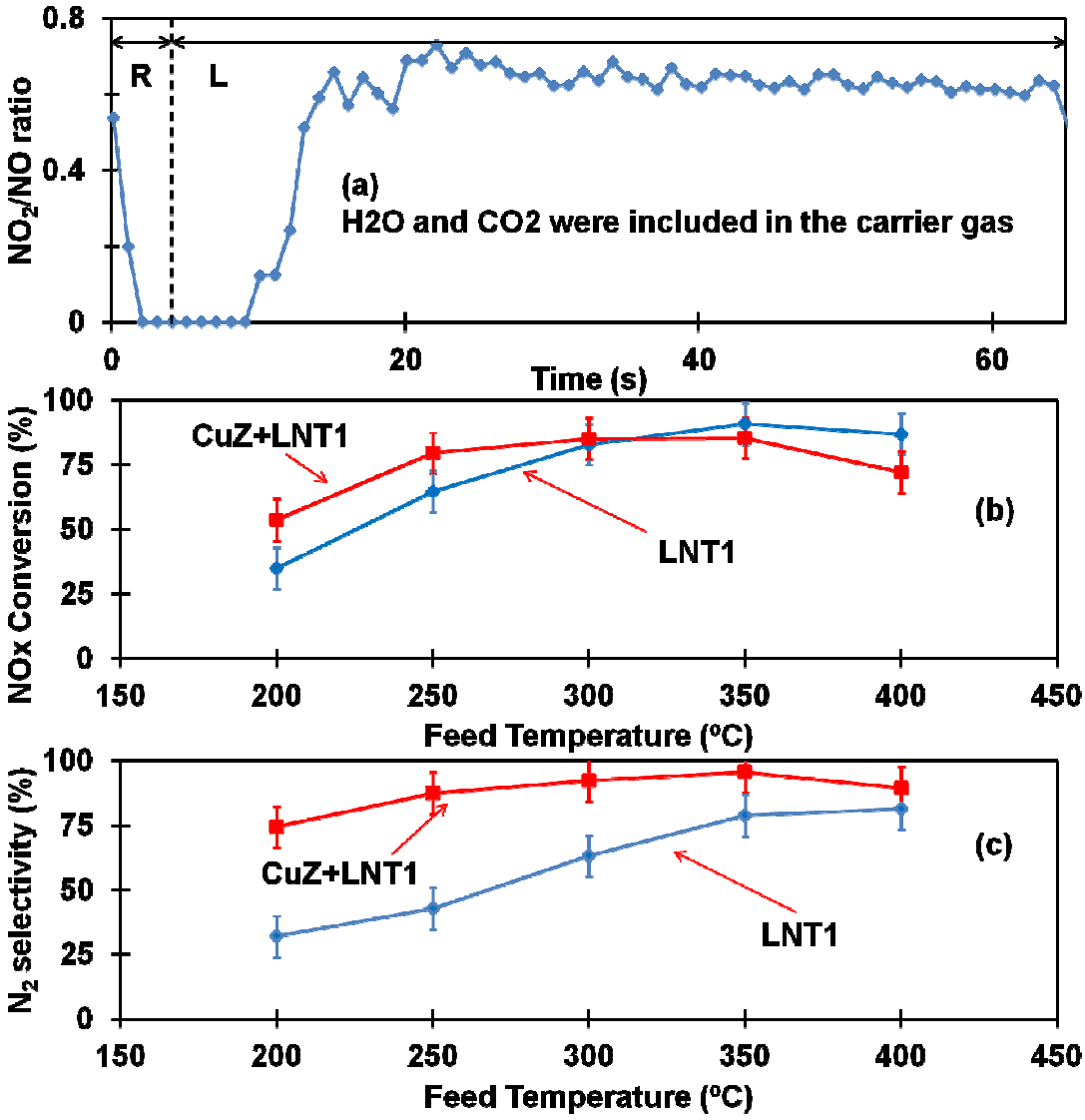

Figure 5-9 (a) Average NO_2/NO ratio during a lean-rich cycle over LNT1 catalyst at 250 ºC; (b) Comparison of NO_x conversion of LNT1 and CuZ-LNT1 catalysts; (c) Comparison of N_2 selectivity of LNT1 and CuZ-LNT1 catalysts.

Different NO_x reduction mechanisms account for the differences between the LNT and dual-layer catalysts. On the LNT catalyst, gaseous NO_x needs to be stored as nitrates and/or nitrites before reduction. In contrast, for the dual-layer catalyst, the gaseous NO_x can be reduced by trapped NH_3 in the SCR layer in addition to being stored

on the LNT layer. Hence, the dependence on the NO_x storage activity of the LNT is weaker. In the presence of CO_2 and H_2O, the LNT1 layer serves as an NH_3 generator during the rich feed (Figure 5-8 (b)) and an NO_2 producer during the lean feed (Figure 5-9 (a)). The SCR catalyst captures the NH_3 produced during the rich feed and uses it to carry out the SCR reactions during the lean feed at a NO_2/NO ratio of 0.6~0.8, which is in the range for fast SCR reaction [9-14]. Complete utilization of NO_2 and NH_3 leads to a higher N_2 selectivity from 200 ºC to 400 ºC and a higher NO_x conversion than that of an LNT catalyst below 300 ºC. However, the rate of NH_3 oxidation by O_2 to NO_x is intensified above 300 ºC and thus the dual-layer catalyst has about the same NO_x conversion as the LNT catalyst at high temperatures.

5.3.3 Impact of Ceria on LNT and LNT/SCR Catalysts

Two LNT catalysts with different ceria loadings of 17 wt % (LNT2) and 34 wt % (LNT3), were prepared. The temperature dependence of the NO conversion and product selectivity of the LNT2 and LNT3 and the Cu-zeolite coated LNT2 and LNT3 catalysts are shown in Figures 5-10 (a-d).

The performance of both the ceria-containing LNT2 and LNT3 catalysts is similar to that of the barium-only LNT1 catalyst over the temperature range, for which N_2, N_2O, NH_3, NO_2 are obtained. According to Figure 5-10 (a) and (c), the cycle-averaged NO conversion and N_2 selectivity increased as the temperature increased, while the N_2O selectivity decreased. The maximum cycle-averaged NH_3 selectivity of about 75 % was achieved at 150 °C. At the same temperature, the NO conversion of the ceria-containing

LNT catalysts was higher than the ceria-free LNT1 sample. The primary product was NH_3 below 250 °C and N_2 above 250 °C.

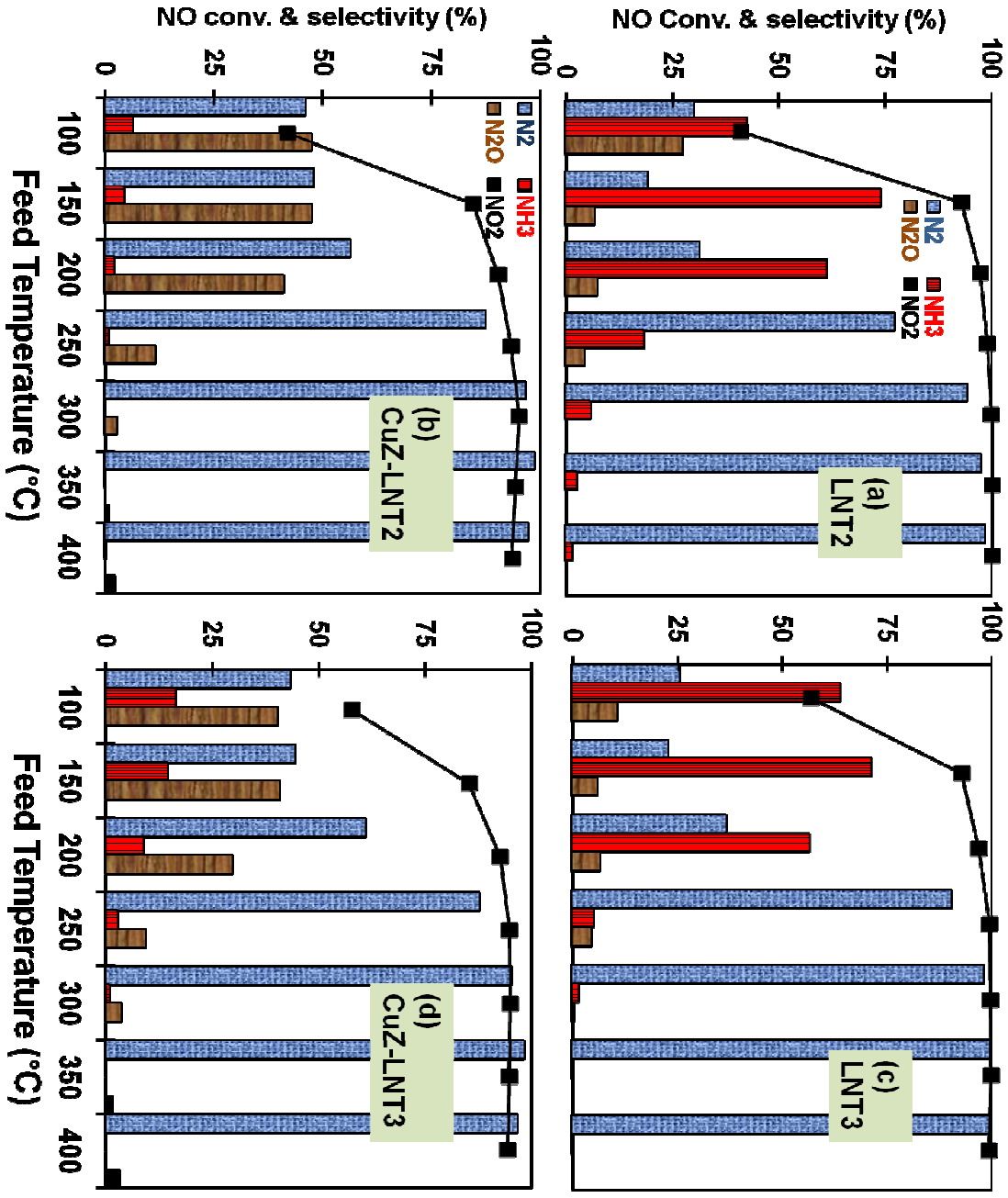

Figure 5-10 Performance of (a) LNT2 catalyst; (b) CuZ-LNT2 dual layer catalyst; (c) LNT3 catalyst; (d) CuZ-LNT3 dual layer catalyst.

The addition of ceria affects some subtle features of the NO conversion and product distribution. First, the cycle-averaged NO conversion and NH_3 yield (product of NO conversion and NH_3 selectivity) are higher below 250 °C. This is due to an increase in the NO_x storage capacity as the ceria provides new storage sites in addition to those already existing on the BaO. This is proven in Figure 5-11 (a), which compares the NO_x storage of the LNT1, LNT2, and LNT3 catalysts. This increase in NO_x storage increases the amount of NO_x available for reduction and increases the NO conversion and the NH_3 yield. Since ceria-based nitrates have lower stability than barium-based nitrates, an easier reduction can be achieved at low temperatures [31]. A second feature is an increase in the N_2 selectivity and decrease in the NH_3 yield above 250 °C. At these high temperatures, ceria increases the NH_3 oxidation rate due to its oxygen storage capacity and oxidation activity [110]. Moreover, NH_3 oxidation has a high selectivity towards N_2 [36].

The increased NO conversion at low temperatures by ceria addition provides a way to reduce the requisite PGM loading. As shown in Figures 5-2 (a), 5-10 (a) and 5-10 (c), the NO conversion obtained at low-temperatures is much lower than the conversion obtained at high temperatures. Thus, the low temperature performance dictates the amount of PGM needed to achieve a prescribed level of NO_x conversion. That is, the largest amount of PGM necessary to achieve a desired NO_x conversion over the anticipated range of typical operating temperatures, i.e., 150 to 400 ºC, is dictated by the lowest temperature. The surplus PGM over that needed at the high temperatures is needed to achieve the same specified conversion at the lowest temperature. Ceria significantly increases the low-temperature NO_x conversion. Thus, the PGM loading in a ceria-

containing LNT can be reduced without comprising NO_x conversion at low temperatures. This decreases the excess PGM at high temperatures.

A Cu/ZSM5 layer was coated on the top of the ceria-containing LNT2 and LNT3 catalysts. Figures 5-10 (b) and 5-10 (d) show the NO conversion and product selectivity for the dual-layer CuZ/LNT2 and CuZ/LNT3 catalysts, respectively. NO conversion increased with temperature up to 300 ºC and then slightly decreased. N_2 selectivity increased with temperature, while N_2O selectivity and NH_3 slip decreased with temperature. Some NO_2 was observed above 350 ºC. The trends of NO conversion and product selectivity are comparable to those of the Cu-zeolite coated LNT1 shown in Figure 5-2 (b). The NO conversions from the three dual-layer catalysts are summarized in Figure 5-11 (b). Clearly, the ceria containing dual-layer catalysts lead to higher NO conversion, especially at low temperatures due to the increased NO_x storage and the lower stored nitrate stability.

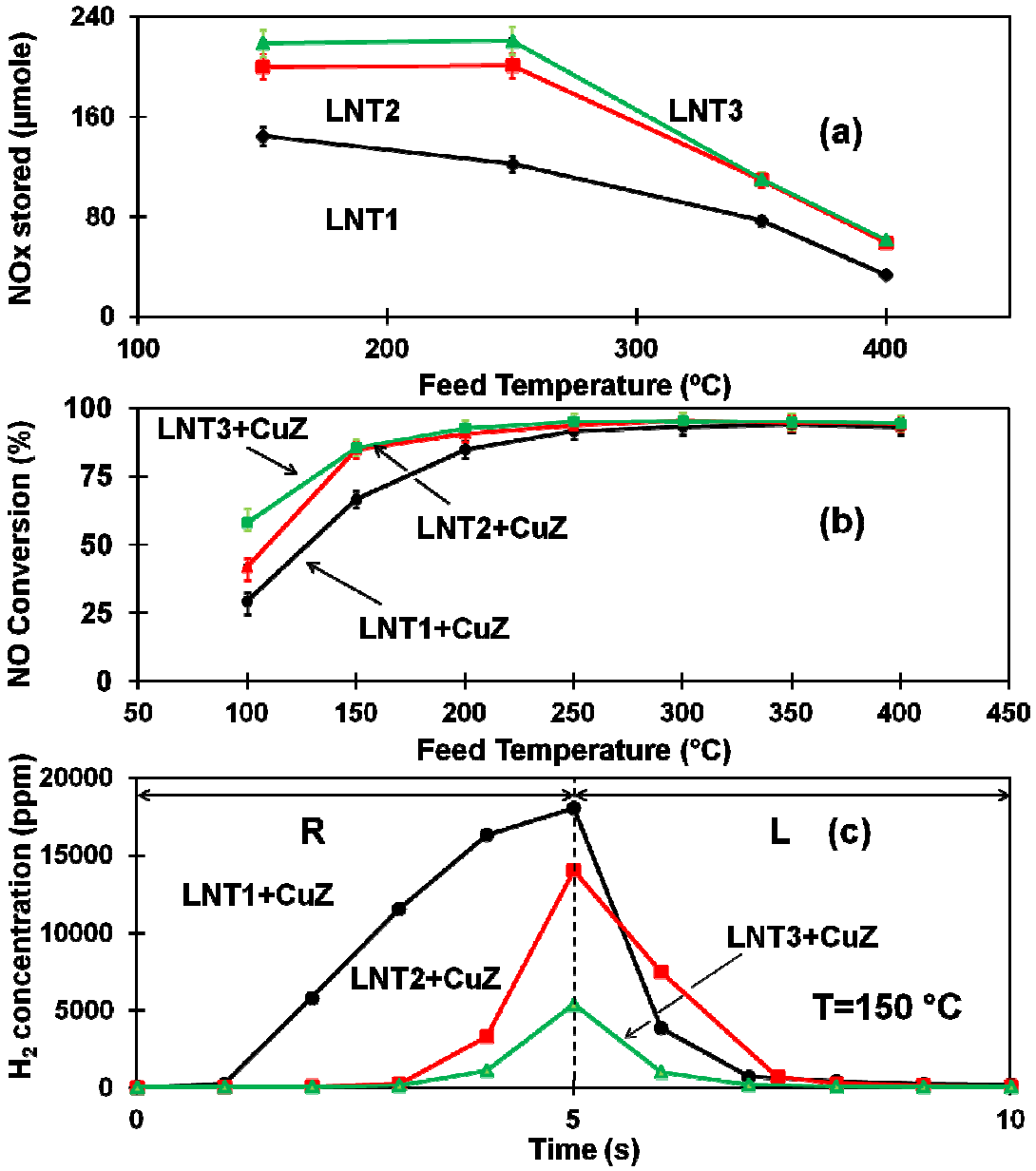

Figure 5-11 (a) NO_x storage capacity of LNT1, LNT2 and LNT3; (b) NO conversions of three dual layer catalysts; (c) the average H_2 effluents in CuZ coated LNT1, LNT2 and LNT3 catalysts at 150 °C during a lean-rich cycle.

The addition of ceria impacts among others the N_2 selectivity and NH_3 slip which exceed the values obtained by the barium-only dual-layer catalyst at low temperatures.

The regeneration of stored NO_x in the presence of ceria increases the N_2 selectivity and decreases the N_2O selectivity. The enhanced NH_3 formation by the ceria-containing dual-layer catalysts is the opposite of that when using a series of monolith bricks [60]. That is, for high loading of OSC (oxygen storage component) NH_3 oxidation is enhanced and thus the NH_3 yield decreases. However, the situation at low temperature is due to the enhancement by ceria of the low-temperature reduction of stored NO_x. As shown in Figure 5-11 (c), the hydrogen conversion increases with the ceria loading in dual-layer catalysts. At 150 ^oC, CuZ-LNT1 leads to an 8% hydrogen conversion, CuZ-LNT2 to 23% and CuZ-LNT3 to 49%. The addition of ceria to LNT catalysts increases the H_2 conversion due to two effects. First, the ceria increases the NO_x and oxygen storage on the catalyst. The barium-only LNT1 has a lower capacity for NO_x and oxygen storage than LNT2 and LNT3. Second, the low-temperature PGM activity is enhanced by the ceria addition [110]. That is, ceria-containing LNT catalysts have a higher, low-temperature regeneration activity than the barium-only catalyst. Better utilization of the feed H_2 generates more NH_3 during the regeneration and more storage sites after the regeneration. In addition, the generated NH_3 is captured by the SCR layer instead of being consumed by the ceria in the LNT layer downstream. The Cu zeolite top layer does not have the capacity to store all the large amount of NH_3 produced. On the other hand, the addition of ceria increases the rate of NH_3 oxidation. As shown by Figure 5-6, the apparent reaction order of NH_3 oxidation increases from 0.46 to 0.68 with an increase of ceria loading in the LNT catalyst. The intensified oxidation consumes more trapped NH_3 in the dual-layer catalysts. Thus, less NH_3 is available for the SCR reactions. Figure 5-12

shows the N_2 effluents from the three dual-layer catalysts at 300 °C. The amount of N_2 formed was similar for the three dual-layer catalysts with 9.6, 10.2 and 10.1 μmole for CuZ-LNT1, CuZ-LNT2 and CuZ-LNT3, respectively. The ceria-containing dual-layer catalysts generated higher N_2 peaks than the one that does not contain ceria during both the lean and rich feeds. The amount of N_2 generated continuously after the first 3-5 s of the switch to the lean feed decreases with the increase of ceria loading. This indicates that ceria addition increases the rate of NH_3 oxidation, which decreases the rate of the desired SCR reactions.

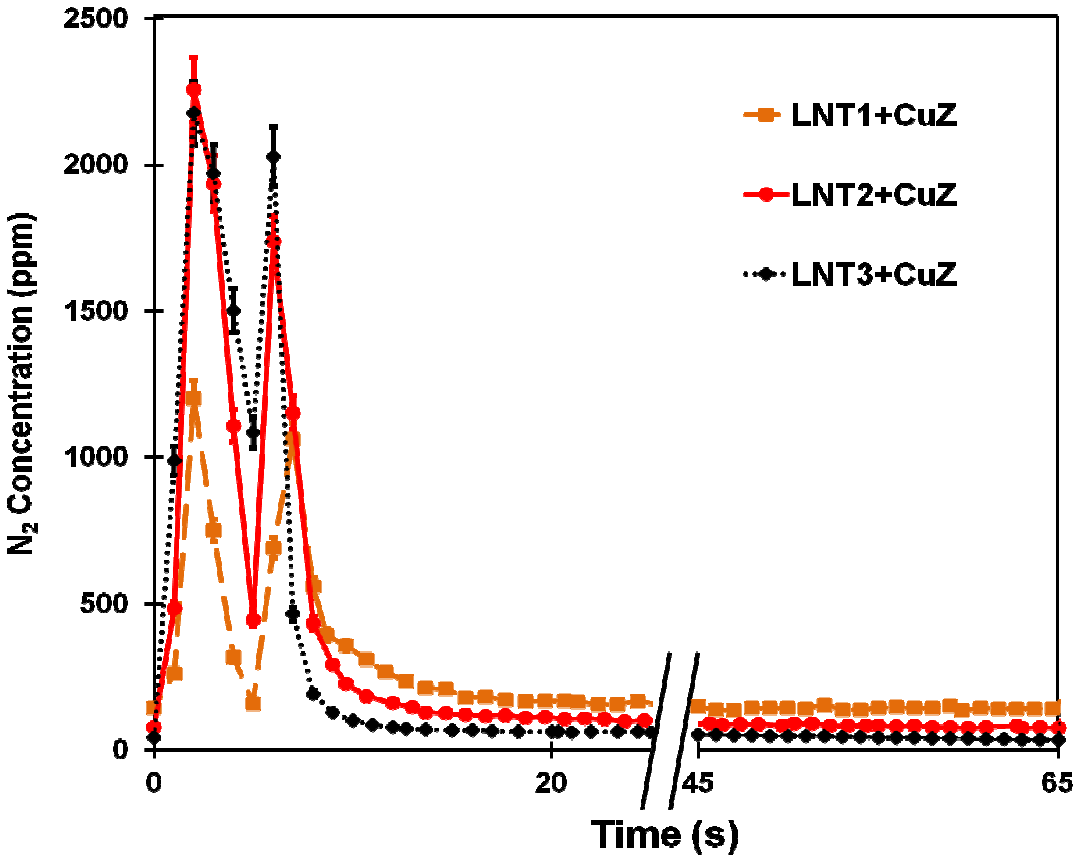

Figure 5-12 Comparison of N_2 effluent from three dual layer catalysts. CuZ/LNT1 is the orange line; CuZ/LNT2 is the red line; CuZ/LNT3 is the black line.

5.3.4 Dual-layer Catalyst Durability

Hydrothermal aging deactivates LNT catalysts due to an increase in the PGM particle size (sintering), resulting in a reduction in the interface between the PGM and barium storage phase [114, 115]. In the absence of ceria, aging of LNT catalysts increases the selective production of ammonia and decreases the overall storage and reduction. On the other hand, the SCR catalyst is deactivated by hydrothermal aging due to dealumination and the decreased oxidation activity of the Cu zeolite [116-118]. This decreases in the ammonia storage capacity and increases the NH_3 slip, assuming the supply of ammonia from the LNT is fixed. The impact of ceria loading on the NH_3 selectivity is undoubtedly affected by the decrease of the ceria surface area and the NO_x storage capacity during the aging [88, 119]. In summary, the effect of aging on the LNT/SCR catalyst performance is complicated by of several competing trends. The decreased NO conversion upon hydrothermal aging of the dual-layer catalysts is due to the deactivation of both the LNT and SCR catalysts.

Hydrothermal aging and SEM-EDS experiments were conducted to understand the durability and quantify the effect of aging on the dual-layer catalyst. Figure 5-13 (a)-(c) describes NO conversion and product selectivity of the three aged dual-layer catalysts for different feed temperatures. For all three LNT catalysts, NO conversion and N_2 selectivity increased with temperature. NH_3 slip from the barium-only LNT1 increased with temperature, while the opposite trend was observed in the ceria-containing LNT2 and LNT3 catalysts. N_2O was mainly produced from 100 to 250 °C for all three catalysts.

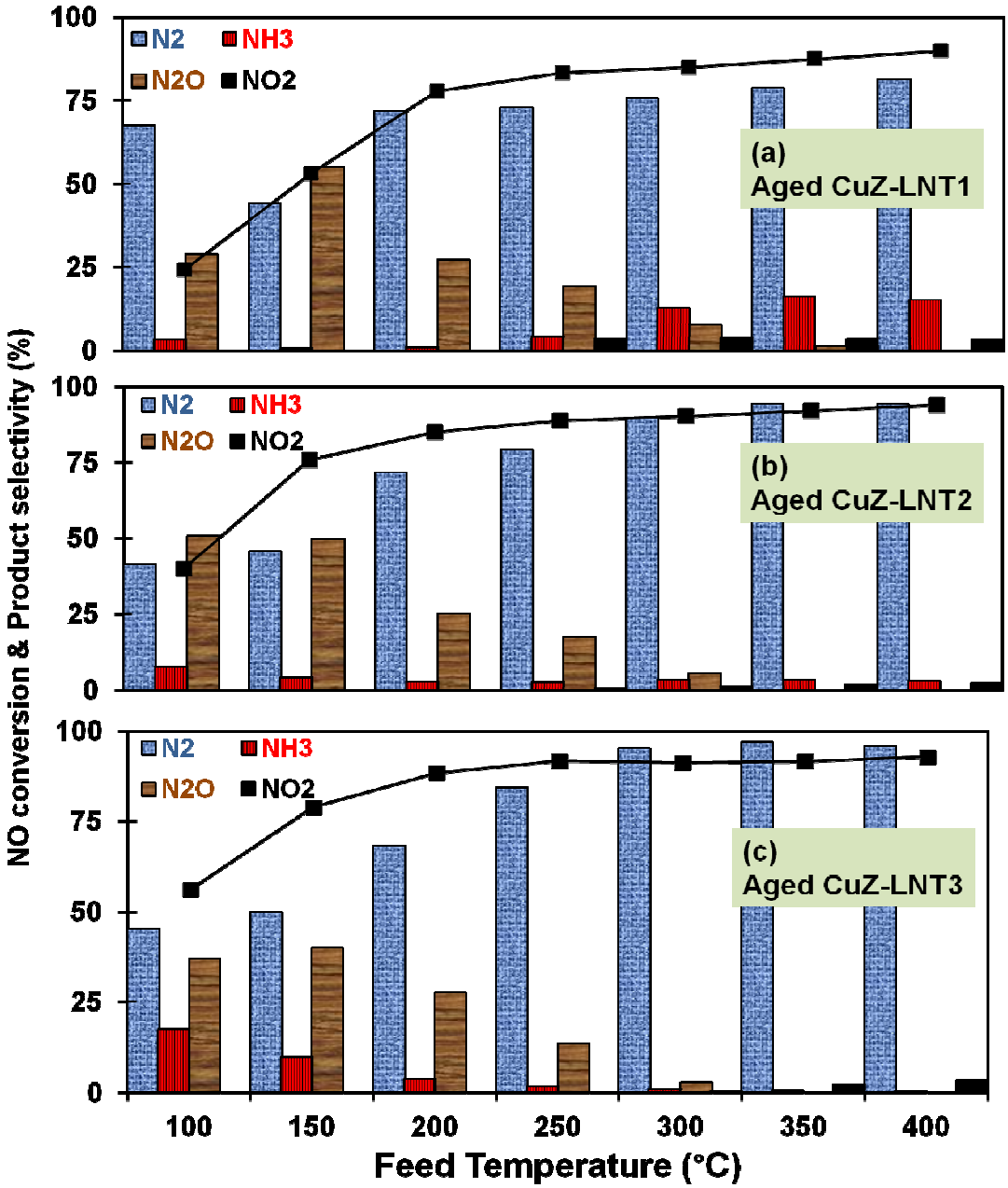

Figure 5-13 Performance of (a) aged CuZ-LNT1 multilayer catalyst; (b) aged CuZ-LNT2 multilayer catalyst; (c) aged CuZ-LNT3 multilayer catalyst.

Figure 5-14 (a) compares the NO conversion of fresh catalysts (solid line) with that of aged ones (dashed lines). The NO conversions of the aged dual-layer catalysts are lower than those of the fresh ones for all feed temperatures. The difference in NO

conversion between the fresh and aged catalysts decreases upon an increase of the ceria loading in the LNT layer. The deactivation is largest for barium-only dual-layer catalyst. The NO conversion decreased by 12.6% at 150 °C for the Cu-zeolite coated LNT1 dual-layer catalyst. These results suggest that the stability of the barium-containing dual-layer catalyst may be enhanced by the addition of ceria.

Figure 5-14 (b) shows that the effect of aging on the ammonia selectivity are rather complex. In the absence of ceria, the ammonia selectivity increases dramatically with aging, especially at high temperatures. The two ceria-containing catalysts response is similar to those of the ceria-free catalyst, but not as dramatic. That is, the ammonia selectivity at high temperature of the aged catalyst is higher than that of a fresh catalyst. For the catalyst with the highest loading of ceria, aging decreases the ammonia selectivity for temperatures below 300 ^{o}C. This could be a result of a decrease in the ceria surface area and a corresponding decrease in the NO_x storage. Additional experiments are needed to elucidate these trends.

The impact of the hydrothermal aging on the profile of the Ce, Ba and Pt elements in the washcoat was studied. Figure 5-15 (a)-(c) shows the normalized Pt concentration profiles versus the dimensionless position. A dimensionless coordinate was used to enable a direct comparison among the three dual-layer catalysts, which have somewhat different washcoat thicknesses. As the thickness of the LNT layer is about 1.5 that of the SCR, we refer to the total washcoat thickness as 2.0 and the interface between the LNT and SCR as 1.2. In Figure 5-15 (a), the Pt concentration in the LNT layer decreased after aging. The PGM migration may lower NO conversion due to intensified NH_3 oxidation

and the separation between PGM and barium. On the other hand, in the ceria-added catalysts the change in Pt concentrations before and after hydrothermal ageing were much less pronounced (Figures 5-15 (b) and (c)). The barium profiles before and after aging were similar to those of the Pt. In the absence of ceria, the barium concentration in LNT and SCR layers became more uniform after aging. That indicates that some barium migrated from the LNT layer to the SCR layer. Ceria mitigated barium migration from the LNT to the SCR in the dual-layer catalyst. The experiments reveal that the ceria addition improves the structural stability of the dual-layer catalysts.

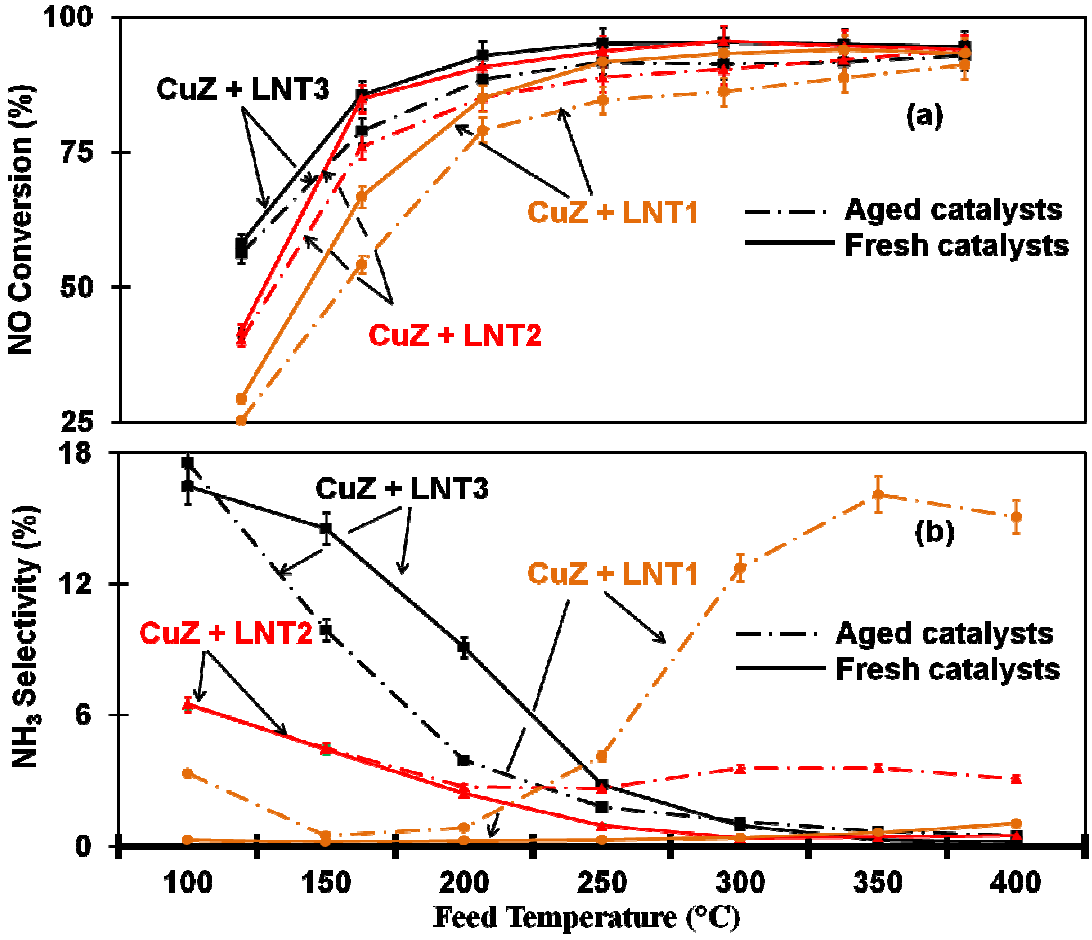

Figure 5-14 (a) Comparison of NO conversion of aged and fresh multilayer catalysts; (b) Comparison of NH_3 selectivity of aged and fresh multilayer catalysts.

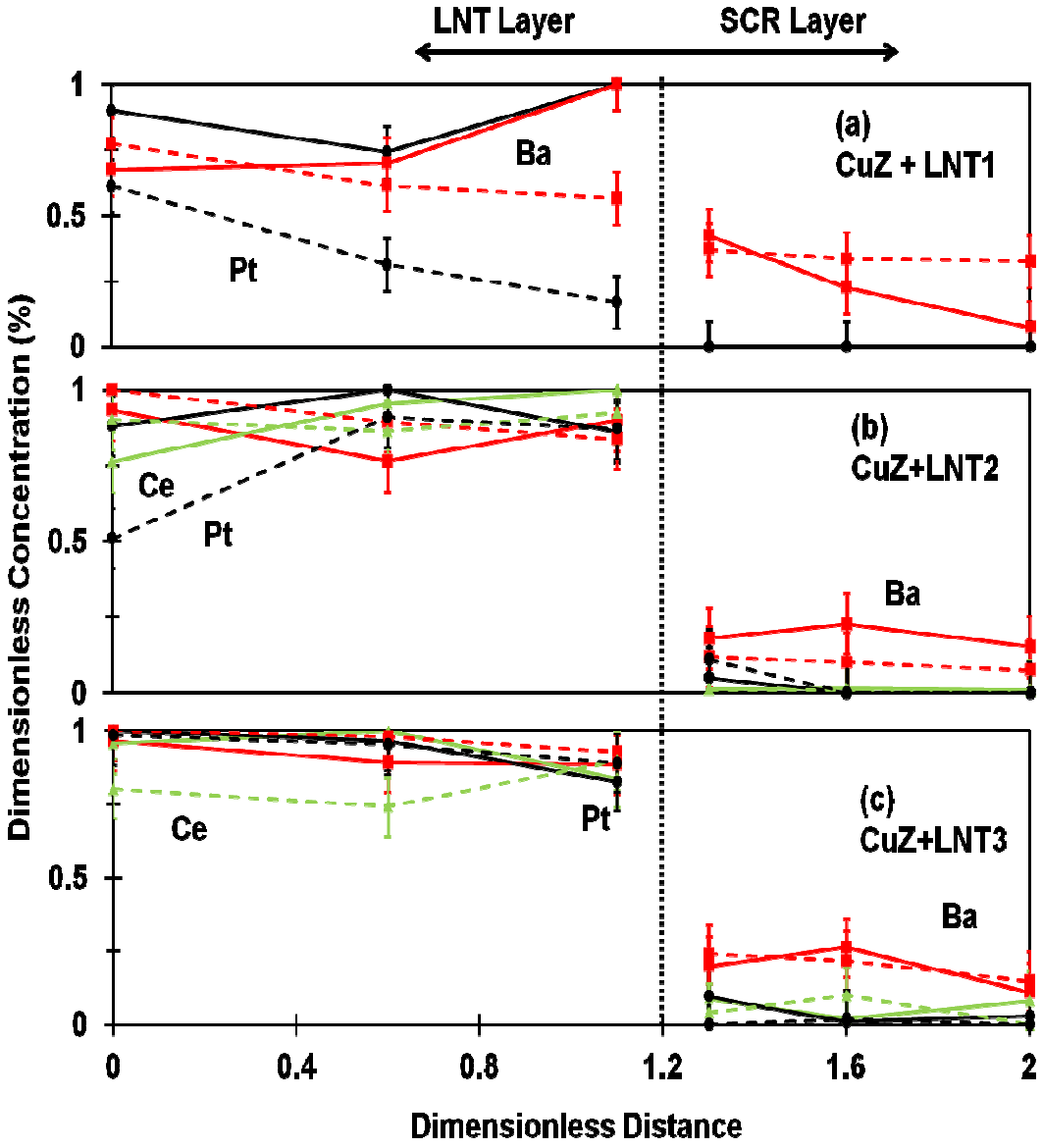

Figure 5-15 Spatial dependence of Pt concentration in the washcoats. Concentrations are normalized by the maximum value of each sample. Solid lines are of fresh catalysts; dashed lines are of aged catalysts. A dimensionless distance 1.0 = 60~67 μm. According to our last discussion, only metal concentration in LNT layer is shown in this figure and the dimensionless distance 1.2 is the interface.

5.4 Conclusions

The behavior of SCR-top LNT dual-layer catalysts was studied during lean-rich cycles in a temperature range from 100 ºC to 400 ºC. The main behavioral features of dual layers catalysts for combined NSR and SCR are:

- Dual-layer catalyst capture NH_3 generated from LNT layer and use it for SCR reactions. As a result, the N_2 selectivity can be increased.
- NH_3 oxidation to NO_x lowers the NO conversion of dual-layer catalyst. This is especially problematic at high temperatures.
- In the presence of CO_2 and H_2O, dual-layer catalyst utilizes well the formed NO_2 and NH_3 for SCR reactions. Hence, the dual-layer catalyst has a higher NO_x conversion from 200 to 300 ºC and a higher N_2 selectivity than LNT catalyst during the whole temperature range.
- The addition of ceria leads to a high NO_x storage capacity and more efficient regeneration at low temperatures. The PGM loading in the ceria containing LNT catalyst can be lower than in the barium-only one. The NH_3 formation at low temperatures increases with a ceria loading increase. However, ceria enhances the NH_3 oxidation at high temperatures.
- The ceria-contained dual-layer catalysts have a higher resistance towards hydrothermal aging than the barium-only one. PGM and barium migration is mitigated by the presence of ceria.

These findings show that the dual-layer catalyst can reduce NO_x emission below 300 ºC, especially in the presence of CO_2 and H_2O. Ceria loading is an important catalyst

design option for the low-temperature performance and catalyst durability. The NH_3 formation is enhanced by ceria at low temperatures. The NO_x reduction depends more on the SCR catalyst than that of the ceria-free dual-layer catalyst. As a result, the PGM loading can be reduced.

Chapter 6 Lean NO_X Reduction on LNT/SCR Dual-Layer Catalyst By H_2 And CO

6.1 Introduction

In Chapter 5, the performance of a LNT/SCR dual-layer catalyst was studied using H_2 as the sole reductant. This chapter reports a continuing study of that in Chapter 5. In the dual-layer catalyst, NH_3 is the key chemical link between the LNT and SCR catalysts. Ammonia is the reductant needed for SCR, so it is important to use reductants that promote NH_3 generation by the LNT catalyst. The use of H_2 as the reductant has been extensively studied. However, typical vehicle exhaust during the fuel-rich operation contains a complex mixture of CO, H_2 and hydrocarbons. The CO concentration may exceed the H_2 concentration during the catalyst regeneration. For diesel vehicles the H_2 concentration is low while the hydrocarbon fraction is high and may contain a wide range of hydrocarbons from low molecular weight alkenes, olefins, and aromatics to the high molecular weight diesel-like molecules. The upstream diesel oxidation catalyst (DOC) reduces the concentrations of these species, but during the rich operation many of these species reach the LNT. The deNO_x performance of a LNT catalyst should be insensitive to the changes in the reductant composition. A desired catalyst should be a periodic NH_3 generator irrespective of whether the feed contains H_2, CO, and/or hydrocarbons. The concentrations of CO and H_2 depend on the air-to-fuel ratio during the regeneration. For example, an air-to-fuel ratio of 9.0 may favor H_2 generation and an air-to-fuel ratio between 12.0 and 13.0 may favor CO generation [120]. Hence, the LNT catalyst may be exposed to varying CO/H_2 ratios during the regeneration.

We studied lean NO_x reduction with H_2 and CO over several synthesized LNT/SCR dual-layer catalysts. The impact of the reductant composition, catalyst composition profile, reactor configuration, and lean-rich switching policy on the cycle-averaged NO_x conversion and product selectivity was studied. The results suggest ways to reduce the loading of the expensive PGM while maintaining a high NO_x conversion over a wide temperature range.

6.2 Experimental

Experiments were performed by periodic shifts between the lean and rich feeds to evaluate the deNO_x performance of dual-layer catalysts. The carrier gas contained 2.5% H_2O and 2.0% CO_2 in Ar. The lean feed contained 500 ppm NO and 5% O_2 in the carrier gas mixture. It was fed between 6 s to 60 s. The total reductant concentration in the rich phase was 2.5% in the same carrier gas. Three reductant compositions were used: 2.5% H_2, 2.0% H_2/0.5% CO and 1.5% H_2/1.0% CO. The corresponding CO/H_2 ratios were 0, 0.25 and 0.67, respectively. The duration of the rich feed varied from 1 to 20 s. The cycle average H_2/NO feed ratio was 1.04 times the stoichiometric ratio needed for NH_3 formation by the reaction,

$$16H_2 + 4NO + 3O_2 \leftrightarrow 4NH_3 + 10H_2O. \quad \text{(R1)}$$

It took approximately 10 minutes to reach a periodic state. The feed temperature was increased from 150 to 400 ºC in steps of 50 ºC. At least 25 cycles were run at each temperature. The cycle-averaged NO_x conversion and product selectivity were obtained

by averaging the last ten cycles. The NO_x conversion, the NH_3 and NO_2 selectivity (S_A) and the N_2O selectivity (S_B) were calculated by

$$X_{NO_x} = 1 - \frac{\int_0^{\tau_s} [F_{NO}(t) + F_{NO_2}(t)\, dt}{\int_0^{\tau_l} F_{NO}^{i}(t)\, dt}. \quad (1)$$

$$S_A = \frac{\int_0^{\tau_s} F_A(t)\, dt}{\int_0^{\tau_l} F_{NO}^{i}(t)\, dt - \int_0^{\tau_s} F_{NO}(t)\, dt} \text{ , and} \quad (2)$$

$$S_B = \frac{\int_0^{\tau_s} 2 * F_B(t)\, dt}{\int_0^{\tau_l} F_{NO}^{i}(t)\, dt - \int_0^{\tau_s} F_{NO}(t)\, dt}. \quad (3)$$

Here τ_l and τ_s are the duration of lean phase feed and a lean-rich total cycle (s). F_{NO}^{i} is the NO feed rate and $F_{NO}(t)$ the corresponding effluent molar flow rates (mole/s). $F_A(t)$ is the effluent molar flow rates of either NH_3 or NO_2 and $F_B(t)$ the effluent molar flow rate of N_2O (mole/s).

A few stationary experiments were conducted over the LNT catalysts to assess the activity of the reverse water-gas-shift reaction (rWGS); i.e.,

$H_2 + CO_2 \leftarrow\rightarrow H_2O + CO.$ (R2)

The total flow rate was 1000 sccm (GHSV= 60,000 h^{-1}, based on total monolith volume). It contained 500 ppm CO and 2.5% H_2O in Ar.

6.3 Results and Discussion

6.3.1 Effect of CO/H_2 ratio on NO_x Reduction on LNT Catalysts

Experiments were conducted to compare the NO_x conversion and product distribution of the three LNT catalysts. Figure 6-1 shows the NO_x conversion for the ceria-free LNT1 catalyst exposed to a 60s lean/5s rich cycle over a range of feed temperatures. The rich feed contained 2.5% reductant in a carrier gas mixture of CO_2, H_2O and Ar. Three different CO/H_2 ratios were used during the LNT regeneration. The solid line describes the NO_x conversion as a function of feed temperature using 2.5% H_2 as the sole reductant. The dashed and dotted lines represent the NO_x reduction by CO/H_2 mixtures with ratios of 0.25 and 0.67, respectively. The NO_x conversion using 2.5% H_2 feed had a local minimum at 200 ^oC and a local maximum at 350 ^oC. The NO_x conversion decrease above 350 °C is likely due to the decreasing stability and an increasing decomposition rate of stored NO_x [36]. The decrease in NO_x conversion between 150 and 200 ^oC is attributed to an onset of the reverse water gas shift reaction, $CO_2 + H_2 \leftrightarrow CO + H_2O$ [17, 36]. This is supported by the fact that the NO_x conversion approaches that obtained for a rich feed having 0.5% CO in 2% H_2, considered in more detail next.

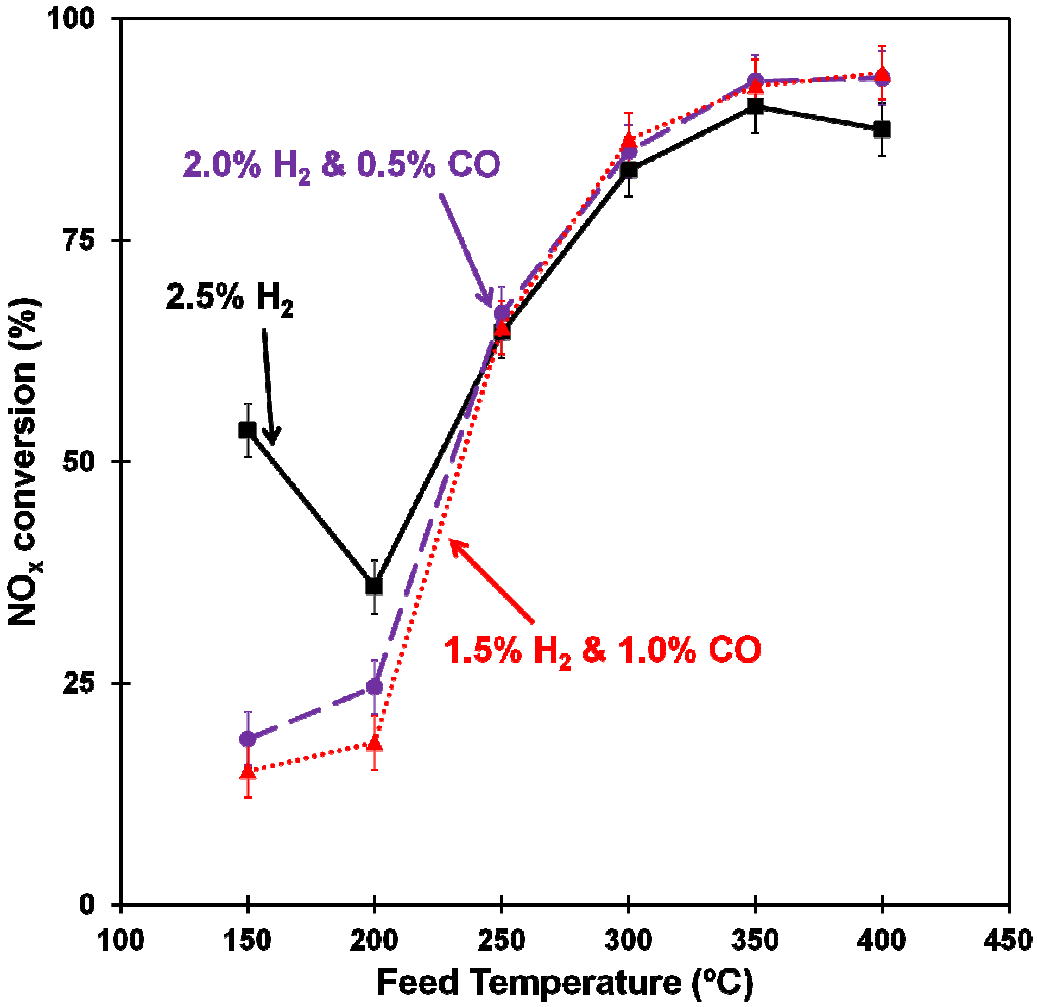

Figure 6-1 Comparison of NO_x conversion by LNT1 catalyst using a mixture containing 2.5% redutants with different CO/H_2 ratios.

The CO-containing feeds led to lower NO_x conversions than that of a feed containing only H_2 at temperatures below 250 ^oC. For example, at 150 ^oC the NO_x conversion was 54% for a CO-free feed but decreased to 15% for the feed with CO/H_2 = 0.67. As the temperature increased above 200 ^oC, the differences between the NO_x conversions for the three different feeds diminished. At temperatures exceeding 350 °C,

the NO_x reduction of mixtures of H_2 and CO was actually slightly higher than that of a feed of pure H_2.

The presence of CO in the reductant mixture greatly diminishes the low-temperature NO_x conversion. This is evident from Figures 6-2.a and b that show the transient effluent composition from the LNT1 catalyst during the 5 s of the rich phase and 5 s of the subsequent lean phase during two typical lean (60s)-rich (5s) cycles, using 2.5% H_2 to regenerate the catalyst. At both 150 °C and 200 °C, N_2O immediately formed during the rich phase, followed by the formation of NH_3. CO was produced after NH_3 at 200 °C, while no CO formed at 150 °C. The appearance of NH_3, a product of deep reduction, shows that excess H_2 was fed in the experiment. When the temperature is at or above 200 °C, H_2 reacts with CO_2 fed in the carrier gas to generate CO via the reverse water-gas-shift reaction. The absence of CO at 150 ^oC suggests that the reaction between H_2 and CO_2 is very slow; therefore sufficient free PGM sites are available for the NO_x reduction to occur. On the other hand, the CO breakthrough at 200 ^oC suggests the formation of enough CO that a fraction of PGM sites become occupied by CO. This decrease of the available PGM active sites decreases the NO_x storage and reduction and leads to the local minimum in the NO_x conversion at 200 °C using pure H_2 as the reductant.

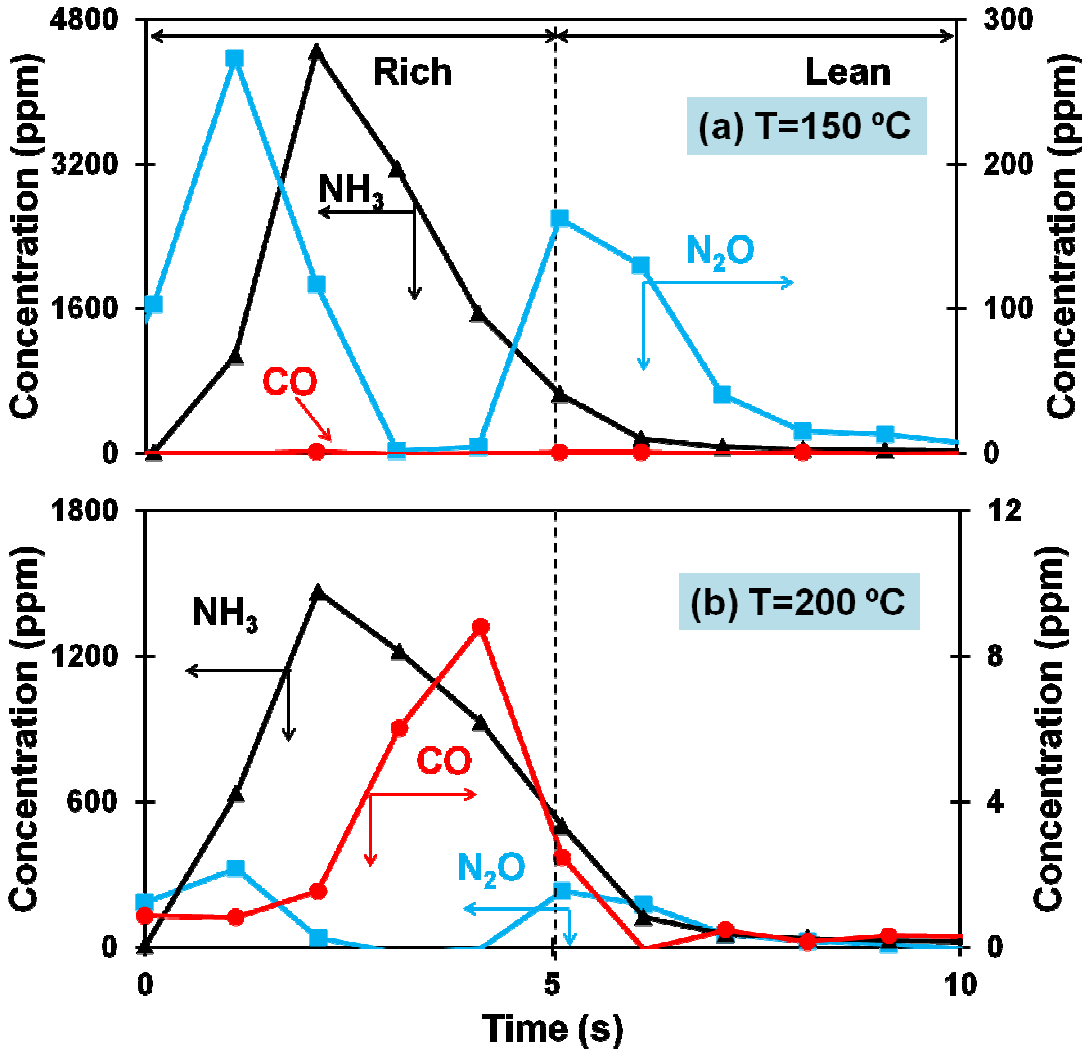

Figure 6-2 The effluent concentrations during the 5 s of rich feed and subsequent 5 s of lean feed using LNT1 at (a) 150 °C and (b) 200 °C. The reductant was 2.5% H_2 and the cyclic feed was of 60 s lean and 5 s rich.

The CO inhibition is more significant when a mixture of H_2 and CO is used as the reductant. This is evident from the much lower NO_x conversion using CO mixtures to conduct the regeneration at 200 °C. As the temperature is increased, the CO inhibition decreases due to an increased rate of CO desorption. In fact, the presence of CO in the

reductant mixture increases the NO_x reduction above 250 °C. According to James et al. [51], the presence of CO facilitates the decomposition of barium nitrates both on the surface and in the bulk. Thus, a more complete regeneration at high temperatures can be achieved using both H_2 and CO compared to pure H_2. The higher utilization of NO_x storage sites on the surface and in the bulk increases the NO_x conversion above that attained with pure H_2 reductant. Corbos et al. [70, 121] also reported that using a H_2 and CO mixture led to the highest NO_x conversion from a LNT-SCR mixture catalyst.

The CO/H_2 ratio affects both the NO_x reduction and the product distribution. Figure 6-3 compares the N_2 and NH_3 selectivities using LNT1 catalyst with reductant mixtures containing different CO/H_2 ratios but fixed total reductant concentration (2.5%). When pure H_2 was used as the reducing agent, the NH_3 selectivity decreased with temperature while the N_2 selectivity increased, except at 200 °C where a local minimum in the NH_3 selectivity (39%) was obtained. In contrast, for NO_x reduction by H_2 and CO mixture, the N_2 and NH_3 selectivities had different temperature dependencies. The NH_3 selectivity increased with temperature below 250 °C and then decreased. The temperature dependence of N_2 selectivity was in general the inverse of the NH_3 selectivity since these two were the primary N-containing products at higher temperature. The NO_x reduction with pure H_2 led to a higher NH_3 selectivity than using mixtures of H_2 and CO over the entire temperature range.

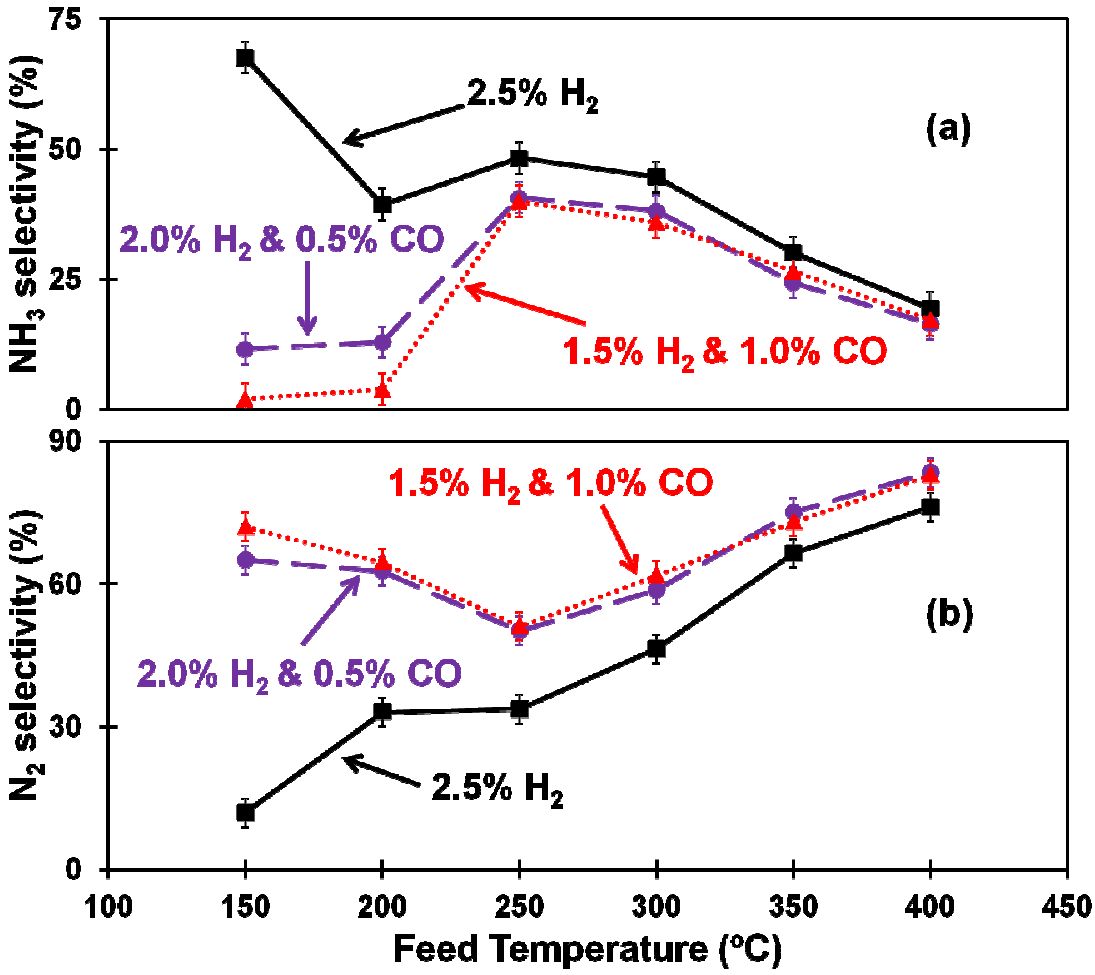

Figure 6-3 Comparison of (a) N_2 and (b) NH_3 selectivities. Catalyst was LNT1. Feed contained 2.5% reductants with different CO/H_2 ratios.

These trends suggest that the presence of CO in the reductant mixture has a significant impact on the regeneration chemistry. When pure H_2 is used as the sole reductant, CO is produced above 200 °C according to Figure 6-2. The formed CO binds to the PGM and inhibits the deep reduction of the stored NO_x [50, 120]. As a result, the NH_3 selectivity reaches a local minimum at 200 °C. The diminution of NH_3 generation in the lower temperature range is more pronounced when CO is present in the reductant mixture.

The lower the CO/H_2 ratio the higher is the NH_3 selectivity. A temperature increase facilitates the CO desorption and enhances the activity of the water-gas-shift reaction. This increases the availability of PGM sites for catalyst regeneration and of H_2 for NH_3 generation. Thus, NH_3 selectivity from NO_x reduction with H_2 and CO increases with temperature up to 250 °C. For all the reductant mixtures increasing the temperature decreases the NH_3 selectivity due to sequential reaction with stored NO_x downstream of its generation [32-33]. The N_2 selectivity increases at the expense of the NH_3 selectivity decrease for all reductant mixture compositions.

6.3.2 LNT/SCR Dual-layer Catalysts for CO/H_2 Reductant Mixtures

The rather high NH_3 selectivities (>50%) obtained with the LNT1 catalyst suggests that a dual layer catalyst will enhance the selectivity to N_2. We have previously shown that this is the case by using H_2 as the sole reductant in the absence and presence of CO_2 and H_2O [123]. Figures 6-4.a-c compare the NO_x conversions from LNT1 and CuZ-LNT1 catalysts using reductant mixtures with the same three CO/H_2 ratios as earlier. The solid lines describe the LNT1 catalyst performance, and the dashed lines those of the corresponding dual-layer catalyst. The dual-layer catalyst had a higher low-temperature NO_x conversion than the LNT1 catalyst for all temperatures except for 400 ^oC. The increase in NO_x conversion from the dual-layer catalyst decreased with an increase of the CO/H_2 ratio. At 200 °C, the NO_x conversion increase was 27%, 21% and 18% for mixtures with a CO/H_2 ratio of 0, 0.25 and 0.67, respectively.

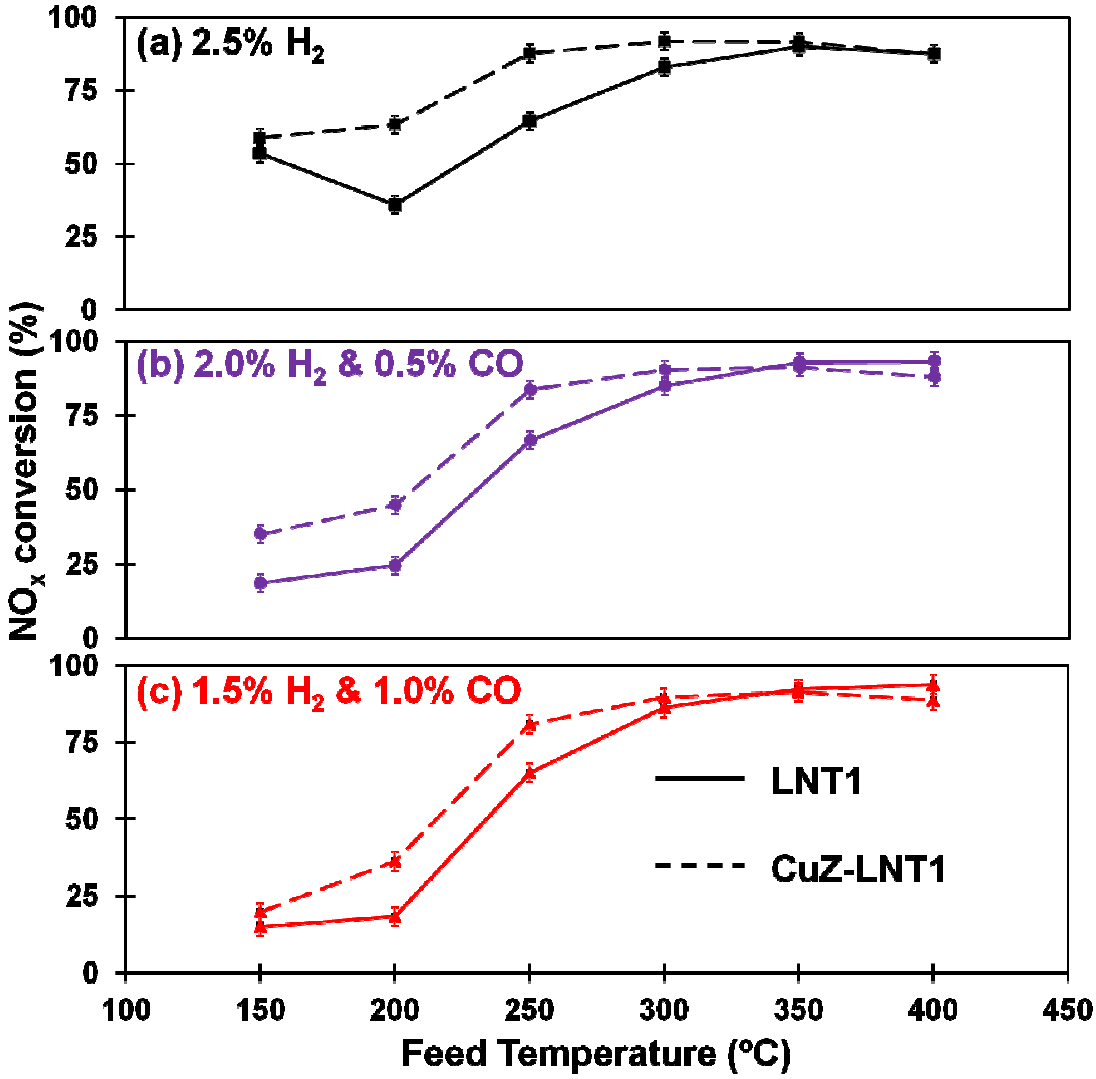

Figure 6-4 Comparison of the NO_x conversion using mixtures with 2.5% reductants with different CO/H_2 ratios conducted over LNT1 and CuZ-LNT1.

The addition of the Cu/ZSM-5 SCR catalyst layer contributes selective reduction activity for the standard SCR reaction between NH_3, NO and O_2. When the dual-layer catalyst is used, NH_3 produced in the underlying LNT layer during the rich phase is captured by the SCR top-layer due to the known strong binding of NH_3 to the Cu/ZSM-5, decreasing the NH_3 slip [123]. The NH_3 stored in the SCR catalyst reduces the NO_x fed

during the lean phase, generating N_2 with high selectivity. Figure 6-5 shows the enhancement in the N_2 selectivity following the deposition of the CuZ layer on top of the LNT1 layer. The large increase in the N_2 selectivity shows the effective SCR utilization of the stored NH_3 for NO_x reduction chemistry. The addition of CO to the reductant limits the SCR pathway because it decreases the NH_3 selectivity, as shown in Figure 6-3. Hence, an increase in the CO/H_2 ratio decreases the NO_x conversion.

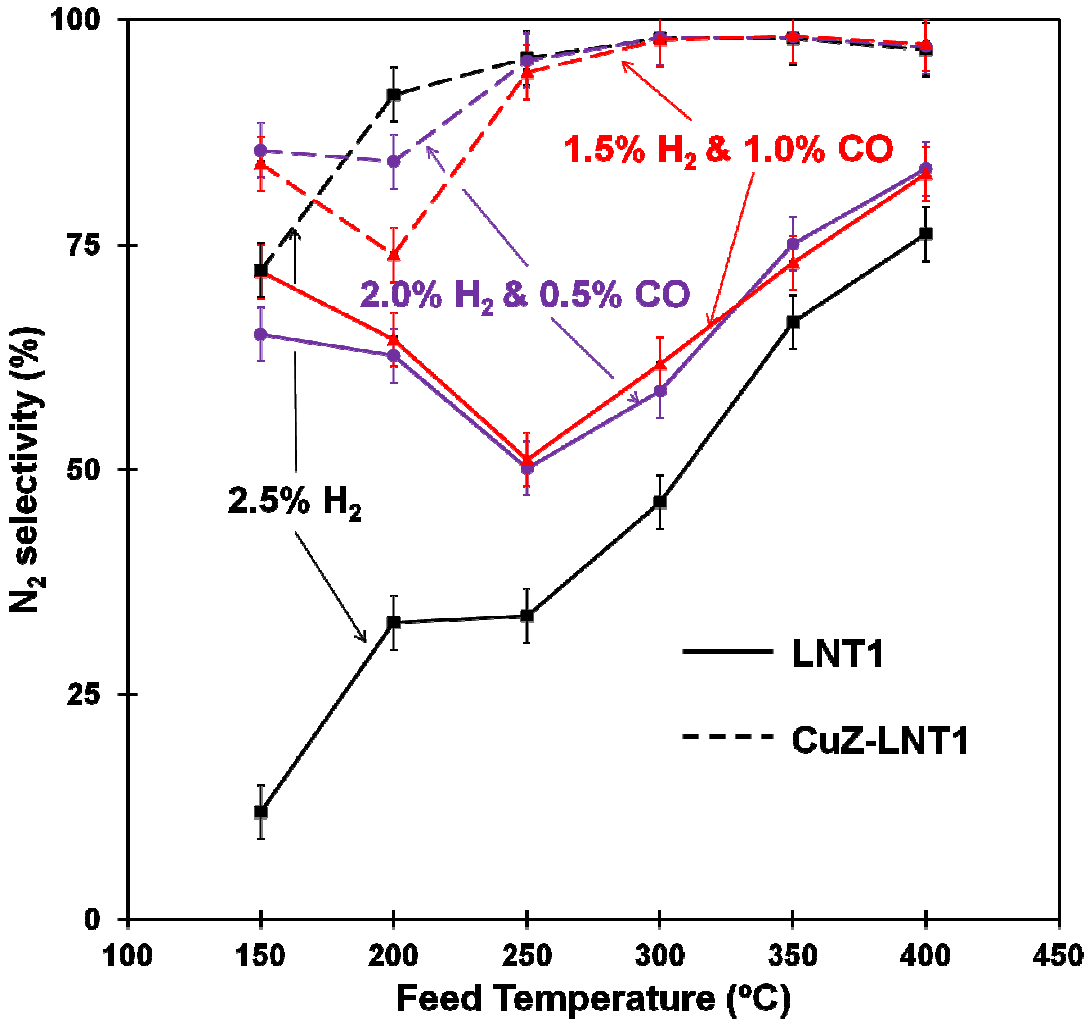

Figure 6-5 Impact of CO/H_2 ratio on the N_2 selectivity over LNT1 and CuZ-LNT1.

The LNT1 and CuZ-LNT1 NO_x reduction with CO and H_2 mixture can be improved by depositing a SCR-layer on top of the LNT layer. An important challenge is to minimize the impact of the CO/H_2 ratio in the reductant mixture on the NO_x conversion, especially at low temperatures. This may be accomplished by optimizing the catalyst design variables, such as the ceria loading in the LNT layer as shown below.

6.3.3 Effect of Adding Ceria to the LNT Layer

Ceria is an established effective promoter of LNT catalysts. It serves several important functions. First, ceria enhances the redox activity of Pt. Phatak et al. [122] reported that the turnover frequency of ceria-supported Pt is 30 times higher than that of alumina-supported Pt. Second, ceria provides additional NO_x storage sites, especially below 250 °C [31]. Third, ceria mitigates CO inhibition by either enhancing the oxidation of CO and, when H_2O is present, enhances the water-gas-shift reaction. By adding ceria, the Pt-catalyzed CO oxidation reaction order changes from -1 to 0 [124-125]. In an earlier study we showed that CO oxidation can be carried out even at 150 °C over a PtCe catalyst [110]. Other benefits from the ceria addition include the resistance toward hydrothermal aging through the stabilization of Pt crystallites and the mitigation of SO_x poisoning. For these reasons, a LNT catalyst containing ceria was used in the study of the dual-layer catalyst.

The temperature dependence of NO_x conversion as a function of feed temperature of the ceria-free LNT1 and ceria-rich LNT3 catalysts is shown in Figure 6-6 using reductant mixtures with different CO/H_2 ratios. The NO_x conversion by the LNT3

catalyst was up to 35% (absolute) higher than that by the LNT1 catalyst. For example, the NO_x conversion from LNT3 was 71% at 200 °C, while the NO_x conversion from LNT1 was 36%. Increasing the CO/H_2 ratio decreased the NO_x conversion using either the LNT1 or LNT3 catalyst. Interestingly, the increase in the NO_x conversion achieved with the addition of ceria (LNT1 to LNT3) was unaffected by the CO/H_2 ratio, except at 150 °C.

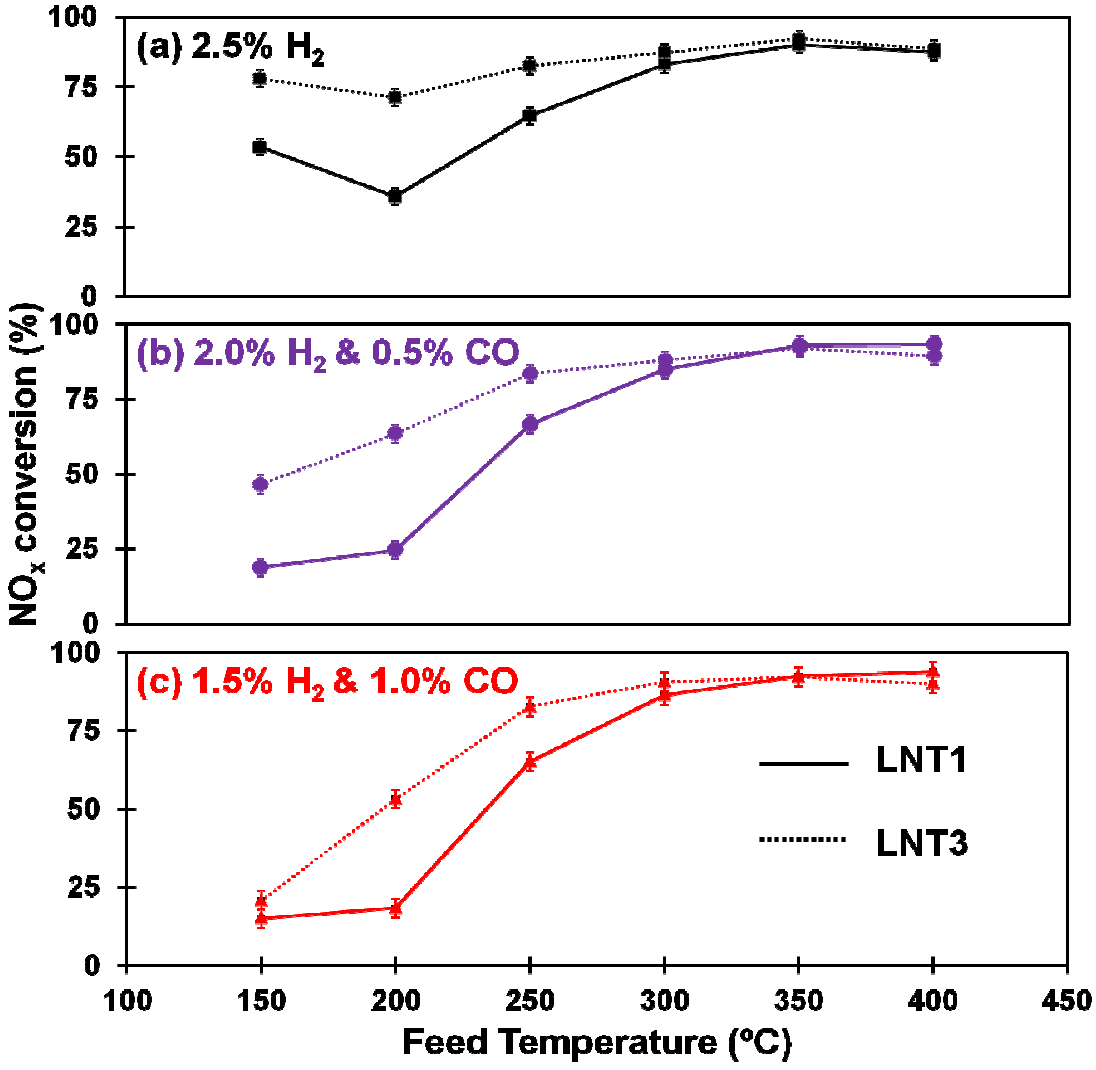

Figure 6-6 Impact of CO/H_2 ratios on NO_x conversion over LNT1 and LNT3.

The mitigation of CO inhibition by ceria addition is likely due to the increase in the rate of the water-gas-shift reaction as shown in Fig 6-6. On the other hand, the reduction in the rate at 200 ^{o}C may be due to the reverse water gas shift reaction as shown in Fig 6-2. To check these assertions, Figure 6-7 compares the extent of the steady-state WGS reaction over the LNT1 and LNT3 catalysts. Figure 6-7.a shows that at low-temperatures the WGS reaction rate significantly increased in the presence of ceria. The light-off temperature, defined as the temperature at 50% CO conversion ($T_{50\%}$), was approximately 50 °C lower for LNT3 than for LNT1. Thus, the effective CO removal and subsequent H_2 generation increased the low-temperature performance of LNT3. Figure 6-7.b shows the steady-state reverse water-gas-shift reaction over LNT1 and LNT3 catalysts. In this experiment a mixture of H_2 (2.5%) and CO_2 (2%) with and without water generated CO even at 200 °C, confirming the earlier observation in Figure 2. A comparison of Figures 6-7.a and b shows that the extent of the reverse WGS reaction is smaller than that of WGS reaction. For example, at 200 ^{o}C the CO conversion over LNT3 was 35% while the CO_2 conversion was only 0.11%. This difference reflects the fact that the water gas shift reaction is exothermic so the thermodynamics favors the forward reaction. Thus, ceria addition primarily enhances the CO conversion to H_2 and therefore promotes the low-temperature performance of the LNT catalyst. This conclusion is in line with the findings of Honda researchers [32, 33]. In a narrow temperature window the reverse water gas shift reaction inhibits the NO_x conversion.

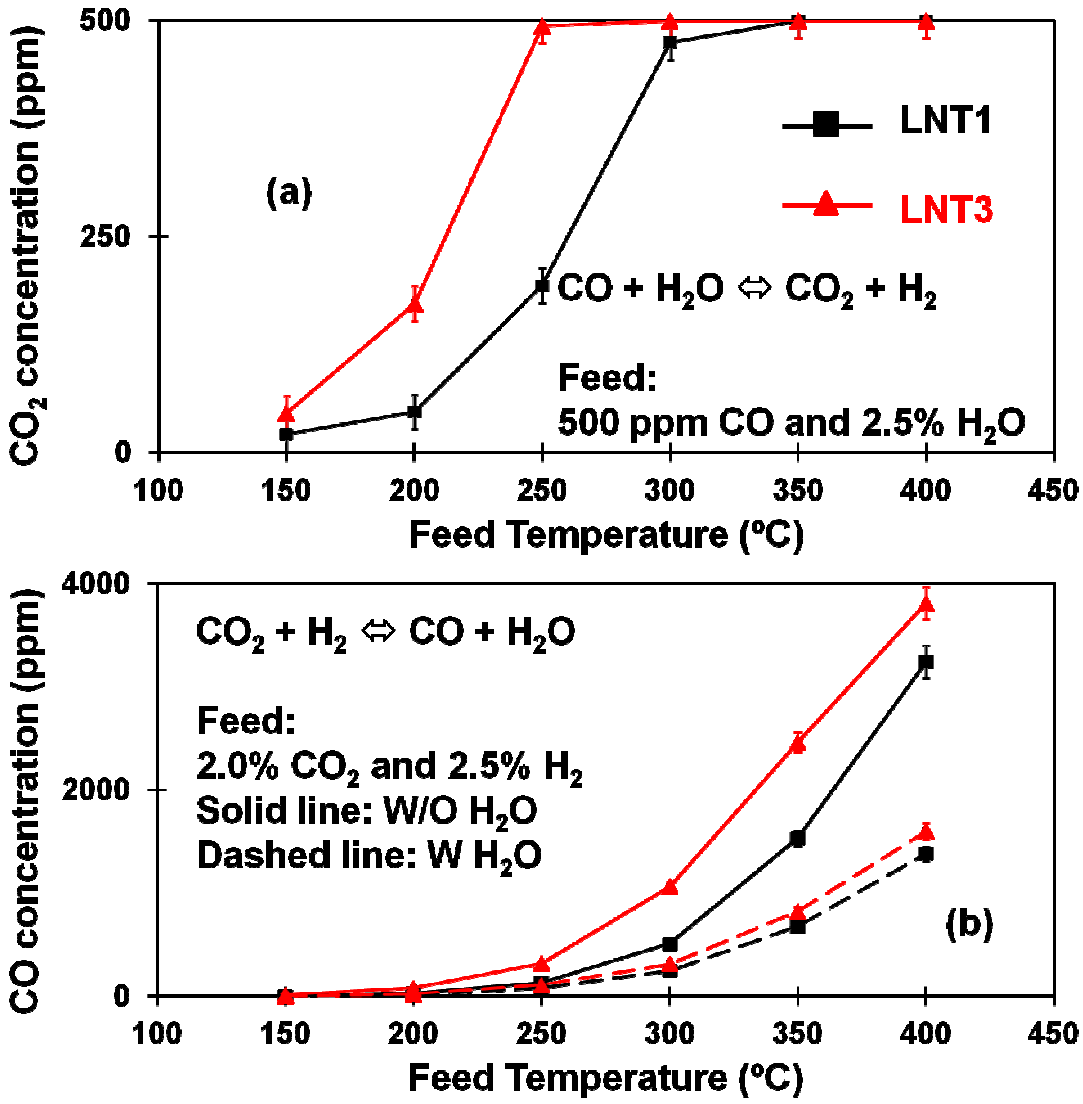

Figure 6-7 (a) CO_2 formation by the water-gas-shift reaction and (b) CO formation by the reverse water-gas-shift reaction conducted over LNT1 and LNT3.

The low-temperature NO_x reduction with H_2/CO mixtures can be improved by adding ceria to the LNT layer or depositing a Cu/ZSM-5 SCR layer on top of the LNT layer. Taking these concepts one step further, a dual-layer of the ceria-containing LNT3 and SCR catalysts were expected to have the best low-temperature performance. Figure 6-8 compares the NO_x conversions by the LNT3 catalyst and the corresponding dual-

layer catalyst using different reductant compositions. When 2.5% H_2 was used as the reductant, the dual-layer catalyst gave a slightly higher NO_x conversion than the LNT3 catalyst at 200 and 250 °C, but a 5-7% lower NO_x conversion above 250 °C. For higher CO/H_2 ratios, the enhanced rate by the SCR addition was more significant at low temperatures. However, the dual-layer catalyst NO_x conversion was still lower than that of LNT3 above 250 °C.

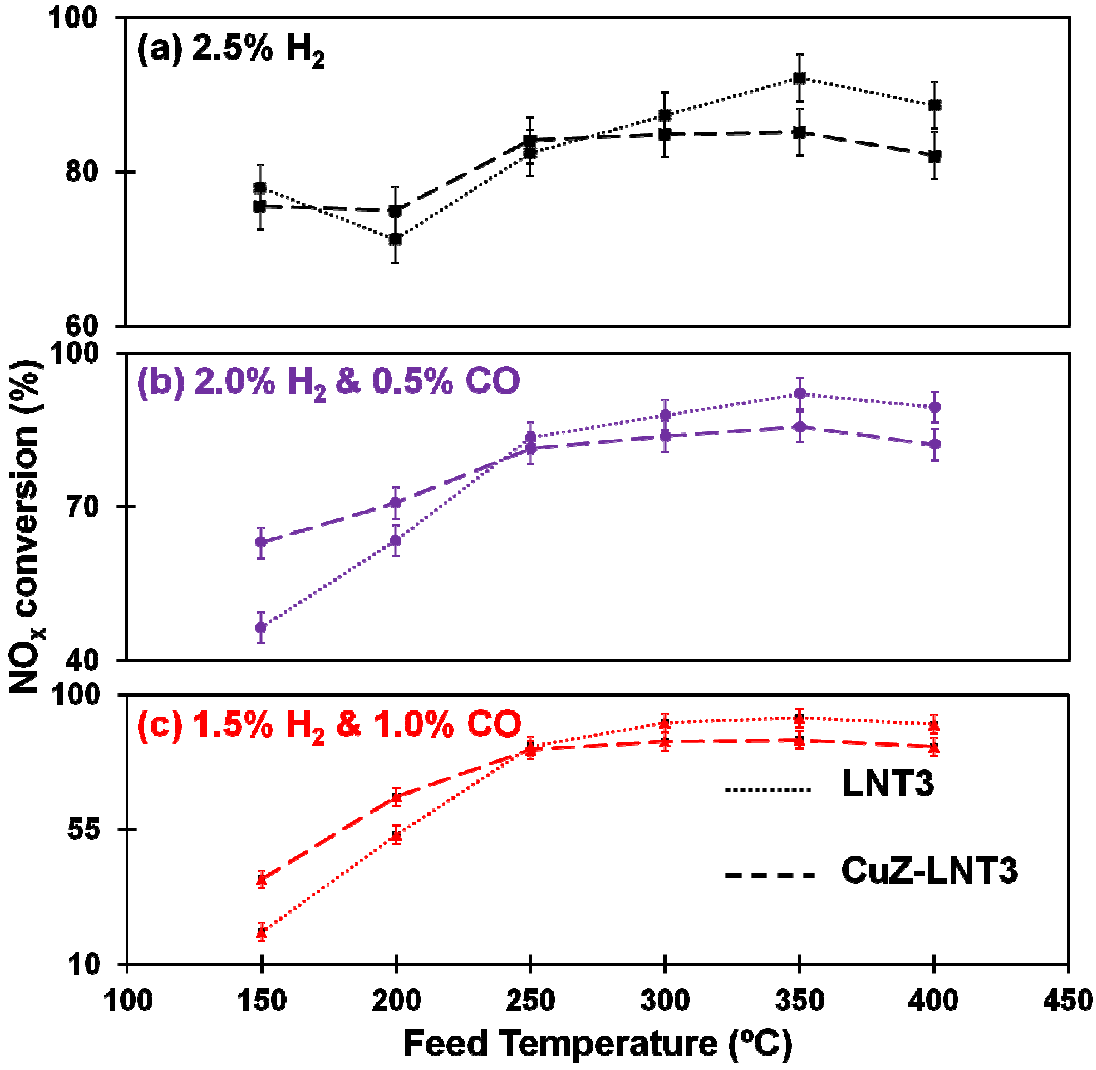

Figure 6-8 NO_x conversion by LNT3 and CuZ-LNT3 using three differet 2.5% CO/H_2 redictant mixtures.

The lower high-temperature NO_x conversion of the dual-layer catalyst than that of the LNT-only catalyst is very likely due to the addition of ceria. As shown in our earlier paper [110, 123], the oxidation of stored NH_3 is increased in the ceria-containing LNTs during the lean phase. That is, during the lean-rich switching the NH_3 stored in the top SCR layer, which desorbs at higher temperatures, can be oxidized to NO_x by the adjacent LNT layer. This undesired reaction can increase the consumption of stored NH_3 that otherwise would react with NO_x. At high temperatures, NH_3 oxidation generates NO_x. Hence, the combination of SCR and the ceria-rich LNT catalysts decreases the high-temperature NO_x conversion below that of LNT3 due to the excessive NH_3 oxidation that generates additional NO_x.

The ceria loading of the dual-layer catalyst should be optimized to balance between low- and high-temperature NO_x reduction. This can be accomplished by the non-uniform addition of ceria along the LNT layer; i.e., zoning. This non-uniform loading of an active catalytic component is a practical method to increase the catalyst performance, according to a patent by Ford [56-58]. For two LNT catalysts with the same PGM loading, the one with a non-uniform PGM profile has a higher NO_x conversion than one with a uniform PGM profile.

Dual-layer catalysts with different ceria profiles in the LNT layer were prepared by attaching halves of dual layer catalysts with different ceria loadings as shown in Figure 6-9. The dual-zoned dual-layer catalyst is named using the combination of abbreviations U, D, L and H. U stands for the upstream half-piece, D the downstream half-piece, L low ceria loading (0 wt%), and H high ceria loading (34 wt%). The dual-

layer catalyst with a ceria-free upstream half-piece and a ceria-rich downstream half-piece is named as UL-DH. The dual-layer catalyst with a reverse ceria profile is referred as UH-DL. The schematics of UL-DH and UH-DL are shown in Figure 6-9.

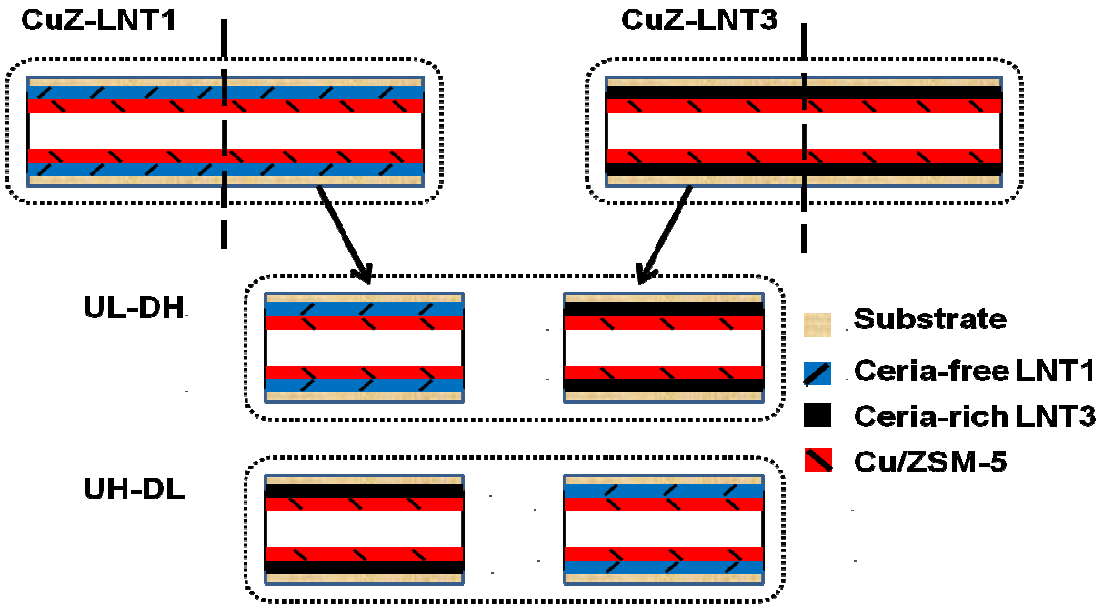

Figure 6-9 Schematics of UL-DH and UH-DL zoned dual-layer catalysts.

Figures 6-10 (a)-(c) compare the NO_x conversion using different CO/H_2 reductant mixtures over three dual-layer catalysts: CuZ-LNT1 (ceria free), CuZ-LNT3 (ceria uniform – 34 wt.%), and UL-DH (ceria nonuniform: none in front half, 34 wt.% in back half).Using pure H_2 as the reductant (Figure 6-10.a), the CuZ-LNT3 low-temperature NO_x conversion exceeded by 18% that obtained by the ceria-free CuZ-LNT1 dual-layer catalyst. At higher temperatures, the NO_x conversion of the ceria-rich CuZ-LNT3 was lower by about 6% than that of the ceria-free CuZ-LNT1. The dual-layer catalyst with a ceria-free front zone and a ceria-rich back zone (UL-DH) had a higher NO_x conversion than either the CuZ-LNT1 or the CuZ-LNT3 over the entire temperature range using H_2

as the sole reductant. When CO was included in the reductant mixture (Figure 6-10.b and c), the zoned dual-layer catalyst with an increasing ceria profile, UL-DH , still provided a good combination of the low- and high-temperatures merits of the CuZ-LNT1 and CuZ-LNT3, respectively. As Figures 6-10 (b) and (c) show, the NO_x conversion of UL-DH always exceeded that of CuZ-LNT1. The UL-DH had a higher NO_x conversion than CuZ-LNT3 above 250 °C, but a lower NO_x conversion below 250 °C. The ceria loading in UL-DH was only 50% of that in the CuZ-LNT3. Yet the NO_x conversion from the UL-DH was at most 10% lower than that of the CuZ-LNT3.

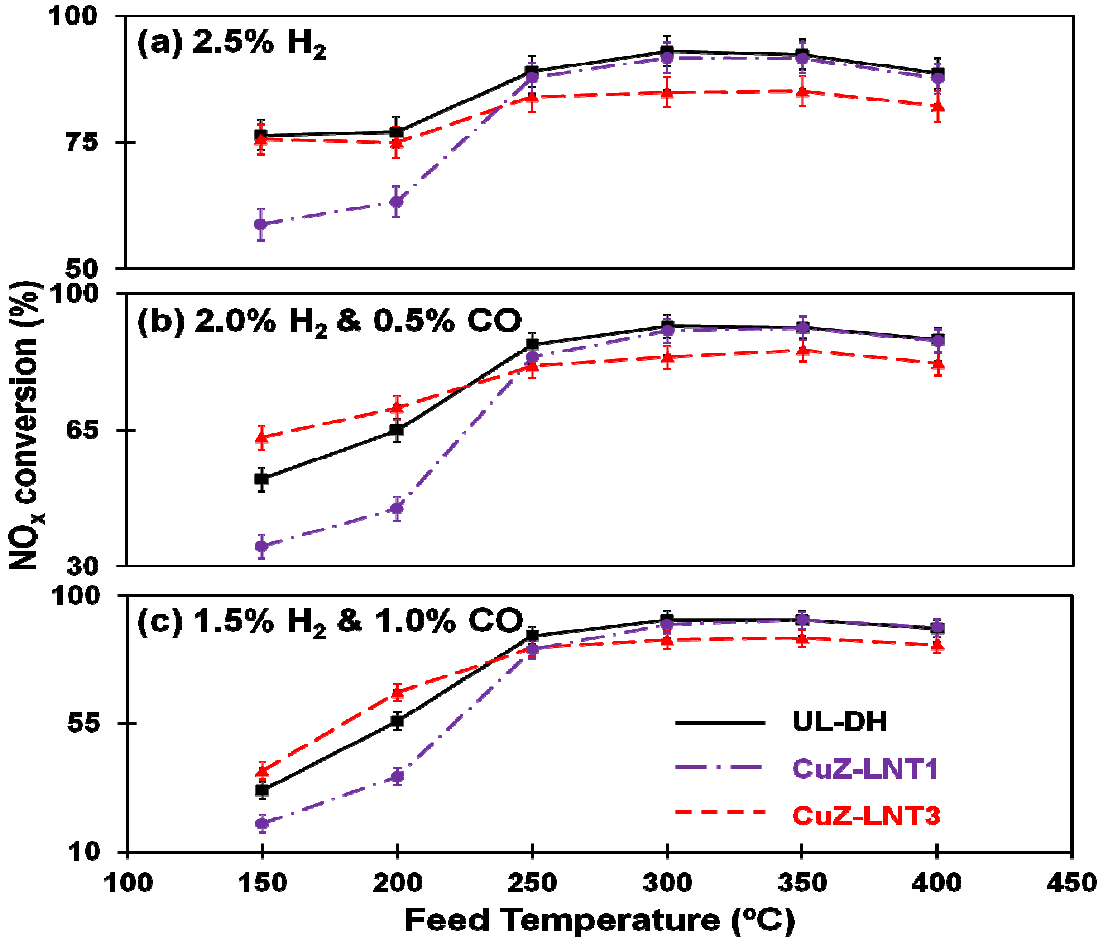

Figure 6-10 The NO_x conversion by three dual-layer catalysts using mixtures with different 2.5% CO/H_2 reductant mixtures.

The non-uniform ceria loading of UL-DH accounts for the enhanced NO_x conversion. Below 250 °C, the NO_x feed is mainly reduced by the downstream zone containing the high ceria loading. During the NO_x storage, ceria enhances the PGM activity for NO oxidation and NO_x spillover and provides additional NO_x storage sites; during the regeneration, Ceria facilitates the reverse NO_x spillover to the PGM and mitigates the CO inhibition. The ceria-free upstream zone works as a secondary NO_x reducer but an effective NH_3 generator at low temperatures. On the other hand, above 250 °C, the majority of the fed NO_x is captured by the upstream ceria-free zone due to the enhanced LNT activity with temperature. During the regeneration, the stored NO_x on the ceria-free upstream zone is reduced to NH_3 and the formed NH_3 is captured by the SCR top-layer. In the absence of ceria, the undesired NH_3 oxidation is lower than with ceria. Some escaping NH_3 is captured by the SCR top-layer in the downstream zone, instead of being oxidized by the LNT3 bottom-layer. Thus, the ceria-rich downstream zone can remove the slipping NO_x and NH_3 from the upstream zone. The synergy between the ceria-free upstream and the ceria-rich downstream zones enhances the loaded ceria utilization. Hence, the UL-DH is the best choice for NO_x reduction at both low- and high-temperatures.

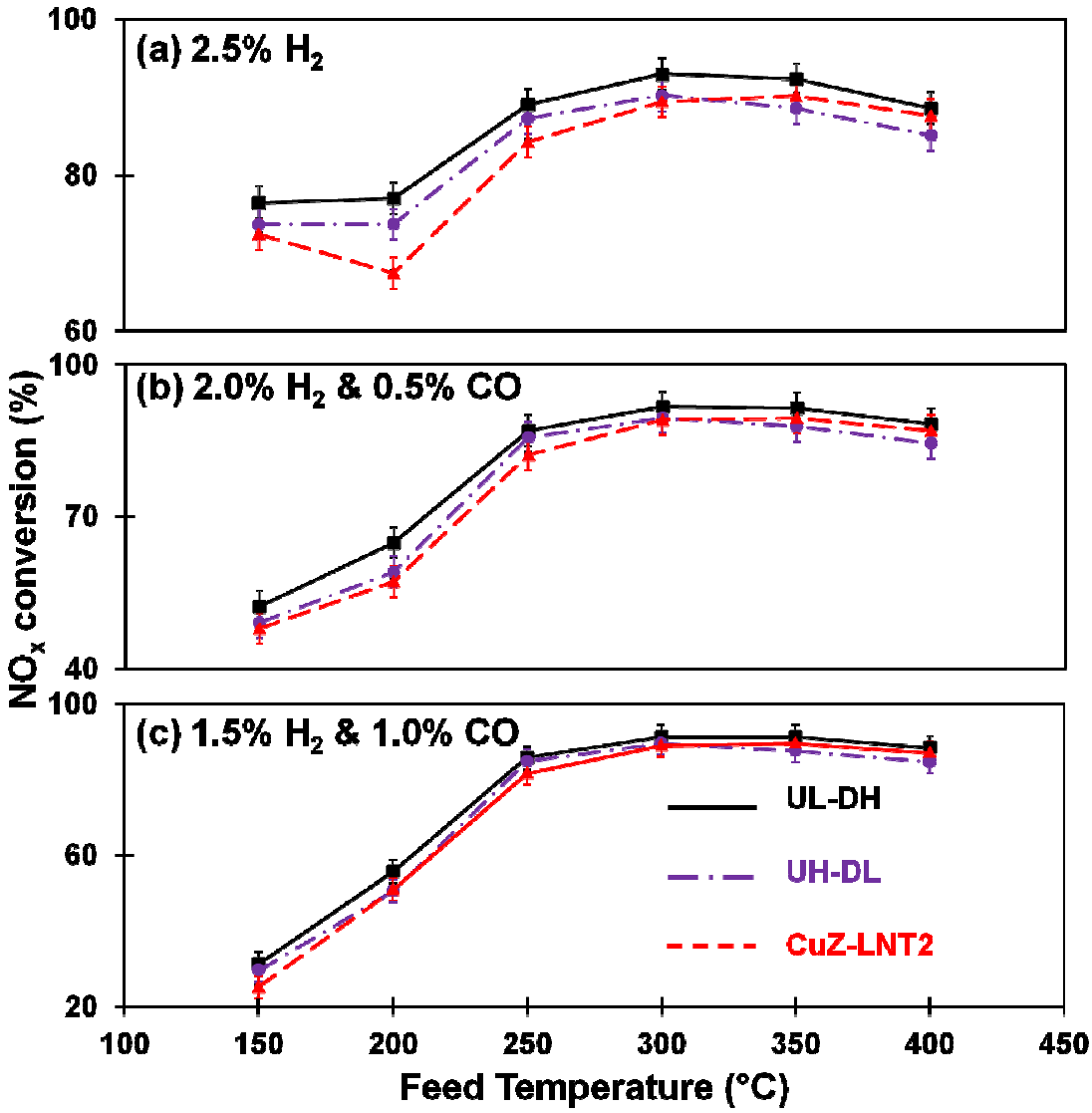

Figure 6-11 Comparison of NO_x conversion by three different zoned dual-layer catalysts using 2.5% CO/H_2 reductant mixtures.

In addition to an increasing ceria deposition profile, there are other possible deposition profiles such as a decreasing ceria profile and a uniform ceria profile. Figures 6-11 (a)-(c) compare the NO_x conversions as a function of feed temperature from three dual-layer catalysts with different CO/H_2 ratios in the reductant feed mixture using three dual-layer catalysts with the same total ceria loadings. In the UL-DH dual-layer catalyst

the upstream zone was free of ceria while the downstream zone had a rich ceria loading, where the UH-DL the upstream zone had a rich ceria loading and the downstream zone was ceria free. In the CuZ-LNT2 the bottom layer was LNT2, which is uniformly loaded with ceria. The UL-DH always had a higher NO_x conversion than the other two catalysts over the entire temperature range for all reductant mixtures. The performance of UH-DL was comparable to that of the CuZ-LNT2: The UH-DL low-temperature NO_x conversion was slightly higher than that of the CuZ-LNT2, which had a better high-temperature conversion.

The best performance of UL-DH is due in part to a more effective utilization of the H_2 reductant. Ideally, the LNT function of the dual layer catalyst should convert half the NO_x to NH_3 so that the SCR function converts resulting 1:1 NH_3:NO_x to N_2 by selective catalytic reduction. However, in the presence of ceria, some H_2 reacts with adsorbed oxygen on Pt and the stored oxygen on the ceria. If the ceria-rich catalyst is placed in the upstream section, the NH_3 formation is decreased by this undesired hydrogen oxidation. The UL-DH zoning guarantees a maximum NH_3 formation from the ceria-free upstream zone. The remaining H_2 and CO reduce the stored NO_x on the ceria-rich downstream zone. Thus, a complete regeneration and a maximum NH_3 formation can be obtained from the LNT bottom-layer by the higher ceria deposition in the downstream. This also maximizes the contribution of the SCR top-layer to the NO_x reduction.

Zoning can produce a non-uniform ceria profile in the dual-layer catalysts. In the UL-DH configuration, the ceria-free upstream zone is the main NO_x reducer at high temperatures and the LNT bottom-layer generates NH_3 at all temperatures. The ceria-rich

downstream zone serves as a major NO_x reducer at low temperatures and an NH_3 eliminator at high temperatures. Thus, the zoned UL-DH is the best choice for NO_x reduction with H_2 and CO.

6.3.4 Using Dual-layer Catalyst to Reduce PGM Loading

A dual-layer catalyst can reduce NO_x either by the NSR or the SCR routes. It is desirable to replace some of the LNT PGM catalyst with the less expensive SCR catalyst. As described earlier, the function of the LNT catalyst is to trap and convert a fraction of the NO_x to NH_3, while the SCR catalyst is used to trap NH_3 and react it with unconverted NO_x. Thus, PGM loading of the LNT catalyst should be the minimal needed to accomplish the partial storage and NH_3 generation. As we show in this section this can be accomplished also with aged or low PGM-loaded LNT catalysts.

There are several similarities between a thermally aged and a low PGM-loaded LNT catalyst. Each has a low NO oxidation activity and both suffer from a low NO_x storage capacity due to the decreased NO oxidation activity. On the other hand, each benefits from a high NH_3 selectivity due to the reduced NH_3 oxidation activity. Clayton et al. [45] showed that LNT catalysts having a low Pt dispersion are more effective NH_3 generation catalysts. Crocker and coworkers [71, 90] have shown that the aged LNT catalysts are more active NH_3 generation catalysts. The reduced oxidation activity is a direct consequence of the smaller interface between the PGM and Ba-based NO_x storage phase. The rate of the reverse NO_x spillover from the barium to the PGM is lowered by the less intimate contact between the PGM and the barium. Thus, the local H_2/NO_x ratio

over PGM increases during the regeneration, increasing the NH_3 selectivity. As shown below, this is an important contributing factor in the design and operation of LNT/SCR catalysts.

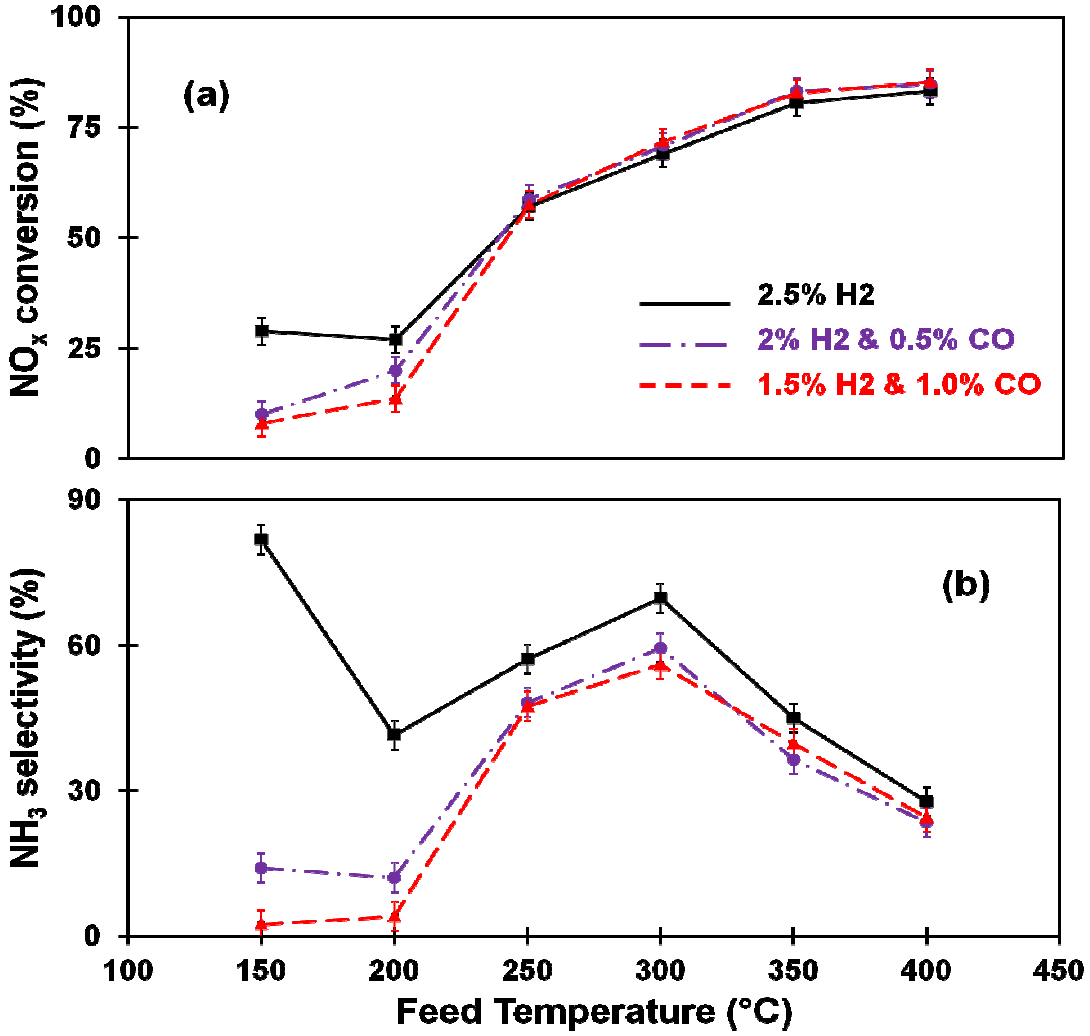

Figure 6-12 (a) The NO_x conversion and (b) NH_3 selectivity of an an aged LNT1 catalyst with different 2.5% CO/H_2 reductant mixtures.

Experiments with a thermally aged LNT catalyst tested the above conjectures. Figures 6-12 (a) and (b) show the NO_x conversion and NH_3 selectivity of aged LNT1 catalyst with different CO/H_2 ratios in the reductant mixtures. The general features of the

NO_x conversion and the NH_3 selectivity of aged LNT1 are similar to those of the fresh LNT1, as shown in Figures 6-1 and 6-3. On the other hand, the NO_x conversion of the aged catalyst was lower by up to 30% from that of the fresh LNT1 catalyst, while the NH_3 selectivity was higher by approximately 10%. Hence, a lower NO_x conversion and higher NH_3 selectivity can be obtained by the aged LNT.

To compensate for the declining activity of the aged LNT catalysts, a higher SCR loading was applied to the dual-layer catalyst. i.e., instead of a 0.9 g/in^3 SCR loading as in earlier experiments, a 2.0 g/in^3 SCR loading was applied. Figure 6-13 compares the cycle-averaged NO_x conversions using different reductant mixtures over three UL-DH catalysts: the first with a 0.9 g/in^3 SCR loading and a fresh LNT1 in the upstream followed by a fresh LNT3 in the back (UL-DH-1; this is the earlier catalyst UL-DH – the "1" is to distinguish it from the other two catalysts); the second with a 0.9 g/in^3 SCR loading and an aged LNT1 in the upstream followed by a fresh LNT3 in the downstream (UL-DH-2); The third with a 2.0 g/in^3 SCR loading and an aged LNT1 in the upstream followed by a fresh LNT3 in the downstream (UL-DH-3). The UL-DH-1 dual-layer catalyst with the fresh LNT and a 0.9 g/in^3 SCR loading had the best performance for all reductant mixtures. The UL-DH-2 dual-layer catalyst with an aged LNT and a 0.9 g/in^3 SCR loading had the lowest NO_x conversion in all cases. For the same LNT bottom-layer, the low-temperature NO_x conversion could be increased by 8-10% by increasing the SCR loading. The impact of the SCR thickness decreased as the temperature is increased. The NO_x conversion using two dual-layer catalysts (UL-DH -2 and -3) with the aged LNT bottom-layer are almost the same above 250 °C.

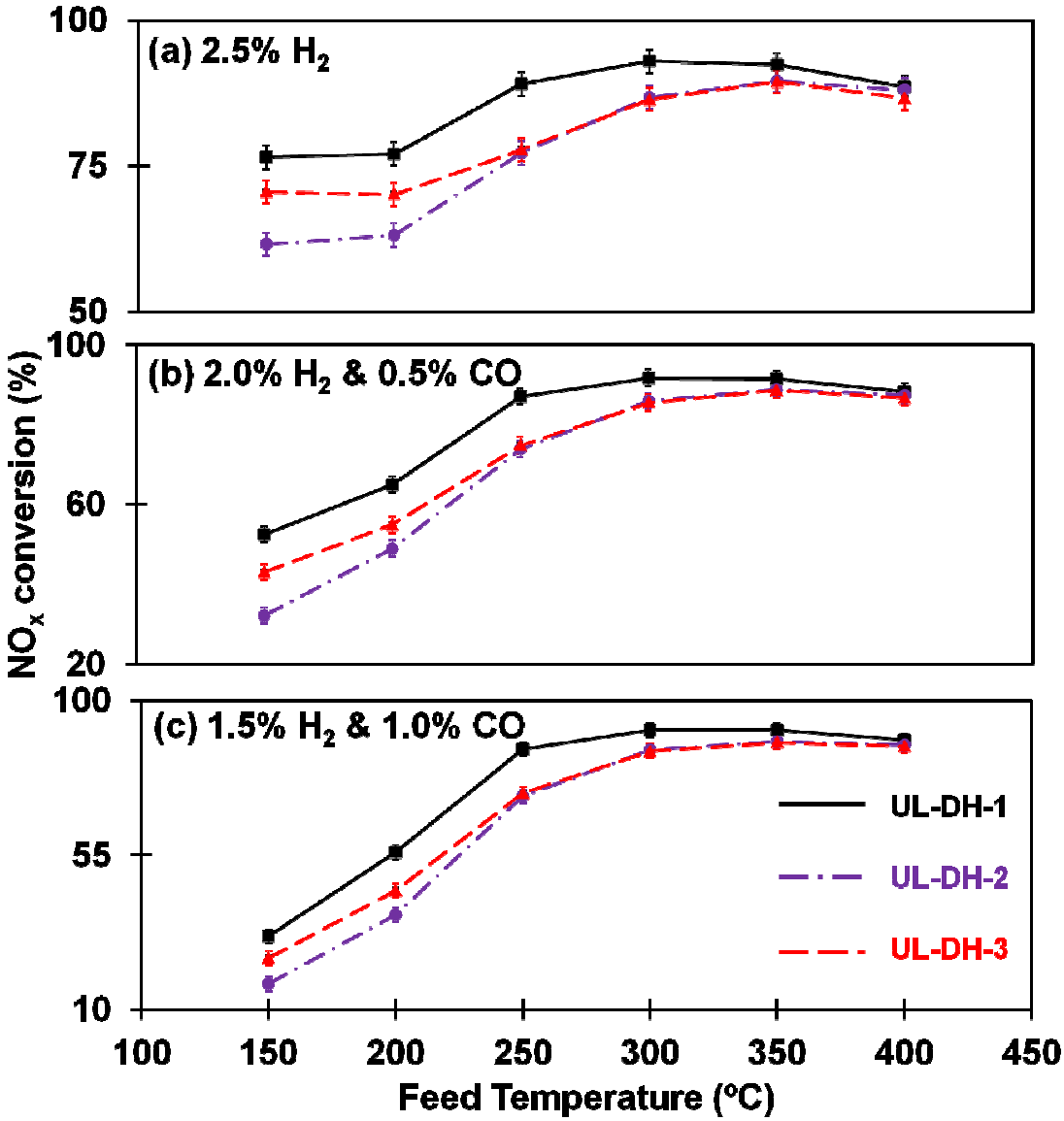

Figure 6-13 The NO_x conversion by three zoned aged dual-layer catalysts with different SCR loadings using 2.5% CO/H_2 reductants mixtures.

The experiments show that a thicker SCR layer can improve the low temperature NO_x reduction performance, while the high temperature performance is less sensitive to changes in the thickness of the SCR layer. This suggests that the low-temperature, dual-layer catalyst performance is limited by the NH_3 utilization of SCR catalyst, while the

high-temperature performance is limited by the NH_3 formation by the LNT catalyst. At low temperatures, the overall NO_x reduction can be enhanced by using the LNT to convert the NO_x to NH_3, and then to react this NH_3 with NO_x in the SCR catalyst. Since the standard SCR reaction ($NO + O_2 + NH_3$) over Cu/ZSM-5 is controlled by kinetic below 250 °C, a higher SCR loading should increase the NO_x conversion. Upon a temperature increase to 300 °C, NO_x reduction over the SCR top-layer is limited by the NH_3 generated by the LNT bottom-layer instead of the SCR catalyst activity. A higher SCR loading cannot improve the high-temperature NO_x conversion. In this scenario, the NO_x reduction is limited by the NO_x storage on the LNT catalyst and the sequential NH_3 generation. The SCR contribution is limited by the rate of NH_3 formation from the LNT bottom-layer.

The low-temperature NO_x reduction from a dual-layer catalyst with an aged LNT bottom-layer can be improved by increasing the SCR loading. The dual-layer catalyst offers an opportunity to reduce the PGM loading by enhancing the SCR reactions at low temperatures. In the operating temperature window of 150 to 400 ºC NO_x reduction on the LNT catalyst faces rate limitations at low temperatures, due in part to the kinetic limitations of NO oxidation and NO_x regeneration. Thus, a high PGM loading may be needed to achieve a desired low temperature NO_x conversion. Some of this PGM may not be needed at high temperatures. By using the dual-layer catalyst, the low temperature NO_x reduction can be improved by increasing the SCR loading. This enables minimization of the PGM load to a level that provides the required NO_x conversion at high temperatures.

The dual-layer catalyst provides an effective, practical solution to reduce PGM loading at high temperatures. One can estimate the efficiency of the loaded PGM by a space time yield defined as

$$STY_{PGM}\left(\frac{mole\,NOx\,converted}{g\,PGM\;\;hr}\right)=\frac{X_{NOx}\bullet\;F^{o}_{NOx}\,(mole/hr)}{PGM\,loading(g)}. \tag{4}$$

The higher the STY_{PGM}, the higher the PGM efficiency. In other words, a high value of STY_{PGM} corresponds to a low loading of PGM needed to achieve a specified NO_x conversion rate. Table 6-1 compares the STY_{PGM} of different LNT/SCR combinations from different research groups at 300 °C. The dual-layer catalyst has the highest STY_{PGM} value. Since the precious group metals, such as Pt and Rh, are the most expensive components in the LNT/SCR, a dual-layer catalyst can reduce the catalyst cost. The successful application of the aged LNT in the dual-layer LNT/SCR catalyst suggests a high feasibility to use a LNT catalyst containing a small PGM loading.

Table 6-1 STY_{PGM} at 300 °C of several LNT-SCR catalyst configurations.

Source	**Catalyst Configuration**	**STY_{PGM} (mol/hr*gPGM)**
This report	dual-layer	0.38
Ref [126]	multi-brick	0.08
Ref [68]	dual-bed	0.18
Ref [70]	mixture	0.30

6.3.5 Optimization of Lean-rich Cycle Time

A lean-rich cycle time can adjust the performance of a dual-layer catalyst. Kabin et al. [20] studied the dependence of the time-averaged NO_x conversion and N_2 selectivity on the lean-rich protocol. Clayton et al. [21] and Ren et al. [36] extended the work of Kabin et al. The rich time needs to be sufficiently long to avoid dilution of the rich feed and to generate NH_3. A too long rich time causes excessive breakthrough of reductant. Thus, an optimal intermediate cycle duration exists. At a fixed lean time and feed composition, the NH_3 selectivity increases with the rich time. Due to the important role of NH_3 in the protocol for the dual-layer catalyst, the optimal lean-rich cycle time has to differ from that for the LNT-only catalyst.

Figures 6-14 (a) and (b) describe the NO_x and H_2 conversions under different lean-rich cycles using the UL-DH-3 dual-zoned dual-layer catalyst. The lean feed was fixed at 500 ppm NO and 5% O_2 in a carrier gas mixture containing 2.5% H_2O and 2.0% CO_2 in Ar. The lean duration was 60 s while the rich cycle duration varied from 3 to 20 s. The total amount of H_2 fed during the rich period was 93.0 μmol. For example, the 60-3 lean-rich cycle consisted of 4.17% H_2 for 3 s during the rich phase and during the 60-20 cycle 0.63% H_2 for 20 s. The 60-3 lean-rich cycle had the lowest NO_x conversion over the entire temperature range. The NO_x conversion increased upon an increase of the rich duration up to a critical value with a corresponding decrease in the H_2 concentration. The critical rich feed time for a 60 s lean feed was 10 s. For example, the NO_x conversion from the 60-5 lean-rich cycles exceeded that of the 60-3 but was smaller than that of the 60-10 lean-rich cycles. An increase in the rich duration above 10 s and a corresponding

decrease in the H_2 concentration decreased the NO_x conversion below that of the 60-10 lean-rich cycle. At the same time, the H_2 conversion during the lean-rich cycle decreased with an increase of the rich duration and the decrease of H_2 concentration.

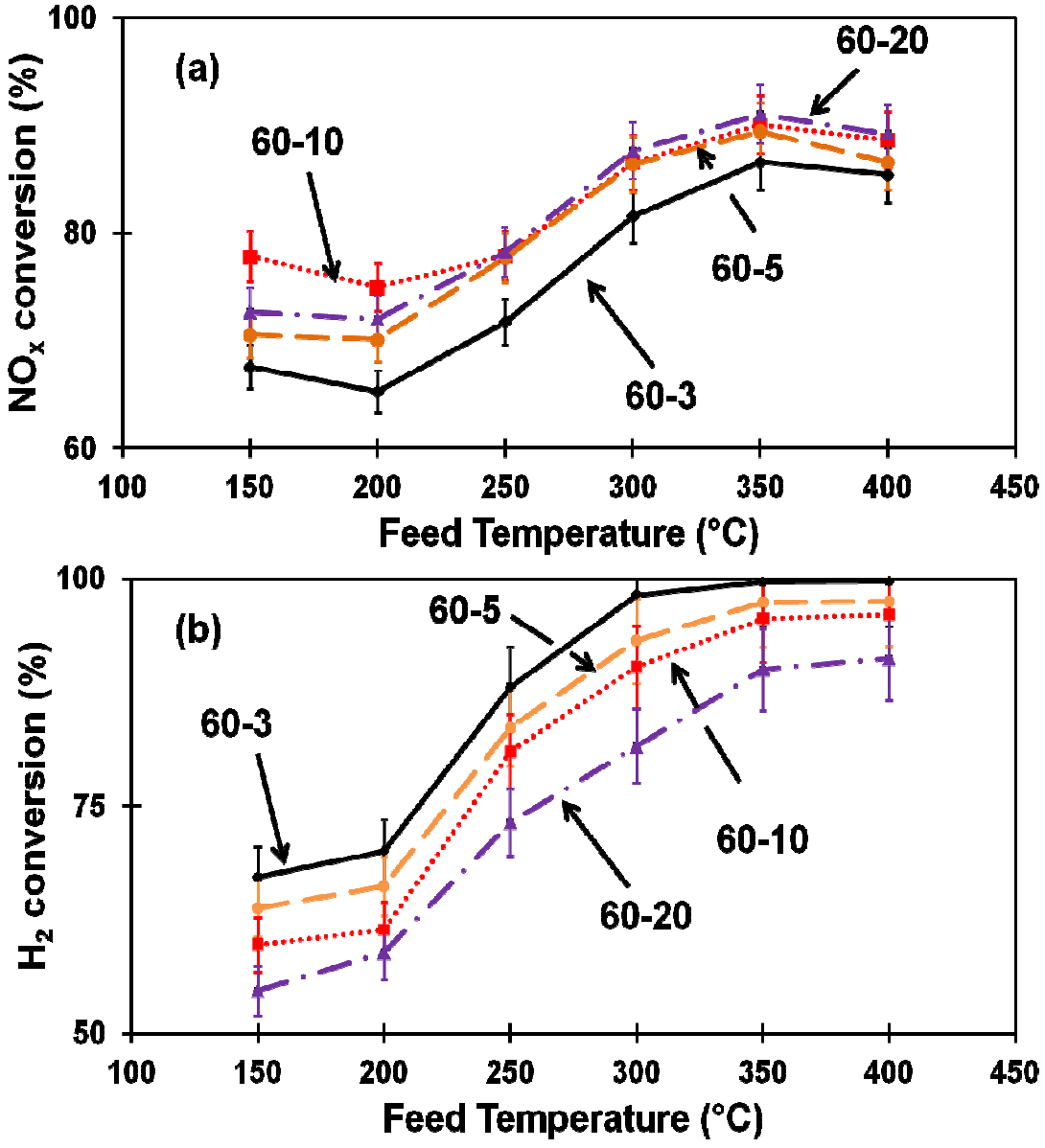

Figure 6-14 Impact of lean-rich cycle ratios on (a) NO_x and (b) H_2 conversion by a zoned aged UL-DH-3 dual-layer catalyst.

The peak NO_x conversion at the 60-10 lean-rich cycle may be due to the maximum H_2 efficiency for NH_3 formation. According to an IR thermography study by Liu et al. [110], the reductant reacts with the residual oxygen held in the catalyst pores upon the switch from lean to rich phase. For a short rich duration with high H_2 concentration, a fraction of the H_2 is wasted in the very beginning due to reaction with residual O_2. This decreases the amount of H_2 available for stored NO_x regeneration and increases the H_2 conversion. The NH_3 produced during the rich phase decreases as well. For a longer duration rich phase having a lower H_2 concentration, the undesired hydrogen oxidation is minimized and the H_2 conversion decreased. On the other hand, a too low H_2 concentration results in a low H_2/NO_x ratio, favoring N_2 formation instead of NH_3. This decreases the NO_x reduction by the SCR layer. This is an undesirable outcome if the goal is to increase the NO_x reduction on the SCR catalyst. Hence, an optimal rich duration and H_2 concentration exist for maximum H_2 efficiency and NH_3 production. For instance, the optimal rich duration and H_2 concentration are 10 s and 1.25%, respectively. This optimization of the lean-rich cycle increases the fuel economy. For example, a processing time of 910 s corresponds to thirteen 60-10 cycles and fourteen 60-5 cycles. The total amount of H_2 injected is 1209 µmol for the 60-10 lean-rich cycle and 1302 µmol for the 60-5 lean-rich cycle. Since the 60-10 lean-rich cycle reduces the amount of H_2 injection, the amount of reductant needed for catalyst regeneration is minimized. The fuel economy can be further improved by shortening the rich duration to avoid excessive H_2 breakthrough and increase the H_2 conversion.

Additional optimization was done for a fixed 6-1 ratio of lean to rich duration, while the total cycle time was changed from 7 to 70 s. Experiments were conducted with three lean-rich cycles: 6-1, 30-5 and 60-10. Figure 6-15 shows the NO_x conversion from these three lean-rich cycles with different reductants. The 6-1 lean-rich cycle had the lowest NO_x conversion under all conditions and the feed temperature had little impact on the NO_x conversion. The 30-5 lean-rich cycle had the highest NO_x conversion, exceeding those of the other two lean-rich cycles even with the highest CO/H_2 ratio. The advantage of 30-5 lean-rich cycle over the 60-10 lean-rich cycle was significant when the temperature was below 300 °C, while these two cycles led to similar NO_x conversion above 300 °C.

A high lean-rich cycling frequency increases the utilization of available NO_x storage sites. Shakya et al. [27] used a crystallite-scale LNT model to simulate different lean-rich cycles over a low-dispersion LNT catalyst. The short lean-rich cycle improves the deNO_x performance, when the storage and reduction are limited by the transport of stored NO_x. More effective NO_x storage and NH_3 generation in the LNT layer leads to a better deNO_x performance from the dual-layer catalyst. Hence, the NO_x conversion by the UL-DH-3 dual-zoned dual-layer catalyst can be improved by a short lean-rich cycle. One important benefit from the short lean-rich cycle is the increase of NO_x conversion in the presence of CO at low temperatures. This implies the possibility to increase the air-to-fuel ratio during the catalyst regeneration, enhancing the fuel economy. On the other hand, a too short lean-rich cycle is harmful to the catalyst performance. According to Kabin et al. [19-20], a short rich duration dilutes the rich feed so that a reducing

environment cannot be created. As a result, the 6-1 lean-rich cycle has the lowest NO_x conversion among all the three tested lean-rich cycles.

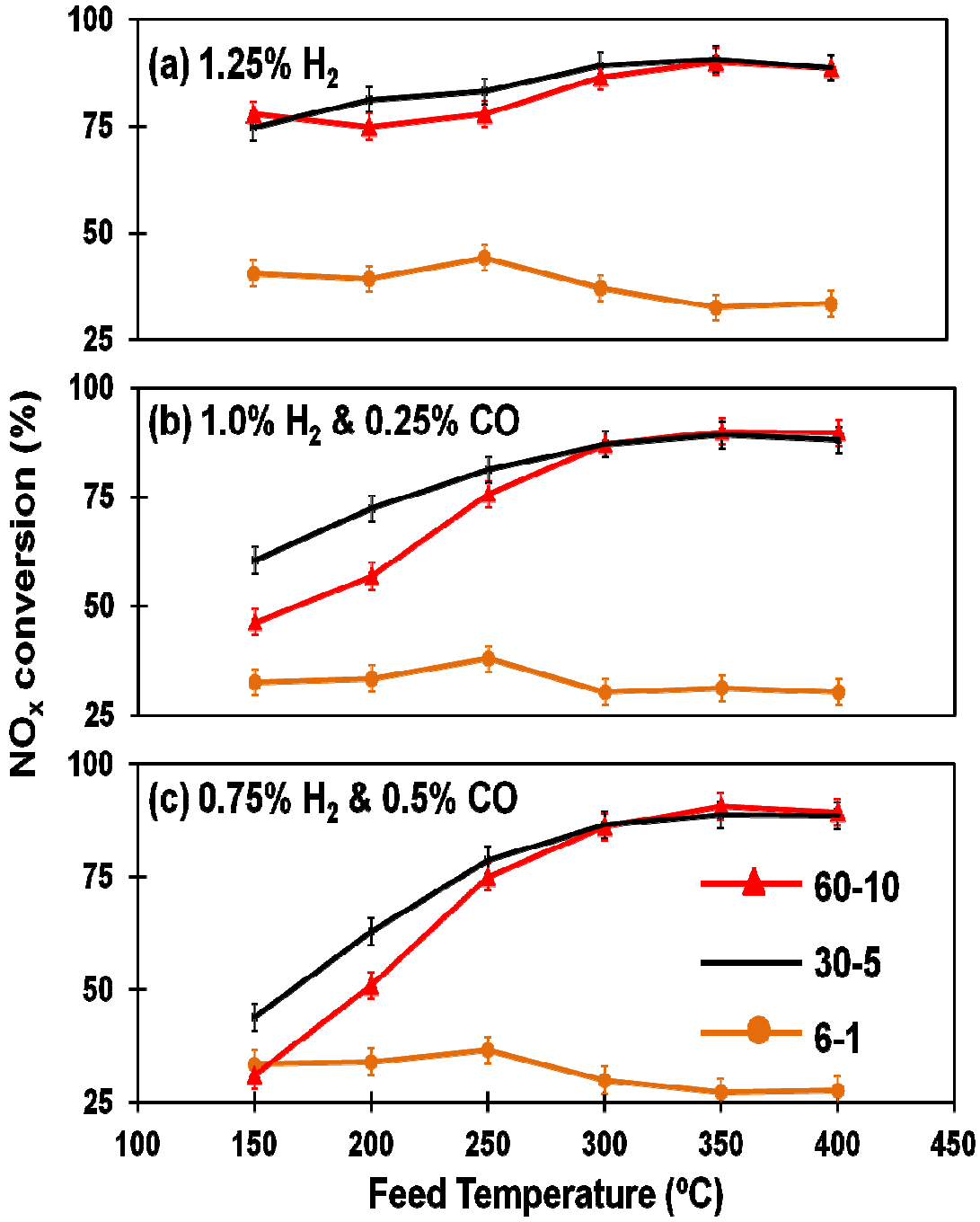

Figure 6-15 Comparison of NO_x conversion under different lean-rich cycles by an aged zoned UL-DH-3 catalyst using mixtures with 1.25% CO/H_2 reductants mixtures.

6.4 Conclusions

The LNT-SCR dual-layer catalyst experiments generated novel information and understanding about the impact of the reductant compositions, the impact of ceria zoning and the feasibility to reduce the PGM loading. The experiments tested proposed key improvements and the main findings were:

- CO inhibition of the LNT catalyst at low temperatures is a key obstacle for NO_x reduction when using mixtures of H_2 and CO. Increasing the SCR loading on the dual-layer catalyst improves the low-temperature NO_x reduction.
- Ceria addition to the LNT layer improves the low-temperature NO_x reduction by enhancing the reverse water-gas-shift reaction, but an undesirable impact is the enhanced NH_3 oxidation at high temperatures.
- Zoned ceria addition to the dual-layer catalyst improves the low temperature NO_x reduction and minimizes NH_3 oxidation at high temperatures. For a fixed total ceria loading, the NO_x conversion by a dual-layer catalyst with a ceria-free upstream zone and a ceria-rich downstream zone is 5-10% higher than one with a uniform ceria deposition.
- The PGM loading in a dual-layer catalyst can be reduced by increasing the SCR loading. A high SCR loading improves the low-temperature NO_x conversion, while the NO_x conversion above 250°C is limited by NO_x storage and the subsequent NH_3 formation from the LNT catalyst.

- Adjustment of the ratio of lean to rich feed time and the total duration of lean-rich cycle can increase the NO_x conversion and enable minimizing the impact of CO inhibition at low temperatures.

These findings reveal that the dual-layer catalyst is an attractive design alternatives has the potential to enhance the NO_x reduction, lower the PGM loading and increase the fuel economy. These improvements can be accomplished by adjusting the catalyst design variables and operating strategies.

Chapter 7 Conclusions And Recommendations

7.1 Conclusions

This study, which consists of two parts, investigated the operation of LNT/SCR dual-layer catalyst. In the first part, the impact of ceria on NO_x storage and reduction was investigated. The second part studied the NO_x reduction over a series of dual-layer catalysts.

7.1.1 Spatio-temporal Features of Periodic Oxidation over the PtCe Catalyst

Infra-Red measurements revealed that the cyclic shifts between the lean and rich (H_2 and/or CO) feeds to a $Pt/CeO_2/\gamma\text{-}Al_2O_3$ monolith catalyst generated a complex, spatio-temporal temperature rise. The effluent concentrations did not reflect these complex interactions. This led to the important conclusion that a study of only the reactor effluents cannot enable the understanding of what occurs inside the monolith. A sharp temperature rise occurred in the upstream of the monolith shortly after the cyclic introduction of H_2/CO to a pre-oxidized catalyst or O_2 to a pre-reduced catalyst. The upstream hot zone temperature decreased with time without forming a downstream moving temperature front. The intricate transient temperature gradients were caused by a competition between the chemical and transport rate process. While the reductant was oxidized in the monolith upstream right after the lean-to-rich (LR) transitions the almost pure nitrogen flow sweeps most of loosely-bound oxygen in the downstream. The majority of the oxygen that reacted was the loosely-held oxygen, which could be easily removed by a gas purge. For example, only about 20% of the total oxygen trapped during

the pre-oxidation with a 5% O_2/N_2 mixture at 350 ^oC was strongly held or chemisorbed. The removal of the loosely held, or physisorbed, oxygen by the introduction of a nitrogen sweep between the lean and rich feeds led to a much more uniform reduction and a moving temperature front. The peak temperature rise after a lean-to-rich (LR) switch was much higher that following a rich-to-lean (RL) switch, because the oxygen adsorbed on the Pt was replenished by spillover from the CeO_2 during the LR switch. Although the spatial features of the thermal fronts were insensitive to the change of operating parameters, the amplitude of the hot spot highly depended on the operating condition. The peak temperature rise decreased with the monolith temperature. It achieved a local maximum at 350 ºC due to the H_2O desorption. The peak temperature rise increased monotonically with the space velocity for a constant monolith temperature. The peak temperature rise increased with the increase of either the fed reductant or oxygen concentration. The peak temperature rise depended on the feed composition due to differences in the temperature dependencies of the oxidation rate of CO and H_2. Using CO as the reductant led to a higher peak temperature rise above 200 ºC than that of H_2, while the strong CO binding below 200 ºC led to a lower peak temperature rise. H_2 assisted the low-temperature CO oxidation.

7.1.2 NO_x Storage and Reduction over the PtCe Catalyst

The NO_x storage experiments over a model $Pt/CeO_2/\gamma\text{-}Al_2O_3$ lean NO_x trap catalyst revealed that the catalyst storage capacity strongly depended on the composition of the fed NO_x mixtures. The NO storage was a Pt-catalyzed process, forming surface

nitrosyl and nitrates in the vicinity of Pt. The NO_2 storage could proceed over the catalyst surface without the Pt participation. The O_2 addition to the NO feed enhanced the NO storage by in situ NO_2 formation. The O_2 addition to the NO_2 feed competed for the catalyst storage sites, lowering the NO_x storage capacity.

The H_2-TPR experiments showed that the first step of the NO_x reduction over Pt/ceria was the Pt surface purging. The reduction of adsorbed oxygen occurred prior to the NO_x reduction over ceria.

The optimal NO_x storage and reduction over the PtCe catalyst occurred at 250 °C when both NO and O_2 were fed.

7.1.3 The Behavioral Features of NO_x Reduction over the Dual-layer Catalyst

The NO_x storage and reduction over monolith-supported dual-layer catalysts consisting of a layer of a metal-exchanged (Fe, Cu) zeolite (ZSM-5) selective catalytic reduction (SCR) catalyst deposited on top of a $Pt/Rh/BaO/CeO_2$ lean NO_x trap (LNT) catalyst revealed several important features.

- The SCR catalyst led to high N_2 selectivity and low NH_3 selectivity over the temperature range of 150 to 300 ºC. The NH_3 generated over the bottom LNT layer was captured by the top SCR layer and used for the N_2 generation.
- The higher low-temperature SCR activity and NH_3 storage capacity of the Cu-exchanged ZSM-5 than the Fe-exchanged ZSM-5 resulted in a higher NO_x conversion and N_2 selectivity of the CuZ-LNT than that of the FeZ-LNT.

- The undesired side reactions in the LNT layer, such as NH_3 oxidation to N_2O at low temperatures and NO_x at high temperatures, hurt the deNO_x performance of the dual-layer catalysts.

The performance of dual-layer catalysts can be tuned by changing the operating environment and the catalyst composition. Feeding H_2O and CO_2 showed that the dual-layer catalyst had a higher NO_x conversion than the LNT catalyst below 300 ºC and a higher N_2 selectivity over the entire temperature range. The addition of CO_2 and H_2O to the feed can enhance the NH_3 selectivity and minimize the NH_3 oxidation in the bottom LNT layer. Ceria in dual-layer catalysts was an important catalyst design parameter. The low-temperature NO_x conversion increased with the ceria loading due to the enhanced NO_x storage capacity and regeneration efficiency. The durability of ceria-containing dual-layer catalysts improved due to a high resistance towards the hydrothermal aging. Ceria avoided the mixing of PGM and barium between the LNT and SCR layers. However, the increase of ceria loading increased the undesired NH_3 oxidation at high temperatures.

7.1.4 Lean NO_x Reduction by H_2 and CO

The NO_x reduction over a ceria-free LNT catalyst revealed that the CO reductant was detrimental to the low-temperature NO_x reduction. The cycle-averaged NO_x conversion decreased with an increase in the CO/H_2 ratio due to the CO poisoning, especially below 250 ºC. The low-temperature NO_x reduction can be increased by changing the catalyst composition. The use of an LNT/SCR dual-layer catalyst improved

the low-temperature NO_x conversion by adding a SCR pathway, while the addition of CeO_2 to the LNT catalyst mitigated the CO poison. However, the ceria-rich dual-layer catalyst decreased the high-temperature reductive conversion of NO_x due to the promotion of the undesired NH_3 oxidation to NO_x. Zoning with a ceria-free front zone and a ceria-rich back zone led to a beneficial interaction of the ceria and H_2. High NO_x conversion was obtained during the entire temperature range.

Dual-layer catalysts with the aged LNT as the bottom layer demonstrated that the PGM loading can be reduced. The performance of the dual-layer catalyst with the bottom aged LNT layer can be improved by increasing the SCR catalyst loading and optimizing the lean-to-rich cycle. A high SCR loading led to a high NO_x conversion at low temperatures, but had little impact on the high-temperature performance. The increase in the rich feed duration with the corresponding decrease in the reductant concentration enhanced the NH_3 production by the bottom LNT layer and thus increased the NO_x conversion. The decrease of the total cycle time improved the utilization efficiency of the fast sites for NO_x storage and NH_3 generation, increasing the NO_x conversion. The highest NO_x conversion using a dual-layer catalyst with a 4.6 g/in^3 aged LNT loading and a 2.0 g/in^3 SCR loading was obtained with a 30s:5s lean-rich cycle for all CO/H_2 ratios.

7.2 Recommendations for Future Work

The previous study shows the important role of NH_3 in NO_x reduction over the dual-layer catalyst. To enhance the NO_x reduction efficiency of dual-layer catalysts, the LNT catalyst should have a high NH_3 generation ability. This can be realized by

modifying the catalyst compositions. For example, a LNT catalyst with low PGM dispersion is a better NH_3 generator than the one with high PGM dispersion. The ceria loading of the LNT catalyst should be optimized to improve the NO_x storage and NH_3 production below 250 ºC and avoid NH_3 oxidation to N_2 or NO_x above 250 ºC. Low-temperature SCR catalysts should be used to improve the NH_3 utilization efficiency. One of the bottlenecks for the current dual-layer catalyst is the low SCR activity at low temperatures. This problem can be solved by changing the zeolitic supports and exchanged metals. Cu/SSZ-13 and Cu/SAPO-34 have better low-temperature SCR activity and thermal stability than Cu/ZSM-5. Also, Mn is a better low-temperature SCR catalyst than Cu. Since the LNT catalyst containing excessive PGM is needed to meet the low-temperature NO_x reduction requirements, the use of active low-temperature SCR catalysts can diminish the NO_x reduction burden on LNT catalyst, leading to a reduction in both PGM and LNT loadings. The system cost may be lowered by using a higher loading of SCR catalyst and a lower loading of LNT catalyst.

A proper arrangement of LNT and SCR catalysts may increase the NO_x conversion and reduce the metal loadings. This requires a comprehensive understandings and appropriate comparisons of LNT/SCR dual-layer, multi-layer, dual-brick, multi-brick and mixture catalysts. Each configuration has advantages and disadvantages. For example, an LNT-bottom SCR-top dual-layer catalyst can maximize the NH_3 storage, but enhance the NH_3 oxidation at high temperatures. The LNT-front SCR-back dual-brick catalyst can minimize the undesired NH_3 oxidation, but the back SCR brick has little contribution to NO_x conversion at high temperatures. A carefully designed LNT/SCR catalyst

configuration can take full advantage of its strengths and minimize its weaknesses. One example is the use of dual-zoned dual-layer catalyst in this study.

Besides H_2 and CO, the use of hydrocarbon reductants should be studied for NO_x reduction. The feed during catalyst regeneration may include hydrocarbon reductants, ranging from C_3H_6, aromatics to even partially oxidized diesel. In this scenario, the catalyst performance could be jeopardized by the possible carbon cake fouling and CO inhibition. This may require the adjustments in the catalyst composition and operating strategy. For example, a fuel reformer may be placed in front of dual-layer catalyst to convert the hydrocarbons to H_2 and CO.

SO_x positioning and the thermal stability of dual-layer catalyst should be studied. PGM-containing LNT catalysts are very vulnerable to SO_x that strongly adsorbs onto the surface of PGM, barium and alumina, sharply decreasing their surface areas and reactivities. SO_x also poisons the active metals, such as Fe and Cu, in the SCR catalysts. Hence, the periodic regeneration of stored SO_x at high temperatures would be necessary to maintain the dual-layer catalyst function. The SO_x regeneration is usually carried out at 600-700 ºC, resulting in a strong sintering of PGM particles and the collapse of SCR zeolitic structures. This sintering hurts the dual-layer catalyst performance. The catalyst composition should be optimized to minimize the impact of SO_x poison and high-temperature aging. For example, the use of the ceria-zirconia solid solutions as the supporter may mitigate the SO_x poisoning of the PGM and stabilize the PGM particles at high temperatures.

Modeling of dual-layer catalyst needs to incorporate the existing understandings about dual-layer catalysts and guide future development efforts. For example, modeling of NO_x reduction chemistry and transport process over dual-layer catalyst may help to reduce the diffusion limitations, and of the amount of catalysts loaded and the system cost. A scale-up of dual-layer catalytic system from the micro reactor scale to the full-size diesel utilities will also benefit from the modeling efforts.

References

1. http://www.epa.gov/ttn/chief/trends/index.html, 1970-2011 Average annual emissions.
2. http://www.dieselnet.com/standards/us/hd.php#pre04, Heavy-Duty Truck and Bus Engines.
3. Abd-Alla, G. H., 2002. Using exhaust gas recirculation in internal combustion engines: a review. *Energy Conversion and Management* 43, 1027-1042.
4. Agarwal, D., Singh, S. K., Agarwal, A. K., 2011. Effect of Exhaust Gas Recirculation (EGR) on performance, emissions, deposits and durability of a constant speed compression ignition engine. *Applied Energy* 88, 2900-2907.
5. Copalakrrshnan, R., Stafford, P. R., Davrdson, J. E., Hecker, W.C., Bartholomew, C. H., 1993. Selective catalytic reduction of nitric oxide by propane in oxidizing atmosphere over copper-exchanged zeolites. *Applied Catalysis B Environmental* 2, 165-182.
6. Kubacka, A., Janas, J., Włoch, E., Sulikowski, B., 2005. Selective catalytic reduction of nitric oxide over zeolite catalysts in the presence of hydrocarbons and the excess of oxygen. *Catalysis Today* 101, 139-145.
7. Amiridis, M.D., Zhang, T., Farrauto, R.J., 1996. Selective catalytic reduction of nitric oxide by hydrocarbons. *Applied Catalysis B: Environmental* 10, 203-227.
8. Burch, R., Breen, J.P., Meunier, F.C., 2002. A review of the selective reduction of NOx with hydrocarbons under lean-burn conditions with non-zeolitic oxide and platinum group metal catalysts. *Applied Catalysis B: Environmental* 39, 83-303.

9. Colombo, M., Nova, I., Tronconi, E., 2010. A comparative study of the NH3-SCR reactions over a Cu-zeolite and a Fe-zeolite catalyst. *Catalysis Today* 151, 223-230.
10. Fedeyko, J.M., Chen, B., Chen, H., 2010. Mechanistic study of the low temperature activity of transition metal exchanged zeolite SCR catalysts. *Catalysis Today* 151, 231-236.
11. Metkar, P.S., Salazar, N., Muncrief, R., Balakotaiah, V., Harold, M.P., 2011. Selective catalytic reduction of NO with NH3 on iron zeolite monolithic catalysts: Steady-state and transient kinetics. *Applied Catalysis B: Environmental* 104, 110-126.
12. Kamasamudram, K., Currier, N.W., Chen, X., Yezerets, A., 2010. Overview of the practically important behaviors of zeolite-based urea-SCR catalysts using compact experimental protocol. *Catalysis Today* 151, 212-222.
13. Kamasamudram, K., Currier, N.W., Chen, X., Szailer, T., Yezerets, A., 2010. Why Cu- and Fe-Zeolite SCR Catalysts Behave Differently At Low Temperatures. *SAE international* 010-01-1182, 664-672.
14. Metkar, P.S., Harold, M.P., Balakotaiah, V., 2012. Selective catalytic reduction of NOx on combined Fe- and Cu-zeolite monolithic catalysts: Sequential and dual layer configurations. *Applied Catalysis B: Environmental* 111-112, 67-80.
15. Paule, M., Mackensen, A., Binz, R., Enderle, C., 2011. Challenges for the Next Generation of BlueTEC Emission Technology. *SAE Technical Paper* 2011-01-0294.
16. Waldbuesser, N., Guenther, J., Hoffmann, H., Erlenmayer, O., Duvinage,F., Enderle, C., Schommers, J., Waeller, D., 2010. Specifics of Daimler's new SCR system

(BLUETEC) in the Diesel Sprinter Van - Certified for NAFTA 2010. *SAE Technical Paper* 2010-01-1172.

17. Epling, W.S., Campbell, L.E., Yezerets, A., Currier, N.W., Parks, J.E., 2007. Overview of the Fundamental Reactions and Degradation Mechanisms of NOx Storage/Reduction Catalysts. *Catalysis Reviews: Science & Engineering* 46, 163-245.
18. Olsson, L., Persson, H., Fridell, E., Skoglundh, M., Andersson, B., 2001. A Kinetic Study of NO Oxidation and NOx Storage on Pt/Al2O3 and Pt/BaO/Al2O3. *Journal of Physical Chemistry B* 105, 6895-6906.
19. Kabin, K.S., Khanna, P., Muncrief, R.L., Medhekar, V., Harold M.P., 2006. Monolith and TAP reactor studies of NOx storage on Pt/BaO/Al2O3: Elucidating the mechanistic pathways and roles of Pt. *Catalysis Today* 114, 72-85.
20. Kabin, K.S., Muncrief, R.L., Harold M.P., Li, Y., 2004. Dynamics of storage and reaction in a monolith reactor: lean NOx reduction. *Chemical Engineering Science* 59, 5319-5327.
21. Clayton, R.D., Harold, M.P., Balakotaiah, V., 2008. NOx storage and reduction with H2 on Pt/BaO/Al2O3 monolith: Spatio-temporal resolution of product distribution. *Applied Catalysis B: Environmental* 84, 616-630.
22. Kumar, A., Harold, M.P., Balakotaiah, V., 2010. Isotopic studies of NOx storage and reduction on Pt/BaO/Al2O3 catalyst using temporal analysis of products. *Journal of Catalysis* 270, 214-223.

23. Kumar, A., Harold, M.P., Balakotaiah, V., 2010. Estimation of Effective Diffusivity of Stored NOx in the Barium Phase of Pt/BaO/Al2O3 Catalysts using TAP. *Industrial & Engineering Chemistry Research* 49, 10334-10340.
24. Sharma, M., Kumar, A., Harold, M.P., Balakotaiah, V., 2005. Analysis of Periodic Storage and Reduction of NOx in Catalytic Monoliths. *Industrial & Engineering Chemistry Research* 44, 6264-6277.
25. Bhatia, D., Clayton, R.D., Harold, M.P., Balakotaiah, V., 2009. A global kinetic model for NOx storage and reduction on Pt/BaO/Al2O3 monolithic catalysts. *Catalysis Today* 147, 250-256.
26. Xu, J., Clayton, R.D., Balakotaiah, V., Harold, M.P., 2008. Experimental and microkinetic modeling of steady-state NO reduction by H2 on Pt/BaO/Al2O3 monolith catalysts. *Applied Catalysis B: Environmental* 77, 395-408.
27. Shakya, B.M., Harold, M.P., Balakotaiah, V., 2012. Crystallite-Scale Model for NOx Storage and Reduction on Pt/BaO/Al2O3: Pt Dispersion Effects on NOx Conversion and Ammonia Selectivity. *Catalysis Today* 184, 27-42.
28. Gorte, R.J., 2010. Ceria in Catalysis: From Automotive Applications to the Water-Gas Shift Reaction. *AIChE* 56, 1126-1135.
29. Damyanova, S., Bueno, J.M.C., 2003. Effect of CeO2 loading on the surface and catalytic behaviors of CeO2-Al2O3-supported Pt catalysts. *Applied Catalysis A: General* 253, 135-150.
30. Yao, H.C., Yao, Y.F.Y., 1984. Ceria in Automotive Exhaust Catalysts I. Oxygen Storage. *Journal of Catalysis* 86, 254-265.

31. Ji, Y., Choi, J., Toops, T.J., Crocker, M., Naseri, M., 2008. Influence of ceria on the NOx storage/reduction behavior of lean NOx trap catalysts. *Catalysis Today* 136, 146-155.

32. Morita, T., Suzuki, N., Satoh, N., Wada, K., Ohno, H., 2007. Study on Low NOx Emission Control Using Newly Developed Lean NOx Catalyst for Diesel Engines. *SAE Technical Paper* 2007-01-0239.

33. Wada, K., Suzuki, N., Satoh, N., Morita, T., Yamaguchi, S., Ohno, H., 2007. Study on Emission Reducing Method with New Lean NOX Catalyst for Diesel Engines. *SAE Technical Paper* 2007-01-1933.

34. Hatanaka, M., Takahashia, N., Tanabea, T., Nagaia, Y., Dohmaea, K., Aoki, Y., Yoshida, T., Shinjoh, H., 2010. Ideal Pt loading for a Pt/CeO2-based catalyst stabilized by a Pt-O-Ce bond. *Applied Catalysis B: Environmental* 99, 336-342.

35. Kwak, J.H., Kim, D.H., Szanyi, J., Peden C.H.F., 2008. Excellent sulfur resistance of Pt/BaO/CeO2 lean NOx trap catalysts. *Applied Catalysis B: Environmental* 84, 545-551.

36. Ren, Y., Harold, M.P., 2011. NOx Storage and Reduction with H2 on Pt/Rh/BaO/CeO2: Effects of Rh and CeO2 in the Absence and Presence of CO2 and H2O. *ACS Catalysis* 1, 969-988.

37. Mulla, S.S., Chen, N., Cumaranatunge, L., Delgass, W.N., Epling, W.S., Ribeiro, F.H., 2006. Effect of potassium and water vapor on the catalytic reaction of nitric oxide and dioxygen over platinum. *Catalysis Today* 114, 57-63.

38. Lietti, L., Nova, I., Forzatti, P., 2008. Role of ammonia in the reduction by hydrogen of NOx stored over Pt-Ba/Al2O3 lean NOx trap catalysts. *Journal of Catalysis* 257, 270-282.

39. Frola, F., Prinetto, F., Ghiotti, G., Castoldi L., Nova, I., Lietti, L., Forzatti, P., 2007. Combined in situ FT-IR and TRM analysis of the NOx storage properties of Pt-Ba/Al2O3 LNT catalysts. *Catalysis Today* 126, 81-89.

40. Lindholm, A., Currier, N.W., Fridell, E., Yezerets, A., Olsson, L., 2007. NOx storage and reduction over Pt based catalysts with hydrogen as the reducing agent Influence of H2O and CO2. *Applied Catalysis B: Environmental* 75, 78-87.

41. Nova, I., Lietti, L., Forzatti, P., Frola, F., Prinetto, F., Ghiotti, G., 2010. Experimental investigation of the reduction of NOx species by CO and H2 over Pt-Ba/Al2O3 lean NOx trap systems. *Catalysis Today* 151, 330-337.

42. Mulla, S.S., Chaugule, S.S., Yezerets, A., Currier, N.W., Delgass, W.N., Ribeiro, F.H., 2008. Regeneration mechanism of Pt/BaO/Al2O3 lean NOx trap catalyst with H2. *Catalysis Today* 136, 136-145.

43. Wang, J., Ji, Y., Easterling, V., Crocker, M., Dearth, M., McCabe, R.W., 2011. The effect of regeneration conditions on the selectivity of NOx reduction in a fully formulated lean NOx trap catalyst. Catalysis Today 175, 83-92.

44. Lietti, L., Nova, I., Forzatti, P., 2008. Role of ammonia in the reduction by hydrogen of NOx stored over Pt-Ba/Al2O3 lean NOx trap catalysts. *Journal of Catalysis* 257, 270-282.

45. Clayton, R.D., Harold, M.P., Balakotaiah, V., Wan, C.Z., 2009. Pt dispersion effects during NOx storage and reduction on Pt/BaO/Al2O3 catalysts. *Applied Catalysis B: Environmental* 90, 662-676.
46. Pereda-Ayo, B., González-Velasco, J.R., Burch, R., Hardacre, C., Chansai, S., 2012. Regeneration mechanism of a Lean NOx Trap (LNT) catalyst in the presence of NO investigated using isotope labelling techniques. *Journal of Catalysis* 285, 177-186.
47. Forzatti, P., Lietti, L., Nova, I., Morandi, S., Prinetto, F., Ghiotti, G., 2010. Reaction pathway of the reduction by CO under dry conditions of NOx species stored onto Pt-Ba/Al2O3 Lean NOx Trap catalysts. *Journal of Catalysis* 274, 163-175.
48. Castoldi, I., Lietti, L., Forzatti, P., Morandi, S., Ghiotti, G., Vindigni, F., 2010. The NOx storage-reduction on Pt-K/Al2O3 Lean NOx Trap catalyst. *Journal of Catalysis* 276, 335-350.
49. DiGiulio, C.D., Komvokis, V.G., Amiridis, M.D., 2012. In situ FTIR investigation of the role of surface isocyanates in the reduction of NOx by CO and C3H6 over model Pt/BaO/Al2O3 and Rh/BaO/Al2O3 NOx storage and reduction (NSR) catalysts. *Catalysis Today* 184, 8-19.
50. Szailer, T., Kwak, J.H., Kim, D.H., Hanson, J.C., Peden, C.H.F., Szanyi, J., 2006. Reduction of stored NOx on Pt/Al2O3 and Pt/BaO/Al2O3 catalysts with H2 and CO. *Journal of Catalysis* 239, 51-64.
51. James, D., Fourré, E., Ishii, M., Bowker, M., 2003. Catalytic decomposition/ regeneration of Pt/Ba(NO3)2 catalysts: NOx storage and reduction. *Applied Catalysis B: Environmental* 45, 147-159.

52. Poulston, S., Rajaram, R.R., 2003. Regeneration of NOx trap catalysts. *Catalysis Today* 81, 603-610.

53. Li, Y., Roth, S., Dettling, J., Beutel. T., 2001. Effects of lean/rich timing and nature of reductant on the performance of a NOx trap catalyst. *Topics in Catalysis* 16/17, 139-144.

54. Scholz, C.M.L., Maes, B.H.W., de Croon, M.H.J.M., Schouten, J.C., 2007. Influence of reducing agent (CO, H2, and C2H4) and of H2O on NOx reduction on a Pt-Ba/γ-Al2O3 catalyst. *Applied Catalysis A: General* 332, 1-7.

55. Jozsa, P., Jobson, E., Larsson, M., 2004. Reduction of NOx stored at low temperatures on a NOx adsorbing catalyst. *Topics in Catalysis* 30/31, 177-180.

56. Gandhi, H.S., Cavataio, J.V., Hammerle, R.H., Cheng, Y., 2009. Catalyst system for the reduction of NOx and NH3 emissions. *United States Patent* 20090149318.

57. Gandhi, H.S., Cavataio, J.V., Hammerle, R.H., Cheng, Y., 2010. Catalyst system for the reduction of NOx and NH3 emissions. *United States Patent* 20100209321.

58. Gandhi, H.S., Cavataio, J.V., Hammerle, R.H., Cheng, Y., 2011. Catalyst system for the reduction of NOx and NH3 emissions. *United States Patent* 20110005200.

59. Rohr, F., Grißtede, I., Sundararajan, A., Müller, W., 2008. Diesel NOx-Storage Catalyst Systems for Tier 2 BIN5 Legislation. *SAE Technical Paper* 2008-01-0766.

60. Chen, H., Weigert, E.C., Fedeyko, J.M., Cox, J.P., Andersen, P.J., 2010. Advanced Catalysts for Combined (NAC + SCR) Emission Control Systems. *SAE Technical Paper* 2010-01-0302.

61. McCarthy, J.E., Dykes, E., Ngan, E., 2010. Aftertreatment System Performance of a Fuel Reformer, LNT and SCR System Meeting EPA 2010 Emissions Standards on a Heavy-Duty Vehicle. *SAE Technical Paper* 2010-01-1942.
62. Xu, L., McCabe, R., Tennison, P., Jen, H., 2011. Laboratory and Vehicle Demonstration of "2nd-Generation" LNT + in-situ SCR Diesel Emission Control Systems. *SAE Technical Paper* 2011-01-0308.
63. Lindholm, A., Sjövall, H., Olsson, L.,2010. Reduction of NOx over a combined NSR and SCR system. *Applied Catalysis B: Environmental* 98, 112-121.
64. Pereda-Ayo, B., Duraiswami, D., González-Velasco, J.R., 2011. Control of NOx storage and reduction in NSR bed for designing combined NSR-SCR systems. *Catalysis Today* 172, 66-72.
65. Seo, C., Kim, H., Choi, B., Lim, M.T., 2011. The optimal volume of a combined system of LNT and SCR catalysts. *Journal of Industrial and Engineering Chemistry* 17, 382-385.
66. Seo, C., Kim, H., Choi, B., Lim, M.T., Lee, C., Lee, C., 2011. De-NOx characteristics of a combined system of LNT and SCR catalysts according to hydrothermal aging and sulfur poisoning. *Catalysis Today* 164, 507-514.
67. Bonzi, R., Lietti, L., Castoldi, L., Forzatti, P., 2010. NOx removal over a double-bed NSR-SCR reactor configuration. *Catalysis Today* 151, 376-385.
68. Forzatti, P., Lietti, L., 2010. The reduction of NOx stored on LNT and combined LNT–SCR systems, *Catalysis Today* 155, 131-139.

69. Castoldi, L., Bonzi, R., Lietti, L., Forzatti, P., Morandi, S., Ghiotti, G., Dzwigaj, S., 2011. Catalytic behaviour of hybrid LNT/SCR systems: Reactivity and in situ FTIR study. *Journal of Catalysis* 282, 128-144.

70. Corbos, E.C., Haneda, M., Courtois, X., Marecot, P., Duprez, D., Hamada, H., 2009. NOx abatement for lean-burn engines under lean-rich atmosphere over mixed NSR-SCR catalysts: Influences of the addition of a SCR catalyst and of the operational conditions. *Applied Catalysis A: General* 365, 187-193.

71. Wang, J., Ji, Y., He, Z., Crocker, M., Dearth, M., McCabe, R.W.,2012. A non-NH3 pathway for NOx conversion in coupled LNT-SCR systems. *Applied Catalysis B: Environmental* 111-112, 562-570.

72. Nakatsuji, T., Matsubara, M., Rouistenmaki, J., Sato, N., Ohno, H., 2007. A NOx reduction system using ammonia-storage selective catalytic reduction in rich/lean excursions. *Applied Catalysis B: Environmental* 77, 190-201.

73. Clayton, R.D., Harold, M.P., Balakotaiah, V., 2008. Selective catalytic reduction of NO by H2 in O2 on Pt/BaO/Al2O3 monolith NOx storage catalysts. *Applied Catalysis B: Environmental* 81, 161-181.

74. Gaillard, F., 2004. Characterisation of Pt/Ceria Catalysts by One-Pass TPD Analysis. *Catalysis Letters* 95, 23-29.

75. Santos, A.C.S.F., Damyanova, S., Texierira, G.N.R., Mattos, L.V., Noronha, F.B., Passos, F.B., Bueno, J.M.C., 2005. Effect of CeO2 loading on the surface and catalytic behaviors of CeO2-Al2O3-supported Pt catalysts. *Applied Catalysis A: General* 290, 123–132.

76. Boaro, M., Vicario, M., de Leitenburg, C., Dolcetti, G., Trovarelli, A., 2003. The use of temperature-programmed and dynamic/transient methods in catalysis: characterization of ceria-based, model three-way catalysts. *Catalysis Today* 77, 407–417.

77. Rinnemo, M.,Fassihi, M.,Kasemo, B.,1993.The critical condition for catalytic ignition. H2/O2 on Pt. *Chemical Physics Letters* 211, 60–64.

78. Joshi, S.Y., Ren, Y., Harold, M.P., Balakotaiah, V. 2011. Determination of kinetics and controlling regimes for H2 oxidation on Pt/Al2O3 monolithic catalyst using high space velocity experiments. *Applied Catalysis B: Environmental* 102, 484-495.

79. Alexeev, O., Kim, D. W., Graham, G.W., Shelef, M., Gates, B.C., 1999. Temperature-Programmed Desorption of Hydrogen from Platinum Particles on γ-Al2O3: Evidence of Platinum-Catalyzed Dehydroxylation of γ-Al2O3. *Journal of Catalysis* 185, 170-181.

80. Bhatia, D., Harold, M.P., Balakotaiah, V., 2009. Kinetic and bifurcation analysis of the cooxidation of CO and H2 in catalytic monolith reactors. *Chemical Engineering Science* 64, 1544-1558.

81. Salomons, S., Votsmeier, M., Hayes, R.E., Drochner, A., Vogel, H., Gieshof, J., 2006. CO and H2 oxidation on a platinum monolith diesel oxidation catalyst. *Catalysis Today* 117, 491-497.

82. Salomons, S., Hayes, R.E., Votsmeier, M., 2009. The promotion of carbon monoxide oxidation by hydrogen on supported platinum catalyst. *Applied Catalysis A: General* 352, 27-34.

83. Hoyle, N.D., Kumaraswamy, P., Self, V.A., Sermon, P.A., Vong, M.S.W.,1999. Catalysis of H2, CO and alkane oxidation-combustion over Pt/Silica catalysts: evidence of coupling and promotion. *Catalysis Today* 47, 45-49.

84. Pedrero, C., Waku, T., Iglesia, E., 2005. Oxidation of CO in H2-CO mixtures catalyzed by platinum: alkali effects on rates and selectivity. *Journal of Catalysis* 233, 242-255.

85. Altman, E.I., Gorte, R.J., 1986. The desorption of CO from small Pt particles on Al2O3. *Surface Science* 172, 71-80.

86. Bourane, A., Derrouiche, S., Bianchi, D., 2004. Impact of Pt dispersion on the elementary steps of CO oxidation by O2 over Pt/Al2O3 catalysts. *Journal of Catalysis* 228, 288-297.

87. Mhadeshwar, A.B., Vlachos, D.G., 2005. Hierarchical, multiscale surface reaction mechanism development: CO and H2 oxidation, water-gas shift, and preferential oxidation of CO on Rh. *Journal of Catalysis* 234, 48-63.

88. Nagai, Y., Dohmae, K., Ikeda, Y., Takagi, N., Hara, N., Tanabe, T., Guilera, G., Pascarelli, S., Newton, M.A., Takahashi, N., Shinjoh, H., Matsumoto, S., 2011. In situ observation of platinum sintering on ceria-based oxide for autoexhaust catalysts using Turbo-XAS. *Catalysis Today* 175, 133-140.

89. Yoshida, K., Asanuma, T., Nishioka, H., Hayashi, K., Hirota, S., 2007. Development of NOx Reduction System for Diesel Aftertreatment with Sulfur Trap Catalyst. *SAE Technical Paper* 2007-01-0237.

90. Ji, Y., Fisk, C., Easterling, V., Graham, U., Poole, A., Crocker, M., Choi, J., Partridge, W., Wilson, K., 2010. NOx storage-reduction characteristics of Ba-based lean NOx trap catalysts subjected to simulated road aging. *Catalysis Today* 151, 362-375.
91. Wang, J., Ji, Y., Graham, U., Cesar, C., Crocker, M., 2011. NOx Reduction on Fully Formulated Lean NOx Trap Catalysts Subjected to Simulated Road Aging: Insights from Steady-State Experiments. *Chinese Journal of Catalysis* 32, 736-745.
92. Itoh, M., Motoki, K., Takehara, M., Saito, M., Machida, K., 2009. Selective NOx reduction in H2 + NO + O2 reaction under oxygen-rich condition over Pt/rare earth oxide catalysts. *IOP Conference Series: Materials Science and Engineering* 1, 1-7.
93. Caglar, B., Uner, D., 2011. NO oxidation and NOx storage over Ce-Zr mixed oxide supported catalysts. *Catalysis Communications* 12, 450-453.
94. Adamowska, M., Krzton, A., Najbar, M., Da Costa, P., Djega-Mariadassou, G., 2008. DRIFT study of the interaction of NO and O2 with the surface of Ce0.62Zr0.38O2 as deNOx catalyst. *Catalysis Today* 137, 288-291.
95. Matsouka, V., Konsolakis, M., Lambert, R.M., Yentekakis, I.V., 2008. In situ DRIFTS study of the effect of structure (CeO2–La2O3) and surface (Na) modifiers on the catalytic and surface behaviour of Pt/g-Al2O3 catalyst under simulated exhaust conditions. *Applied Catalysis B: Environmental* 84, 715-722.
96. Maeda, N., Urakawa, A., Baiker, A., 2009. Support Effects and Chemical Gradients along the Catalyst Bed in NOx Storage-Reduction Studied by Space- and Time-Resolved In Situ DRIFTS. *Journal of Physical Chemistry C* 113, 16724-16735.

97. Azambre, B., Zenboury, L., Delacroix, F., Weber, J.V., 2008. Adsorption of NO and NO2 on ceria-zirconia of composition Ce0.69Zr0.31O2: A DRIFTS study. *Catalysis Today* 137, 278-282.

98. Franchini, C.A., Cesar, D.V., Schmal, M., 2010. The Interaction of Oxides of the Pd/Ce/Zr/Al2O3 Catalysts Prepared by Impregnation Over Alumina and Promoting Effects on Surface Properties. *Catalysis Letter* 137, 45-54.

99. Hadjitvanov, K. I., 2007. Identification of Neutral and Charged NxOy Surface Species by IR Spectroscopy. *Catalysis Reviews: Science and Engineering* 42, 71-144.

100. Liu, Y., Meng, M., Zou, Z., Li, X., Zha, Y., 2008. In situ DRIFTS investigation on the NOx storage mechanisms over Pt/K/TiO2–ZrO2 catalyst. *Catalysis Communications* 10, 173-177.

101. Azambre, B., Zenboury, L., Koch, A., Weber, J.V., 2009. Adsorption and Desorption of NOx on Commercial Ceria-Zirconia (CexZr1-xO2) Mixed Oxides: A Combined TGA, TPD-MS, and DRIFTS study. *Journal of Physical Chemistry C* 113, 13287-13299.

102. Azambre, B., Atribak, I., Bueno-Lopez, A., Garcia-Garcia, A., 2010. Probing the Surface of Ceria-Zirconia Catalysts Using NOx Adsorption/Desorption: A First Step Toward the Investigation of Crystallite Heterogeneity. *Journal of Physical Chemistry C* 114, 13300-13312.

103. Ji, Y., Toops, T.J., Graham, U.M., Jacobs, G., Crocker, M., 2006. A kinetic and DRIFTS study of supported Pt catalysts for NO oxidation. *Catalysis Letters* 110, 29-37.

104. Hensel, K., Morvova, M., 1996. The Conversion of NOx in a Corona Discharge with an Electrode Material Variation. *Contributions to Plasma Physics* 36, 51-61.

105. Philipp, S., Drochner, A., Kunert, J., Vogel, H., Theis, J., Lox, E.S., 2004. Investigation of NO adsorption and NO/O2 co-adsorption on NOx-storage-components by DRIFT-spectroscopy. *Topics in Catalysis* 30/31, 235-238.

106. Huang, S.J., Walters, A.B., Vannice, M.A., 2000. TPD, TPR and DRIFTS studies of adsorption and reduction of NO on La2O3 dispersed on Al2O3. *Applied Catalysis B: Environmental* 26, 101-118.

107. Sedlmair, C., Seshan, K., Jentys, A., Lercher, J.A., 2003. Elementary steps of NOx adsorption and surface reaction on a commercial storage-reduction catalyst. *Journal of Catalysis* 214, 308-316.

108. Berner, U., Schierbaum, K., Jones, G., Wincott, P., Haq, S., Thornton, G., 2000. Ultrathin ordered CeO2 overlayers on Pt(111): interaction with NO2, NO, H2O and CO. *Surface Science* 467, 201-213.

109. Bhatia, D., McCabe, R.W., Harold, M.P., Balakotaiah, V., 2009. Experimental and kinetic study of NO oxidation on model Pt catalysts. *Journal of Catalysis* 266, 106-119.

110. Liu, Y., Harold, M.P., Luss, D., 2011. Spatio-temporal features of periodic oxidation of H2 and CO on Pt/CeO2/Al2O3. *Applied Catalysis A: General* 397, 35-45.

111. Nova, I., Lietti, L., Forzatti, P., 2008. Mechanistic aspects of the reduction of stored NOx over Pt-Ba/Al2O3 lean NOx trap systems. *Catalysis Today* 136, 128-135.

112. Grossale, A., Nova, I., Tronconi, E., Chatterjee, D., Weibel, M., 2010. The chemistry of the NO/NO2–NH3 “fast” SCR reaction over Fe-ZSM5 investigated by transient reaction analysis. *Journal of Catalysis* 256, 312-322.

113. Zhang, X., Shen, Q., He, C., Ma, C., Cheng, J., Li, L., Hao, Z., 2012. Investigation of Selective Catalytic Reduction of N2O by NH3 over an Fe–Mordenite Catalyst: Reaction Mechanism and O2 Effect. *ACS Catalysis* 2, 512-520.

114. Ji, Y., Easterling, V., Graham, U., Fisk, C., Crocker, M., Choi, J,. 2011. Effect of aging on the NOx storage and regeneration characteristics of fully formulated lean NOx trap catalysts. *Applied Catalysis B: Environmental* 103, 413-427.

115. Toops, T.J., Bunting, B.G., Nguyen, K., Gopinath, A., 2007. Effect of engine-based thermal aging on surface morphology and performance of Lean NOx Traps. *Catalysis Today* 123, 285-292.

116. Wilken, N., Wijayanti, K., Kamasamudram, K., Currier, N.W., Vedaiyan, R., Yezerets, A., Olsson, L., 2012. Mechanistic investigation of hydrothermal aging of Cu-Beta for ammonia SCR. *Applied Catalysis B: Environmental* 111-112, 58-66.

117. Toops, T.J., Nguyen, K., Foster, A.L., Bunting, B.G., Ottinger, N.A., Pihl, J.A., Hagaman, E.W., Jiao, J., 2010. Deactivation of accelerated engine-aged and field-aged Fe–zeolite SCR catalysts. *Catalysis Today* 151, 257-265.

118. Cheng, Y., Hoard, J., Lambert, C., Kwak, J.H., Peden, C.H.F., 2008. NMR studies of Cu/zeolite SCR catalysts hydrothermally aged with urea. *Catalysis Today* 136, 34-39.

119. Rogemond, E., Fréty, R., Perrichon, V., Primet, M., Chevrier, M., Gauthier, C., Mathis, F., 1997. Evolution of the ceria surface area of Pt/Rh ceria-alumina catalysts

submitted to hydrothermal aging at 1273 K. *Applied Catalysis A: General* 156, 253-265.

120. Lafayatis, D. S., Ansell, G.P., Bennett, S.C., Forst, J.C., Millington, P.J., Rajaram, P.R., Walker, A.P., Ballinger, T.H., 1998. Ambient temperature light-off for automobile emission control. *Applied Catalysis B: Environmental* 18, 123-135.

121. Corbos, E.C., Haneda, M., Courtois, X., Marecot, P., Duprez, D., Hamada, H., 2008. Cooperative effect of Pt–Rh/Ba/Al and CuZSM-5 catalysts for NOx reduction during periodic lean-rich atmosphere. *Catalysis Communications* 10, 137-141.

122. Phatak, A.A., Koryabkina, N., Rai, S., Ratts, J.L., Ruettinger, W., Farrauto, R.J., Blau, G.E., Delgass, W.N., Ribeiro, F.H., 2007. Kinetics of the water-gas shift reaction on Pt catalysts supported on alumina and ceria. *Catalysis Today* 123, 224-234.

123. Liu, Y., Harold, M.P., Luss, D., 2012. Coupled NOx storage and reduction and selective catalytic reduction using dual-layer monolithic catalysts. *Applied Catalysis B: Environmental* 121-122, 239-251.

124. Harold, M.P., Garske, M.E., 1991. Kinetics and multiple rate states of CO oxidation on Pt I. Model development and multiplicity analysis. *Journal of Catalysis* 127, 524-552.

125. Harold, M.P., Garske, M.E., 1991. Kinetics and multiple rate states of CO oxidation on Pt II. Linking UHV and atmospheric pressure kinetic behavior. *Journal of Catalysis* 127, 553-575.

126. Theis, J., Dearth, M., McCabe, R., 2011. LNT+SCR Catalyst Systems Optimized for NOx Conversion on Diesel Applications," *SAE Technical Paper* 2011-01-0305.